Electrodeposition and Characterisation of Semiconductor Materials

Cummings, Charlie

Award date:
2012

Awarding institution:
University of Bath

Electrodeposition and Characterisation of Semiconductor Materials

Charles Yianni Cummings

A thesis submitted for the degree of Doctor of Philosophy

University of Bath

Department of Chemistry

May 2012

Charles Yianni Cummings

Table of Contents

Abstract

The general theme of this thesis is the investigation of light harvesting materials as solar absorbers. The chapters reported within this thesis can be divided into two domains. The first half concerns issues for the electroformation of uniform copper indium diselenide (CISe) thin films and the latter half investigates surface electrochemical processes exhibited by mesoporous, nanocomposite thin films.

Several strategies were investigated concerning the formation of reproducible, large area (ca. 10 cm^2), uniform CISe thin films. The examination of a novel substrate for the electrodeposition of CISe is discussed in chapter 2. Here molybdenum coated glass slides undergo a pre-selenisation to form $MoSe_2$/Mo/glass. The $MoSe_2$ is inert and resistant to chemical attack as well as degenerate in nature. Photoactive CISe films were formed on $MoSe_2$/Mo electrodes to demonstrate their potential as substrates for devices.

The use of a rocking disc electrode for the electroformation of large area (ca. 12.1cm^2) copper and CISe films is shown in chapters 3 and 4 respectively. The rocking disc electrode induces mass transport by rocking (vibrating) the cell. The induced convection was investigated by monitoring limiting currents of $Ru^{II/III}(NH_3)_6^{3+}$ and potentiostatic deposition of uniform copper films free from pitting and pores was performed. Under rocking disc conditions it is possible to attain a 1:1 ratio in CuIn films using a tartrate based plating bath. Films are selenised to form CISe and as a by-product Cu_xSe. The photoactivity of the films is non-uniform and patchy due to the presence of Cu_xSe and/or pin holes which occur from either under or over etching the film. Various post selenisation treatments were performed to improve the photoactivity of the films such as the dilution of etchant, re-annealing the CISe film and the use of an oxidising agent in conjugation with the etchant.

The second part of this thesis investigates the surface electrochemistry of nanocomposite films Fe_2O_3 and di-ruthenium-bis(benzimidazolyl)pyridine – TiO_2 which are shown in chapters 5 and 6, respectively. Mesoporous Fe_2O_3 thin films exhibit a higher oxidation state which is likely to be a key intermediate for the oxidation of water. By using the spectro-electrochemical methods potential

modulated spectroscopy and light induced spectroscopy it is possible to attain *in situ* transmission spectra of this state. The spectra correspond to a surface trapped hole which has been reported by others. The frequency dependence of this surface state was investigated and correlated with theory.

In the final experimental chapter films composed of an inorganic di- ruthenium-bis(benzimidazolyl)pyridine complex (Ru_2) and TiO_2 nanoparticles were produced. The films exhibited an immobilised Ru signal. Using focus ion beam methods the creation of a nano-trench in a film of ITO was undertaken. The immobilisation of this material within the trench allowed bi-potentiostatic experiments to be conducted which evaluated the charge diffusion processes. An apparent diffusion coefficient of D_{app} = 2.5 x 10^{-15} ms^{-2} was attained using generator and collector experiments. The potential use of these junction electrodes for other nanocomposite materials is highlighted.

Acknowledgements

First and foremost I would like to thank my supervisor, Professor Frank Marken, who's enthusiasm and dedication has truly been inspirational and it has been a pleasure to work under this supervision for the past 3 years. I would also like to thank numerous undergraduate, PhD students and postdoctoral members (past and present) of the Marken group and as well as a friends outside of the group.

Various research collaborators should be acknowledged such as Dr. Phil Dale in Luxembourg University, Luxembourg who's post doc at the University of Bath was the basis for the funding of my PhD. Professor Masa-aki Haga in Chuo University, Tokyo, Japan for hosting me as a JSPS funded fellowship during the latter stages of my PhD and provided the di-ruthium bipypdimal complexes used in chapter 6. Dr. Ian Forbes and Dr. Gulliume Zoppi at Northumbria University, Newcastle for the general CISe based discussions and for providing the many molybdenum substrates. Dr. Dave Lane and Prof. Keith Rogers at Cranfield University who performed many XRD measurements on my behalf. Mr. Paul Frith in mechanical engineering, University of Bath for making the rocking disc electrode.

I would like to thank my family for all their support during my undergraduate and PhD and who's support over the years has allowed me to pursue my aspirations, I am immensely grateful, thank you.

Finally I would like to thank my financial support, Supergen, (EPSRC grant: Photovoltaic Materials for the 21st Century EP/F029624/1) for funding my PhD.

Chapter 1

Introduction

Contents

1.1. Introduction to Photovoltaics

1.1.1. Photovoltaics commodity or necessity

The importance of the generation of electricity from renewable or carbon neutral sources is becoming more relevant as the human race enters the 21st century. Fossil fuels are a finite resource and the combustion of which has been taken for granted for the last 50 years. As economies of countries around the world grow, an increase in the demand for energy is inevitable.

The burning of fossil fuels, from carbon sinks such as oil, gas and coal releases carbon dioxide, CO_2, into the atmosphere. The CO_2 molecule absorbs photons from the solar spectrum that are usually reflected away from earth and into outer space.

Strong evidence for climate change was propositioned by the international panel on climate change or IPCC. This report concluded that there is a 90 % chance that climate change in the last fifty years is due to humans activity [1]. The sudden increase in CO_2 in the atmosphere is most likely to be the largest contributor to climate change. Nonetheless the extent of this change is a matter of debate in the literature [2]. It has been projected that to avoid catastrophic climate change, 10 Terra Watts of the worlds energy needs will have to come from clean renewable sources by 2050 [3]. This is why it is of upmost importance that mankind investigate different resources for the producing electrical energy.

There are many different renewable resources from which electricity can be generated from. Prime examples include wind, tidal, geothermal, bio-fuels, hydroelectric, solar thermal and photovoltaics. All of these renewable resources (excluding geothermal) are driven by solar radiation as the fundamental energy input. A surprising amount of energy is provided from the sun in the form of solar radiation as on a cloudless day and for a fully optimised tilt angle the amount of solar radiation hitting the earth can reach ≈ 1 kW/m^2 [4].

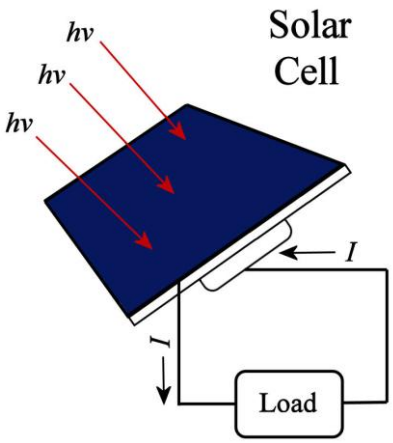

Figure 1.1: Principle of a solar cell used to absorb radiation to then convert it into direct current (D.C.) which can be used by an electrical load.

An attractive alternative to fossil fuels are photovoltaics or solar cells which convert sunlight into DC electricity. Key advantages are that they have no moving parts and that most are quoted to have a useful shelf life of 20-30 years. Currently the applications of photovoltaics vary from two extremes; the domestic markets and the much larger solar farms. The domestic market is comprised of the fitting of photovoltaics onto roof tops to supplement the energy requirements of the property and in some cases feeding it back into the national grid. Examples of domestic applications can be seen all over Germany due to an attractive feed-in tariff [5]. Commercial applications include very large solar farms which can generate up to MW of electricity per year [6]. In either case there isn't an outstanding device type, be it silicon, thin film or organic. By simultaneously reducing the cost and increasing the efficiency of devices, the use of photovoltaics as an alternative energy source will economically complete with fossil fuels. Despite the free energy concept of photovoltaic devices, there are some drawbacks:

- Photovoltaics have a complete dependence on the available sunlight:
  - The intermittence of sunlight
  - Seasonality of sunlight
- Photovoltaics have a low power density
- Photovoltaics require of high purity of the starting materials.
- Most photovoltaics require technological advanced techniques used in the preparation of photovoltaics
- Extensive control of parameters during semiconductor growth [7]

The first two points are fundamental limitations and are as a consequence of the flux (or intermittence) of solar radiation. The last three issues have been investigated since the birth of photovoltaics. For photovoltaics to compete with fossil fuels as a viable source of energy, the devices have to be prepared at low cost and high efficiency.

1.1.2. History of photovoltaics

The study of photovoltaics can be divided into two main branches; solid state devices, the study of light upon solid state materials and photo-electrochemistry, the study of the influence of light at the solid | liquid interface(s). Becquerel is generally regarded as the founder of photovoltaics as during 1839 he investigated and reported the effects of light at silver chloride coated platinum electrodes [7,8].

Solid state photovoltaic devices were discovered by Ohl working at Bell Labs in 1941 [9]. A semiconductor│semiconductor homojunction was formed when he re-crystallised high purity silicon. The semiconductor│semiconductor junction was attributed to the presence of impurities in the film which created a *p*-n barrier. The first publication concerning the photo-diode characteristics of a germanium semiconductor│semiconductor junction was in 1946 [10]. Below in figure 1.2 is a schematic of a solid state photovoltaic device. Here the material is composed of two different semiconductors which upon illumination create an electrochemical gradient of electrons. These electrons can flow through and external circuit performing electrical work.

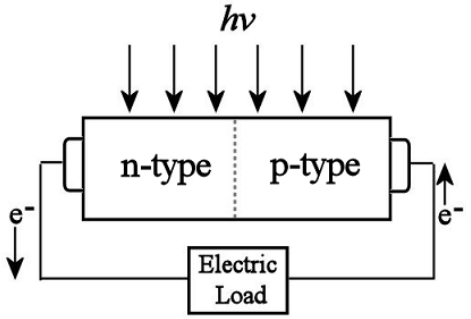

Figure 1.2: Schematic of a photovoltaic device. Here the device is composed of two different semiconductors that are sandwiched together. During the illumination of light an electrochemical gradient is created causing a flow of electrons via and external circuit.

The need for an energy source for space applications was the initial drive for the development of photovoltaics. This is because photovoltaics have a longer lifetime compared to primary batteries and are far cheaper than nuclear reactors. Initially, silicon was used as a solar absorber in space however, a substantial amount of research and development into other materials such as gallium arsenide, indium phosphide and copper indium diselenide was undertaken [7].

1.1.3. Types of solar cell

Photovoltaics can be divided in three main categories; first, second and third generation solar cells as shown in the plot below which consists of the relative costs versus the efficiency [11]. First generation solar cells are devices which have reasonable efficiency but are manufactured at a high cost. These primarily include various silicon based photovoltaic technologies. Second generation solar cells are thin film devices which are direct band gap absorber materials including CISe, cadmium telluride (CdTe), amorphous-silicon, organic (polymer) solar cells and dye-sensitised solar cell devices. These devices are cheap to manufacture however the efficiencies are not as high as the silicon based devices. Third generation devices are advanced concept devices which include multi-junction cells, hot carrier devices and quantum dots. The third generation concepts essentially combines the low cost of the second generation devices with the higher efficiencies of silicon based devices. Multi-junction based photovoltaics are the only devices that truly meet this criteria however these are produced at a high cost.

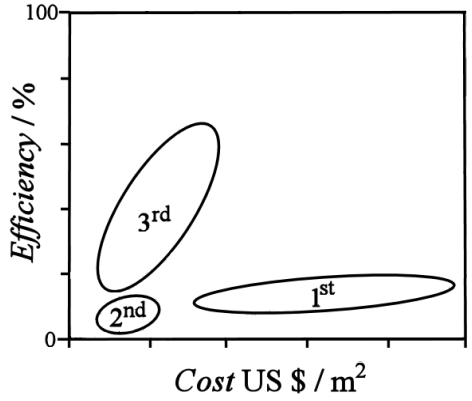

Figure 1.3: Plot of efficiency versus the relative production cost. On the graph are three areas which correspond to the 1st generation, 2nd generation and 3rd generation based photovoltaic devices. Plot adapted from reference [11].

1.1.4. 1st Generation photovoltaic devices: Silicon based solar cells

Silicon, in its semiconductor form, is a widely used material in the electronics industry having use in sensors, microelectromechanical systems and microsystems [12]. As a consequence of transferring knowledge and technology to the photovoltaic industry, silicon devices have dominated the solar cell market since it began.

Commercial multi-crystalline and mono-crystalline silicon based devices both have modest efficiencies of 12-20%. They also have a long expected lifetime and do not contain harmful materials, however there are some major drawbacks. The fabrication costs of obtaining high purity silicon is a major issue as is it a multi-step, energy intensive procedure. To prepare crystalline high purity silicon, seeded growth methods (such as the Czochralski method) are typically used whereby the growth of the crystal has to be monitored very precisely. These complications correspond to a high production cost and a long carbon payback for the production of silicon based devices [13].

Another drawback is that silicon is an indirect band gap absorber and has a relatively low absorption coefficient. The silicon absorber film thickness for a reasonable efficiency crystalline silicon device is about 250 μm. Light trapping methodologies (such as surface textursiation) has been developed to reduce the thickness of the absorber layer. This reduces the required film thickness to about 80 μm without significant loss of efficiency [14].

1.1.5. 2nd Generation photovoltaic devices: Thin film based solar cells.

Thin film photovoltaics have advantages over silicon based devices in that they are direct band-gap materials. This means that they have a large absorption coefficient, for example, CISe is about 10^5 cm^{-2} [15]. As of a consequence the absorber layer thickness within thin film based devices can be as low as 2-3 μm. Thin films have four key advantages over silicon based technologies: reduction in cost for the raw materials, low process control, cheap deposition processors and the presence of relativity high impurities in the absorber layer film.

Thin films are polycrystalline in nature, meaning that the films are composed of micron sized grains of crystalline material. Thin film devices contain at least two different semiconductors: one p-type and one n-type, a heterojunction. CdS is a common photoactive n-type material [16] and is present in a number of thin film absorbers such as: CdTe, and CISe as it is easy to deposit and forms efficient junctions.

A major drawback to thin film technologies, with respect to silicon, is that they are not extensively used in the electronics industry and less fundamental and practical knowledge is known. However, both CdTe and CISe show promise as they have demonstrated efficiencies of 16.5 % and 20.3 % on the laboratory scale and offer real competition to mono/multi crystalline silicon based photovoltaics [17].

1.1.6. Introduction to photo-electrochemical systems

As stated earlier Becquerel was the first scientist to investigate the chemical effect of light upon a material and hence invent photochemistry. His experiment was a primitive photo-electrochemical cell composed of two electrodes immersed in a solution. Below in figure 1.4 is a schematic of a photo-electrochemical cell. Here light illuminates either both or one of the electrodes causing chemistry to occur at the electrode | electrolyte interface. According to reference [18], Becquerel coated one of the electrodes in silver chloride and the presence of light caused the reduction of silver and hence current (photocurrent) to be flow from one electrode to another via an external circuit [8].

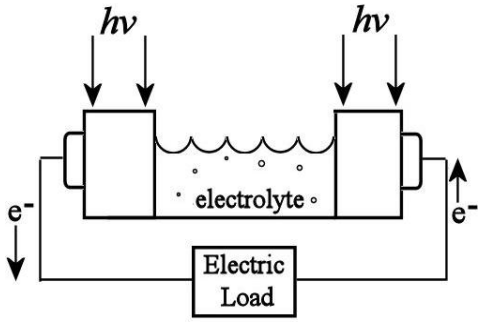

Figure 1.4: Schematic a photo-electrochemical cell. Here the device is composed of two different materials separated by an electrolyte (liquid). Other configurations are possible however an electrolyte must be in contact with both electrodes.

From this primitive investigation there have been a number of reports in the literature examining photo-electrochemical effects of absorbent materials [18]. A key milestone was a nature paper released by Fujishima and Honda in 1972 where the irradiation of a TiO_2 electrode split water into molecular hydrogen and oxygen [19]. This was the first example of producing useful chemical products from a photo-electrochemical system. Photo-electrochemical generation of hydrogen is particularly important as hydrogen gas been proposed as a clean energy fuel to support the hydrogen economy [20]. Photo-electrochemical methods provide a potential renewable solution as most of the commercial hydrogen produced today is manufactured from the reforming of methane under energy intensive conditions [20].

Research interest in photo-electrochemical cells increased after a publication by O'Regan *et al.* which documented the preparation of a self contained, efficient ruthenium dye sensitised, photo-electrochemical device (dye-sensitised solar cell) [21]. This device combined the fields photo-electrochemistry and dye sensitisation which was studied primarily by Gerischer [22,23] and one of the first dye-sensitised solar cells was documented by Tsubomura *et al.* [24]. In either case the configuration of the cell is similar to that shown in figure 1.4. One of the electrodes is composed of porous oxide network coated with a dye. Upon illumination the dye becomes excited and injects electrons into the oxide creating an electrochemical gradient of electrons. These electrons flow from the oxide to the secondary electrode via an external circuit where they reduce a redox couple present in the electrolyte. This redox couple reduces the oxidised dye completing the cycle. Dye-sensitised solar cells are typically produced from mundane materials using low cost methods and although there are technical issues with devices degradation they offer a real alternative to silicon and thin film solar cells.

A minor but valuable application of photo-electrochemical cells is for the testing of single semiconductors. All photovoltaic devices are based on having at least two materials. If both materials are problematic to produce it can be difficult to quantify single aspects. A single semiconductor can be analysed when immersing the film in a photo-electrochemical environment. An added advantage is that the electrolyte is not subject to small changes in composition that can drastically alter its photochemical efficiency. Before entering further detail on specific systems it is necessary to

explain the theory behind the photo-electrochemistry. Further information on electrochemistry can be found in the appendix.

1.2. Photovoltaic Device Physics

1.2.1. Semiconductors

Bonding differs between that of the discrete molecule and an extended covalent structure of a macromolecule. For a discrete molecule the frontier orbitals are comprised of the highest occupied molecular orbital (HOMO) and the lowest unoccupied molecular orbital (LUMO) which are described by molecular orbital theory (figure 1.5A). Bulk materials such as conductors, semiconductors and insulators have their electronic configuration described by band theory. During the formation of a solid from an ensemble of discrete molecules, atomic orbitals will linearly combine to form molecular orbitals. For example during the formation of diamond, the frontier atomic orbitals of carbon are 4 equivalent sp^3 hybridised lobes. A carbon atom will bond with an adjacent carbon atom by the combination of 2 sp^3 orbitals (one from each carbon atom) to create a bonding and an anti-bonding orbital. As diamond is an extended structure of sp^3 bonded carbon atoms the molecular orbitals must shift to satisfy the Pauli Exclusion Principle which states that no two quantum particles can be described by the same position [25]. As a consequence the orbitals split into bands becoming the valance and the conduction band [26].

Unlike metals which have free electrons within a continuous set of energy levels, diamond like other semiconductor and insulators exhibits the phenomenon of having an interrupted band of energy levels. This arises from the periodicity of the atoms nuclei within the lattice structure. This causes an exclusion of certain energies of the electron where the wavelength maxima superimposes onto the nuclei of the atoms, thus creating a band gap. In the case of diamond which has a large band gap (figure 1.5D), the atoms are very tightly bound inferring that small wavelength (i.e. high energy) energies of the electrons are not allowed.

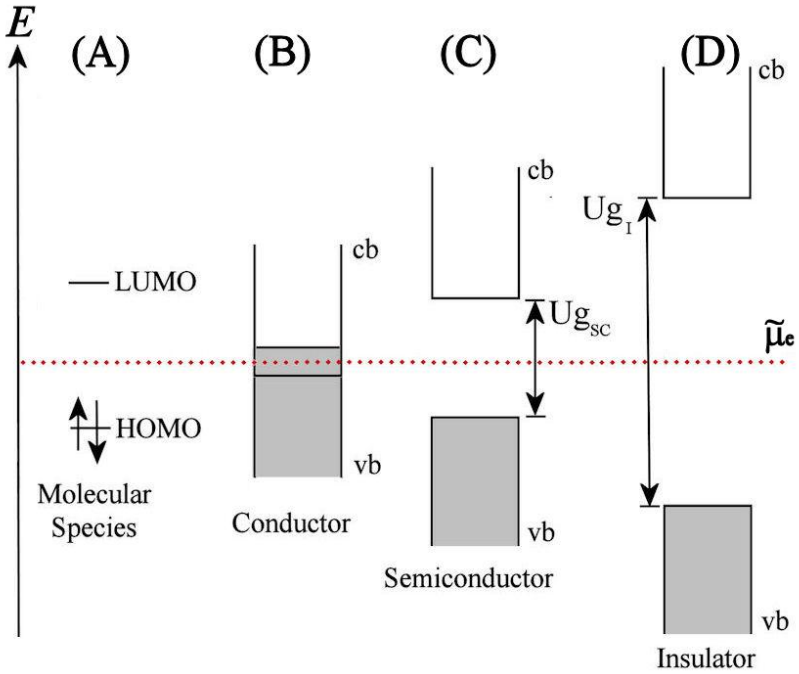

Figure 1.5: A relative representation of the molecular or band of orbitals present within a (A) discrete molecular species, (B) conductor, (C) semi-conductor and (D) an insulator. The chemical potential of the electrons in the materials is displayed as $\tilde{\mu}_e$.

Due to the strength of the bonds formed in diamond which originate from the high charge density and efficient overlap the difference between the bands, the band gap (Ug) is large ca. 500 kJ/mol. As a consequence of the large band gap diamond is considered an insulator as it exhibits no intrinsic electronic conductivity. Progressing down the group IV elements the band gap decreases due to weaker overlap and lower charge density [27]. Silicon has a band gap of 1.2 eV and germanium has a band gap of 0.7 eV. Both are classed as semiconducting materials (figure 1.5C) as a room temperature they weakly conduct electricity which can be increased by raising the temperature. Conductors such as metals have either bands that overlap or electrons that semi-populate a band creating continuum of energy levels. This continuum of energy levels allows for thermal excitation of electrons states allowing charges to move very quickly through the material which gives it a very low resistively (figure 1.5B) [26].

1.2.2. Electrons and holes

Figure 1.6 gives a general overview for the electronic configuration of an intrinsic semiconductor ca. a semiconductor containing perfect crystals with no defects or dopants. The basic band model of semiconductors shown in figure 1.6A. This can be expanded to give information about the electronic distribution within a semiconductor.

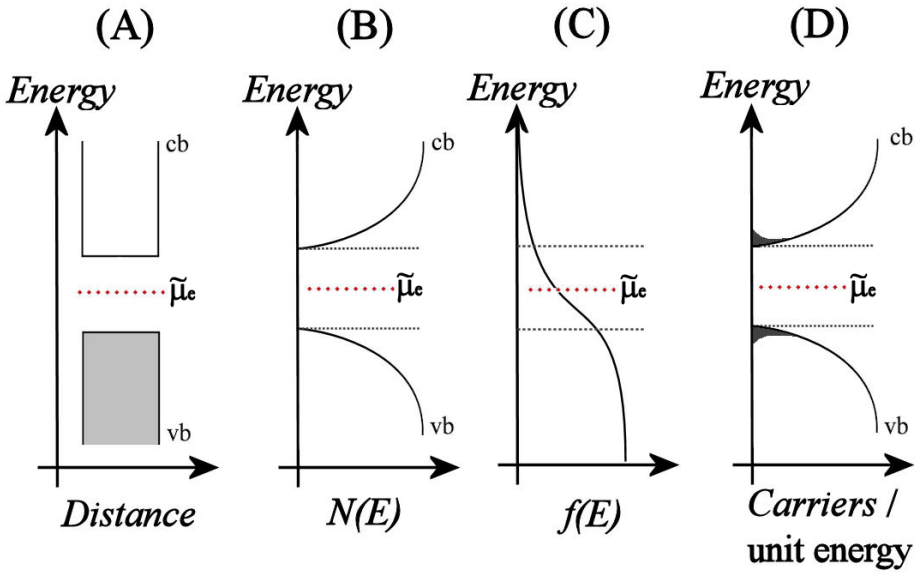

Figure 1.6: Various representations of the electronic configuration of the bands; (A) simple band diagram, (B) density of states of the electronic configuration, (C) Fermi-Dirac distribution of electrons within a solid (at 298K) and (D) the electron and hole concentrations.

Figure 1.6B is a plot of the density of states of a semiconductor. This is the number of available orbitals that an electron (or hole) can reside within. These can be calculated from first principles models. Figure 1.6C is the Fermi-Dirac distribution for electrons within a solid (expressed at 298 K) and is mathematically expressed below, equation 1.1.

$$P(E) = \oint (E)dE = \frac{dE}{1+\exp\left[\left(E-\mu^{M}_{e^{-}/pze}\right)/k_{B}T\right]} \qquad (1.1)$$

Here $P(E)$ is the probability of finding an energy level between E and, $E+dE$ and $\mu^{M}_{e^{-}/zpe}$ is the chemical potential of the electron expressed in its lowest electronic state

(potential of zero charge energy), k_B is the Boltzmann constant and T is the absolute temperature. A general approximation can be that $\mu^{M}_{e^-/pze} \approx E_f$ as temperature has little effect on changing the Fermi level for metals and doped semiconductors. As a consequence of this distribution the probability for finding an electron in the highest possible energy of the valence band, is not one and that the probability of finding an electron in the lowest energy of the conduction band is not zero. The product of the density of states and the Fermi-Dirac distribution gives the true electronic distribution of electrons in a semiconductor figure 1.6D. Here it is seen that intrinsic semiconductors (at 298 K) have a small but significant population of free electrons in the conduction band and hence, electron vacancies (holes) in the valence band. As these species are mobile and can migrate, if an external electric field is applied, these species can act as charged carriers which gives rise to a mechanism of conductivity through the material. Due to this non-ohmic behaviour a general equation can be used to describe the conductivity of a semiconductor/insulator that arises from a purely thermal excitation which is observed empirically.

$$\sigma = \sigma_0 \exp\left(\frac{-Ug}{2k_B T}\right) \tag{1.2}$$

Here σ is the conductivity, σ_0 is the limiting electronic conductivity when $T \to \infty$ and Ug is the band gap. A more fundamental approach to assess the intrinsic carrier concentration is given by another Arrhenius like dependence, where n_i is the intrinsic carrier concentration, N_C is the effective density of states in the conduction band and N_V is the effective density of states in the valence band.

$$n_i = N_C N_V \exp\left(\frac{-Ug}{2k_B T}\right) \tag{1.3}$$

By substituting in values experimental determined for intrinsic silicon (ca. $N_C = 2.80x10^{19} cm^{-3}$, $N_V = 1.04\text{x}10^{19} cm^{-3}$, $Ug = 1.4eV$, $T = 300K$ and $k_B = 1.38x10^{-23} m^{-2} kgs^{-2} K^{-1}$) it is possible to get an intrinsic carrier concentration for silicon of $n_i = 1.45x10^{10} cm^{-3}$ at room temperature [28]. The number of charge

carriers in intrinsic and extrinsic (doped) semiconductor varies from 10^{10} and 10^{18} carriers per cm^3 which is low compared to a full conductor 10^{22} per cm^3 hence they have a lower conductivity compared to conductors. Intrinsic diamond has low number of charge carriers (resulting from the large Ug) and results in a poor electrical conductivity and unless heavy doped (ca. B-doped diamond) is classed as an insulating solid.

1.2.3. Semiconductor type and doping

Extrinsic semiconductors are those which had have external dopants added to change the chemical or electrical properties of the material. This gives rise to either p-type or n-type semiconductors where there is either a deficiency or an excess of electron density.

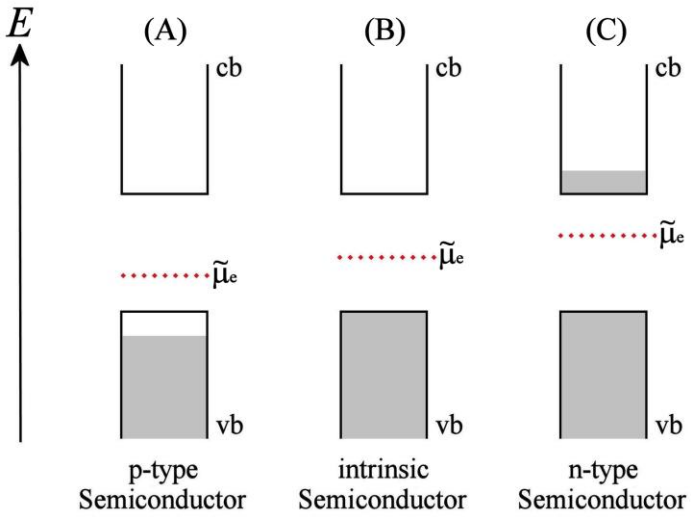

Figure 1.7: The electronic distribution within a (A) p-type semiconductor (B) an intrinsic semiconductor and (C) an n-type semiconductor.

A p-type semiconductor has a lower electron density compared to that of the intrinsic case. This defiling of the valence band causes the predominate charge carriers (or majority carriers) are holes, vacancies of electrons. Electrons present in the conduction band either by thermal or photo- excitation are known as minority carriers. It is the opposite situation in an n-type semiconductor where there is an excess of electrons with respect to the intrinsic case and as a consequence of this the excess of electrons over spills into the conduction band. Here the electrons in the

conduction band are known as majority carriers whereas the holes in the valence band are known as the minority carriers. Intrinsic semiconductors have no majority or minority carriers as the number of electrons in the conduction band and holes in the valence band are equal. Majority carriers are the species that create the conductivity within the solid as there is a high population of species. Minority carriers contribute to the conduction but due to the lower concentration it is small.

Intrinsic semiconductors have a high resistivity at room temperature (ca. ≈1 $M\Omega cm^{-2}$) due to the smaller number of charge carriers which arising from thermal excitation. The number of charge carriers can be increased by extrinsically doping the semiconductor. Doping is when hetero-valent atoms are incorporated into the material without affecting the crystal structure to either reduce or increase the amount of electron density within the valance/conduction bands. Essentially, these materials have identical composition and structural components to the prefect crystals however, dopants are present on a very small scale (0.01 %), which alters the electronic properties of the material. Figure 1.8 is a schematic explaining the nature of doping.

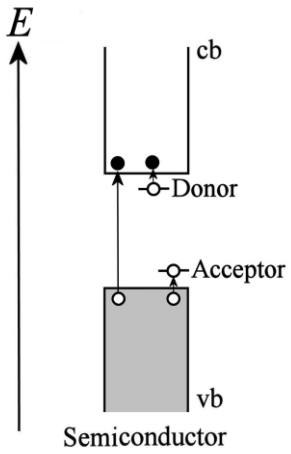

Figure 1.8: A schematic depicting the thermal/photochemical or atomic doping of a semiconductor to generate charged carriers. The presence of donor/acceptor molecules that can either donate or remove electron density from a semiconductor.

It is possible to create p-type semiconductors by adding acceptor atoms to the crystals ca. the addition of boron to a crystalline silicon material. It can be imagined that a boron atom will occupy a silicon site in the crystal structure but will only donate three electrons instead of the typical four to the crystal lattice. This charge

difference creates an electronic deficiency in the electronic structure of the material and the creation of holes. The charge inbalance is counterbalanced elsewhere in the material (equation 1.4). This boron is now free to accept an electron from the valance band creating a charge deficiency (equation 1.5).

$$B^{X} + Si_{Si}^{X} \rightarrow B_{Si}^{\cdot} + Si_{(Surface)}^{\prime} \quad (1.4)$$

$$B_{Si}^{\cdot} + e_{vb}^{-} \rightarrow B_{Si}^{x} + h_{vb}^{\cdot} \quad (1.5)$$

An n-type semiconductor has a partially filled conduction band and an example of which is crystalline silicon doped with phosphorus. Again, phosphorus is incorporated in to the silicon lattice to create an excess of electron density by donated five electrons instead of four. The chemical equations describing this are equations 1.6 and 1.7.

$$P^{X} + Si_{Si}^{X} \rightarrow P_{Si}^{\cdot} + Si_{(Surface)}^{\cdot} \quad (1.6)$$

$$P_{Si}^{\prime} \rightarrow P_{Si}^{x} + e_{cb}^{-} \quad (1.7)$$

Some intrinsic semiconductors exhibit charged defects which can create either a loss or gain in electron density. An example of this is the semiconductor CISe where in the thin film form copper vacancies (or defects) gives rise to a p-type conductivity [7]. As a consequence of the doping the semiconductor either intrinsically or extrinsically, the Fermi energy will change giving a p-type or n-type material.

1.3. Semiconductor Photo-Electrochemistry

1.3.1. Semiconductor electrochemistry

The use of semiconducting materials in electrochemistry differs from that of the metal electrodes as the electrical properties of electrode is vastly different. This first paper published on the use semiconductors as electrodes was by Brattain and Garrett in 1954 [29].

Below in figure 1.9A is a schematic image of a semiconductor interface. As established in the metal | electrolyte interface, (see appendix) the bulk electric

potential of the semiconductor generally will not equal that of the electric potential of the bulk solution. As a result an electric potential gradient needs to be induced figure 1.9B. To do this charge forms at the interface and in this case positive charge forms on the semiconductor and negative charge concentrates in the electrolyte side of the interface as shown by figure 1.9C.

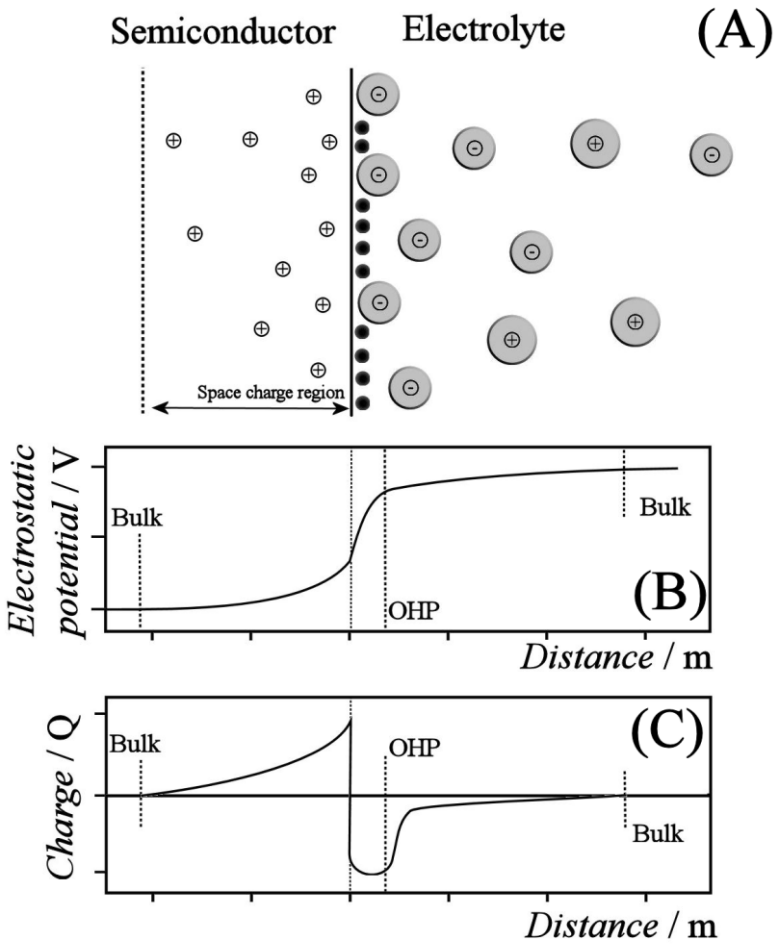

Figure 1.9: (A) the energy model of the surface of an semiconductor with a deficiency of charge and (B) the potential distribution from the bulk semiconductor to the bulk solution. Adapted from ref [30]

A double layer exists at the semiconductor | electrolyte interface which is very similar to that discussed with a metal | electrolyte interface. A key difference is that the potential drop for a metal electrode is at the electrolyte interface whereas for a semiconductor electrode it is within the semiconductor. The length of the region within the semiconductor where is an excess of charge resides is known as the space charge region. The space charge region has its own capacitance and needs to take into account when measuring the capacitance.

$$\frac{1}{C_{\text{Total}}} = \frac{1}{C_{SC}} + \frac{1}{C_{IHP}} + \frac{1}{C_{OHP}} \tag{1.8}$$

For highly doped semiconductors such as PbO_2 the space charge region is minimal and these materials behave more like metal electrodes. Essentailly the Fermi level (or chemical potential of the electrons) overlap either the conduction band or the valence band. These materials are typically known as degenerate semiconductors.

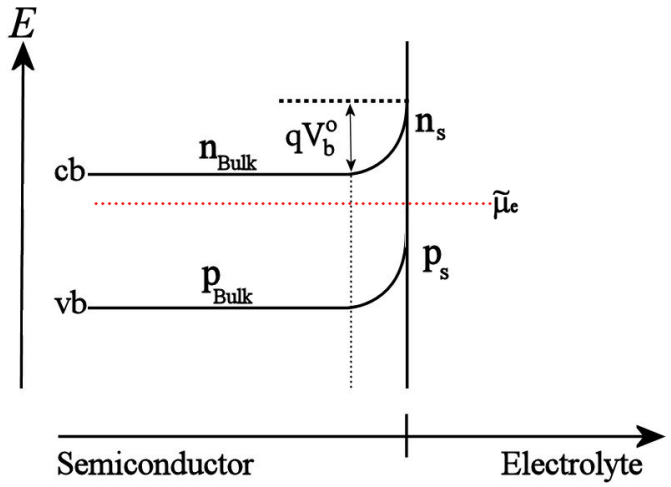

Figure 1.10: The energertics of the surface of an n-type semiconductor with an upwards band bending. An accumulation of holes within the space charge region occurs. Adapted from ref [30]

Above is a pictorial image of a semiconductor | electrolyte interface in terms of energetics of the bands. As observed with the metal surface the sudden termination of the lattice crystal of the semiconductor at the interface breaks the symmetry established in the bulk. This distortion in symmetry and the interaction of charges on the other side of the interface gives rise to a deformation in the band structure known as band bending. The Fermi level of a semiconductor at equilibrium will be constant over the entire structure whether it is the bulk or surface. As a result any excess/deficiency of charge will cause the bands to bend up or down to maintain a constant Fermi energy. A deficiency of electrons at the semiconductor surface will cause an upward bending of the bands whereas an excess of electrons will cause a decrease in the energy level. The extent at which the bands are not flat is the space charge region. This region can extended up to anything like 100-1000 Å into the bulk of the semiconductor. Band bending can be induced by applying bias to the

surface of the semiconductor. The density of electrons n_s and holes p_s at the surface of the semiconductor is related to the bulk carrier concentrations (electrons n_{Bulk} and holes p_{Bulk}) and the applied bias by the following equations

$$n_s = n_{Bulk} \exp\left(\frac{-qV_b^o}{k_B T}\right) \tag{1.9}$$

$$p_s = p_{Bulk} \exp\left(\frac{qV_b^o}{k_B T}\right) \tag{1.10}$$

Where qV_b^o denotes the extent of the band bending (expressed in volts) at the semiconductor surface. This equation is valid for surfaces where the absorption/reaction of molecules at the semiconductor | electrolyte to create surface states is negligible [30].

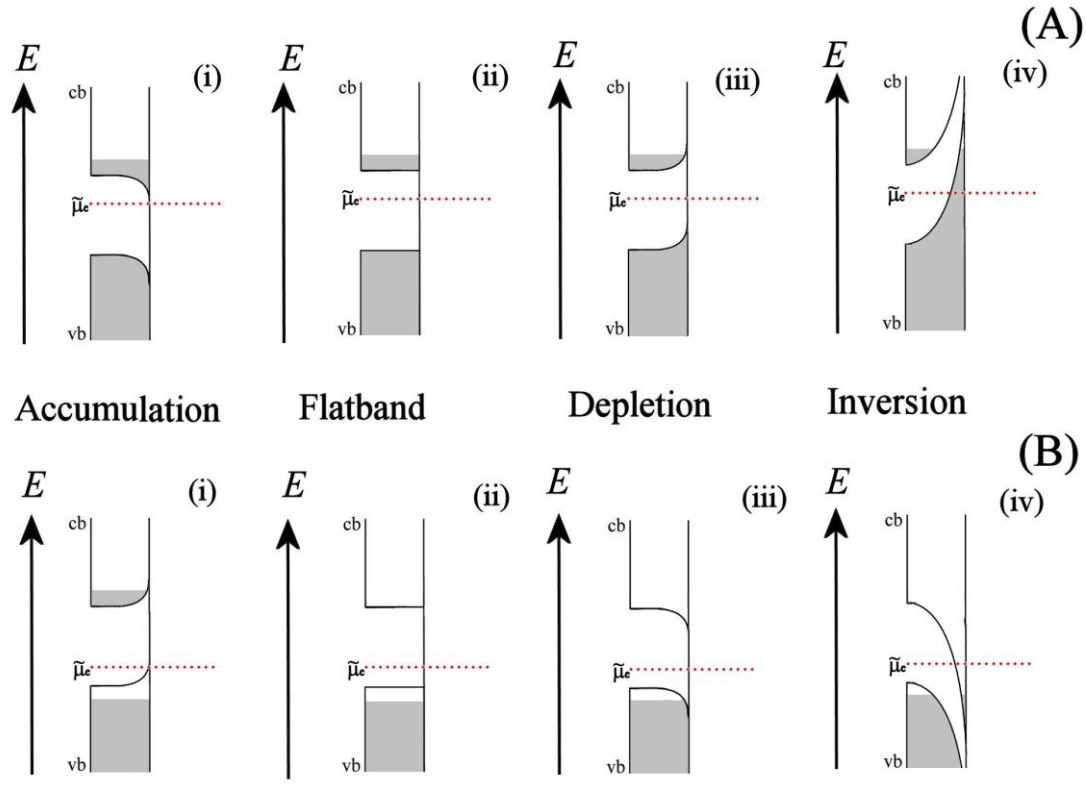

Figure 1.11: Band models for the four types of band bending exhibited at a semiconductor | electrolyte interface. (A) n-type semiconductor displaying (i) accumulation, (ii) flatband, (iii) depletion and (iv) inversion band bending. (B) p-type semiconductor displaying (i) accumulation, (ii) flatband, (iii) depletion and (iv) inversion band bending.

Electrode reactions at semiconductor | electrolyte interfaces differ from that of metal electrodes as the feasibility of a reaction occurring at the interface is strongly dependant on the presence of charge carriers. In metals this is not a problem as the carrier concentration is typically 10^{22} with the carriers distributed evenly over the entire sample. However for semiconductors, the carrier concentration is much lower which can implicate the observed electrochemistry. Different types of semiconductors will have consequences when the bands are bent at the semiconductor | electrolyte interface.

The flat band potential, as shown for p/n-type semiconductors in figure 1.11Aii and 1.11Bii, is the potential required for the semiconductor to have flat bands present across the space charge region. This is to counteract the charge either donated or accepted when the semiconductor first came into contact with the electrolyte. This can either be an application of a positive or negative voltage as the excess or deficiency of charge is dependant of what the environment is the semiconductor is immersed in.

If a positive potential is applied to a p-type semiconductor or a negative potential applied to an n-type semiconductor then an accumulation of majority carriers at the interface will form. An accumulation layer is formed under forward bias and is shown in figure 1.11Ai and 1.11Bi. Ignoring any side reactions such as anodic or cathodic dissolution an increase in majority carriers at the interface will bend bands accordingly. The presence of majority carriers at the interface allows chemical reactions to occur e.g. electron transfer reactions to and from the electrode surface.

A depletion layer can form when a positive potential is applied to an n-type semiconductor or a negative potential is applied to a p-type semiconductor (reverse bias, figure 1.11Aiii and 1.11Biii). Again ignoring side reactions and conducting experiments without the presence of light, this band bending removes majority carriers from the semiconductor interface. This results in an insulating layer at the electrode surface and will not allow the propagation of electrons and electrochemical reactions will not be observed.

A final type of band bending is the formation of an inversion layer occurs (figure 1.11Aiv and 1.11Biv). It can be imagined that a depletion layer has formed at the interface and by bending the bands further a scenario will occur where the valence

and conduction bands will overlap. This will allow population of the conduction band of the p-type semiconductor and population of the valence band of the n-type semiconductor as tunnelling of the majority carriers can occur. This causes a switch from the surface composed of minority carriers (as in the depletion region) to a surface populated with majority carriers.

1.3.2. Photo-effects of semiconductor electrodes

As previously stated an increase in the number of charge carriers at the semiconductor | electrolyte interface will increase the conductivity and will allow electron transfer to occur between the electrode and the electrolyte. By shining light (of greater energy than that of the band gap) minority carriers will be created (equation 1.11). The light absorption causes promotion of electrons to the conduction band creating holes in the valance band (figure 1.12Ai and 1.12Bi). The charge carriers will obey Fick's laws of diffusion and diffuse throughout the material. As minority carriers are not the lowest energy state, they will eventually recombine. There are a few recombination mechanisms such as radiative recombination, non-radiative recombination and Auger recombination [28] but essentially electrons in the conduction band recombine with holes in the valance band.

$$h\nu + e^{-}_{vb} \rightleftharpoons h^{+}_{vb} + e^{-}_{cb} \qquad (1.11)$$

If an acceptor molecule is present in close proximately to the electrode surface for an illuminated p-type semiconductor then an electron can transfer from the semiconductor to the acceptor molecule (figure 1.12Aiii). The same can be said of an illuminated n-type semiconductor with a donor molecule present at the interface. The donor molecule can donate electrons to the semiconductor, essentially reacting with holes present in the valance band (figure 1.12Biii).

$$Ox + e^{-}_{cb} \rightarrow Red \qquad (1.12)$$

$$Red + h^{+}_{vb} \rightarrow Ox \qquad (1.13)$$

As the minority carrier undergoes an electron transfer either to or from the semiconductor an in balance of charge is counter by the electron transfer of a

majority carrier to or from the substrate. This process occurs simultaneously to keep the conservation of charge.

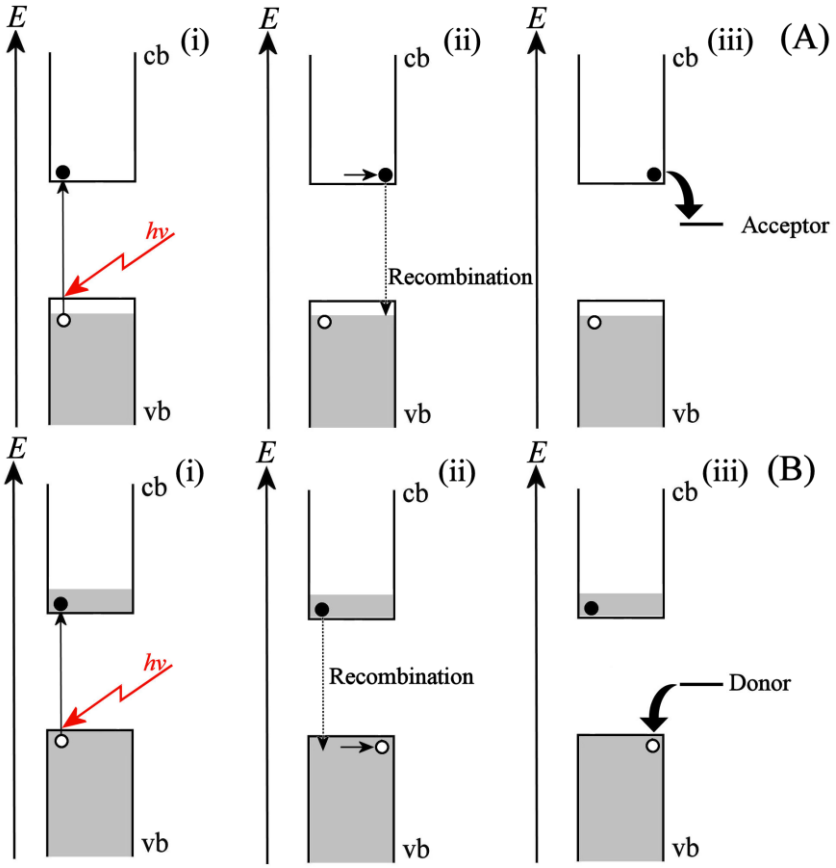

Figure 1.12: Photo-electrochemistry of semiconductors in contact with an electrolyte. (A) p-type semiconductor (i) upon illumination, (ii) movement/decay of minority carriers and (iii) donation of charge to an acceptor molecule in the electrolyte. (A) n-type semiconductor (i) upon illumination, (ii) movement/decay of minority carriers and (iii) acceptance of charge from a donor molecule in the electrolyte.

As there will be a competition between recombination and electron transfer the band structure of the semiconductor can be manipulated to increase the likely hood of a reaction occurring at the interface. For a charge to be transferred to and from a semiconductor minority carriers must be present at the surface. By applying a voltage that results in a depletion region it is possible to concentrate the minority carriers at the interface (figure 1.12). This is because when a depletion region exists, an energy well for minority carriers is present at the interface. As a consequence the movement of the minority carriers is not only governed by diffusion but is influenced by the lower energy states of the depletion region at the interface.

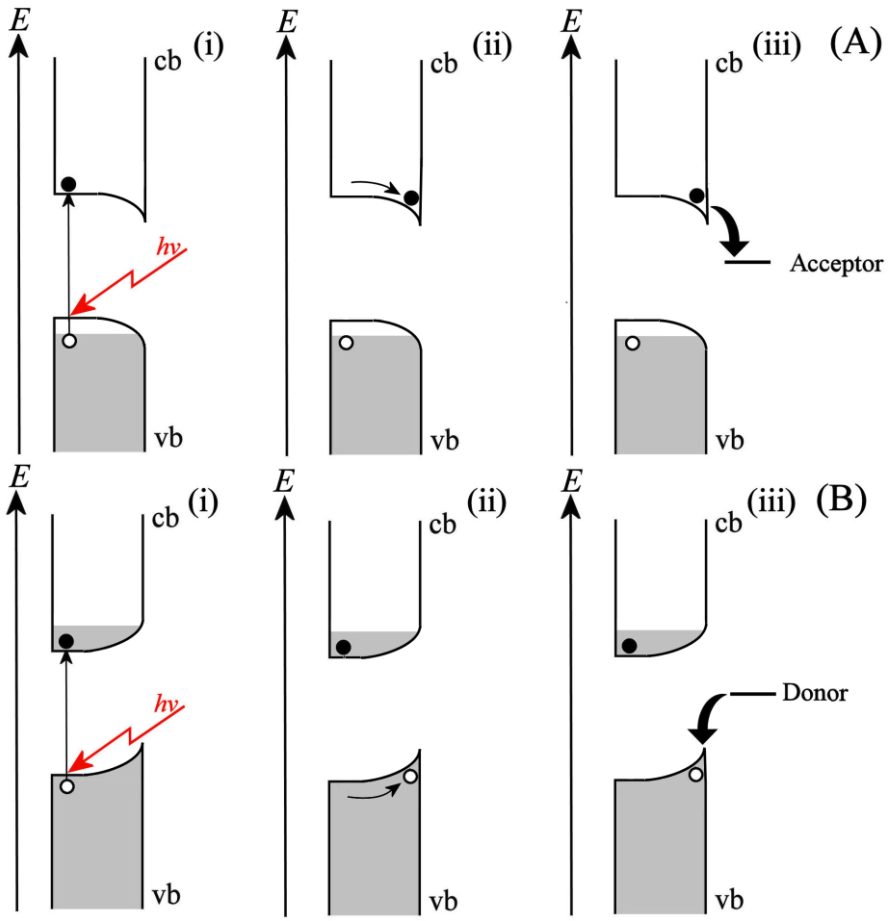

Figure 1.13: Depleted regions applied to a semiconductors with the interaction of light. (A) p-type and (B) n-type (i) is the illumination of light greater than the band gap of the electrode, (ii) is the diffusion/migration of charge to the electrode surface and (iii) the charge transfer between the semiconductor and an electrolyte.

The concentration of minority carriers at the semiconductor electrode interface can be increased by applying a depletion voltage to the semiconductor surface as shown in figure 1.13. This will enhance the minority carriers undergoing an electron charge transfer either to or from the semiconductor [30].

1.3.3. Reported photo-electrochemical effects at the semiconductor electrolyte | interface

As stated in section 1.1.6 photo-electrochemistry has been studied since water was split with TiO_2 [19]. TiO_2 is an n-type semiconductor that has a large band gap (ca. 3

eV) which means it only absorbs light in the blue/UV. This equates to only about 3 % of the incident solar spectrum [31] and therefore is not practical an atmospheric device. As a consequence a number of other materials with more appropriate band gaps for absorbing the solar spectrum have been analysed in photo-electrochemical cells. This have included traditional semiconductors and chalcogenides; p-Si [32], p-Ge and n-Ge [29], p-GaAs [33], n-GaAs [34], p-InP [35] and CdS [36] as well as various oxides; n-Fe_2O_3 [31, 37], and n-WO_3 [38].

A number of different donor and acceptor molecules have been used have been used such as the H_2O/O_2, H_2/H_2O V^{2+}/V^{3+}, I^-/I_3^-, Fe^{2+}/Fe^{3+} and Eu^{2+}/Eu^{3+} [33] as well as poly-chalogens S^{2-}/S_2^{2-}[39], Se^{2-}/Se_2^{2-} [33] and Te_2/Te_2^{2-} [40] Light to electricity efficiencies have been documented around 10 % [35].

However, the reasons why these photo-electrochemical technologies have been not been commercialised is because most of the devices stated above use single crystals which can be difficult to prepare. Also, side reactions can occur at the electrode | electrolyte interface such a cathodic/anodic dissolution. These considerations should be taken into consideration when studying the photo-electrochemistry of a semiconductor. The one exception is dye-sensitised solar cells where photo-electrochemical devices are based on using a redox couple in conjugation with either a redox active dye molecule or a nano-sized semiconductor is implemented [41].

1.4. Introduction to the topics of the thesis

The first part of this PhD thesis concerns the uniformity issues surrounding the preparation of the semiconductor copper indium diselenide, CISe. Initially a novel electrochemical substrate (ca. 1 cm^2) was used to see if photoactive CISe thin films could be formed. The photoactivity of the CISe thins were tested using photo-electrochemical methods. The films were immersed in a solution containing an electron acceptor electrolyte (ca. $Eu(NO_3)_3$). Films were placed under depleting conditions and light (greater than the band gap) was pulsed onto the surface. The current resulting from the electron transfer from the electrode to the electrolyte was measured as current. Discussed are a number of factors affecting the magnitude of the photocurrent.

Large area CISe thin films (ca. 12.1 cm^2) were also formed and tested under photo-electrochemical conditions. Here the entire electrode was immersed in an electron acceptor electrolyte as described above however here a modulated focused light source was rastered across the surface. As a consequence of this the photocurrent could be assigned to specific locations. Methods are introduced to increase the magnitude and uniformity of the photocurrents.

The second part concerns the physical and chemical phenomenon that occur in photo-electrochemical systems of iron oxide and a Gräztel-like dye immobilised onto TiO_2. Mesoporous films of iron oxide were immobilised onto FTO substrates. Under photo-electrochemical conditions iron oxide can oxidise water via a complex 4 electron process. The spectro-electrochemical investigation of these films under light and dark conditions revealed that an intermediate exists at the surface of these films. The intermediate correspond to holes in the valance band and were characterised using impedance and spectro-electrochemical methods. The investigation of a surface bound dye on TiO_2 mesoporous systems was evaluated. In a configuration not dissimilar to that of a Graztel solar cell, the charge propagation through the dye layer was characterised. This is not the predominate mechanism for charge transport in Graztel cells however a new technique introduced to measure the diffusion of charges has the potential for use in this field. Each chapter has a further explanation of the background of the topic under investigation.

1.5. References

[1] G. Hegerl, F. Zwiers, P. Braconnot, N. Gillett, Y. Luo, J. Marengo Orsini, N. Nicholls, J. Penner, P. Stott, *Understanding and Attributing Climate Change. In: Climate Change 2007: The Physical Science Basis. Contribution of Working Group I to the Fourth Assessment Report of the Intergovernmental Panel on Climate Change*. Cambridge University Press, (2007)

[2] A. Schmittner, N. Urban, J. Sharkun, N. Mahowald, P. Clark, P. Bartlein, A. Mix, A. Rosell-Melé Science, 334 (2011) 1385

[3] M. Hoffert, K. Caldeira, A. Jain, E. Haites, L. Harvey, S. Potter, S. Schlesinger, S. Schneider, R. Watts, T. Wigley, D. Wuebbles, Nature, 395 (1998) 881

[4] D. MacKay, *Suitable energy without hot air*, web: http://www.withouthotair.com/

[5] Erneuerbare-Energien-Gesetz, EEG web: http://www.erneuerbare-energien.de/inhalt/42934/40508/

[6] First Solar Ground Mounts web: http://www.firstsolar.com/Applications/Ground-Mount

[7] M. Archer, R. Hill, *Clean Electricity from photovoltaics*, Imperial College Press, 1 (2001)

[8] A. Becquerel, E. Compt. Rend. Acad. Sci., 9 (1839) 145

[9] R. Ohl, L. Silver, Light Sensitive Electric Device (1947) U. S. Patent No. 2,402,662

[10] S. Benzer, Phys. Rev. 70 (1946) 105

[11] M. Green *Third generation photovoltaics: advanced solar energy conversion* Springer (2005)

[12] K. Wise, Sens. and Act. A, 136 (2007) 39

[13] S. Ranjan, S. Balaji, Rocco A. Panella, B. Erik Ydstie, Comp. and Chem. Engin.,35 (2011) 1439

[14] P. Campbell, M. Green, J. Appl. Phys., 62 (1987) 243

[15] A. Rockett, R. Birkmire, J. Appl. Phys., 70 (1991) R81

[16] D. Reynolds, G. Leies, L. Antes, R. Marburger Phys. Rev., 96 (1954) 533

[17] A. Bosio, A. Romeo, D. Menossi, S. Mazzamuto, N. Romeo Cryst. Res. Technol., 46 (2011) 857

[18] R. Williams, J. Chem. Phys., 32 (1960) 1505

[19] A. Fujishima and K. Honda, Nature, 238 (1972) 37

[20] M. Momirlan, T. Veziroglu, Inter. J. Hyd. Ener., 30 (2005) 795

[21] B. O'Regan, M. Grätzel, Nature, 335 (1991) 737

[22] G. Oster, J. Bellin, R. Kimball, M. Schrader J. Am. Chem. Soc., 81 (1959) 5095

[23] H. Gerischer, Faraday. Discus. Chem. Soc., 58 (1974) 219

[24] H. Tsubomura, M. Matsumura, Y. Nomura, T. Amaiya, Nature, 261 (1976) 402

[25] P. Atkins, J. Paula, *Physical Chemistry*, Oxford University Press (2002)

[26] H. Rosenberg, *The Solid State* 3rd ed., Oxford science Publications (1988)

[27] H. Girault, *Analytical and physical electrochemistry*, EPFL Press (2004)

[28] S. Sze, K. Ng, *Physics of Semiconductor Devices*, 3rd ed., Wiley-Blackwell, (2006)

[29] W. Brattain, C. Garrett, The Bell Sys. Tech. J., (1955) 129

[30] V. Pleskov, Y. Myamlin, *Semiconductor Electrochemistry*, Plenum Press, (1967)

[31] K. Hardee, A. J. Bard, J. Electrochem. Soc., 123 (1976) 1024

[32] A. Heller, H. Lewerenz, B. Miller J. Am. Chem. Soc., 103 (1981) 200

[33] F. Fan, A. Bard, J. Am. Chem. Soc. 102 (1980) 3677

[34] K. Chang, A. Heller, S. Schwartz, S. Menezes, B. Miller, Science, New Series, 196 (1977) 1097

[35] A. Heller, B. Miller, H. Lewerenz, K. Bachmann, J. Am. Chem. Soc., 102 (1980) 6555

[36] G. Hodes, J. Manassen, D. Cahen, Nature, 261 (1976) 403

[37] K. Sivula, F. Le Formal, M. Grätzel, Chem. Sus. Chem., 4 (2011) 432

[38] G. Hodes, D. Cahen, J. Manassen, Nature, 260 (1976) 312

[39] A. Ellis, S. Kaiser, M. Wrighton, J. Am. Chem. Soc., 98 (1976) 1635

[40] A. Ellis, I. Steven, W. Kaiser, M. Wrighton, J. Am. Chem. Soc., 98 (1976) 6418

[41] M. Grätzel, J. Photochem. Photobio. C Photochem. Rev., 4 (2003) 145

Chapter 2

$CuInSe_2$ (CISe) via Electro-Deposition onto Mo/$MoSe_2$ Film Electrodes

Contents

This work is published as:
C. Cummings, G. Zoppi, I. Forbes, P. Dale, J. Scragg, L. Peter, G. Kociok-Köhn, F. Marken Journal of Electroanalytical Chemistry 645 (2010) 16

2.1 Abstract

$Mo/MoSe_2$ thin film electrodes formed by selenisation of molybdenum are investigated as chemically robust substrates for the electrodeposition of $CuInSe_2$ (CISe) solar cell absorber films. Exposure of molybdenum film to selenium vapour at 550 ^oC produces thin and chemically robust heterostructures of $Mo/MoSe_2$. This film exhibits the characteristics of a degenerate semiconductor and provides close to metallic electrical conductivity ideal for electrodeposition processes in acidic or in alkaline aqueous media. The $Mo/MoSe_2$ films are characterised by cyclic voltammetry for the reduction of $Ru(NH_3)_6^{3+}$ in aqueous 0.1 M KCl, for the oxidation of 1,1'-ferrocenedimethanol in aqueous 0.1 M KCl, for the reduction of 0.1 M In^{3+} in aqueous 0.5 M LiCl pH 3, and for the reduction of 0.1 M Cu^{2+} in aqueous 3 M NaOH with 0.2 M D-sorbitol. In all four cases well-defined and reversible voltammetric responses are observed. For the formation of CISe films initially In^{3+} is deposited chronoamperometrically followed by electrodeposition of Cu^{2+} and selenisation at 550 ^oC in selenium vapour. Mechanically stable CISe films are produced. The effects of the stoichiometry of the resulting films on photo-electrochemical responses are investigated.

2.2. Introduction

2.2.1. Introduction to CISe based solar cells

The photo-properties of CISe ($CuInSe_2$) was first investigated by Wagner *et al.* [1] who prepared a 12 % efficient solar device from a single crystal of CISe and a thin layer of CdS. CISe has a direct band gap of about ≈1.04 eV [2] which is lower than the optimal terrestrial bad gap of ≈1.38 eV for a single junction device [3] however can still absorb a significant proportion of the solar spectrum. A wider band-gap material can be prepared by doping with Ga^{3+} to form CIGSe ($CuIn_xGa_{1-x}Se_2$) which leds to a higher open circuit voltage and hence ≈20 % efficient devices [4]. Both CISe and CIGSe have tetragonal chalcopyrite crystal structures with CISe having the space group $I\bar{4}2d$ [2]. This is a variation of the zinc blend structure where the unit cell is doubled along the vertical axis and the zinc sites are alternating occupied by the M^+ (Cu^+) and M^{3+} (In^{3+} or Ga^{3+}) ions and the M^{2-} (Se^{2-}) are located on the anion sites.

The thin film formation of CISe can be done by a variety of available techniques each with advantages and disadvantages. These include, electrodeposition [5], co-evaportion/physical vapour deposition [4] a combination of both [6], sputtering [5], molecular bean epaxtiy [7] and chemical vapour deposition [8]. Electrodeposition has the advantages that the precursors are in solution and are therefore easier to handle and the deposition of the film only occurs at the working electrode and not on the entire chamber or its furniture. Electroplating has been scaled up for numerous industrial processes (e.g. copper/chrome plating) and plating large areas at room temperature can be performed on an industrial scale [9]. There are three electrodeposition strategies to form CISe;

- One-step deposition of CISe with no post-treatment
- Deposition of the ternary/binary compounds, metal-selenides (CISe, CuSe and In_2Se_3) followed by an annealing/selenisation step
- The electrodeposition of elemental metallic layers followed by selenisation.

The basic principle of the electrodeposition is that a negative bias is applied to the working electrode reducing ions in solution which precipitate onto the electrode. The optimisation of this methodology is a complex task as there are many factors that

affect the quality of the electrodeposit such as precursor salt species, concentration of species, pH of electrolyte, nature of supporting electrolyte, deposition potential and substrates used.

The majority of the literature concerning the electroformation of CISe thin films has included an additional high temperature step (either annealing or selenisation) to re-crystallise the material. The first paper on the two step co-electrodeposition then annealing to form CISe was by Bhattacharya [10]. The electrodeposition was from an acidic solution (pH 1) containing $InCl_3$, CuCl and SeO_2 with the complexing agent triethanolamine. The presence of a complexing agent is to chelate and stabilises the copper ions in solution. This in turn shifts the reducing potential of copper ions more negative, similar to that of indium. Selenates and selenites are reduced more readily than the copper and indium ions and react via the Kröeger mechanism to form various metal selenides (ca. CISe, Cu_xSe and In_2Se_3). These are then processed (annealed, selenised) into CISe films

There are a number of articles documenting the electrodeposition of CISe films. The use of various complexing agents including critic acid [11], ammonia [12], ethylenediamine [13], ethylenediaminetetrataacetic acid [14] (EDTA) and thiocyanate [15] have been reported. Other background electrolytes used have been both chlorides [16] and sulphates [17]. The use of an acidic medium is favoured as selenide dioxide dissolves to form $HSeO_3^-$ and that the reduction of which occurs more readily than in basic solutions [18]. However, J. Araujo and co-workers [19] showed that it is possible to electrodeposit all three elements from a weakly alkaline medium (p.H. 8.5). Using the complexing agent diethylenetriamine it was possible to form an In-poor film of stoichiometry $Cu_{2.40}In_{1.00}Se_{3.40}$, analysed by atomic emission spectroscopy coupled with inductive coupling plasma. Although the external quantum efficiencies are not mentioned, the band gap of the material was recorded as 1.09 eV. Various authors have investigated the effect of temperature of deposition in both aqueous [20] and glycol [21] electrolytes. Both reports conclude that the deposition temperature has no major influence on the films electronic and structural properties. The electrodeposition of CISe on to flat and nanoparticulate titanium dioxide has also been documented [22]. Initially, dense films of titanium dioxide

were prepared on fluorine-doped tin oxide, SnO_2:F, substrates. Then, a nanoparticlate (NP) film of TiO_2 was deposited by doctor blading. A buffer layer of In_2Se_3 was electrodeposited onto the titanium dioxide and then a layer of CISe on the In_2Se_3. The films were then annealed and etched and finally a graphite layer was deposited as a back contact to create a device of configuration.

CISe based devices have reached efficiencies of 20 % when physical vapour deposition is used as the primary deposition technique [4]. Despite the large amount of literature on the electrodeposition of CISe films, few contain any photocurrents/activity, however, below are some examples on the photo-efficiencies of some electrodeposited devices. Sudo *et al* [23] electrodeposited CISe from the metal chlorides and selenium oxide salts onto SnO_2:F in an aqueous HCl medium. As-deposited films were annealed and a CdS layer deposited to produce the device with an efficiency of 1.49 %.

A cadmium free, superstrate device containing the configuration of indium tin oxide (ITO)/In_2Se_3/CISe/Au is documented in reference [24]. The In_2Se_3 and CISe layers were deposited electrochemically. Replacing the cadmium sulphide with indium selenide is advantageous as this reduces health and safety risks associated with cadmium-containing devices. The device is reported to have an efficiency of 2.8 %. Dale *et al* [5] produced an article that compared the preparation of devices from electrodeposited and sputtered precursors. The highest efficiency of the electrodeposited samples was 6.6 % with the sputtered counterpart having an efficiency of 8.3 %. The current world record for the electrodeposition of CISe is 8.8 % by Guimard *et al* [25], however the device area is very small (ca. 0.06 cm^2).

There have been even fewer reports on the electrodeposition of CIGSe. This is because gallium is a highly electropositive metal causing stability problems. Zank *et al.* used a cyanide bath containing both In and Ga to electrodeposit an alloy of In and Ga. Cu was sputtered onto the alloy then the films were annealed in an Se atmosphere. The resultant device efficiency was 6.6% [26]. The electrodeposition of all three elements (Cu, In and Ga) was reported by Kang *et al.* [27]. A single solution containing the metal chlorides was used in conjugation with citrate acid to stabilise the Ga. The best photovoltaic devices showed a conversion efficiency of 2.0 +/-

0.5%. A recent report by Ribeaucourt *et al.* [28] electrodeposited CuInGa films from an acidic electrolyte (ca. pH ≈2) and selenised to produce CIGSe. Devices had an impressive efficiency of 9.3 %.

Sebastian *et al* [6] used a combination of deposition technologies to prepare a device with an efficiency of 10 %. First electrodeposition of a CISe film was carried out in an acidic bath medium. The composition of the film was analysed by inductive coupled plasma spectroscopy and then the stoichiometry was adjusted using physical vapour deposition (added the elements In, Ga and Se). An industrially promising report was by Kampmann *et al* [29] whereby CISe was electrodeposited from the sulphate salts onto relativity large substrates (ca. 80 cm^2). The as-deposited films were annealed in the presence of excess selenium at 500 ^oC. The resulting efficiencies of the devices were 4.8 %.

2.2.2. Introduction to $MoSe_2$

The transition metal dichalcogenide molybdenum diselenide, $MoSe_2$, is regarded as a versatile semiconductor material. In crystalline form $MoSe_2$ contains layers of Se-Mo-Se covalently bonded together with weak Se-Se van der Waals interactions. The presence of this gap between layers of Se-Mo-Se allows the intercalation of other atoms or molecules [30]. Excess selenium can reside within this space to give the resulting semiconductor material n-type characteristics. Also p-type doping can be achieved by creating selenium deficient crystals [31] or by low temperature processing [32]. As a result, both n-type [33] and p-type [34] $MoSe_2$ materials have been reported and studied. The n-type $MoSe_2$ material is photoactive. Single crystals have been shown to give impressive photo-electrochemical efficiencies of over 10 % [35]. $MoSe_2$ has also been studied in nanoparticate form [36,37] and as polycrystalline thin films [30]. Films of $MoSe_2$ have been used for a substrate for the electrodeposition of silver [34] and for the oxidation of methanol [38]. This chapter presents work on the electrodeposition of metallic precursors onto Mo/$MoSe_2$ films for the generation of photoactive CISe.

The electrodeposited films of Cu/In alloys as a precursor to produce polycrystalline

CISe has been documented before [39,40]. The preferred substrate used in the electrodeposition CISe films is Mo sputtered on soda-lime glass. During selenisation, selenium will diffuse through the film and react to the underlying Mo layer to produce p-type $MoSe_2$. This $MoSe_2$ layer is advantageous because it improves adhesion, stops Se further reacting with Mo, reduces recombination, and creates a low resistivity ohmic contact between the substrate and CISe film [41]. Mo has similar lattice constants to those of CISe, however, Mo is not chemically inert and it undergoes degradation/oxidation when exposed to harsh/aggressive chemical environments. This causes considerable problems with reproducibility in particular for larger substrates. $MoSe_2$ on Mo metal films have been proposed as an alternative substrate material for the physical vapour deposition of $Cu(In,Ga)Se_2$ photovoltaic absorbers [41]. The sub-layer of $MoSe_2$ was shown to provide an ohmic rather than Schottly contact and it improved adhesion. The $MoSe_2$ film is studied here for electrodeposition processes.

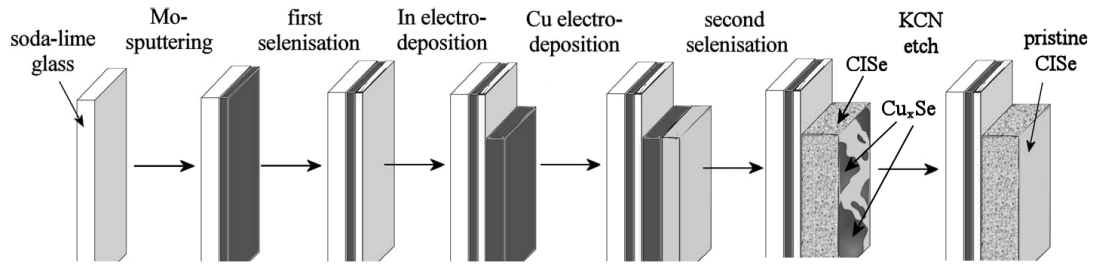

Figure 2.1: Schematic of the route chosen to prepare CISe absorber layers.

It is shown in this chapter that thin films of nanocrystalline $MoSe_2$ produced by selenisation of sputter-coated Mo films provide excellent substrates for CISe electrodeposition. The $Mo/MoSe_2$ heterostructure is chemically robust and electrochemically active. Irreproducibility problems encountered when using Mo-metal films can be avoided. Degenerate semiconductor properties and reversible voltammetric responses are observed in the potential range where copper and indium are plated. Figure 2.1 describes the route taken for the preparation of pristine CISe on $Mo/MoSe_2$ electrodes. Films of indium and copper are sequentially electrodeposited and converted into a photoelectrochemically active CISe layer. The new methodology will be beneficial for the scale up of CISe electrodeposition.

2.3. Experimental Methods

2.3.1. Reagents

Copper(II) sulfate (99.999 %), indium(III) chloride (99.999 %), lithium chloride (99.99%), sodium hydroxide (99.99 %), hexamine ruthenium(III) chloride (99+% %), 1,1'-ferrocenedimethanol , potassium chloride (98 %), D-sorbitol (98%), europium nitrate (99.999%), potassium cyanide (ACS, 96.0%), and selenium powder (99.999%) were purchased from either Sigma Aldrich or Alfa Aesar and used without further purification. Filtered and demineralised water was taken from a Thermo Scientific water purification system (Barnstead Nanopure) with a resistivity of not less than 18.2 MOhm cm.

2.3.2. Instrumentation

For voltammetric and impedance studies a microAutolab III potentiostat system (EcoChemie, Netherlands) was employed with a Pt foil (4 cm × 2 cm) counter electrode and a saturated calomel (SCE) reference electrode (Radiometer, Copenhagen). The working electrode was soda-lime glass sputter-coated with approximately 1 μm thick Mo layer. PTFE tape was used to delineate the deposition area. All electrochemical experiments were conducted in open air without inert atmosphere (to mimic industrial electro-deposition conditions) and the temperature during experiments was $22 \pm 2\ ^{o}C$.

The phases present and the structure of each phase were investigated by x-ray diffraction (XRD) using a Siemens D-5000 diffractometer (Cu Kα line). The surface morphology and topology of the films were observed using a JEOL JSM6480LV scanning electron microscope (SEM), and qualitative compositional analysis of the precursors performed using the energy dispersive x-ray analyzer (EDX) connected to the SEM. Samples examined for cross sectional analysis were gold sputter-coated prior to imaging and analysis. Elemental analysis for re-dissolved deposits was performed by Butterworth Laboratories (Teddington, Middlesex) and based on inductively coupled plasma optical emission spectroscopy, ICP-OES. For Photo-electrochemical experiments a green LED (Farnell, UK) was used in conjunction

with a waveform generator (PP RK, HI-TECK- Instruments, England).

2.3.3. Selenisation of molybdenum films

Prior to selenisation, Mo films were cleaned by sonication in (i) 5 % decon and (ii) ethanol for one minute each followed by drying in a stream of nitrogen. The selenisation of Mo coated glass slides took place inside a custom-made graphite box (Carbon Lorraine UK) with dimensions 10 cm × 7 cm × 1.6 cm within a sealed quartz tube. A horizontal tube furnace (Elite) was used with a constant flow of nitrogen. The tube reactor was evacuated and then filled with nitrogen. Selenisation took place under atmospheric pressure with a flow of nitrogen (10 cm^3 min^{-1}) and with excess of elemental selenium (15 mg placed with the sample into the graphite box). The sample was heated with a ramp rate of 15 ^oC min^{-1} until 550 ^oC and held at this temperature for 1 hour and then allowed to cool to room temperature at a rate of 0.5 ^oC s^{-1}. After this process Mo films were coated with a thin layer of $MoSe_2$ were stored in air.

2.3.4. Electro-deposition of InCu films and CISe formation

Electrical contacts were made directly to the Mo. Mo/$MoSe_2$ electrodes of 1 cm^2 were employed. Prior to electrochemical experiments Mo/$MoSe_2$ substrates were cleaned by dipping into 1M HCl for 10 seconds, rinsing, and drying. The electro-deposition of indium thin films was performed in an aqueous solution of 0.1 M $InCl_3$ and 0.5 M LiCl at pH 3 (adjusted with HCl) [42]. Deposition of indium metal occurred at -0.9 V vs. SCE in chronoamperometry mode. After completion of the indium plating the electrode was rinsed with water and dried in nitrogen. Copper plating was performed in 3.0 M NaOH, 0.2 M D-sorbitol, and 0.1 M $CuSO_4$ and at a deposition potential of -1.105 V vs. SCE [43] in chronoamperometry mode. After completion of the plating step the electrode was rinsed with water and dried in a stream of nitrogen. Selenisation and high temperature annealing were performed by using the same programme and conditions as described above for the selenisation of Mo.

2.3.5. Photoelectrochemical characterisation of CISe films

Prior to photoelectrochemical measurements the Mo/$MoSe_2$/CISe films were immersed in an etch solution of potassium cyanide (5 %w/w) for a variable amount of time. Photoelectrochemical measurements were carried out in a 3-electrode cell where the CISe film, platinum wire counter, and SCE reference electrode were immersed in 0.2 M $Eu(NO_3)_3$. Samples were held at a potential of -0.36 V vs. SCE for 10 seconds in the dark. Then a LED pulsed green light (ca. 530 nm) at the film electrode and photocurrents were measured [44].

2.4. Results and Discussion

2.4.1. Voltammetric characterisation of Mo/$MoSe_2$ electrodes: $Ru(NH_3)_6^{3+}$ reduction and Fe-$(CpMeOH)_2$ oxidation

Molybdenum film electrodes are sensitive to exposure to aqueous electrolyte environment as the metal will readily form a variety of oxide coatings. The solid oxides MoO_2 and MoO_3 can form in an acidic medium whereas the soluble MoO_4^{2-} can form in alkaline electrolyte [18]. When molybdenum is employed in the electro-deposition of semiconductor (or metallic) films reproducibility issues can occur. In this study the pre-selenisation of Mo to $MoSe_2$ is investigated as a methodology to avoid these problems. Bulk $MoSe_2$ usually exhibits n-type semiconductor properties [30] but very thin films (as shown here) provide sufficient metallic/ohmic conductivity for metal plating and other redox processes.

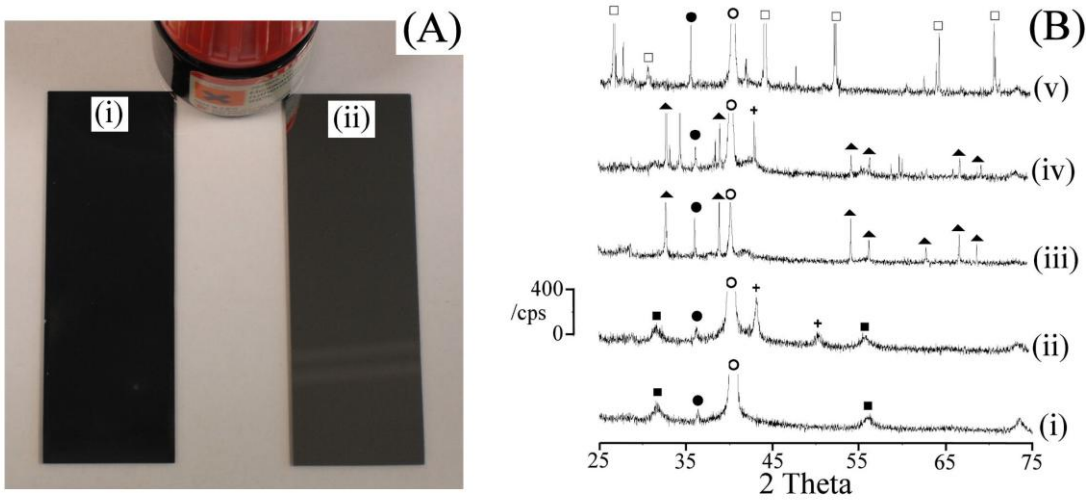

Figure 2.2: (A) Photograph taken of (i) $MoSe_2$ and (ii) Mo coated glass slides. (B) XRD patterns of various film compositions: (i) Mo/$MoSe_2$ (ii) Mo/$MoSe_2$/Cu (iii) Mo/$MoSe_2$/In (iv) Mo/$MoSe_2$/InCu (v) Mo/$MoSe_2$/CISe. Filled circles: Substrate holder, Unfilled circles: Mo, Filled squares: MoSe2, Unfilled Squares: CISe, Crosses: Cu and triangles: metallic In.

Sputter-coated Mo onto soda lime glass results in Mo films that are bright and shiny (figure 2.2Aii). Subsequent selenisation (550 ^oC for 1 hour, see experimental) produced darker films figure 2Ai which exhibit both Mo [45], and $MoSe_2$ [46] reflections (figure 2.2Bi) suggesting that a Mo/$MoSe_2$ heterostructure exists. The

formation of a $MoSe_2$ film from selenium vapour and metallic Mo is expected at temperatures above 440 ^oC [47]. Other authors have observed the Mo/$MoSe_2$ heterostrucutre post- annealing of CISe deposits on Mo substrates [5]. The presence of a $MoSe_2$ film may be regarded as a layer protecting the metallic Mo layer from chemical attack without significantly impeding electrochemical activity. Reported thicknesses for $MoSe_2$ produced under selenisation conditions are typically between 100-500 nm [41,48].

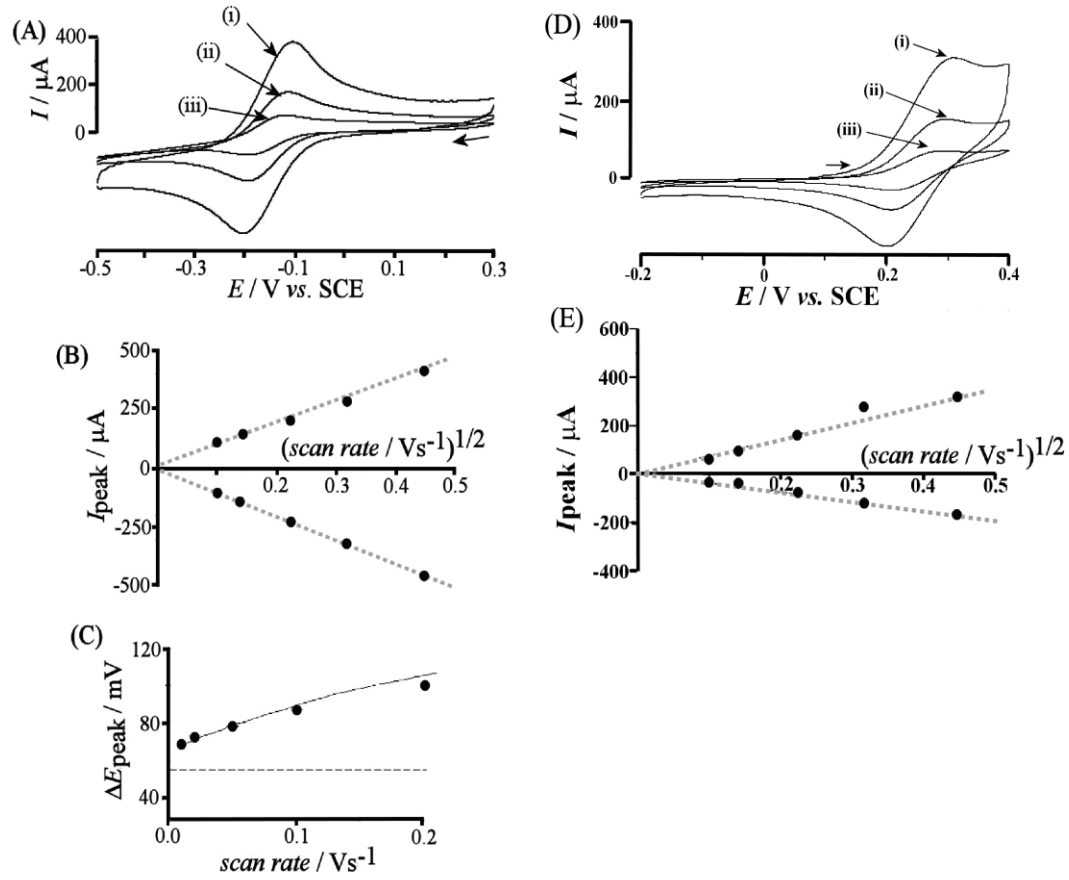

Figure 2.3: (A) Cyclic voltammograms (scan rate (i) 0.2, (ii) 0.05, and (iii) 0.01 Vs^{-1}) for the reduction of 1 mM $Ru(NH_3)_6^{3+}$ in aqueous 0.1 M KCl at a 1 cm^2 Mo/$MoSe_2$ electrode. (B) Plot of the peak currents for reduction and re-oxidation versus square root of scan rate. (C) Plot of the peak to peak separation ΔE_{peak} versus scan rate. The dashed line shows the expected separation for a reversible voltammogram and the line fitted into the data corresponds to a heterogeneous standard rate constant of $k_s = 6 \times 10^{-5}$ m s^{-1} (see text). (D) Cyclic voltammograms (scan rate (i) 0.2, (ii) 0.05, and (iii) 0.01 Vs^{-1}) for the oxidation of 1 mM 1,1'-ferrocenedimethanol in aqueous 0.1 M KCl at a 1 cm^2 Mo/$MoSe_2$ electrode. (B) Plot of the peak currents for reduction and re-oxidation versus square root of scan rate.

To illustrate the degenerate nature of the $MoSe_2$ electrode figure 2.3A shows cyclic voltammograms for the one-electron reduction of $Ru(NH_3)_6^{3+}$ in aqueous 0.1 M KCl (see equation 2.1). Both the reduction of $Ru(NH_3)_6^{3+}$ and the re-oxidation of $Ru(NH_3)_6^{2+}$ are facile processes, Emid = ½($E_{p,\,ox}$ + $E_{p,\,red}$) = -0.15 V vs. SCE.

$$Ru(NH_3)_6^{3+}(aq) + e^- \rightleftharpoons Ru(NH_3)_6^{2+}(aq) \qquad (2.1)$$

The plot of the peak current versus square root of scan rate (see figure 2.3B) confirms diffusion controlled voltammetric responses. The rate of electron transfer is fast and the heterogeneous standard rate constant $k_s = 6 \times 10^{-5}$ m s^{-1} can be estimated from the peak-to-peak separation (see figure 2.3C) by fitting based on equation 2.2 [49].

$$\log_{10}\left(k_s\sqrt{\frac{RT}{nFvD}}\right) = 0.294\left(\frac{nF}{RT}\Delta E - 2.218\right)^{-1} - 0.0803 - 0.108\left(\frac{nF}{RT}\Delta E - 2.218\right) \qquad (2.2)$$

Figure 2.3D shows cyclic voltammograms for the oxidation/reduction of 1,1'-ferrocenedimethanol (equation 2.3). The Emid = ½($E_{p,\,ox}$ + $E_{p,\,red}$) = 0.25 V vs. SCE is reversible, has a $E_{peak\ to\ peak}$ = 100 mV, similar to the ruthenium hexamine redox couple. The 1,1'-ferrocenedimethanol voltammetry signal is superimposed onto the oxidation of the substrate.

$$Fe\text{-}(CpMeOH)_2(aq) \rightleftharpoons Fe\text{-}(CpMeOH)_2^+(aq) + e^- \qquad (2.3)$$

From the quasi-reversible voltammetric characteristics of both ruthenium and 1,1'-ferrocenedimethanol it is inferred that the $MoSe_2$ coated Mo film electrode is behaving like a degenerate semiconductor. Additional impedance measurements performed in aqueous 0.1 M KCl suggest simple RC behaviour with a resistance of ca. 50 Ω and a capacitance of ca. 250 μF cm^{-2} constant over a potential range from 0 to -1 V vs. SCE.

2.4.2. Voltammetric characterisation of $Mo/MoSe_2$ electrodes: Cu^{2+} Electrodeposition

For the deposition of copper metal, alkaline conditions (cyanide free) were chosen following a procedure developed recently [43]. The $Mo/MoSe_2$ electrode was immersed into aqueous 3 M NaOH with 0.2 M D-sorbitol and the open circuit potential monitored. No erosion or dissolution was observed after 10 minutes. Cyclic voltammetry experiments were conducted in the absence and in the presence of 0.1 M $CuSO_4$ (see figure 2.4A and 2.4B, respectively). Over the potential window investigated (-0.4 to -1.4 V vs. SCE) the $MoSe_2$ film electrode was stable. A broad reduction response commencing at -0.7 V vs. SCE can be attributed to the reduction of oxygen (all experiments were conducted in air). In the presence of 0.1 M $CuSO_4$ (copper(II) under these conditions is in the form of cuprate $Cu(OH)_4^{2-}$ [50] or a D-sorbitol copper complex [43]) a reduction and re-oxidation response are observed (see figure 2.3B) consistent with the formation of copper metal (equation 2.4).

$$Cu(OH)_4^{2-} + 2\,e^- \rightleftharpoons Cu(metal) + 4\,OH^-(aq) \qquad (2.4)$$

During the first potential cycle a nucleation of copper on the $Mo/MoSe_2$ film electrode is observed at ca. -0.65 V vs. SCE. During the second potential cycle this process is not observed probably due to remaining copper nuclei on the electrode surface. A deposition potential of -1.105 V vs. SCE was chosen and chronoamperometry experiments conducted. Figure 2.4D shows typical chronoamperomentry data with a deposition current of ca. 1 mA cm^{-2}.

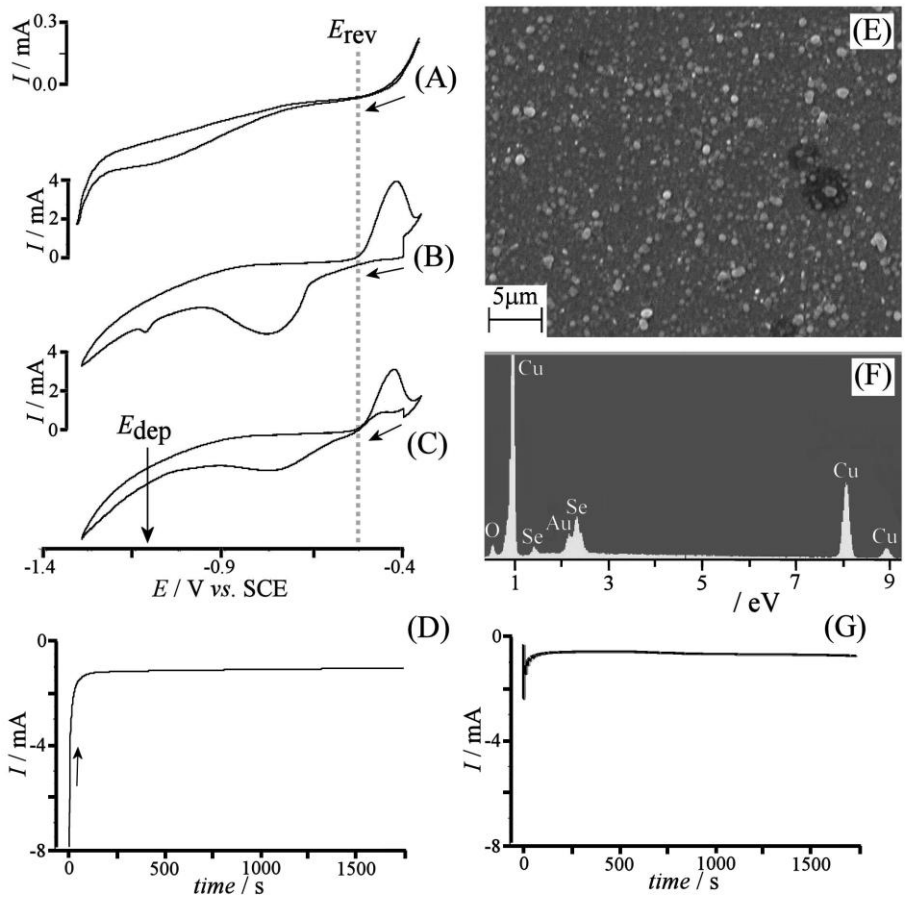

Figure 2.4: (A,B,C) Cyclic voltammograms (scan rate $0.02 Vs^{-1}$) for $Mo/MoSe_2$ electrodes immersed in aqueous 3 M NaOH containing 0.2 M D-sorbitol without (A) and with (B,C) 0.1 M $CuSO_4$ (shown in (B) 1st cycle and in (C) 2nd cycle). (D) Chronoamperogram for the electro-deposition of copper metal onto $Mo/MoSe_2$ with a deposition potential of –1.105 V vs. SCE and a cut-off charge of 2.03 C. (E,F) SEM image and EDS on a 0.75 μm Cu film on top of a $Mo/MoSe_2$ electrode and (G) Chronoamperogram for the electro-deposition of copper metal onto $In/Mo/MoSe_2$ with a deposition potential of –1.105 V vs. SCE.

An SEM image of a copper film deposited under these conditions (a cut-off value of 2.03 coulombs was set which corresponded to an average film thickness of 0.75 μm, confirmed by SEM) is shown in figure 2.4E. A nodular deposit with features ca. 1 μm in size is observed. EDS data clearly reveal the presence of Cu, O, and Se within the film. XRD data are shown in figure 2.2Bii shows the presence of new diffraction peaks corresponding to (111) and the (200) planes for the copper crystal lattice [51].

2.4.3. Voltammetric characterisation of Mo/$MoSe_2$ electrodes: In^{3+} electrodeposition

The electro-deposition of In metal can be achieved in aqueous 0.5 M LiCl at pH 3 [42]. $MoSe_2$ coated Mo film electrodes appear inert under these conditions as seen in figure 2.5A. In the presence of 0.1 M $InCl_3$ (see figure 2.5B) the reversible deposition and stripping of indium metal (see equation 2.5) is observed with E_{rev} = -0.66 V vs. SCE consistent with the value reported by Muñoz and co-workers for the deposition onto carbon substrates [42].

$$In^{3+}(aq) + 3\,e^- \rightleftharpoons In(metal) \qquad (2.5)$$

The indium deposition and stripping processes are effective (the charges under reduction and re-oxidation peaks are almost identical) and consecutive cyclic voltammograms show essentially identical features.

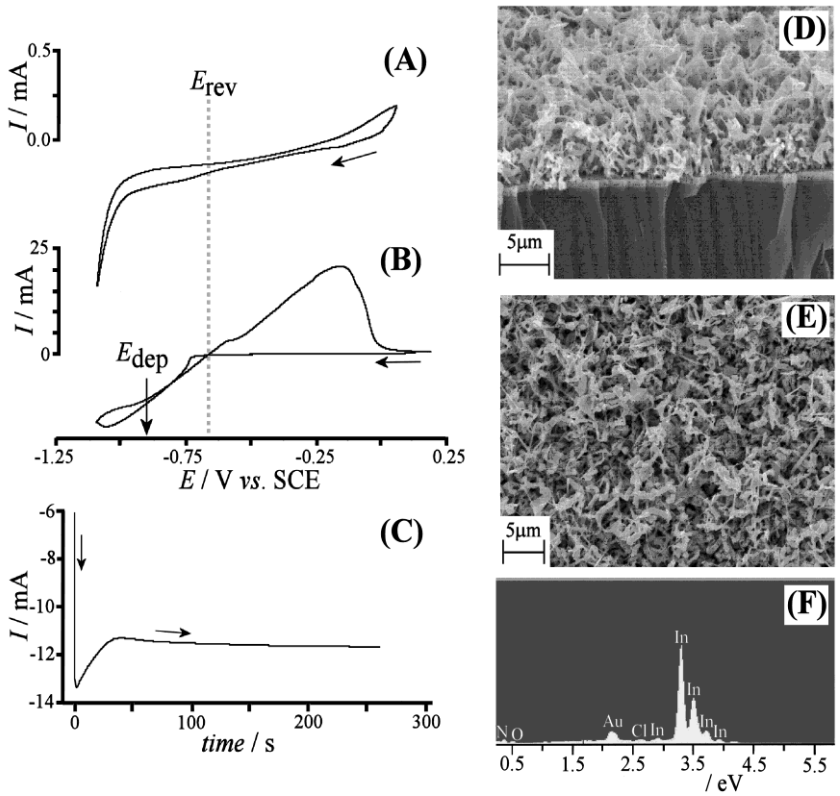

Figure 2.5: (A,B) Cyclic voltammograms (scan rate 0.02Vs^{-1}, area 1 cm^2) obtained at a Mo/$MoSe_2$ electrode immersed in aqueous 0.5 M LiCl at pH 3 without (A) and with (B) 0.1 M $InCl_3$. The deposition potential E_{dep} and the reversible potential E_{rev} are indicated (C) Chronoamperogram for the electrodeposition of In metal onto a Mo/$MoSe_2$ electrode with applied deposition potential -0.9 V vs. SCE. The cut-off of charge was 3.04 C. (D,E) SEM images and (F) EDS data for an In metal deposit on Mo/$MoSe_2$.

The electrodeposition of indium metal was carried out in chronoamperometry mode at a potential of E_{dep} = -0.9 V vs. SCE (see figure 2.5C). A cut off value of 3.04 C was chosen to produce an indium film of 1.6 μm theoretical thickness (assuming 100% current efficiency). The deposition current remains relatively constant at ca. 12 mA cm^{-2}. SEM images of typical deposits are shown in figure 2.5D and 2.5E. A porous high surface area indium film is formed with rod-like features 100 to 200 nm in diameter. The EDS analysis reveals the presence of indium and chloride impurities. The XRD reflections of this film see figure 2.2Biii shows diffraction peaks for Mo, $MoSe_2$, and metallic In [52] which includes diffraction peaks for (002), (110), (112), (200), (114), (211), and (202).

2.3.4. Voltammetric characterisation of Mo/$MoSe_2$ electrodes: CuIn alloy electrodeposition and photo-electrochemistry

In order to form CuIn alloy deposits as precursor for the formation of $CuInSe_2$, there are two possible strategies: (i) first plating the more noble copper film and second plating indium or (ii) first plating indium followed by copper plating. The former strategy failed due to the formation of a white product, possibly an oxide, when immersing the electrode into the indium plating bath. However, the deposition of copper onto indium was successful and the electrodeposition of 0.75 μm of Cu on top of 1.64 μm was undertaken. Chronoamperometry data for the deposition of copper onto indium are shown in figure 2.4G. In comparison to data for the deposition of copper on Mo/$MoSe_2$ the deposition current is lower indicating a slower rate of copper plating onto indium.

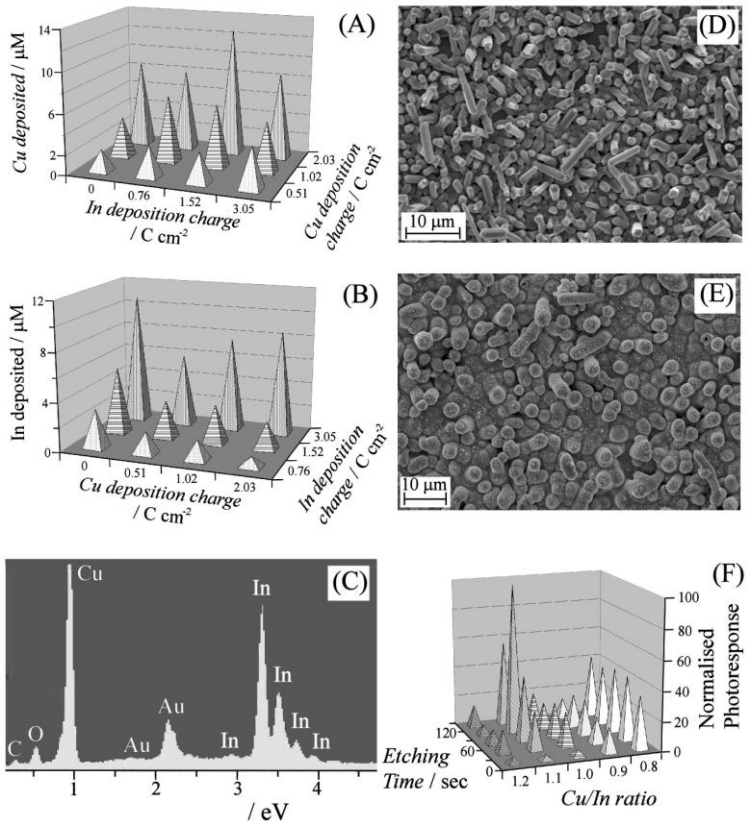

Figure 2.6: (A) The amount of Cu (concentration in 10 cm^3, by elemental analysis) and (B) the amount of In (by elemental analysis) present in InCu film deposits as a function of deposition charge for In and Cu. (C) EDS of a InCu film deposit (Au coated). (D) SEM image for an as-deposited InCu film. The theoretical ratio of Cu to In is 1:1 with a theoretical thickness of the Cu layer as 0.75µm. (E) The InCu film after annealing in Se. (F) Preliminary photocurrents of CISe films as a function of theoretical Cu/In ratio and etching time. Data were recorded for CISe films immersed 0.2 M $Eu(NO_3)_3$ with an applied potential -0.36 V vs. SCE and a pulsed 530 nm light source.

The XRD recorded of the resultant film has a variety of reflections, this is due to the CuIn system having many stable alloys at room temperature which include δ–Cu_7In_3, η–Cu_2In and $Cu_{11}In_9$ as well as metallic systems (ca. pure indium or copper) [53]. SEM images and EDS data for the resulting composite film (see figure 2.6D and 2.6E) suggest successful formation of a mixed In/Cu film deposit. In the SEM image rod-like features dominate. Elemental analysis of alloy deposits (after dissolution in concentrated nitric acid) suggests reasonable reproducibility and successful alloy formation (see figures 2.6A and 2.6B). Typical plating efficiencies of 90% and 80% where observed for In and Cu, respectively (compared to 94 % for Cu [43]).

Interfering oxygen reduction processes may somewhat lower the current yield but could be tolerated. SEM images taken after In/Cu was deposited (see figure 2.6D) revealed a rod like morphology which is to be expected as the indium deposition product similar structure. Thickness measurements were taken by imaging a cross section of the porous film and revealed a typical film thickness of 4-5 μm.

$$CuIn + 2Se(gas) \rightleftharpoons CuInSe_2 \qquad (2.6)$$

The selenisation process (selenium vapour at 550 ^{o}C, see experimental) is known to lead to CISe and is confirmed by the XRD figure 1iv. As expected the (112) lattice plane dominates with other reflections (103) (220/204) (312) (008/400) (316/332) [54] present. The other peaks (unlabelled) correspond to copper selenide reflections [55,56]. The formation of CISe results in a morphology change (see figure 2.6E) with most deposits fusing to form a continuous film with circular grains of the order of 1-3 μm. Rod like features are present with lengths of 5-7 μm. Some pinholes (after KCN etch) can also be observed.

The photoresponse of the resulting CISe films was examined using photo-electrochemistry with film electrodes immersed into aqueous 0.2 M $Eu(NO_3)_3$ [57]. A green LED light source is employed and generation of electron-hole pairs at the semiconductor – electrolyte junction are monitored as photo-reduction responses (equations 5). The surface of the semiconductor was under depleted conditions (ca. -0.36 V vs. SCE).

$$Eu^{3+}(aq) + e^{-}(CISe) + h\nu \longrightarrow Eu^{2+}(aq) \qquad (2.7)$$

Preliminary data in figure 2.6F shows that un-etched CISe films produce a low photocurrent of < 5 μA cm^2 presumably due to the presence of some $Cu_{2-x}Se$. Un-etched CISe films with a higher concentration of In show a better photoresponse, probably due to less $Cu_{2-x}Se$. However, because these CISe films are indium-rich the photoresponse is not significantly improved even after etching. Films with a higher Cu/In ratio are more responsive to the potassium cyanide etch. In general, the gradual etching process was found to provide the highest observed photocurrent 14.9 μA cm^{-2} for a Cu/In ratio of 1.1. Further etching is likely to create pinholes (which reach the underlying substrate) where recombination occurs and then the photocurrent

decrease. Further improvements will be possible by improving the deposition conditions, the formation of more uniform and more finely grained CISe films, and a better control of the mass transport during the electrodeposition process.

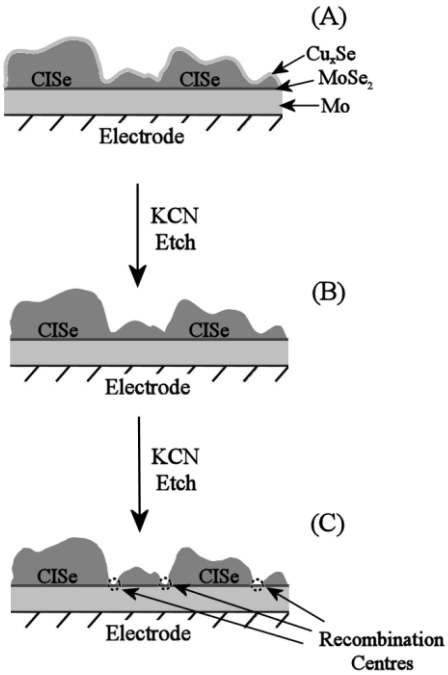

Figure 2.7: Diagram representation of the KCN etching of a CISe surface. (A) is an under etched samples that contains Cu_xSe and CISe. (B) is a pristine sample where the surface is purely CISe. (C) is an over etched case where the CISe and Cu_xSe has been removed to produce pin holes exposing the substrate which act as recombination centres.

2.5. Conclusions

Chemically robust and electronically degenerate Mo/$MoSe_2$ thin film electrodes have been produced and employed for the formation of CISe solar cell absorber films. In contrast to the chemically highly sensitive bare molybdenum surface, the Mo/$MoSe_2$ electrode surfaces exhibit chemically robust characteristics in acidic and in alkaline aqueous media. Reversible electrochemistry occurred for a number of redox systems when using Mo/$MoSe_2$ substrates. Films of CISe were formed by sequential electrodeposition and selenisation. The resulting CISe films were tested for their photo-electrochemical performance. The new methodology based on $MoSe_2$ coated Mo film electrodes is amendable to scaling up and with improved mass transport control during the electrodeposition process further improvements in the photo-electrochemical properties are expected.

2.6. References

[1] S. Wagner, J. Shay, P. Migliorato, H. Kasper, Appl. Phys. Lett. 25 (1974) 434

[2] J. Shay, B. Tell, H. Kasper, L. Schiavone, Phys. Rev. B. 7 (1973) 4485

[3] T. Zdanwicz, T. Rodziewcz, M. Zabkowska-Waclawek, Sol. Ener. Mater. Sol. Cells 87 (2005) 757

[4] I. Repins, M. Contreras, B. Egaas, C. DeHart, J. Scharf, C. Perkins, B. To., R. Noufi Prog. Photovolt: Res. Appl. 16 (2008) 235

[5] P. Dale, A. Samantilleke, G. Zoppi, I. Forbes, L. Peter, J. Phys D: Appl. Phys. 41 (2008) 8

[6] P. Sebastian, M. Calixto, R. Bhattacharya, R. Noufi, J. Electrochem. Soc. 145 (1998) 3435

[7] S. Niki, Y. Makita, A. Obara, S. Misawa, O. Igarashio, K. Aoki, N. Kutsuwada, Jap. J. Appl. Phys. Part 2 – Lett. 33 (1994) L500

[8] P. Gallon, F. Ouchen, M. C. Artaud, S. Duchemin, Proc. 2nd World Conf. Photovolatic Convesion EUR18656EN (1998) 515.

[9] D. Pletcher, F. Walsh *Industrial electrochemistry*, 2nd edition Blackie Academic & Professional (1993)

[10] R. N. Bhattacharya, J. Electrochem. Soc. 130 (1983) 2040

[11] T. Pottier, G. Maurin, J. Electrochem. Soc. 19 (1989) 361

[12] J. Bekker, V. Alberts, M. J. Witcomb, Thin Solid Films 387 (2001) 40

[13] F. Pern, R. Noufi, A. Mason, A. Franz, Thin Solid Films 202 (1991) 299

[14] R. Ugarte, R. Schrebler, R. Córdova, E. A. Dalchiele, H. Gómez, Thin Solid Films 340 (1999) 117

[15] M. Ganchev, K. Kochev, Ener. Mater. Sol. Cells 31 (1993) 163

[16] P. Garg, A. Garg, A. Rastogi, J. Garg, J. Phys. D: Appl. Phys. 24 (1991) 2026

[17] A. Chowles, J. Neethling, H. van Niekerk, J. Engelbrecht, V. Watters, Renew. En. 6 (1995) 613

[18] M. Pourbaix, *Atlas of Electrochemical Equilibria in Aqueous Solutions*, Pergamon Press, New York, (1966)

[19] J. Araujo, R. Ortíz, A. López-Rivera, J. Ortega M. Montilla, D. Alarcón, J. Solid State Electrochem, 11 (2007) 407

[20] M. Benaicha, N. Benouattas, C. Benazzouz, L. Ouahab, Sol. Ener. Mater. Sol. Cells 93 (2009) 262.

[21] J. Wellings, A. Samantilleke, S. Heavens, P. Warren, I. Dharmadasa Sol. Ener.

Mater. Sol. Cells 93 (2009) 1518

[22] M. Valdes, M. Vazquez, A. Goossens, Electrochimica Acta 54 (2008) 524

[23] Y. Sudo, S. Endo, T. Irie, Jap. J. Appl. Phys. 32 (1993) 1562

[24] A. Kampmann, A. Abken, G. Leimkuhler, J. Rechid, V. Sittinger, T. Wietler, R. Reineke-Koch, Prog. Photovoltaics 7 (1999) 129

[25] D. Guimard, 2002 *Conf. Record of the 29th IEEE Photovoltaic Specialists Conf. (New Orleans, LA, 2002)* pp. 692–5

[26] J. Zank, M. N. Mehlin, H. P. Fritz, Thin Solid Films 286 (1996) 259

[27] Kang, F.A, J. P.Sun, G. Z.He, Q.Sun, Y. Semicond. Sci. Technol. 24 (2009) 075015

[28] L. Ribeaucourt, G. Savidand, D. Lincot, E. Chassaing, Electrochimica Acta 56 (2011) 6628

[29] A. Kampmann, Symposium on Chalcogenide Semiconductors for Photovoltaics at the 1999 E-MRS Spring Conference (1999) 309

[30] W. Sienicki, J. Mat. Chem. Phys. 68 (2001) 119

[31] M. Zoaeter, A. Conan, D. Delaunay, Phys. Stat. Sol. 41 (1977) 629

[32] C. Sumesh, K. Patel, V. Pathak, R. Srivastava, Chalcogenide Lett. 5 (2008) 170A

[33] A. Chaparro, P. Salvador, A. Mir, J. Electroanal. Chem. 418 (1996) 175

[34] T. Ohmori, C. Cabrera, Langmuir 14 (1998) 3723

[35] V. Pathak, K. Patel, R. Pathak, R. Srivastava, Sol. Ener. Mat. Sol. Cells 73 (2002) 117

[36] J. Huang, D. Kelley, J. Chem. Mat. 12 (2000) 2825

[37] S. Bastide, C. Levy-Clement, A. Albu-Yaron, A. C. Boucher, N. Alonso-Vante, J. Electrochem. Sol. State Lett. 3 (2000) 450

[38] H. Bolivar, S. Izquierdo, R. Tremont, C. R. Cabrera, J. App. Electrochem. 33 (2003) 1191

[39] T. Gujar, V. Shinde, J. Park, H. Lee, K. Jung, O. Joo, J. Electrochem. Soc. 155 (2008) E131.

[40] D. Cahen, G. Hodes, Ternary Adamantine materials for low cost solar cells Tech. Rep. SERT IL5-04132-1, Solar Energy Res. Inst., Golden, CO.

[41] T. Wada, N. Kohara, S. Nishiwaki, T. Negami, Thin Solid Films 387 (2001) 118

[42] A. Muñoz, S. Saidman, J. Bessone, J. Electrochem. Soc. 146 (1999) 2123

[43] L. Barbosa, M. de Almeida, R. Carlos, M. Yonashiro, G. Oliveira, I. Carlos, Surf. Coat. Tech. 195 (2005) 145.

[44] J. Scragg, P. Dale, L. Peter, Thin Solids Films 517 (2009) 2481

[45] A. Hull, W. Davey, Phys. Rev. 17 (1921) 571

[46] P. James, M. Lavik, Acta Cryst. 16 (1963) 1183

[47] W. Kim, E. Payzant, S. Yoon, T. Anderson. J. Cry. Grow. 294 (2006) 231

[48] O. Volobujeva, J. Kois, R. Traksmaa, K. Muska, S. Bereznev, M. Grossberg, E. Mellikov, Thin Solid Films 516 (2008) 7105

[49] F. Scholz, *Electroanalytical methods*, Springer, (2009)

[50] D. Richens, *The chemistry of aqua ions*, Wiley, New York, (1997)

[51] W. Bragg, Phil. Magazine 28 (1914) 255

[52] A. Hull, W. Davey, Crystal. Phys. Rev. 17 (1921) 266

[53] Z. Bahari, E. Dichi, B. Legendre, J. Dugue, Thermochim. Acta. 401 (2003) 131

[54] J. Parkes, R. Tomlinson, M. Hampshire, J. of App. Cryst. 6 (1973) 414

[55] J. Earley, American Mineralogist 33 (1948) 194

[56] W. Davey, Physical Review 21 (1923) 380

[57] A. Vijh, *Electrochemistry of metals and semiconductors*, Marcel Dekker, Inc., New York (1973)

Chapter 3

Rocking Disc Electrodeposition of Copper Films on Mo/$MoSe_2$ Photovoltaic Substrates

Contents

This work is published as
C. Cummings, P. Frith, G. Zoppi, I. Forbes, K. Rogers, D. Lane, F. Marken, Thin Solid Films 519 (2010) 7458

3.1. Abstract

A novel electrodeposition method based on a rocking disc system with π/3 amplitude and variable frequency is introduced. In order to plate large electrode surfaces (up to 50 mm x 50 mm) a cylindrical cell with rocking motion around the symmetry axis (0.84 Hz – 16.67 Hz) is employed. The turbulent mass transport conditions are investigated as a function of frequency and position on the electrode surface. Investigation of the mass transport conditions suggest (i) uniform diffusion over the sample, (ii) a rate of convection proportional to the square root of the rocking rate, and (iii) turbulent conditions which are able to dislodge gas bubbles during electro-deposition. Uniform copper films (thickness variation of +/- 5% over 12.1 cm^2 based on XRD scans) are deposited from a 0.1 M $CuSO_4$/3.0 M NaOH/0.2 M sorbitol bath directly onto 12.1 cm^2 photovoltaic Mo/$MoSe_2$ substrates.

3.2. Introduction

3.2.1. Introduction to uniformity issues in electrodeposition

The movement of ions to an electrode surface is governed by three processes; migration, diffusion and convection. Migration effects aid electrophoretic deposition but are usually not exploited by electrochemists as it has a minimum influence on the electrochemistry when a background electrolyte is present. Diffusion and convection are the two physical processes that give reproducible and reliable data. The natural phenomenon of diffusion is a consequence of entropy and is related to the concentration gradient by Fick's laws of diffusion [1]. Convection (or flow) is typically induced by applying hydrodynamic forces. Several methods can be used to induce convection, these include the rotating disc electrode [2], jet [3], ultrasound [4] and vibration [5].

Novel methodologies using convection within electrochemistry include hydrodynamic modulation voltammetry which can be induced by using either a rotating disc [6] or a jet system [7]. Modulating the convection can increase the sensitivity of detecting an aqueous analyte as its electrochemistry can be deconvoluted from background processes, such as electrode surface reactions, double layer charging, and solvent decomposition.

Electrodeposition is a widely used technology in industry having applications in films and coatings, namely the electrodeposition of metals [8], metal alloys [9], semiconductors [10] and more recently photovoltaics [11]. Electrodeposition is favoured in industry due to a number of reasons: a high throughput method, allows coatings to form onto non-ideal (planar) substrates, morphology, thickness and composition of resultant films can be controlled by external parameters and equipment costs are low [12]. For the preparation of semiconductors for the photovoltaic industry, electrodeposited films must be highly uniform over large areas. As a consequence substrates must be uniform and convection must be induced during electrodeposition to thin the diffusion length, $\delta_{Diffusion}$, uniformly at the electrolyte | electrode interface. This creates a highly defined, controllable profile and allows for a fast rate of deposition.

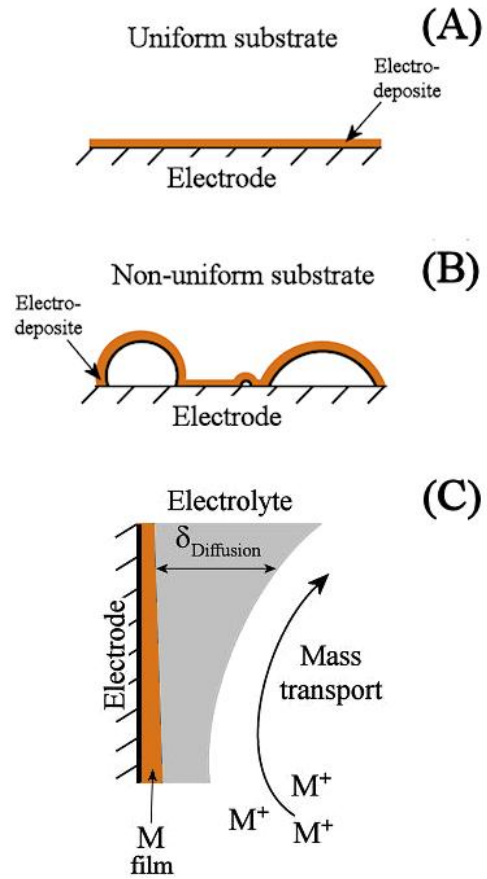

Figure 3.1: Two key factors that affect the uniformity of the resulting films. (A) Drawing of a uniform deposit formed on a uniform substrate. (B) Drawing of a deposit on a non-uniform electrode which results in a non-uniform film. (C) Schematic representing convection processes that can exist at the electrode | electrolyte interface for a static, vertically aligned electrode.

Non-uniformities originating from the substrate will be superimposed on the electrodeposited film (see figure 3.1A and 3.1B). The film morphology shown in figure 3.1B can be detrimental to a photovoltaic device as the deposition of further materials (which can be performed using non-electrochemical methods) will create irregularities such as a variation in thickness.

Static, vertical aligned electrodes do not create uniform films (see figure 3.1C) as an ill-defined convection exists which originates from the following processes. During the electrodeposition, removal of ions at the electrode | electrolyte interface causes a decrease in the concentration of the electroplated ion. As a consequence this reduces the density of the electrolyte at the electrode | electrolyte interface causes an ill-defined convection flowing against gravity. Hydrogen evolution can occur when a

highly electropositive element is being electroplated. The hydrogen reduction reaction completes with the reduction of the metal and as a consequence hydrogen bubbles form on the electrode. Hydrogen bubbles forming on the evolving film disrupted the microscopic diffusion length and the detachment of which will cause an ill-defined convection. Hydrogen bubbles forming on the substrate cause the creation of pits and pores by the exclusion of the electrolyte.

3.2.2. The rotating disc electrode

Industrial electrochemists are concerned about two factors: the mixing of the electrolyte during the electrodeposition to create a homogenous solution and the uniform flow of the electrolyte to the electrode surface. Most industrial mass transport methods such as the jet, vibration, or gas sparging do homogenise the solution however, they do not create a well-defined diffusion length profile across the entire electrode surface [13]. The exception is the rotating disc which both homogenises the solution but also depresses the diffusion length almost equally across the electrode surface (see figure 3.2). The rotating disc can also cause a high rate of deposition which leads to a higher productivity.

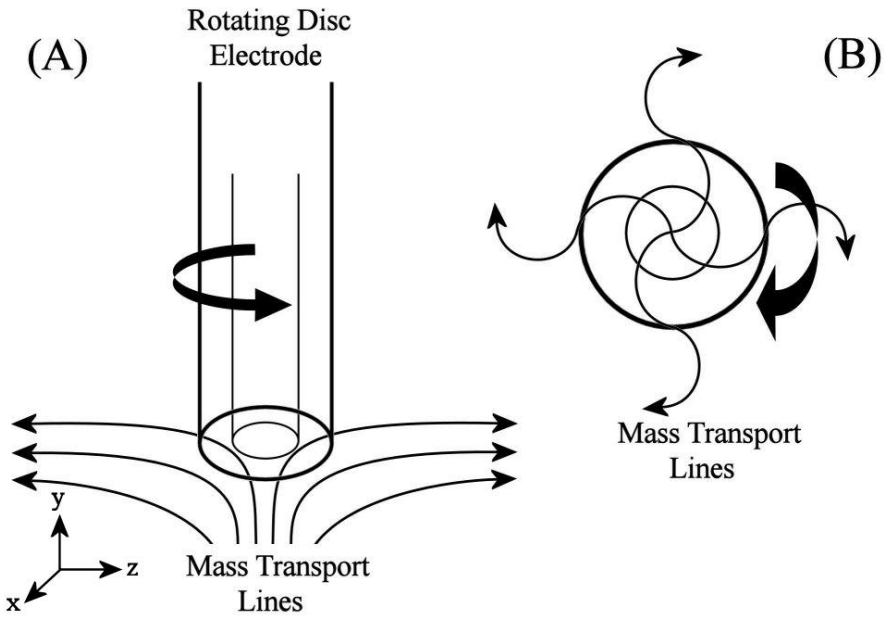

Figure 3.2: Schematics of the rotating disc electrode under two positions (A) normal to the electrode (B) end on to the electrode. The convection lines are superimposed to imitate the flow of the electrolyte.

The rotating disc electrode induces convection by rotating a planar working electrode that is immersed in the electrolyte. The solution at the electrode | electrolyte interface is forced along the axis of the electrode (as shown z axis) and acts as a pump drawing the electrolyte perpendicular to the electrode surface. At the surface of the rotating disc it is possible to estimate the velocity of the electrolyte v_Z as a function of *z* by the following equation.

$$v_Z \approx -0.51\omega^{2/3} v_{Bulk}^{1/2} D^{-1/3} z^2 \qquad (3.1)$$

In this expression ω is the rotational speed in radians (defined as the frequency of rotation multiplied by 2π), v_{Bulk} is the kinematic viscosity of the electrolyte, D is the diffusion coefficient of the concerned electro active species and z, is the distance along the electrode surface. Equation 3.1 dictates that the speed of the electrolyte at position *z* is dependant upon the square of the distance away from the central axis of the electrode.

The frequency of rotation rate can vary between 5 and 50 Hz for which the flow is predominately laminar. Setting boundary conditions where convection is the predominate mechanism of mass transport and where a high overpotential is applied to an electrode, the resultant (limiting) current can be predicted by the Levich equation (equation 3.2).

$$I_{Lim} = 0.62nFA[Ox]_{Bulk} D v_{Bulk}^{-1/6} \omega^{1/2} \qquad (3.2)$$

Here I_{Lim} is the limiting current, n is the number of electrons transferred during the reaction F is the Faraday constant, A is the area of the electrode and $[Ox]_{Bulk}$ is the concentration of oxidised species in the bulk. The average diffusion length profile under the rotating disc conditions δ_{Rot} can be estimated using the following equation:

$$\delta_{Rot} = 1.61 D^{1/3} v_{Bulk}^{1/6} \omega^{-1/2} \qquad (3.3)$$

The rotating disc electrode has been used extensively academically, for applications in electrodeposition of solar cells [14] and the evaluation of mass transfer kinetics on electrodeposition [15], with various reports examining its theory [2,16]. Despite this, there are some important issues that have to be taken into consideration when

implementing a rotating disc electrode for large area, industrial applications. The rotating disc is not mechanically simple as contact to the continuous rotating working electrode can be problematic. This also does not allow for a continuous process. The entire rotating disc surface has to be larger than the electrode and that the vessel containing the entire electrolyte has to be big enough not to interference with the convection emanating from the rotating disc.

3.2.3. The rocking disc electrode

This chapter demonstrates an alternative to the rotating disc electrode which induces both electrolyte homogeneity and well defined convection to the electrode surface. The use of the semi-rotation (vibration or rocking motion) of the entire cell to induced mass transport is both technically and mechanically simpler than the rotating disc electrode. The rocking disc electrode is industrially more applicable to scale up due to its simplicity. By perturbing the system at a periodic and set frequency it is possible to show that the convection induced is turbulent in nature to remove forming hydrogen bubbles but highly defined and uniform. The uniform rocking disc electrodeposition of copper from an alkaline electrolyte onto large substrates, 12.1 cm^2 is reported.

3.3. Experimental Methods

3.3.1. Reagents

Sodium hydroxide (97 %), D-sorbitol (98 %), potassium chloride (98 %) hexamine ruthenium(III) chloride (99.9 +%), were obtained from Aldrich and used without further purification. Copper sulphate, (A.C.S. grade) was purchased from Alfa Asear. Solutions were prepared in demineralised and filtered water taken from an Elgastat water purification system (Elga, High Wycombe, Bucks) with a resistivity of not less than 18.2 MOhm cm.

3.3.2. Instrumentation

For voltammetric studies a microAutolab II potentiostat system (EcoChemie, Netherlands) was employed with a saturated Calomel (SCE) reference electrode (Radiometer, Copenhagen). For all experiments the reference was placed 2 mm away from the working electrode. The counter electrode was positioned at the top of the cell and was composed of a sheet of metallic copper (Advent 99.99 %), dimensions 5 mm x 5 mm. The working electrodes where either the Au calibration electrode, (see section 2.4.) or Mo/$MoSe_2$ (see section 2.5.). For both types of electrodes, the dimensions of the substrate were of a glass microscope slide (75 mm × 26.5 mm) which was placed at the base of the cell facing the counter. Electrochemical experiments using solutions containing hexamine ruthenium(III) chloride were degassed using BOC argon for 15 minutes before use. The electrodeposition of copper was conducted in open air without inert atmosphere (to mimic industrial electrodeposition conditions) with the temperature for all experiments was 22 ± 2 ^{o}C.

The surface morphology and topology of the films were observed using a JEOL JSM6480LV scanning electron microscope (SEM). Qualitative compositional analysis was performed using energy dispersive x-ray analysis (EDS). For the proportion of copper and oxygen present within the film the EDS collected counts for 100 seconds at an acceleration voltage of 20 kV. X-ray diffraction analysis was carried out using a PANalytical X'Pert PRO Multi-Purpose Diffractometer with Cu Kα radiation. XRD measurements were taken at various points on the copper

electrodeposits.

3.3.3. Design and operation of the rocking disc electrode

The rocking disc electrode consists of the electrochemical cell mounted on a freely rotating platform (figure 3.3A) connected with a fly wheel (linked to an IKA Eurostar digital motor) via a crank arm. The electrodeposition cell is a hollow poly-carbonate cylinder with external dimensions (height 38 mm and radius 57 mm) and internal dimensions (height 21 mm and radius 25 mm). The rocking rate (f) is defined as frequency of rotation of the fly wheel, e.g. the complete rocking motion (forwards and backwards) of the cell per second. The working electrode was placed in a cavity at the bottom of the cell (figure 3.3B).

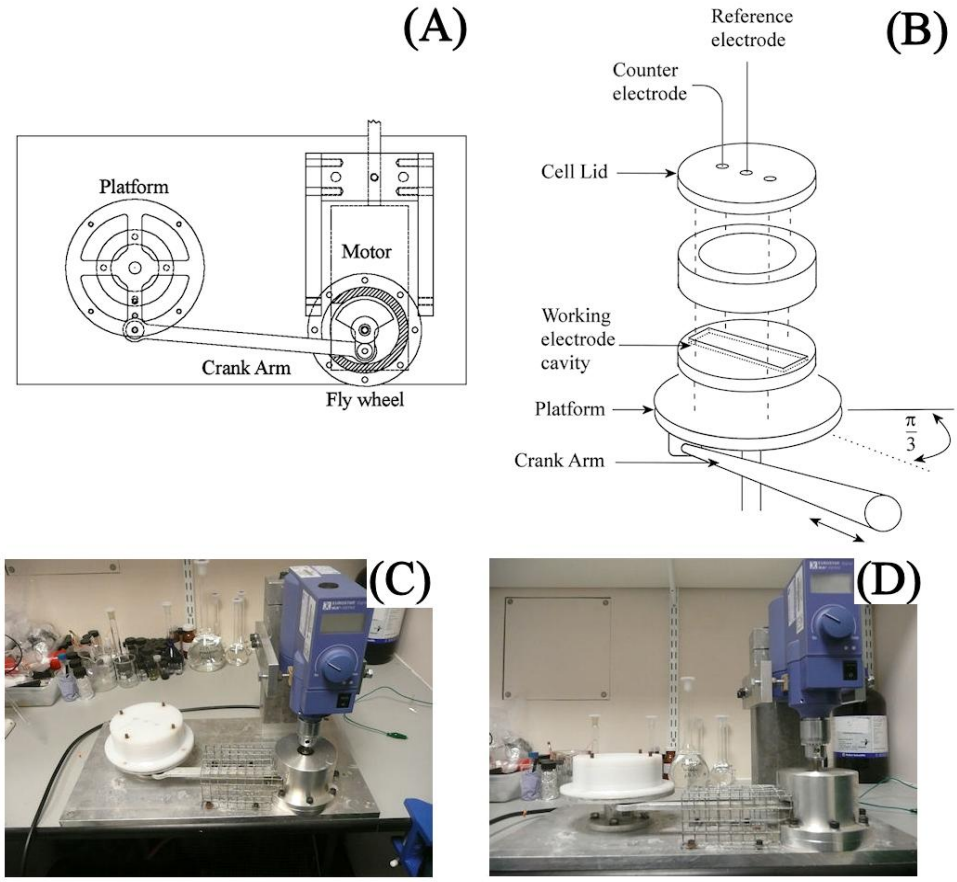

Figure 3.3: (A) Schematic drawing of the rocking disc voltammetry system with an electrochemical cell mounted on a rocking platform. (B) The electrochemical cell consists of a working electrode inlaid at the bottom of the cell with a central reference in ca. 2 mm distance and a counter electrode disc (copper) embedded into the cell lid. The cell allows a volume of ≈45 cm^3 electrolyte solution to be employed. (C) and (D) are photographs taken of the rocking disc setup.

The working electrode is a glass slide 75 mm × 26.5 mm with a central circular region exposed to the electrolyte solution. The working electrode was either Mo/$MoSe_2$ film (area 12.1 cm^2) or the calibration electrode. The calibration electrode (figure 3.4) with three gold working electrodes (area 5 mm × 5 mm; 5 mm gap; with electrode 3 in the centre, electrode 2 between the two electrodes and electrode 1 placed 3 mm from the cell wall) was employed to determine local mass transport conditions. The calibration electrode was prepared by evaporation deposition of an adherent thin Ti layer followed by 50 nm of Au film. Insulating paste (nail varnish) was used to cover the contract to the electrodes.

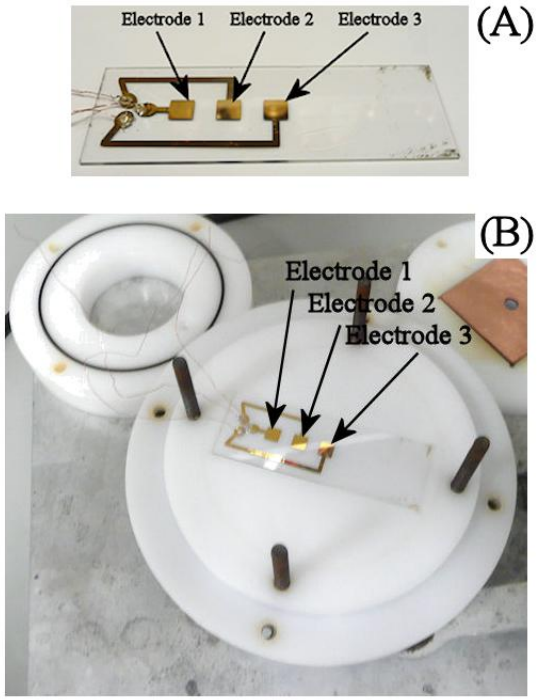

Figure 3.4: Photographs taken of the calibration electrode by itself (A) and placed in the rocking disc cell (B). The individual electrodes are displayed.

3.3.4. Formation and characterisation of Mo/$MoSe_2$ electrodes

Mo working electrodes where made with a ca. 0.8 μm thick film of metallic Mo RF-sputtered onto soda-lime glass slides (75 mm × 26.5 mm). The selenisation of the Mo-coated glass slides was similar to that reported in chapter 2 but the conditions were altered to give more reproducible films. Briefly, the selenisation was performed by placing a clean Mo-coated glass slide (sonicated in Decon 90 and in 5 %w/w and

ethanol, both 1 minute, drying under nitrogen) in a custom-made carbon box charged with 15 mg of elemental selenium. The box (figure 3.5A) was placed in a selenisation tube furnace, evacuated, and filled with nitrogen. Selenisation took place under flow of nitrogen (10 cm^3 min^{-1}) and by heating to 500 ^oC (ramp rate 10 ^oC min^{-1}) and holding 500 ^oC for 1 hour. The chamber was then cooled to room temperature (with -0.5 ^oC min^{-1}). Electrical contact to the underling Mo film was possible by gently removing part of the $MoSe_2$ layer (with a cotton bud) and adhering a Cu wire (Advent 99.99 %) using silver epoxy (RS). The exposed area of the working electrode was 12.1 cm^2.

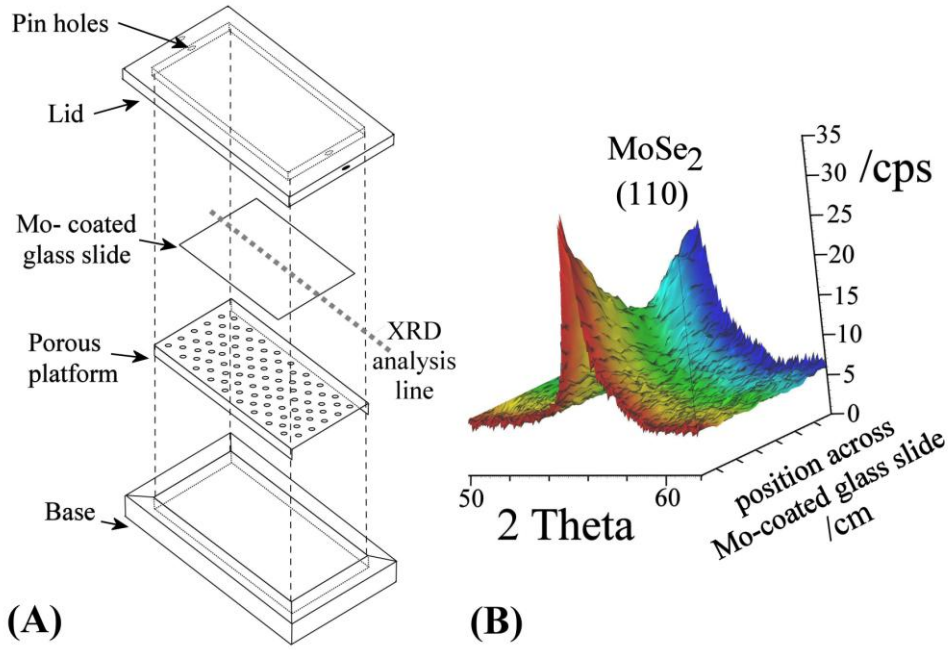

Figure 3.5: (A) Schematic drawing of the carbon selenisation box which was charged with 15 mg Se and placed into a flow of N_2 in a furnace. The Mo-coated glass slide is placed on a porous platform to react with the selenium vapour. (B) XRD of 110 $MoSe_2$ diffraction line as a function of position across the Mo/$MoSe_2$ electrode substrate (see dashed line in figure 3.5A).

In XRD analysis of the Mo/$MoSe_2$ film electrodes both Mo and $MoSe_2$ crystalline phases are observed. The $MoSe_2$ 110 diffraction maxima is shown in Figure 3.5B as a function of position along the Mo/$MoSe_2$ electrode. Relatively large widths at half peak heights are observed for the $MoSe_2$ reflections, presumably because of a significant amount of lattice disorder. From the peak height versus position it is

apparent that the selenisation of molybdenum does not create completely uniform $MoSe_2$ thin films. The 110 reflections are higher at either end of the electrode which infers that a gradient in thickness and/or crystal morphology exists. This could be caused by a chemical and thermal gradient that is present during selenisation (see figure 3.5A). However, the electrical conductivity of the $MoSe_2$ film is high and this effect should be minimal.

3.3.5. Cu plating procedure

For the electrodeposition of metallic copper, a non-cyanide, highly alkaline plating bath was used. As proposed by Barbosa et al [17], the copper plating solution contained 3.0 M sodium hydroxide and 0.2 M D-sorbitol, and either 0.01 M (for voltammetry) or 0.1 M (for plating) copper sulphate was employed. Using this solution, copper was electroplated onto $Mo/MoSe_2$ electrode substrates for a pre-defined charge with the rocking disc electrodeposition system.

3.4. Results and Discussion

3.4.1. Voltammetric characterisation of the rocking disc electrode: $Ru(NH_3)_6^{3+}$ reduction at the calibration electrode

There are many examples of the use of convection in electrochemistry ranging from the rotating disc to jet systems. Convection is typically induced using a rotating disc electrode, however there are drawbacks when using it for industrial applications. A technologically simpler and industrially more practical idea is to induce mass transport using a periodic vibration. Vibrating an electrochemical cell is expected to induce turbulent flow however, by using a symmetric and free flowing cell it is possible to induce reproducible convection.

Calibration of the rocking disc electrode was done using a model redox system, $Ru^{II/III}(NH_3)_6^{3+}$ (equation 3.4). This redox couple is appropriate as the gold electrodes were sensitive to anodic dissolution and both the reduced and oxidised form (of the $Ru^{II/III}$) are both stable in aqueous environments. Using the calibration electrode it was possible to investigate the magnitude of convection at specific areas of the electrode.

$$Ru(NH_3)_{6(aq)}^{3+} + e^- \rightleftharpoons Ru(NH_3)_{6(aq)}^{2+} \qquad (3.4)$$

Typical voltammetric responses are shown in figure 3.6A. The reversible $Ru(NH_3)_6^{3+/2+}$ redox system is observed at ca. -0.18 V vs. SCE [18]. In the absence of agitation, identical voltammograms are observed at gold electrodes 1, 2, and 3. The effect of rocking motion of the electrochemical cell upon the electrochemical process is clearly observed as an increase in reduction current and a change in shape from a typical transient voltammogram (see figure 3.6Ai) to a steady state voltammogram (see figure 3.6Av). For a high rocking rate (ca. 16.7 Hz) the limiting current exhibits some superimposed noise due to the turbulent flow induced under these conditions, but also a well-defined steady state limiting current response is observed. This is similar to that observed under rotating disc conditions [19].

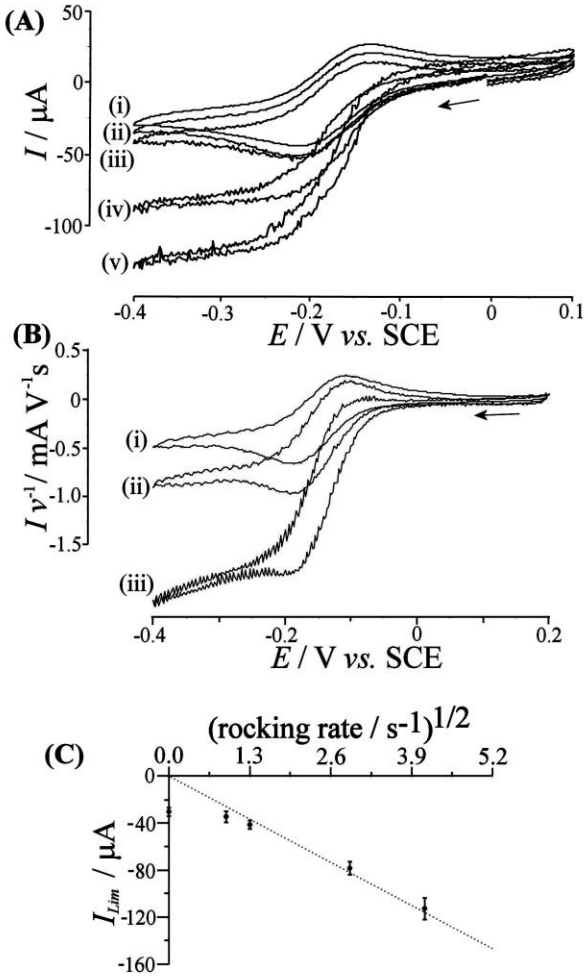

Figure 3.6: (A) Cyclic voltammograms (scan rate 0.02 Vs^{-1}) for the reduction of 1 mM $Ru(NH_3)_6^{3+}$ in aqueous 0.1 M KCl at a gold electrode (electrode 3 in Figure 1C, area 25 mm^2, located in the centre of the working electrode area) obtained at rocking rates of (i) 0 Hz, (ii) 0.83 Hz, (iii) 1.67 Hz, (iv) 8.33 Hz, and (v) 16.7 Hz. (B) Cyclic voltammograms as in (A) for a rocking rate of 3.3 s^{-1} and a scan rate of (i) 0.1, (ii) 0.05, and (iii) 0.02 Vs^{-1}. (C) Plot of the limiting current (the average of the limiting currents at -0.3 V vs. SCE for electrodes 1, 2, and 3) versus square root of rocking rate (error bars represent the standard deviation in current between the three electrodes).

Figure 3.6B demonstrates the corresponding transition from a transient voltammograms to a steady state voltammogram as a function of scan rate. Altering the scan rate changes the apparent reversibility of the cyclic voltammograms. At slow scan rates the $Ru(NH_3)_6^{2+}$ intermediate is transported away from the electrode surface whereas at fast scan rates the $Ru(NH_3)_6^{2+}$ intermediate is still in close vicinity to the electrode surface and can be re-oxidised.

Furthermore, a comparison of the magnitude of the current responses at electrode 1 (at the outer limit of the working electrode area), electrode 2 (in the middle), and electrode 3 (in the centre of the electrochemical cell, see table 3.1) suggests insignificant differences and essentially identical limiting currents as a function of rocking rate. This result implies a uniform current density across the electrode surface and therefore good electroplating conditions.

Table 3.1. Voltammetric data for the reduction of 1 mM $Ru(NH_3)_6^{3+}$ as a function of rocking rates.

ω / s^{-1}	Electrode 1 I_{lim} / μA	Electrode 2 I_{lim} / μA	Electrode 3 I_{lim} / μA	Average I_{lim} / μA	Standard Deviation ΔI_{lim} / μA
0	-28	-28	-34	-31	4.1
0.83	-31	-33	-40	-36	5.0
1.7	-41	-38	-45	-41	4.7
8.3	-77	-73	-84	-79	7.8
16.7	-116	-102	-120	-111	12.7

(limiting currents recorded at -0.3 V vs. SCE)

A plot of the average limiting current versus the square root of rocking rate is shown in figure 3.6C. There are three distinct regions see in figure 3.6C; (i) zero vibration, (ii) slow rocking rates (0.84 – 1.67 Hz) and (iii) faster rocking rates (>1.67 Hz). At zero vibration, the magnitude of the current is given by purely the diffusion process. Slow rocking rates causes the cyclic voltammograms to be a mixture of both diffusion and convection. Under steady state conditions (with a rocking rate higher than 2 s^{-1}) a linear dependence of limiting current on the square root of the rocking rate is empirically observed. This result suggests that in spite of the complex π/3-rocking motion, conditions at the electrode surface are similar to those under rotating disc voltammetry conditions.

The limiting current, I_{lim} = 120 μA, observed at a 16.7 s^{-1} rocking rate can be translated into an average diffusion layer thickness δ based on equation 3.5.

$$\delta = \frac{nFDAc}{I_{lim}} \qquad (3.5)$$

In this equation the average diffusion layer thickness δ is given by *n*, the number of

electrons transferred per molecule diffusion to the electrode, *F*, the Faraday constant, *D*, the diffusion coefficient (here 0.9×10^{-9} m^2s^{-1} [20]), *A*, the electrode area, *c*, the bulk concentration of the redox active component, and I_{lim}, the observed limiting current. At a rocking rate of 16.7 s^{-1} the average diffusion layer thickness is δ = 18.1 μm. This rocking rate can be compared with a corresponding rotation rate for a rotating disc voltammetry experiment (see equation 3 [21]) of 11.8 s^{-1}.

$$\delta_{RDE} = \frac{D^{1/3}\nu^{1/6}}{0.62\sqrt{2\pi f}} \qquad (3.6)$$

In this equation δ_{RDE} is the diffusion layer thickness at a rotating disc electrode, ν denotes the kinematic viscosity, and *f* is the rate of revolution in s^{-1}. The similarity in values for rocking rate and the rotating rate suggests that comparable convection conditions occur at the electrode surface. The origin in the difference could be due the rocking disc electrode being less efficient at generating flow from the rocking motion. The rocking amplitude (here π/3) is an important parameter which could allow further adjustment of the rate of mass transport.

Bi-potentiostatic experiments were performed on the ruthenium hexamine redox couple to investigate the direction of convection between the three electrodes. Typically in bi-potentiostatic measurements, the generator electrode is scanned (in this case between +0.1 V and -0.4 V vs. SCE) and a second working electrode, a collector electrode is held at a constant potential (in this case +0.1 V vs. SCE). The negative potential of the generator electrode will cause the production of $Ru(NH_3)_6^{2+}$ intermediate. The $Ru(NH_3)_6^{2+}$ can now be progress (by convection) to the collector electrode and be re-oxidsed by the anodic potential.

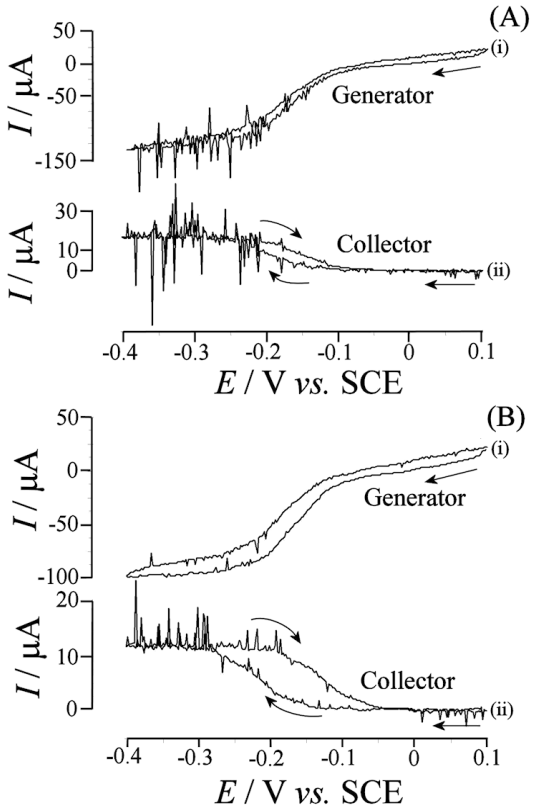

Figure 3.7: (A) Bi-potentiostatic cyclic voltammetry (rocking rate 16.7 s^{-1}, scan rate 0.02 Vs^{-1}) for the reduction of 1 mM $Ru(NH_3)_6^{3+}$ in 0.1 M KCl at electrode 2 (generator, scanning) and the re-oxidation at electrode 1 (collector, at 0.1 V vs. SCE). (B) Bi-potentiostatic cyclic voltammetry (rocking rate 8.3 s^{-1}, scan rate 0.02 Vs^{-1}) for the reduction of 1 mM $Ru(NH_3)_6^{3+}$ in 0.1 M KCl at electrode 2 (generator, scanning) and the re-oxidation at electrode 1 (collector, at 0.1 V vs. SCE).

Bi-potentiostatic experiments between electrode 2 (the generator) and electrode 1 (the collector) are shown in figure 3.7A and 3.7B for two different frequencies (16.7 Hz and 8.3 Hz respectively). It is apparent that convection of electrolyte is occurring from electrode 2 to the electrode 1. This is due increase in the oxidation current recorded at electrode 1 when electrode 2 has produced $Ru(NH_3)_6^{2+}$. It is also noticed that upon lowering the frequency of perturbation the magnitude of the cathodic and anodic currents (of the generator and collector electrodes respectively) decreases. A hysteresis time for the onset of the oxidation of $Ru(NH_3)_6^{2+}$ at electrode 1 is also seen. Table 3.2 displays the hysteresis and the collection efficiency. The hysteresis (delay time) is present due to the velocity of the electrolyte being linearly dependent on the magnitude of rocking rate.

Table 3.2. Voltammetric data for bipotentiostatic experiments using Electrode 2 (generator) and Electrode 1 (collector).

	Limiting currents			
ω / s^{-1}	Electrode 2 / μA	Electrode 1 / μA	Collection efficiency	Delay time / s
1.67	-40	5.5	13.8	8
4.17	-70	8.2	11.7	5
8.33	-95	12.5	13.2	3
16.67	-137	17.5	12.8	2

Figure 3.8 is a plot for the different generator and collector currents for a range of rocking rates. An average collection efficiency of 12.5 % ±0.75 for rocking rates between 1.67-16.67 Hz assuming that oxygen reduction is negligible. The constant collection efficiency even at relativity low rocking rate is industrially advantageous as high rocking rates will be energy intensive.

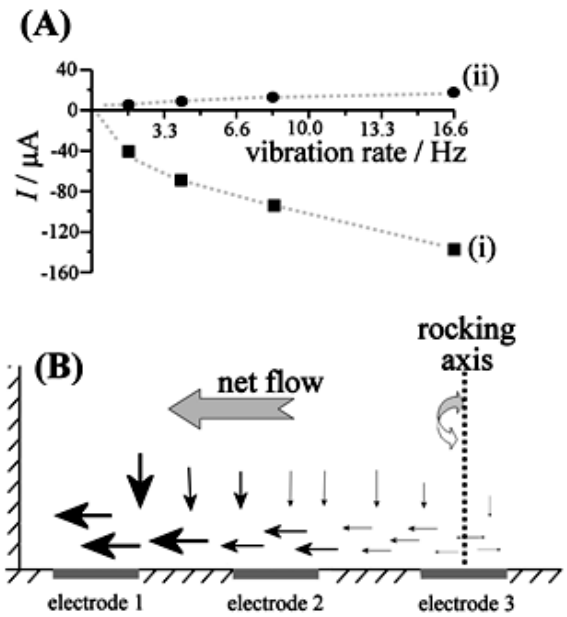

Figure 3.8: (A) Plot of the (i) generator and (ii) collector currents versus rocking rate. (B) Schematic drawing of the flow conditions in the rocking electrochemical cell.

Bi-potentiostatic experiments were conducted whereby electrode 1 was the generator and electrode 2 was the collector to measure any convection from the outer side of the cell inwards. Only ruthenium reduction was observed at electrode 1 implying that

there is minimal mass transport from the outer part of the cell inwards. Further bi-potentiostatic experiments were carried out between electrode 3 (generator) and electrode 2 (collector) showed that there was no oxidation of the $Ru(NH_3)_6^{2+}$ by electrode 2. This indicates that there is either a slow convection of flow from the centre of the cell outwards i.e. from electrode 3 to electrode 2 or none at all.

A possible explanation is that the mass transport experienced by electrode 1 is predominately turbulent in nature. The turbulence depresses the diffusion length by mixing the electrolyte perpendicular to the electrode surface. The further away from the centre of the cell the mass transport becomes more laminar and lateral in nature. A diagram depicting the flow lines is shown in figure 3.8B. The mass transport flows to the walls of the cell and then rises and comes back on itself. Despite the difference in mass transport mechanisms the magnitude of mixing is uniform across the electrode surface.

3.4.2. Voltammetric characterisation of the rocking disc electrode: Cu reduction on Mo/$MoSe_2$ electrodes

The investigation of a redox system with more of a photovoltaic relevance was performed. Copper is a key constitute of thin film solar cells as it's 4d orbital combines with the p orbitals of chalcogenides (sulphur, selenium and tellurium) to form lower than expected valence band [22]. This gives rise to an optically useful band gap for harvesting solar energy. A number of thin film solar cells have copper as key constitutes including CIS (copper indium sulphide [23]), CISe (copper indium selenide [24]), cuprous oxide [25], and CZTS (copper zinc tin sulphide [26]).

The electrodeposition of copper was done using a non-cyanide solution which has been previously reported [17]. Figure 3.9A shows a typical voltammetric response for the initial reduction of 0.1 M Cu(II). A nucleation process occurs at ca. -0.75 V vs. SCE and peaks for the reduction and stripping of copper are observed in the absence of agitation. In continuous potential cycles a stable voltammetric response is observed with a reversible potential of ca. -0.67 V vs. SCE (see equation 3.7).

$$Cu(OH)_{4\,(aq)}^{2-} + 2\,e^- \rightleftharpoons Cu_{(metal)} + 4\,OH_{(aq)}^- \qquad (3.7)$$

To observe the effect of mass transport upon the cyclic voltammometry the concentration of the cuprate within the plating bath was reduced by a factor of ten. In the presence of rocking disc agitation an increase in the cathodic deposition current and a change from a peak to a steady state response are observed (figure 3.9C). The magnitude of the cathodic limiting current at 16.7 s^{-1} rocking rate, I_{lim} = ca. 15 mA, is only weakly dependant on the rocking rate and low when compared to the approximate limiting current assuming pure mass transport control, I_{lim} = 56 mA (based on equation 3.5 with an estimated diffusion coefficient of 0.5×10^{-9} m^2s^{-1}). The copper electrodeposition onto $Mo/MoSe_2$ films is therefore only weakly mass transport dependent.

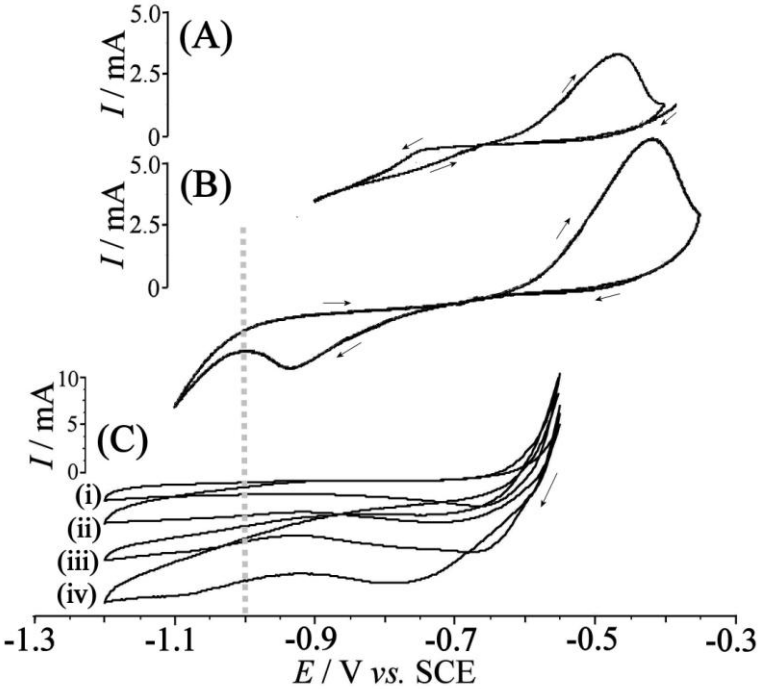

Figure 3.9: (A) Cyclic voltammogram (scan rate 50 mVs^{-1}, area 1 cm^2) for the 1st potential cycle for the reduction of 100 mM $CuSO_4$ in 3 M NaOH/0.2 M D-sorbitol at a $Mo/MoSe_2$ electrode. (B) 3rd potential cycle. (C) Cyclic voltammograms (scan rate 20 mVs^{-1}, area 12.1 cm^2, rocking rate (i) 0 s^{-1}, (ii) 0.83 s^{-1}, (iii) 8.3 s^{-1}, (iv) 16.7 s^{-1}) for the reduction of 10 mM $CuSO_4$ at a $Mo/MoSe_2$ electrode immersed in 3 M NaOH/0.2 M D-sorbitol. The dashed line indicates the electrodeposition potential of -1.0 V vs. SCE.

The effect of rocking motion should be to; (i) homogenise the solution, (ii) depresses the diffusion length of the copper ions across the entire surface and (iii) remove any forming hydrogen bubbles resulting in a highly uniform film for use in the

semiconductor/photovoltaic industry. The plating bath had a composition of 3 M NaOH, 0.2 M D-sorbitol, and 0.1 M $Cu(SO_4)$, as this was found to give optimised plating conditions for copper electrodeposition. For the creation of a thin Cu film a fresh $MoSe_2$/Mo electrode was placed in the rocking disc electrode and copper was cathoidically deposited using chromoampeometry. A cut of charge of 14.3 C was used as this is the equivalent to 0.5 μm thick copper deposits assuming oxygen/hydrogen reduction is negligible. The deposition potential was chosen as -1 V vs. SCE for chronoamperometry experiments as this minimises hydrogen evolution. Two films were prepared, one under a rocking rate of 16.7 Hz and another under a rocking rate of 8.3 Hz. Figure 3.10A shows the chromoamperogram of copper deposited at 8.3 Hz within the rocking disc electrode. Films were bright and shiny and showed good adhesion to the underling Mo/$MoSe_2$ substrate. A photograph of the copper film electrodeposited under 8.3 Hz is shown in Figure 3.10B.

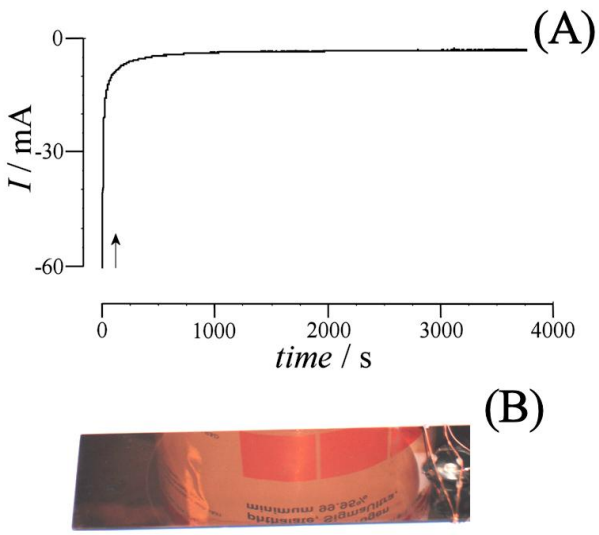

Figure 3.10: Typical Cu deposition 3 M NaOH, 0.2 M D-sorbitol, 0.1 M $Cu(SO_4)$ 8.34 Hz at a voltage of -1 V vs. SCE within the rocking disc electrode. Photograph of a 14.3 C copper film (ca. 0.5 μm thick) electrodeposited onto Mo/$MoSe_2$ from 0.1 M Cu(II) at 8.3 s^{-1} rocking rate.

Figure 3.11A and 3.11B are SEMs of the 8.3 Hz and 16.7 Hz respectively. EDS counts obtained along the central axis of the film during SEM imaging indicated a uniform deposits with minimal variation in copper concentration. The oxygen content within the film was low (< 5% atomic). XRD scans across the surface

provide a sensitive tool for thickness measurements (using the diffraction peak area) and therefore XRD data were used to assess the thickness of the copper films along vertical and horizontal axes (figure 3.11E). Figure 3.11C and 3.11D shows data for two reflections corresponding to the (200) and (111) lattice planes which are both uniform. XRD data are summarised in Table 3.3.

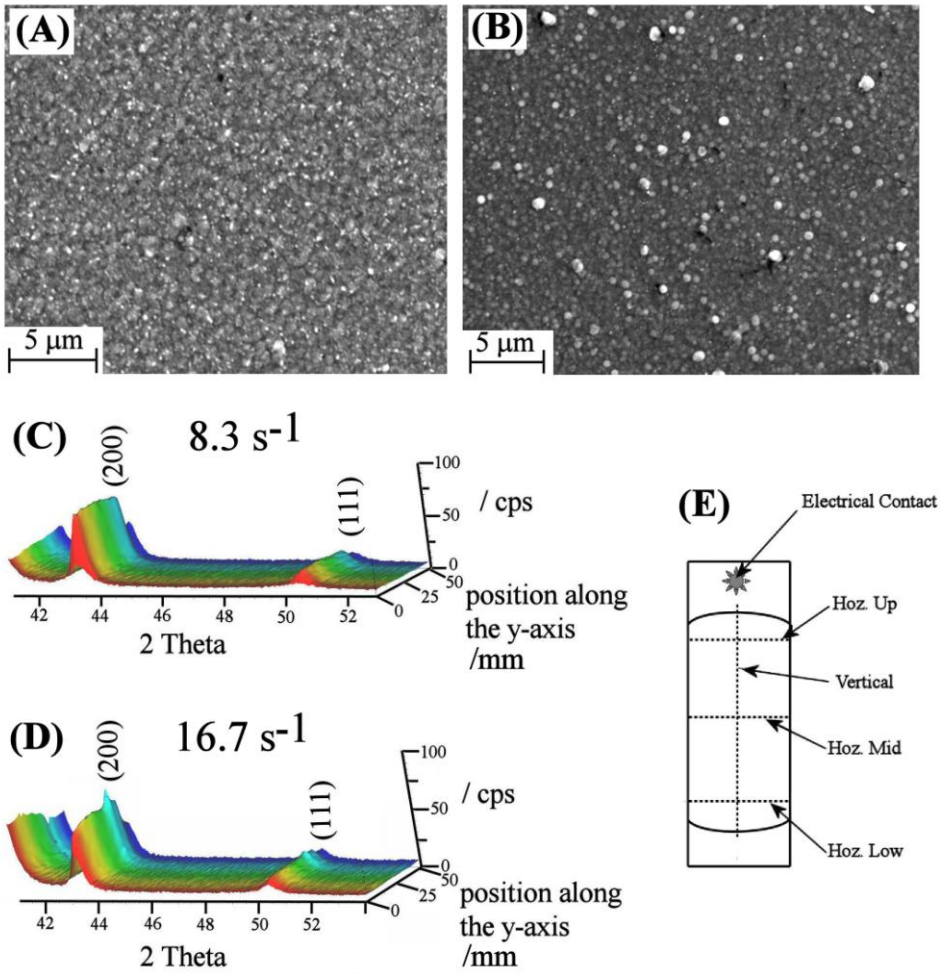

Figure 3.11: SEM images for copper films grown at -1.0 V vs. SCE with a rocking rate of (A) 8.3 s^{-1} and (B) 16.7 s^{-1}. Plots of the XRD scans along the vertical axis for the copper films formed at rocking rates of (C) 8.3 s^{-1} and (D) 16.7 s^{-1}. (E) Schematic drawing of the line scan position across the working electrode.

The average peak area of the XRD refractions was chosen as a suitable method to analyses the uniformity as the intensity is related the number of reflected planes (or the crystallinity) within the material. The average peak areas are similar in magnitude for both electrodes. It is seen from the table that the Cu film prepared under 16.7 Hz conditions exhibits a high standard deviation suggesting irregularities are present. A

spike is seen in figure 12D in the Cu reflections at approximately 35 mm. The Cu film prepared at 8.3 Hz has a higher uniformity due to a lower standard deviation. This could be due to the conditions at 16.7 Hz the convection induced was more where turbulent in nature and as a result 8.3 Hz was chosen as a rocking rate to deposit CuIn films (see chapter 4).

Table 3.3. Average XRD peak area data and standard deviation in peak area based on the sum of Cu (200) and Cu (111) XRD reflections

	8.3 s^{-1}		16.7 s^{-1}	
XRD scan path	Average (200) and (111) peak area / a.u.	Standard deviation[a] in peak area / %	Average (200) and (111) peak area / a.u.	Standard deviation[a] in peak area / %
Vertical	7.39	5.7	6.68	10.3
Hoz. Up	7.25	2.0	6.40	2.6
Hoz. Mid	7.77	2.7	6.64	4.8
Hoz. Low	7.38	3.3	6.91	5.1

[a] relative standard deviation calculated as the variance divided by the mean. Horizontal scans based on 25 data points and vertical scans based on 31 data points.

3.5. Conclusions

A new methodology of inducing convection on an electrochemical system has been documented. The rocking disc electrode is mechanically simpler than the rotating disc electrode and is inherently useful for industrial applications whereby large areas need to be electrodeposited in a highly uniform manner. Benefits of this system are (i) the electrode size can be increased (here up to 12.1 cm^2) without complications in the experimental method or reproducibility, (ii) the mass transport is uniform over the electrode surface and can be controlled by changing the rocking rate, (iii) gas bubbles get dislodged and separate from the surface, and (iv) Mo/$MoSe_2$ photovoltaic substrates can be readily coated with uniform copper films with +/- 5 % thickness variation (based on XRD scans for films deposited with 8.3 s^{-1} rocking rate) in a 0.5 μm thick film. This methodology will be of wider use for the electrodeposition of multi-layer absorber layers and for bigger wafer-sized photovoltaic substrates.

3.6. References

[1] A. Fick, J. of Science 16 (1855) 30

[2] V. Levich, *Physicochemical Hydrodynamics*, Prentice-Hall, Inc. (1962)

[3] P. He, P Watts, F. Marken, S. Haswell, Green Chem., 9 (2007) 20

[4] B. Pollet, J. Hihn, M. Doche, J. Lorimer, A. Mandroyan, T. Mason, J. Electrochem. Soc., 154 (2007) E131

[5] S. Schuette, R. McCreery, Anal. Chem. 58 (1986) 1778

[6] J. Macpherson, Electroanalysis., 12 (2000) 1001

[7] J. Kuleshova, P. Birkin, J. Elliott, J. Electroanal. Chem. 617 (2008) 185

[8] D. Pletcher, F. Walsh, *Industrial electrochemistry*, 2nd edition Blackie Academic & Professional (1993)

[9] J. Dini, *Electrodeposition; The Materials Science of Coatings and Substrates*, Noyes Publications, (1992).

[10] D. Lincot, Thin Solid Films 487 (2005) 40

[11] J. Scragg, D. Berg, P. Dale, J. Electroanal. Chem., 646 (2010) 52

[12] A. Brenner, *Electrodeposition of Alloys; Principles and Practice*, Vol 2 Academic press, New York (1963)

[13] D. Gabe, Trans. Inst. Metal Finish. 84 (2006) 67

[14] M. Kurihara, D. Berg, J. Fischer, S. Siebentritt, P. Dale, Physica Status Solidi C - Current Topics in Solid State Physics 6 (2009) 1241.

[15] E. Chassaing, E. Ramdani, P. Grand, J. Guillemoles, D. Lincot, Symposium on Chemical and Electrochemical Synthesis of Advanced Materials and Nanostructures on Solid Surfaces held E-MRS Fall Meeting Warsaw, POLAND (2007) 3445.

[16] M. Thompson, R. Compton, J. Electroanal. Chem. 583 (2005) 318

[17] L. Barbosa, M. de Almeida, R. Carlos, M. Yonashiro, G.Oliveira, I. Carlos, Surf. Coat. Technol. 195 (2005) 145

[18] K. McKenzie, P. King, F. Marken, C. Gardner, J. Macpherson, J. Electroanal. Chem. 579 (2005) 267

[19] C. Brett, A. Brett, *Electrochemistry: Principles, Methods, and Applications*, Oxford University Press, Oxford (1993)

[20] F. Marken, J. Eklund, R. Compton, J. Electroanal. Chem. 395 (1995) 335

[21] Southampton Electrochemistry Group, Instrumental Methods in Electrochemistry, Horwood, (2004)

[22] M. Archer, R. Hill, *Clean Electricity from photovoltaics*, Imperial College Press, 1

(2001)

[23] D. Shivagan, P. Dale, A. Samantilleke, L. Peter, Thin Solid Films 515 (2007) 5899

[24] T. Gujar, V. Shinde, J. Park, H. Lee, K. Jung, O. Joo, J. Electrochem. Soc. 155 (2008) E131

[25] S. Joseph, P. Kamath, J. Electrochem. Soc. 156 (2009) E143

[26] J. Scragg, P. Dale, L. Peter, G. Zoppi, I. Forbes, Phys. Status Solidi B-Basic Solid State Phys. 245 (2008) 1772.

Chapter 4

Rocking Disc Electrodeposition of CuIn Alloys and Subsequent Selenisation for CISe Solar Cells

Contents

This work is submitted as
C. Cummings, G. Zoppi, I. Forbes, D. Colombara, L. Peter, F. Marken Electrochimica Acta. (Submitted)

4.1 Abstract

Building on the work performed on the electrodeposition of copper with the rocking disc electrode shown in the previous chapter, the co-electrodeposition of the metallic elements copper and indium within the rocking disc electrode onto Mo substrates is studied. Non-convection induced cyclic voltammograms indicate the presence of defined Cu and In reductions. Conditions were found for the electrodeposition of 1:1 CuIn films as precursors for CISe. CuIn electrodes were converted to CISe films by a selenisation step ca. 500 ^{o}C for 30 minutes with selenium vapour present. Large area films (ca. 4.5 x 2.5 cm) were mapped using the photo-electrochemical reduction of $Eu(NO_3)$ to asses the relative photoactivity as a function of electrode position. Important parameters that determine the absorber efficiency and uniformity are the presence of either copper selenide, Cu_xSe, or pin holes within the microstructure of the film. In large substrates the presence of both Cu_xSe and pin holes can occur. Alternatives to the traditional 5 %w/w KCN etch are proposed. The CISe films were etched with diluted KCN (ca. 0.5 %w/w) where the kinetics of etching were retarded allowing for a better process control. Over-etched films were then re-annealed at 500 ^{o}C for 30 minutes and then etched in dilute KCN. The resultant photoactivity was high with the largest recorded photocurrent as I_{ph} = 1.8 mA (0.2 M $Eu(NO_3)_3$, 35 mW cm^{-2} LED) before decaying. In contrast to this typical etch method the use of an oxidising agent HClO (5 %w/w) in conjugation with a KCN etch (5 %w/w) was performed. An over-etched CISe film exposed to the HClO etchant solution to allow the oxidation of Mo. A further KCN (5 %w/w) etch increased photoactivity to a high magnitude (ca. I_{ph} = 1.2 mA, 0.2 M $Eu(NO_3)_3$, 35 mW cm^{-2} LED) due to the removal of the pin holes. This is a low temperature alternative to the re-annealing to improve the photocurrent.

4.2. Introduction

4.2.1. Introduction to semiconductor formation

The preparation of large area wafers of semiconductors is problematic. Despite various deposition techniques available to the manufacturer such as chemical vapour deposition, physical vapour deposition, spin coating, chemical bath deposition and electrodeposition, achieving uniformity over a large area is a problem. Irregularities in the film can be detrimental to the semiconductors overall electronic properties and it is essential that precise control over composition and morphology is achieved. The electrodeposition of metal and semiconductor films is plagued with various challenges to attain uniform thin films. The most important factors are the substrate uniformity and achieving a constant diffusion layer thickness over the entire electrode surface. The previous chapter documented the use of the rocking disc electrode to induce uniform mass transport to the electrode surface. The resultant electroplated copper films were found to be highly uniform (see chapter 3). In this chapter CuIn co-electrodeposition is investigated.

4.2.2. Electrodeposition of binary systems

The electrodeposition of binary systems for solar cell applications has been investigated before for both metals [1,2] and semiconductors [3,4]. The kinetics of electrodeposition of alloys is not trivial as complications due to nucleation (progressive and instantaneous), alloy formation/growth and the Kröger mechanism cause a deviation from the simple electron transfer behaviour. The electrodeposition of the bimetallic alloy CuNi as a model system to study Cu-In deposition has been investigated by Ollivier *et al.* [2]. Ignoring complications from alloy formation and nucleation kinetics, the two different metals (Cu and Ni) are electroplated onto an electrode under mass transport controlled conditions. The Cu and Ni species have different nobilities as Cu has a more positive formal potential ($E^{o\prime}$) compared to that of Ni. During the electrodeposition if the potential of the electrode is more negative than the $E^{o\prime}(Cu^{o}/Cu^{2+})$ then the rate of formation of Cu(s) will be constant and controlled by mass transport. Approaching $E^{o\prime}(Ni^{o}/Ni^{2+})$ will begin the

electrodeposition of Ni. Varying the deposition potential (i.e. selecting its position relative to $E^{o\prime}(Ni^{o}/Ni^{2+})$) will cause a controlled rate of deposition of Ni(s) and hence the stoichiometry of the resultant film.

The electrodeposition of chalcogenide semiconductors is typically dictated by the Kröger or the induced deposition mechanism. Here the formation of a reactive species at the electrode surface governs that rate of inclusion of a less noble element. This is the case for the electrodeposition of CdTe as a Te^{2-}(aq) species is produced at the electrode surface and reacts with Cd^{2+}(aq) ions causing the spontaneous formation of CdTe(s) at the surface of the electrode. The rate of electrodeposition is governed by the formation of Te^{2-}(aq) and electrodeposits can be prepared with ratios of 1:1 [4].

The co-electrodeposition of metallic CuIn [5,6], InGa [7] and CuInGa[8,9] films from a single solution has been documented before. Typically reports have used the effect of potential, concentration and additives to produce films with a desired stoichiometry. Various additives in the form of complexing agents are added to a variety of solution media, some examples include citrate [10] and ethylamine [11]. The purpose of complexing agents or additives is to bind and stabilise aqueous ions and to lead to a higher quality deposit. For the plating of CuIn films from a dual electrolyte bath a complexing agent is typically added to bind to the copper causing a shift in the reduction potential closer to that of indium.

4.2.3. Introduction to wet chemical semiconductor processing

During the preparation of semiconductors minor phases exist as by-products of chemical treatments. Minor phases can be detrimental as these can affect the properties of the resultant films. The removal of these phases can expose pin holes which can act themselves as non-uniformities and can be detrimental. Pin holes can act as recombination centres or electronic short circuits which can corrupt the properties of a semiconductor film. As a consequence of this, a balance must be struck between the removal of unwanted material and the creation of pin holes. A typical method to remove unwanted phases is to etch the substrate.

The definition of etching is the controlled removal of material from a substrate's surface using either a wet chemical or dry etching technology. In general, wet chemical etchants have the advantages over dry etchants in that they can be selective, high throughput, low cost and are handled under safe conditions. The selectivity of the chemical etchants comes from the fact that different surface species will have different binding constants associated between the etchant and themselves.

An etchant solution is typically prepared with three components: an oxidising agent that forms an oxide coating, a complexing agent that binds to the substrate and a solvent that acts as a medium which the substrate etchant complex dissolves in. Most systems are aqueous based (either acid or alkali) with a hydrogen peroxide used as an oxidising agent. The use of strong complexing agents can diminish the need for an oxidising reagent. The kinetic aspects of etching are shown below in figure 4.1.

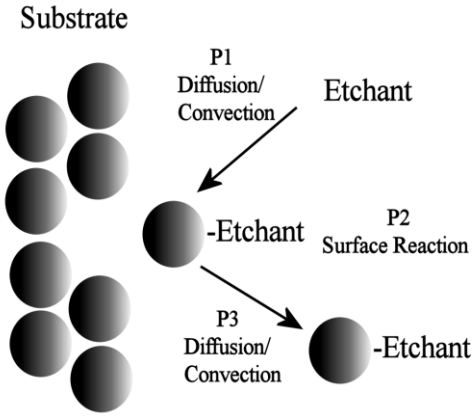

Figure 4.1: Schematic of the three processes controlling the kinetics of etching a substrate.

The rate of etching of a substrate can be split into two extreme categories, either kinetically controlled or diffusion controlled. The rate of dissolution of the substrate under diffusion controlled conditions is dependant on the flux of etchant towards the substrate or the removal of products away from the substrate, denoted as processes P1 and P3 in figure 4.1. Hence, diffusion controlled etches are more likely to give an isotropic etch, an etch independent of substrate geometry and can be controlled by varying physical parameters such as concentration, temperature and flow (agitation).

The rate of dissolution for kinetic controlled reactions is dominated by the surface

reaction between that of the etchant(s) and the surface. The surface reaction is a generalised term that includes a number of complex steps such as: etchant adsorption, chelation, and de-adsorption.

Kinetically-controlled etching is more likely to create an anisotropic etch due to different surface sites such as crystal faces, defects and dislocations having different rates of dissolution [12]. Kinetically-controlled etches can be useful as in the silicon mono- or multi-crystalline photovoltaic industry surface texturization (for light trapping) of a solar cell can be done using an anisotropic etch [13].

4.2.4. Etches used for CISe films

Etching is performed on CISe based films to remove various Cu_xSe phases (ca. Cu_2Se, CuSe, $CuSe_2$) that reside at the surface of the CISe grains. These phases were formed during the deposition or post heat treatment (anneal or selenisation) of the CISe film. The presence of Cu_xSe phases is detrimental as it is more metallic in nature and hence acts a recombination centres for electrons and holes [14]. The most commonly used etchant to remove Cu_xSe from CISe based devices is a potassium cyanide, KCN [15,16,17]. This is a diffusion-controlled etch for the removal of Cu_xSe phases but is kinetically hindered to remove CISe. The cyanide has a high affinity for Cu_xSe phases and can dissolve these as chelated cuprates/cuprics ($Cu(CN)_4^{3-}$)and selenates (SeO_4^{2-}) [18].

There are a number of different etchant systems documented in the literature. One of the earliest examples of using an etch on CISe based materials to cleave a surface species is by Cahen *et al.* Here single crystals of n-CISe were etched with a methanol/bromine mix [19]. The etching caused the formation of a near stoichiometric surface which was oxidised to form indium oxide bonds. These stabilised the material when operated in a photo-electrochemical configuration. Delsol *et al* [20] investigated the use of a variety of etchants on electrodeposited CIGSe, including an acid chloride/nitric etch, alkaline H_2O_2, alkaline potassium dichromate, alkaline thiosulphate and alkaline ammonia etching solutions. From XPS measurements taken it was revealed that the surface becomes deficient in

selenium when exposed to the peroxide etch, most likely as the selenide is being oxidised to selenates. An enhancement of oxygen most likely related to the formation of surface oxides. It was also found that ammonium will preferably remove the indium from the film. Dichormate and thiosulphate etches selectivity dissolved metals at the surface enriching the selenium present. The acids nitric/chloride systems didn't appreciably change the concentration of the surface species when compared to an un-etched sample. Other authors have documented using HBr [21] on CIGSe to given well defined surfaces.

Electrochemical etching is the use of electrochemistry to produce species which can be dissolved into solution was performed by the Kios *et al.* on CISe films [22]. The report documents an improved photoactivity of films after electrochemical etching. There are a number of articles documenting the use of electrochemical etching on $CuInS_2$ films [23 24,25] all revealing the plausibility of the technique.

It is also possible to selectivity remove indium from the surface of CIGSe to create $CuSe_2$ phases at the surface of the film. Here, Hunger *et al* used synchrotron excited photo-electron spectroscopy to investigate the ratio of surface species at the CIGSe grain boundaries after the film had been exposed to humility, distilled water and ammonia. It was found that ammonia selectivity binds to indium causing a simultaneous decrease in the indium 4d signal and increase the Cu 3d signal [26] which is in agreement with ref [20].

The previous chapter documented the use of the rocking disc electrode as a new methodology for the electrodeposition of films. Inherent advantages of this system over the standard rotating disc electrode are that the rocking disc electrode is technically simpler, follows reproducible 'Levich' mass transport laws and produces uniform films. This chapter concerns the co-electrodeposition of two metals from the same solution to form a bi-metallic alloy film. The film can be subsequently processed to form CISe absorber films. From chapter 2 and literature [15] Cu_xSe is a minor phase that is produced as a by-product of the selenisation step. Over etching of CISe films produces pin holes which act as recombination centres. Three industrially relevant alternatives to the traditional KCN etch (5 %w/w) are documented to improve the photoactivity.

4.3. Experimental Methods

4.3.1. Reagents

Copper(II) sulphate (99.999 %), indium(III) chloride (99.999 %), lithium chloride (99.99 %), sodium hydroxide (99.99 %), tartaric acid (ACS grade) europium(III) nitrate (99.999 %), potassium cyanide (ACS, 96.0 %), hypochlorite solution (5 %w/w) and selenium powder (99.999 %) were purchased from either Sigma Aldrich or Alfa Aesar and used without further purification. Filtered and demineralised water was taken from a Thermo Scientific water purification system (Barnstead Nanopure) with a resistivity of not less than 18.2 MOhm cm.

4.3.2. Instrumentation

For voltammetric and potentiostatic investigations an Autolab III potentiostat system (EcoChemie, Netherlands) was employed with a saturated calomel (SCE) reference electrode (Radiometer, Copenhagen). The working electrodes were ≈1 μm sputtered Mo films on soda lime glass. For non-mass transport induced, voltammetric studies an open electrochemical cell with a 1 cm^2 working Mo electrode and a Pt foil (4 cm × 2 cm) counter electrode was used. For experiments involving the rocking disc electrode a counter electrode of pure copper (99.9 %) was fixed to the top of the rocking disc electrode. Further details on the rocking disc electrode can be found in chapter 3. All electrochemical experiments were conducted in open air without inert atmosphere (to mimic industrial electro-deposition conditions) and the temperature during experiments was 22 ± 2 ^oC.

The surface morphology and topology of the films were observed using a JEOL JSM6480LV scanning electron microscope (SEM). Qualitative compositional analysis was performed using calibrated energy dispersive x-ray analysis (EDS). For the EDS determination of the ratio of copper to indium present within the film the acceleration voltage was set to 25 kV, with a low magnification (x200 times) and measured for 100 seconds. Probe lines are shown in figure 4.2:

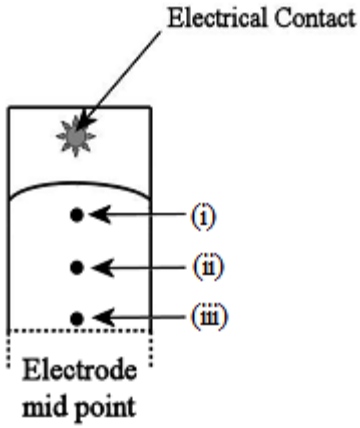

Figure 4.2: Schematic indicating the areas analysed using the SEM/EDS. Three areas were chosen along the central axis of the CuIn film at varying distances away from the electrical contact (during the electrodeposition). (i) is 1 cm, (ii) is 2 cm and (iii) is 3 cm.

4.3.3. Composition of the CuIn plating solution

For the electrodeposition of metallic copper/indium alloys a novel, non-toxic bath was used. 60 ml of electrolyte was prepared containing the metal salts, 0.5 M LiCl, 0.125 M Na-tartrate, 50 mM $InCl_3$ and 25 mM $CuSO_4$. The solution was brought to pH 3 by the addition of NaOH. The solution was placed in the rocking disc electrode and films were formed using potentiostatic control. The applied deposition potential was varied during experiments but the rocking rate and charge deposited were constant, ca. 8.3 Hz and 21.8 C (endpoint) respectively. A 21.8 C charge corresponded to a ≈550 nm thick thin film assuming negligible hydrogen reduction. Care was taken to minimise the contact time of the Mo electrode and the tartaric electrolyte when not under applied potentiostatic conditions. The plating solution allowed for the electroformation of two CuIn films (area 12.1cm^2) to be created.

4.3.4. Selenisation of the CuIn films and re-anneal treatments

Stoichiometric or slight indium-rich CuIn films (Cu/In = 0.9-1) were selenised using procedure using a standard procedure. Films were enclosed in a carbon box (as descried in chapters 2 and 3) with 150 mg of selenium powder. Films were placed

under a N_2 atmosphere and heated to 500 ^oC at a heating rate of 10 $^oCmin^{-1}$ for 30 minutes. Films were cooled at a rate of 1 $^oCmin^{-1}$ until room temperature. CISe electrodes that were over-etched were re-annealed in the same selenisation chamber as the selenisation. The films were placed in the same carbon box heated to 500 ^oC for 30 minutes (ramp rate 10 $^oCmin^{-1}$) under a steady flow of N_2. Here the carbon box was not cleaned and selenium vapour was present during this re-anneal.

4.3.5. Photo-electrochemical mapping of large area CISe films (ca. 12.1 cm^2)

A home made mapping system was constructed. This consisted of an electrochemical cell shown in figure 4.3 mounted on a manual X-Y stage (position ±0.25 cm) fitted with a green laser pointer (525 nm, ≈35 mW cm^{-2}, illuminated ≈80 mm^2, ThorLabs). The electrochemical cell which contained ca. ≈20 ml of 0.2 M $EuNO_3$ and was fully enclosed (figure 4.3B). The reference and counter electrodes were present as a Ag/AgCl electrode (World Precision Instruments Inc.) and a Pt wire mounted at the end and the middle of the cell as shown. The CISe coated microscope slide was placed in a recess at the base of the cell. A potential of -0.4 V vs. Ag/AgCl was applied to the entire CISe film for 10 seconds prior to the start of the recording of the chromoampogram. A high resolution setting for the chromoampogram (set on a single current range setting) was recorded at -0.4 vs. Ag/AgCl for 4 seconds whilst modulated light (ca. 1 Hz) was shone from above through a transparent window onto the film. Films containing the detrimental phase copper selenide were exposed to an etching solution contain 5% KCN dissolved in water. The films were immersed for 30 second intervals removed washed with deionised water thoroughly and dried under N_2.

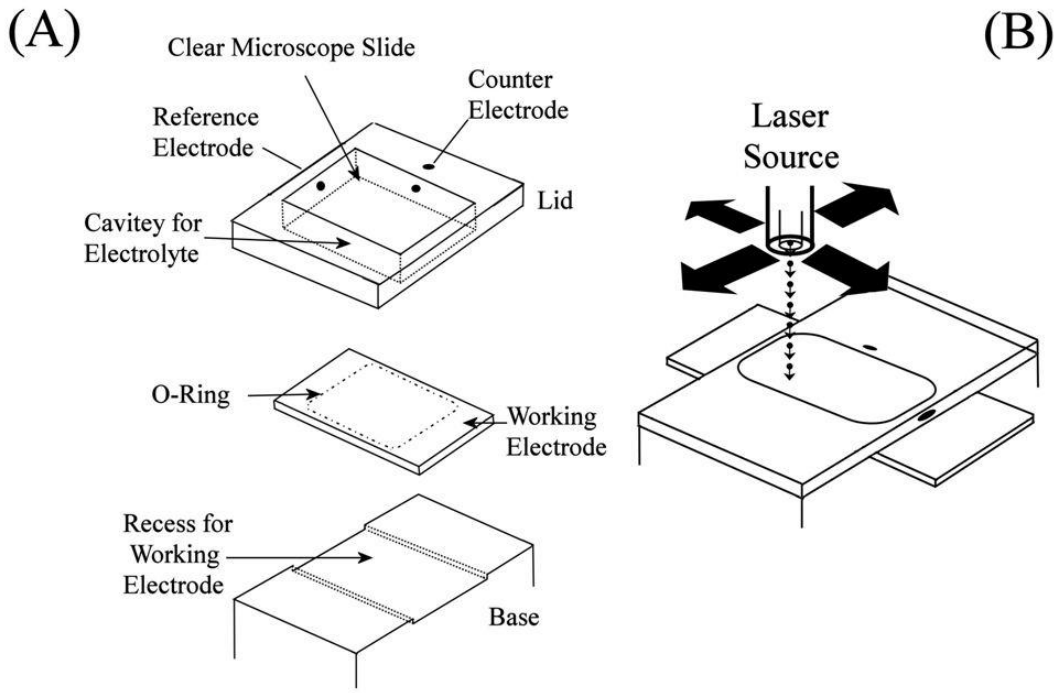

Figure 4.3: Schematics of the photo-electrochemical scanning light microscopy. (A) Is a view of the individual segments with the top containing a glass window to allow light to penetrate. The base has a recess that accommodates the working electrode (dimensions 72 x 25 mm). The top is compressed onto the base with reference and counter electrodes connected. (B) Is a view of the cell fully assembled, light is shown from above and rastered across the surface.

4.3.6. Etching and photo-electrochemistry of small CISe films (ca. 1 cm^2)

There are three different types of etchant solutions documented in this chapter. The first was the traditional KCN etch (5 %w/w) in water, as stated above. The second was a diluted concentration of aqueous KCN (0.5 %w/w) to retard the etching rate. The third was the oxidative etch which was composed of aqueous HClO (5 %w/w) which was used in conjugation with the 5 %w/w KCN etch. The films were immersed for typically 30 second intervals where then removed washed thoroughly with demonised water and dried under a stream of N_2. Films were photo-electrochemically tested in a cell similar to that described in chapter 2 whereby films were immersed into a solution of 0.2 M $Eu(NO_3)_3$ and held at a potential of -0.4 V vs. Ag/AgCl for 10 seconds. Photocurrent was recorded in response to square wave modulated ≈10 mW green LED (ThorLabs) for 4 seconds at potential of -0.4V vs. Ag/AgCl.

4.4. Results and Discussion

4.4.1. Photoactive CISe by rocking disc electrodeposition: voltammetric investigation of CuIn plating

In this study the plating solution was composed of the metal salts 0.5 M LiCl, 50 mM $InCl_3$ and 25 mM $CuSO_4$ with 0.125 M Na-tartrate added as a complexing agent. Before the use of the rocking disc electrode to produce large area copper-indium films, cyclic voltamametry using small Mo electrodes (ca. 1 cm^2) was undertaken. Here the electrolyte was not under mass transport conditions and the corresponding cyclic voltammograms are shown below in figure 4.4.

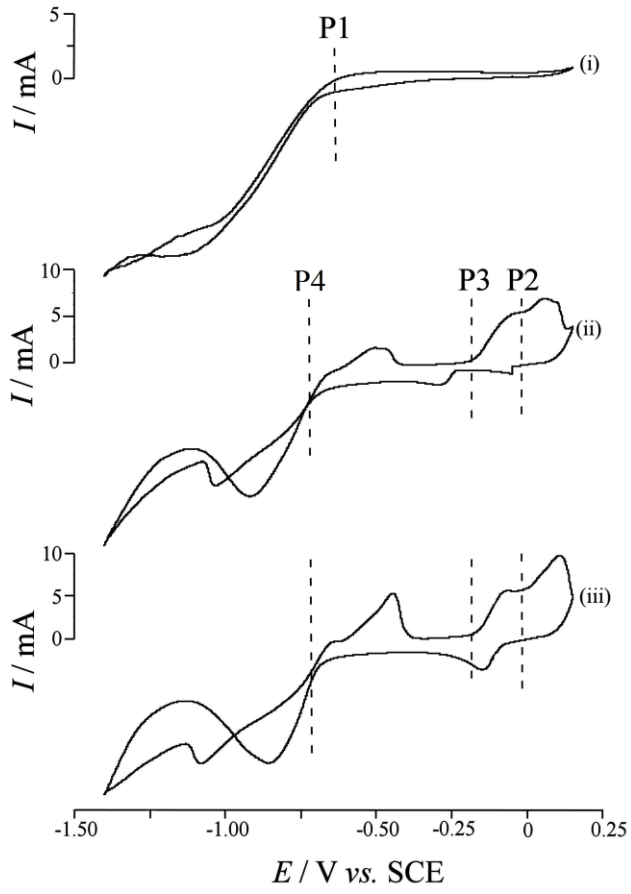

Figure 4.4: Cyclic voltammograms (1 cm^2, 20 mVs^{-1}) of plating solution with/without copper(II) sulphate and indium(III) chloride. Mo electrode immersed in (i) 0.5 M LiCl and 0.125 M Na-tartrate, (ii) and (iii) 0.5 M LiCl, 0.125 M Na-tartrate, 50 mM $InCl_3$ and 25 mM $CuSO_4$, first and second cycle respectively.

Figure 4.4i, shows the electrochemistry of the background electrolyte (0.5 M LiCl and 0.125 M Na-tartate) with a Mo electrode. The only predominant electrochemical signal is the irreversible reduction of protons at potentials more negative than -0.65 V vs. SCE, P1(H_2/H^+). The evolution of hydrogen (equation 4.1) is to be expected as the solution is acidic (pH 3) and its potential onset can be predicted by the Nernst equation [27] which at pH 3 gives $E^{o\prime}(H_2/H^+)$ = -0.42 V vs. SCE. The 230 mV overpotential calculated from the deviation in the theoretical and experimentally determined value is due to the complex kinetics of molecular hydrogen formation on Mo. Most non-precious metals have an overpotential associated with the reduction of protons when compared to platinum electrodes (which are used in the derivation of the standard electrochemical potential of hydrogen) [28]. The formation and detachment of hydrogen bubbles is seen optically at voltages more negative than ≈-0.8 V vs. SCE. This process induces mass transport to the electrode surface which explains the limiting current at highly cathodic potentials (ca. -1.1 V vs. SCE).

$$2H^+(aq) + 2\,e^- \rightleftharpoons H_2(gas) \qquad (4.1)$$

Upon addition of the metal salts, copper sulphate and indium chloride, the cyclic voltammograms increase in complexity. For the first cyclic voltammogram (figure 4.4ii) there are three apparent reductions, P2(Cu^+/Cu^{2+}) at +0.05 V vs. SCE, P3(Cu^o/Cu^+) at -0.2 V vs. SCE, and P4(In^o/In^{3+}) at -0.7 V vs. SCE. The waves corresponding to P2(Cu^+/Cu^{2+}) are the reduction and re-oxidation of copper(II) and copper(I) (equation 4.2). The presence of the copper (I) species is due to the excess of tartrate and chloride ions which bind to the cuprous ions stabilising it. Another well known cuprous chloride species is $CuCl_2^-$ [29]. Scanning the potential more negative another signal corresponding to the reduction of copper (I) to metallic copper (P3(Cu^o/Cu^+), equation 4.3) is observed. This occurs at approximately 100 mV more negative than the standard formal potential $E^{o\prime}$ = -0.084 V vs. SCE suggesting that electrodeposition is affected by a nucleation overpotential.

$$Cu^{2+}(aq) + 1\,e^- \rightleftharpoons Cu^+(aq) \qquad (4.2)$$

$$Cu^+(aq) + 1\,e^- \rightleftharpoons Cu\ (metal) \qquad (4.3)$$

Scanning the potential more negative reveals P4(In^o/In^{3+}) occurring at roughly the same potential as the onset of the hydrogen reduction (ca. -0.7 V vs. SCE). This is attributed to the reduction of indium (III) chloride into indium metal (equation 4.4). It can be assumed that this is a full three electron reduction as the indium intermediates (In^{2+} and In^{+}) are likely to have a short lifetime and not detectable using cyclic voltammetry. The position of P4(In^o/In^{3+}) occurs at 120 mV more negative to the $E^{o\prime}(In/In^{3+})$ (ca. -0.58 V vs. SCE). This reduction potential is similar to that reported by other authors [30,31] as well as what was observed in chapter 2 suggesting that the tartate is having a minimal effect on the indium electrochemistry.

$$In^{3+}(aq) + 3\,e^- \rightleftharpoons In(metal) \qquad (4.4)$$

The backward scan induces the stripping of the electrodeposited films which has complex features resulting from the stripping of copper, indium and copper-indium alloys. It is likely that copper-indium alloys are present as it is known that they can exist at room temperature [32] however the distribution of phases within the film cannot be determined by cyclic voltammetry alone. Valderrama *et al.* [31] examines the phase formation of electrodepositing of indium onto copper substrates. The formation of a copper indium alloy occurs when a more negative potential is applied to the electrode surface. During the electrode stripping more anodic peaks are observed which are attributed to the oxidation of a copper indium alloy.

4.4.2. Photoactive CISe by rocking disc electrodeposition: uniform electrodeposition onto Mo

For the deposition of highly uniform and large area thin films, convection must be induced. This is especially important when applying a large negative potential as hydrogen bubbles are likely to form creating pin holes and/or a non continuous film. Pin holes are problematic as they are sources of recombination for resultant semiconductor films (chapter 2). In chapter 3 it has been shown that the rocking disc electrode induces turbulent convection that can remove forming hydrogen bubbles. To some extent this will minimise the dynamic fluctuations that occur on the diffusion length scale giving more uniform films.

The electrodeposition of both copper and indium onto Mo substrates within the rocking disc electrode were undertaken. The deposition rocking rate (ca. 8.3 Hz) and a deposition charge (endpoint 21.8 C) were both kept constant for all experiments. Below are chromoampograms for the electrodeposition of CuIn films (figure 4.5).

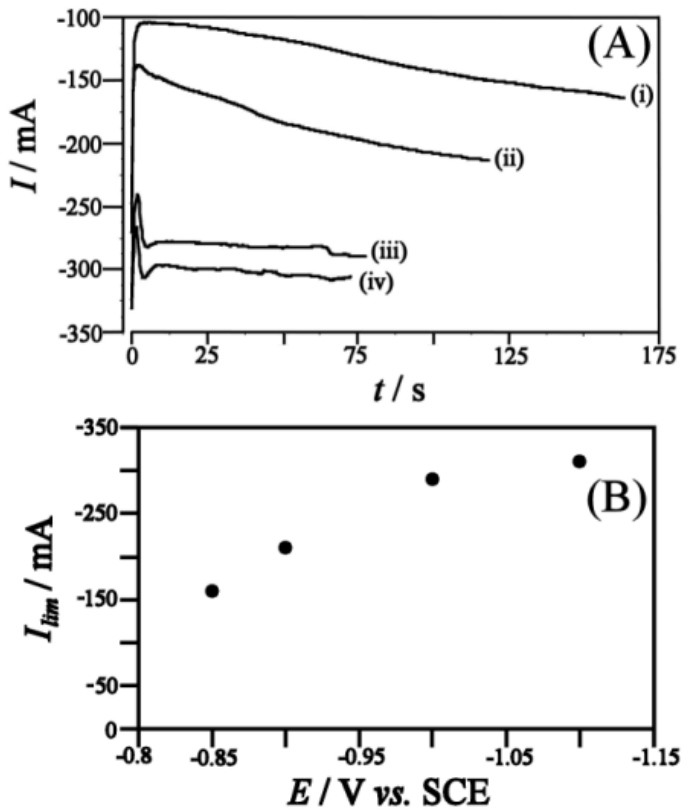

Figure 4.5: (A) Chronoampometry for the rocking disc electrodeposition of CuIn films onto Mo electrodes with a rocking rate 8.3 Hz for 21.8 C. The plating solution contained 0.5 M LiCl, 0.15 M Na-tartrate, 50 mM $InCl_3$ and 25 mM $CuSO_4$. Different potentials were applied were (i) -0.85, (ii) -0.9, (iii) -1.0, and (iv) -1.1 V vs. SCE. (B) plot of limiting current (measured at end point) versus applied potential.

The limiting currents of the measured chronoamperograms are approximately constant. As expected a more negative applied deposition potential increases the observed plating current chronoamperograms. This is due to more indium and hydrogen reduction occurring at the electrode | electrolyte interface at more negative potentials. This can be seen easily in the plot of limiting current versus applied deposition potential is shown in figure 4.5B. The current increases is a linearly until an applied potential of -1.0 V vs. SCE after which the current seems to plateau. The surface morphology was investigated using SEM figure 4.6.

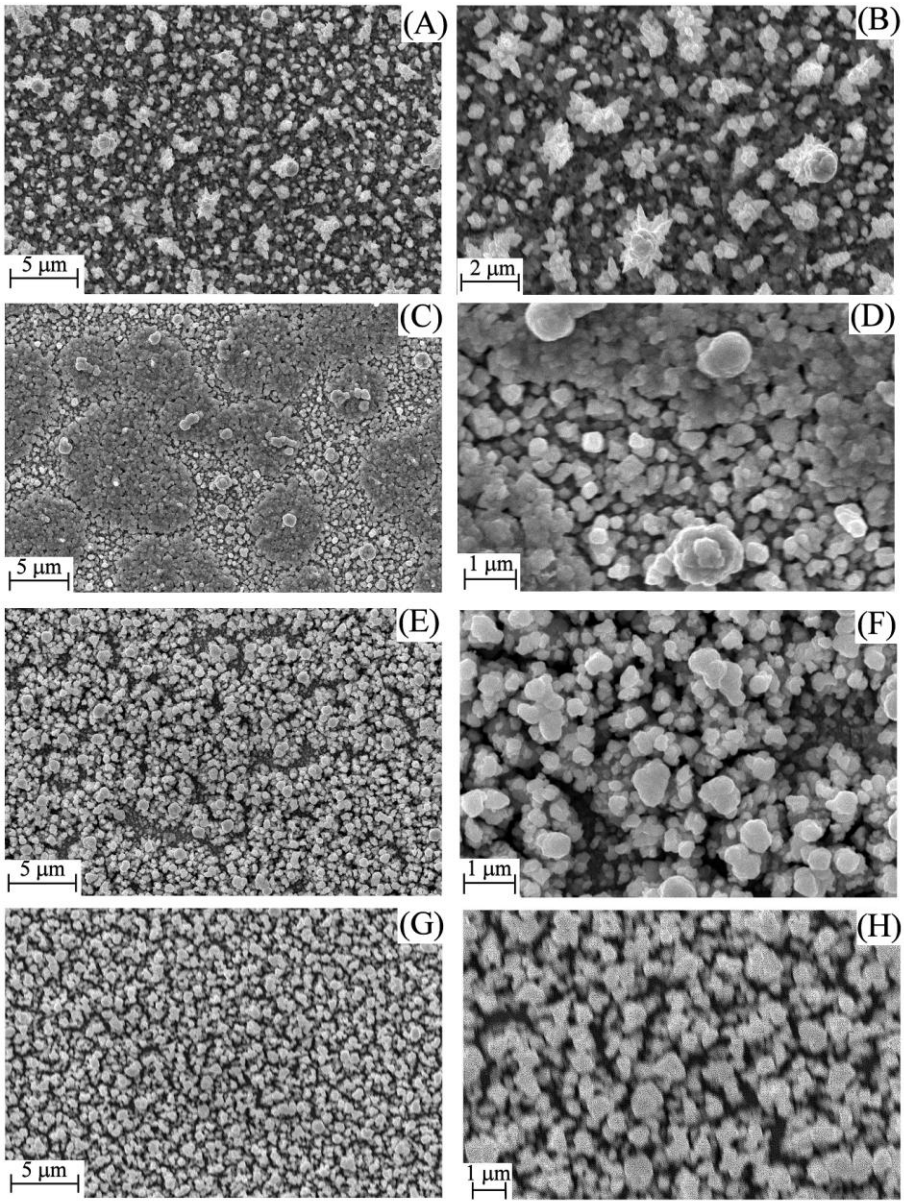

Figure 4.6: High and low resolution SEM images of the electrodeposits formed on Mo substrates. The plating solution contained 0.05 $InCl_3$, 0.025 M $CuSO_4$, 0.5 M LiCl and 0.125 M Na-tartrate and the films were deposited at various potentials. Films were deposited at (A) (B) -0.85 V vs. SCE, (C) and (D) -0.9 V vs. SCE, (E) and (F) -1.0 V vs. SCE and (G) and (H) -1.1 V vs. SCE.

From figure 4.6 it is apparent that the CuIn films are compact in nature. The morphology or composition of the films does change as a function of position. Electrodeposits formed at -0.85 V vs. SCE have slightly dendritic grains varying in size between 0.5 μm to 2 μm. Similar morphology is seen for electrodeposits formed at potentials more negative than -0.9 V vs. SCE. The grains are smaller (ca. 1 μm) and somewhat discontinuous giving the films a roughen appearance. The formation

of hydrogen bubbles during film formation is disrupting the film uniformity as areas of depressions exist within the film, figure 4.6C, 4.6E and 4.6G. Low resolution EDS analysis was performed on the samples to estimate the Cu/In stoichiometry of the electrodeposit figure 4.7.

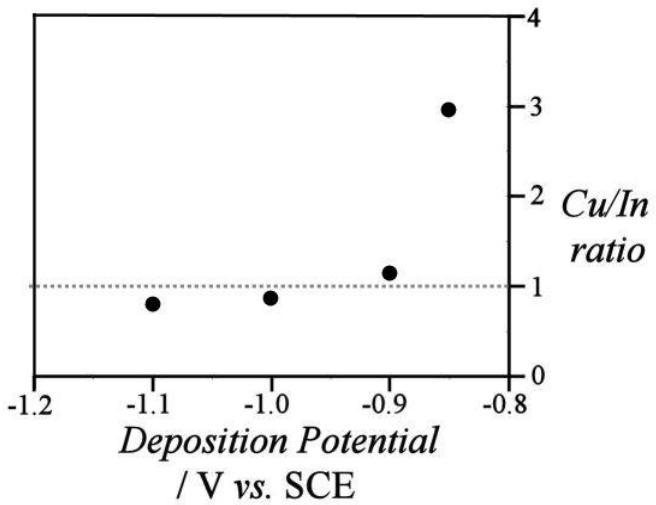

Figure 4.7: A plot of the Cu/In ratio as confirmed by EDS analysis. The EDS was recorded at a low resolution x200, at 25 kV acceleration voltage and for 60 seconds. Three points were chosen over the entire electrode surface and averaged.

From figure 4.7 it is seen that a Cu/In ratio of 1:1 can easily be attained by applying a deposition potential between -0.9 V vs. SCE and -1.0 V vs. SCE. The grains are most likely to be the alloys such as $Cu_{11}In_9$ (which is seen in chapter 2) and possibly metallic species.

4.4.3. Photoactive CISe by rocking disc electrodeposition: selenisation to form CISe

The previous section documented the optimization for CuIn deposition evaluating the stoichiometry and morphology. From the these findings, Cu/In films of ratio 1:1 were deposited onto Mo substrates at a potential of -1.0 V *vs.* SCE under a rocking rate of 8.3 Hz for 21.8 C. Films were then placed in a carbon box with elemental selenium and heated to 500 ^{o}C for 30 minutes (see experimental). This converted the metallic CuIn films into the CISe by the reaction between the film and the selenium vapour (see chapter 2).

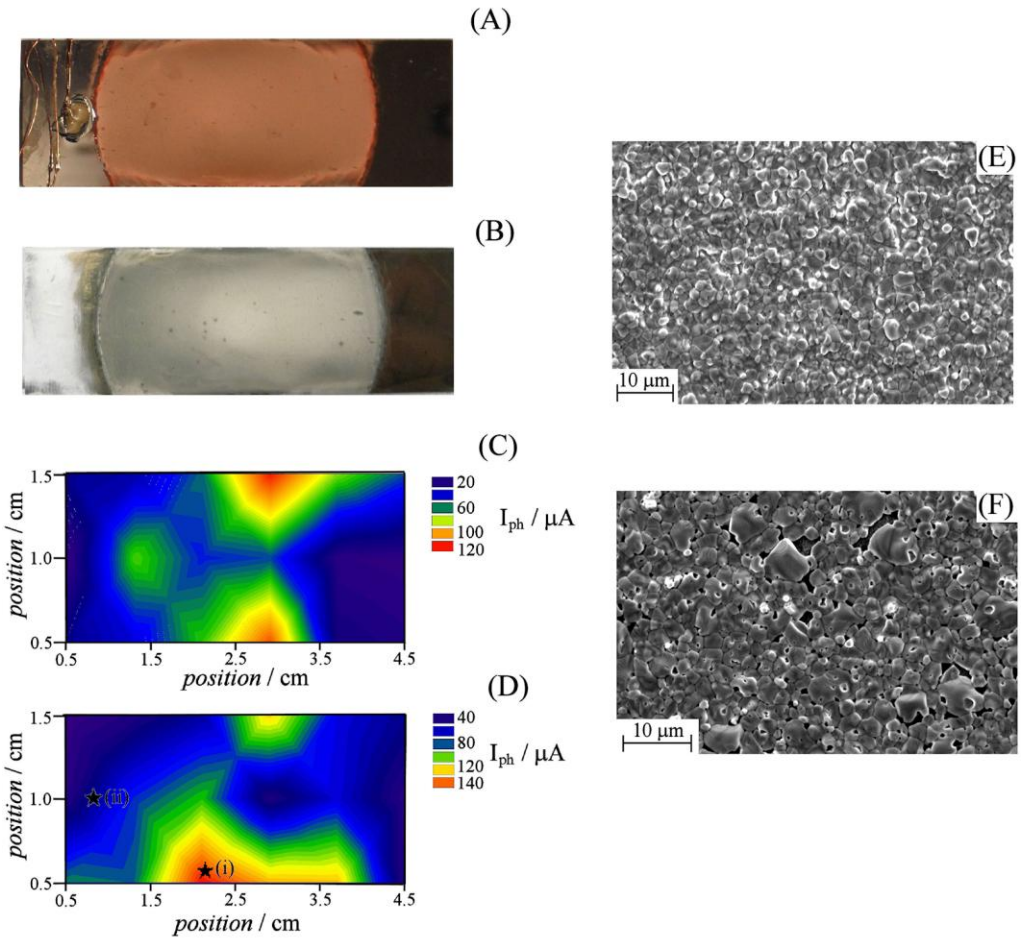

Figure 4.8: Photographs of (A) as-deposited CuIn films (B) selenised CuIn films. Films were selenised at 500 ^{o}C for 30 minutes in an atmosphere of selenium. Photoresponse of a CISe film after (C) t = 60 seconds and (D) t = 90 seconds of 5 %w/w KCN etching. SEM images of the CISe film after t = 90 seconds etching at different areas. (E) is a highly photoactive area (>120 μA) shown as (i). (F are areas of low photoactivity (20 μA) shown as (ii).

Above in figure 4.8A and 4.8B are photographs of the films pre-selenisation and post selenisation. The selenisation step converts the electrode from a dull orange/red to a silver/grey which is consistent with previous work (chapter 2). Figure 4.8B eludes to the fact that the large area CISe films are not uniform as there are different shades of grey across the CISe film. The photoactivity of the films was also examined using the same methodology implemented in chapter 2. Here only a small point of modulated light is rastered across the film and the photocurrent (the difference between the light and dark current) is recorded as a function of position (see experimental). The intensity of the light has to be high (ca. 35 mWcm^{-2}) to discriminate between the darkcurrent and the photocurrent.

Figure 4.8C and 4.8D are photoactivity maps of the same CISe film as a function of etching time in 5 %w/w KCN, t = 60 seconds and t = 90 seconds respectively. The photoactivity of the films is irregular and patchy as in both cases there are areas where the films have simultaneously a photocurrent of ≈100 μA and <20 μA. The electrode was not completely over-etched but stopped at t = 90 seconds of etching to investigate two different regions (figure 4.8i and 4.8ii). The difference in morphology between the photoactive area (figure 4.8i) and the photo-inactive area (figure 4.8ii) is shown in figure 4.8E and 4.8F respectively. From these SEM images it is apparent that photoactive regions are composed of dense packed grains of CISe. In contrast the areas of low photoactivity exhibit the presence of pin holes exposing a large amount of the underlying substrate. In a report by Repins *et al.* [33] a world record device was prepared by physical vapour deposition (efficiency 19.9 %) the morphology shown is highly smooth and uniform with large grains. This is consistent to the films reported here as the areas of high photoactivity are large grain species that are interconnected with the absence of pin holes (figure 4.8E).

There are a number of reasons where this non-uniformity originates from. It is most likely from the poor process control in the selenisation step as there is the possibility of chemical and thermal gradients. These gradients cause a difference in selenisation kinetics as a function of position. There are number of reports that investigate the effect of selenisation or sulphurisation of metallic films for CISe or $CuInS_2$ [34,35].

4.4.4. Photoactive CISe by rocking disc electrodeposition: Effect of diluted KCN and re-annealed treatments

The dilution of cyanide from the standard 5 %w/w to 0.5 %w/w was investigated. The chemical action of the cyanide at the CISe surface is to bind selectivity to Cu_xSe phases in an isotropic and diffusion controlled manner. Diffusion controlled etching can have the rate of etching altered by varying physical parameters such as concentration or temperature. By decreasing the concentration of the KCN in the aqueous etching solution from 5 %w/w to 0.5 %w/w will have two advantages for industrial applications. The first is that this will retard the etching rate as there will be a lower concentration of cyanide at the interface and hence will give a higher

process control. The second advantage is that the solution has a lower health and safety impact as the concentration of cyanide is less. Below in figure 4.9A to 4.9D are photo-electrochemical maps for a CISe film etched with 0.5 %w/w cyanide.

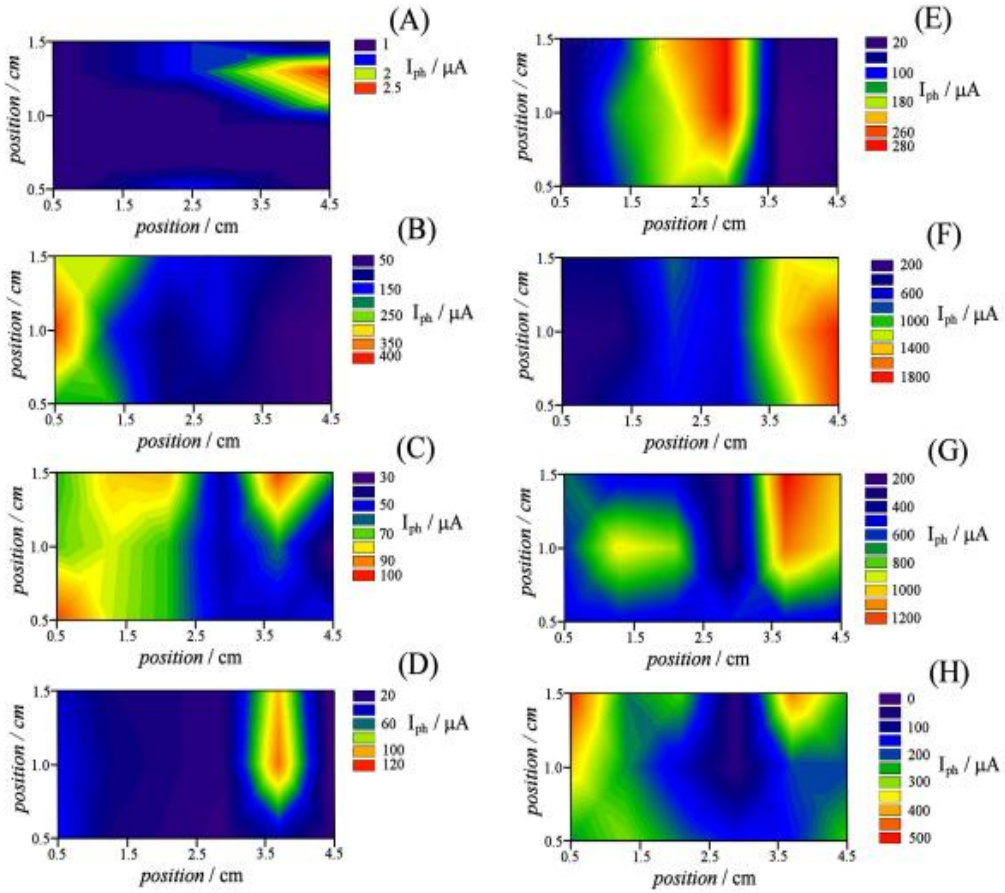

Figure 4.9: Photo-electrochemical maps of CISe thin film at various time intervals during the etching of dilute cyanide (0.5 %w/w KCN). (A) t = 0 seconds, (B) t = 320 seconds, (C) t = 350 seconds and (D) t = 500 seconds. After etched for 500 seconds the film was annealed again at 500 ^{o}C for 30 minutes and etched in dilute cyanide (0.5 % w/w KCN). The photoactivity was recorded at the time intervals of (E) t = 0 seconds, (F) t = 30 seconds, (G) t = 60 seconds and (H) t = 120 seconds.

The use of the diluted cyanide as an etchant increases the etching time required to reach the peak photoactivity ca. I_{ph} = 450 μA at 320 seconds (figure 4.9B). This peak in photoactivity is approximately triple the etching time of the standard 5 %w/w KCN etch on CISe films where the highest photoactivity period is after 90-120 seconds. The over-etching of the film is detrimental to the photoactivity as at 500 seconds of etching the film has a minimal photocurrent (figure 4.9D). This is most likely due to the formation of pin holes at the electrode surface.

The detrimental activity of the pin holes seem to be either become deactivated or reduce in number when the films undergo another heat treatment. By taking the same over-etched film and re-annealing it at 500 ^{o}C, 30 minutes (see experimental) an increase in the photoactivity and uniformity is seen in figure 4.9E to 4.9H. The photoactivity of the films prior to etching is quite high, I_{ph} = 260 μA (figure 4.9E) however this is only a small area. Upon immersing the film into a solution of 0.5 %w/w KCN for 30 seconds the film exhibits a large increase in the photoactivity whereby part of the film has almost I_{ph} = 1.8 mA of photocurrent. A further 30 seconds more etching (figure 4.5G) produces a film with a lower photoactivity (ca. I_{ph} = 1.2 mA) but higher uniformity as more of the film possesses a higher photocurrent. Further etching of the films degrades the photoactivity implying that the sample is being over-etched and the pin holes are being reformed. The use of diluted cyanide suggests that the films are highly sensitive to the etching post the re-anneal treatment.

4.4.5. Photoactive CISe by rocking disc electrodeposition: Effect of HClO and KCN etchants

The previous section documented the use of a re-anneal procedure to enhance the photoactivity and uniformity. This is not a prefect methodology as the resultant films still exhibit non-uniform photoactivity. This section concerns the removal of pin holes from over etched films by the use of a room temperature chemical process. Here the films were subjected to room temperature oxidative etch which is less energy demanding compared to the re-anneal procedure.

The use of an oxidising agent in conjugation with a cyanide etch is investigated. A fleshly prepared CISe film was cut into a smaller electrode shape with an exposed area of 1 x 1.2 cm^2. Photo-electrochemical experiments performed this small electrode using a (5 %w/w HClO solution) in combination with a (5 %w/w) KCN solution. Below in figure 4.10 is a plot of etching time versus photocurrent.

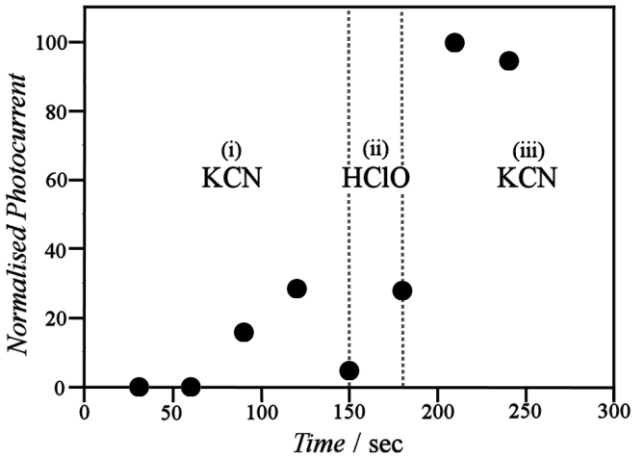

Figure 4.10: Normalised photocurrent measurements for a CISe film immersed in a solution containing 0.2 M Eu(NO_3) held at -0.4 V vs. SCE with a modulated green LED (10 $mWcm^{-2}$) being used to distinguish between the darkcurrent and the photocurrent. In region (i) the film was etched in 5 %w/w KCN, in region (ii) the film was etched in 5 %w/w HClO and in region (iii) the film was etched in 5 %w/w KCN.

Figure 4.10 shows the expected increase in photocurrent is observed when immersing the electrode in a solution of 5 %w/w KCN up until 120 seconds. After this immersion time the photocurrent decreases due to the over-etching and forming of pin holes (figure 4.10i). This over-etched electrode was then immersed in a solution containing 5 %w/w HClO (figure 4.10ii) after which the photocurrent was tested. It is seen that the photocurrent now returns to the same magnitude before the over-etching. The film is then etched in a solution of 5 %w/w KCN for 30 seconds and the photocurrent triples. A further 30 seconds of etching the film in KCN causes a slight degradation of the photocurrent.

Due to the link between microstructure and photocurrent the morphology of the CISe electrode was analysed during different stages of this KCN/HClO etching. To do this a small electrode was cut into four quadrants which were each area was subjected to the same chemical treatments as described above. (i) an electrode was not etch, (ii) an electrode was etched in 5 %w/w KCN for 120 seconds and (iii) an electrode was etched in 5 %w/w KCN for 120 seconds followed by 30 seconds in 5 %w/w HClO followed by 30 seconds in 5 %w/w KCN.

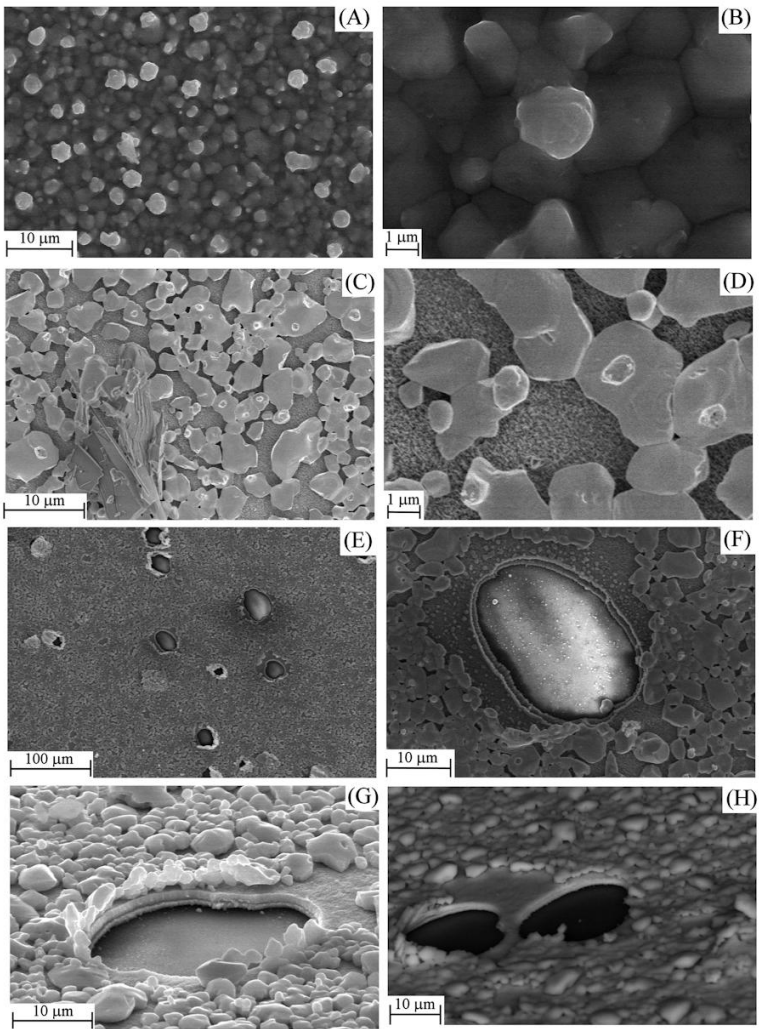

Figure 4.11: High and low resolution SEM images of the same CISe film during different times of etching. (A) and (B) are SEMs of the un etched films, (C) and (D) are SEMs of the CISe film etched in 5 %w/w KCN for 120 seconds, (E), (F), (G) and (H) are SEMs of the film after 5 %w/w KCN etch followed by 30 seconds in a 5 %w/w HClO followed by a final 30 seconds in 5 %w/w KCN etch. (G) and (H) backscattered images.

As seen above in the unetched sample figure 4.11A and 4.11B the films exhibit a very compact and dense morphology as these films are composed of both Cu_xSe and CISe. After 120 seconds of etching (figure 4.11C and 4.11D the typical time it takes to over-etch a sample) it appears that the films are composed of large grains which are interconnected. The film exhibits a high level of pin holes and porosity which has a negative effect on the photocurrent. By exposing the film to 5 %w/w HClO for 30 seconds and 5 %w/w KCN the morphology of the film drastically changes (figures 4.11E, 4.11F, 4.11G and 4.11H). Large area circular pin holes (ca. 20-30 µm) are

created whereby the $MoSe_2$ and the Mo have both been etched away and the underlying soda lime glass substrate is exposed. The chemical action of HClO is to oxidise the surface of the material. As a consequence the most likely products during the HClO etch is the formation of molydenates (MoO_4^{2-}), selenates (SeO_4^{2-}) as well as some copper and indium oxides [18]. The oxide growth on the CISe seems to be passivate the CISe grains as the CISe material was observed to be reasonably stable. The immersing of the film into the KCN etch most probably removes the passive oxide on the surface of the CISe films revealing a pristine CISe surface. This explanation is also consistent when measuring the EDS to estimate the atomic ratios.

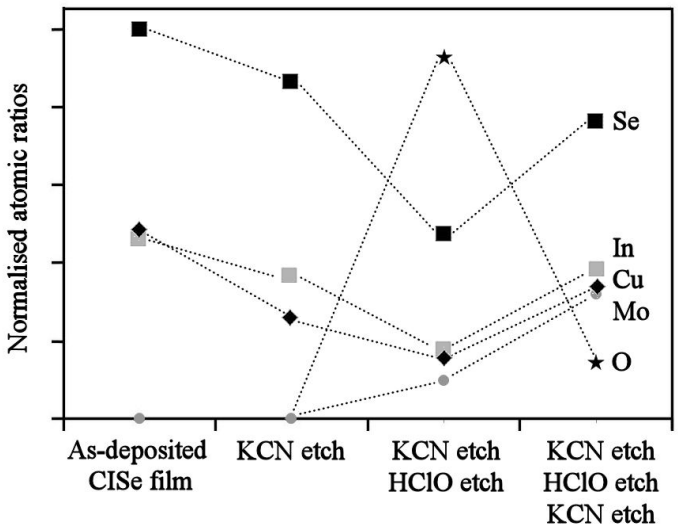

Figure 4.12: Plot of the normalised atomic ratios for a CISe film during different stages of the post treatment anneal. (A) is the film as-annealed. (B) is the film after 120 seconds of 5 %w/w KCN etching, (C) is after 30 seconds of 5%w/w HClO and (D) is after 30 seconds of KCN etching.

The samples were analysed using EDS to assess their atomic ratios during different stages of the etching (figure 4.12). In the un-etched sample the Cu:In ratio is 1:1 and the selenium is slightly in excess most likely due to the presence of residual selenide from selenisation. The molybdenum and oxygen signals are negligible. Upon immersing the film in a 5 %w/w KCN etch the film becomes more indium rich in comparison which is to be expected as the Cu_xSe phases are removed by the KCN. The molybdenum and oxygen signals are still minimal. Immersing the film into a solution containing 5 %w/w HClO for 30 seconds creates a large oxygen signal seen in the EDS. However the atomic ratio's between the Cu, In and Se have not changed.

A molybdenum signal is now seen as the exposure of the pin holes are allowing the X-rays to penetrate to the substrate. A further etching of the film in 5 %w/w KCN produces a film which has the desired stoichiometry of CISe but also some stray Mo (from the pores) and oxygen signals (from the oxide and underlying glass).

To investigate the possibility of the using this additional oxidative etching step on larger substrates another large area CISe film was prepared using the rocking disc electrode and subsequent selenisation (see experimental). The film was over etched (120 second, 5 %w/w KCN) and mapped before immersing in 5 %w/w HClO for 30 seconds followed by 5 %w/w of KCN for 30 seconds and mapped again. Below in figure 4.13 is the photoactivity map before and after the HClO and KCN etch.

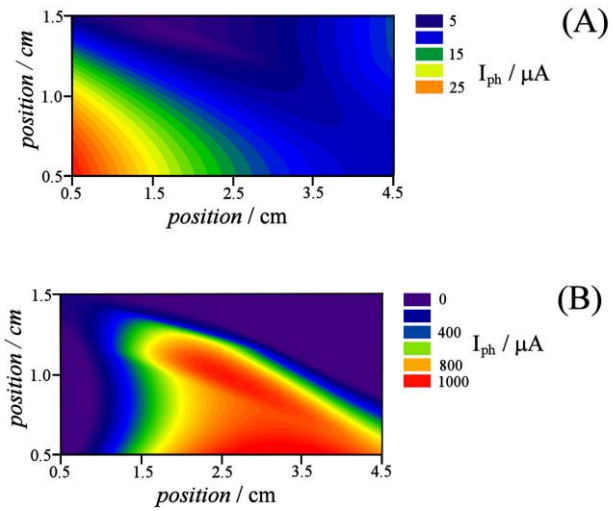

Figure 4.13: Photo-electrochemical maps of a CISe film. (A) CISe film after 120 seconds of etching in 5 %w/w KCN. (B) CISe film after etching in 5 %w/w KCN for 120 seconds, 5 %w/w HClO for 30 seconds followed by 5 %w/w KCN for 30 seconds.

Figure 4.13A displays the photoactivity for the substrate after 120 seconds of etching in 5 %w/w KCN. The photocurrents are low over the entire sample and clearly the sample has been over etched. By immersing the film in the 5 %w/w HClO and then 5 %w/w KCN for 30 seconds (each), an increase in the photoactivity occurs (figure 4.13B). The measured photocurrent is approaching 1 mA for a large part of the electrode indicating that the photoactivity is becoming more uniform. This is a valuable technique to improve the photoactivity of over-etched CISe samples as it is an alternative to using the energy expensive re-anneal heating procedure.

4.5. Conclusion

This chapter has documented the formation of 1:1 ratio of the CuIn electrodeposit using the rocking disc electrode on Mo substrates. A precise control of the stoichiometry is attained by varying the deposition potential but keeping the frequency of perturbation and the deposition charge constant. Morphology of the CuIn films was composed of small grains (ca. 1 μm). The annealing and selenisation process is also a key part in the creation of photoactive absorber layer and the minor phase Cu_xSe. The presence of Cu_xSe is detrimental as this acts as a recombination centre and the complete removal exposes pin holes on the electrode surface. Three alternative methods were investigated to improve the uniformity of the CISe films. The use of a diluted KCN etch, the use of thermally re-annealing the samples, and the use of an oxidising agent in conjugation with the KCN etch. By diluting the KCN etch it was found that the etching process is retarded allowing for a higher process control. The photoactivity of the film was of a similar magnitude to that of the 5 %w/w KCN etch. Re-annealing the same film and etching it further in diluted KCN (0.5 %w/w) increased the photoactivity (ca. I_{ph} = 1.8 mA, 0.2 M $Eu(NO_3)_3$, 35 mW cm^{-2} LED). An alternative was developed where an oxidising solution was used in conjugation with KCN. A CISe film was over etched and then dipped in a solution of HClO which oxidised the film including the pin holes. Upon another etching step (KCN 5 %w/w) which removed the oxide the resultant photoactivity was again high (ca. I_{ph} = 1 mA, 0.2 M $Eu(NO_3)_3$, 35 mW cm^{-2} LED).

4.6. References

[1] A. Brenner, *Electrodeposition of Alloys,* Vol. 1 and 2, Academic Press, New York (1963)

[2] A. Ollivier, L. Muhr, S. Delbos, P. Grand, M. Matlosz, E. Chassaing. J. Appl. Electrochem., 39 (2009) 2337

[3] F. Kröger, J. Electrochem. Soc., 125 (1978) 2028

[4] D. Lincot, Thin Solid Films, 487 (2005) 40

[5] G. Hodes, D. Cahen, Sol. Cells, 16 (1986) 245

[6] J. Herrero, J. Ortega, Sol. Ener. Mat., 20 (1990) 53

[7] J. Zank, M. Mehlin, H. Fritz, Thin Solid Films, 286 (1996) 259

[8] J. Kois, M. Ganchev, M. Kaelin, S. Bereznev, E. Tzvetkova, O. Volobujeva N. Stratieva, A. Tiwari, Thin Solid Films, 516 (2008) 5948

[9] L. Ribeaucourt, G. Savidand, D. Lincot, E. Chassaing, Electrochimica Acta., 56 (2011) 6628

[10] C. Guillén, J. Herrero, Sol. Ener. Mat., 23 (1991) 31

[11] F. Pern, J. Goral, R. Matson, T. Gessert, R. Noufi, Sol. Cells, 24 (1988) 81

[12] D. Lee, J. Appl. Phys., 40 (1969) 4569

[13] P. Campbell, M. Green, J. Appl. Phys., 62 (1987) 243

[14] M. Archer, R. Hill, *Clean Electricity from photovoltaics*, Imperial College Press, 1 (2001)

[15] C. Guillen, J. Herrero, J. Electrochem. Soc., 141 (1994) 225

[16] C. Cummings, G. Zoppi, I. Forbes, P. Dale, J. Scragg, L. Peter, G. Kociok-Köhn, F. Marken, J. Electroanal. Chem., 645 (2010) 16

[17] P Dale, A. Samantilleke, G. Zoppi, I. Forbes, L. M. Peter, J. Phys. D: Appl. Phys., 41 (2008) 8

[18] M. Pourbaix, *Atlas of Electrochemical Equilibria in Aqueous Solutions*, Pergamon Press, New York, (1966)

[19] D. Cahen, Y. Chen, Appl. Phys. Lett., 45 (1984) 746

[20] T. Delsol, M. Simmonds, I. Dharmadas, Sol. Ener. Mat. Sol. Cells, 77 (2003) 331

[21] B. Canava, J. Guillemoles, J. Vigneron, D. Lincot, A. Etcheberry, J. Phys. Chem. Sol., 64 (2003) 1791

[22] J. Kois, S. Bereznev, O. Volobujeva, E. Mellikov, Thin Solid Films, 515 (2007) 5871

[23] U. Störkel, M. Aggour, C. Murrell, H. Lewerenz, Thin Solid Films, 387 (2001) 182

[24] B. Berenguier, H. Lewerenz, Electrochem. Comm., 8 (2006) 165

[25] S. Nakamura, Phys. Stat. Sol. (c), 3 (2006) 2564

[26] R. Hunger, T. Schulmeyer, M. Lebedev, A. Klein, W. Jaegermann, R. Kniese, M. Powalla, K. Sakurai, S. Niki, 3rd World Conference on Photovoltaic Energy Conversion ,May 11-18. 2003 Osaka, Japan, (2003) 566

[27] P. Atkins, J. Paula, Physical Chemistry, 7th edition, Oxford (2005)

[28] M. Walter, E. Warren, J. McKone, S. Boettcher, Q. Mi, E. Santori, N. Lewis, Chem. Rev., 110 (2010) 6446

[29] A. Moreau, Electrochimica Acta., 26 (1981) 497

[30] T. Gujar, V. Shinde, J. Park, H. Lee, K. Jung, O. Joo, J. Electrochem. Soc., 155 (2008) E131.

[31] R. Valderrama, M. Miranda-Hernandez, P. Sebastian, A. Ocampo, Electrochimica Acta., 53 (2008) 3714.

[32] Z. Bahari, E. Dichi, B. Legendre, J. Dugue, Thermochim. Acta., 401 (2003) 131

[33] I. Repins, M. Contreras, B. Egaas, C. DeHart, J. Scharf, C. Perkins, B. To., R. Noufi Prog. Photovolt: Res. Appl., 16 (2008) 235

[34] K. Ramakrishna Reddy, P. Datta, M. Carter, Phys. Stat. Sol. (a), 182 (2000) 679

[35] O. Volobujeva, J. Kois, R. Traksmaa, K. Muska, S. Bereznev, M. Grossberg, E. Mellikov, Thin Solid Films, 516 (2008) 7105

Chapter 5

Surface Spectro-Electrochemistry of Mesoporous Fe_2O_3 for use in Water Splitting

Contents

This work is published as:
C. Cummings, F. Marken, L. Peter, K. Upul Wijayantha, A. Tahir, Journal of the American Chemical. Society, 134 (2012) 1228

5.1. Abstract

The last two experimental chapters of this thesis deviate from the CISe based chapters previously presented in first half of this thesis. Here the general theme changes to the investigation of the electrochemical properties of mesoporous metal oxide films. This chapter in particular documents the investigation of mesoporous α-Fe_2O_3 (haematite) thin films for use in the oxygen evolution reaction. Mesoporous thin films were prepared using the layer-by-layer assembly whereby 4 nm hydrous iron oxide nanoparticles were absorbed onto an FTO substrate in conjugation with carboxyl methyl cellulose. Films were calcined at 500 ^oC for 30 minutes to remove the carboxyl methyl cellulose binder and produce a purely mesoporous α-Fe_2O_3 electrodes. These electrodes were studied in both the dark and under illumination. *In situ* techniques such as potential-modulated absorption spectroscopy, light-modulated absorption spectroscopy and impedance spectroscopy were used to probe the unique characteristics of the mesoporous α-Fe_2O_3. Spectra of a surface-bound higher valent iron species (or 'surface trapped holes') was observed using potential-modulated absorption spectroscopy at potentials more positive than the onset of the oxygen evolution reaction. Spectra with weaker features were recorded at more negative potentials using light-modulated absorption spectroscopy, indicating the same species are formed under potential or light induced conditions. The electrochemical impedance response of the mesoporous α-Fe_2O_3 electrodes exhibits characteristic transmission line behaviour of slow transport. This is attributed to slow hopping of holes, probably between surface iron species. Frequency-resolved potential modulated absorption spectroscopy measurements revealed slow relaxation behaviour that can be related to the impedance response and which indicates that the lifetime of the intermediates (or surface trapped holes) involved in the oxygen evolution reaction is long lived (ca. ≈ms).

5.2. Introduction

5.2.1. Introduction to the photo-electrochemical splitting of water

The first paper documenting the photoelectrolysis of water was by Fujishima and Honda in 1972 [1]. Here the photo-electrochemical cell was constructed of two compartments. One was comprised of a single crystal of n-TiO_2 which is immersed an electrolyte (photoanode). The other half of the cell was the cathode which was comprised of an electrode coated in platinum black immersed in an electrolyte. The two electrodes were connected via an electrical contact and electrolytes by a salt bridge (KCl). A schematic of the devices is shown below in figure 5.1A.

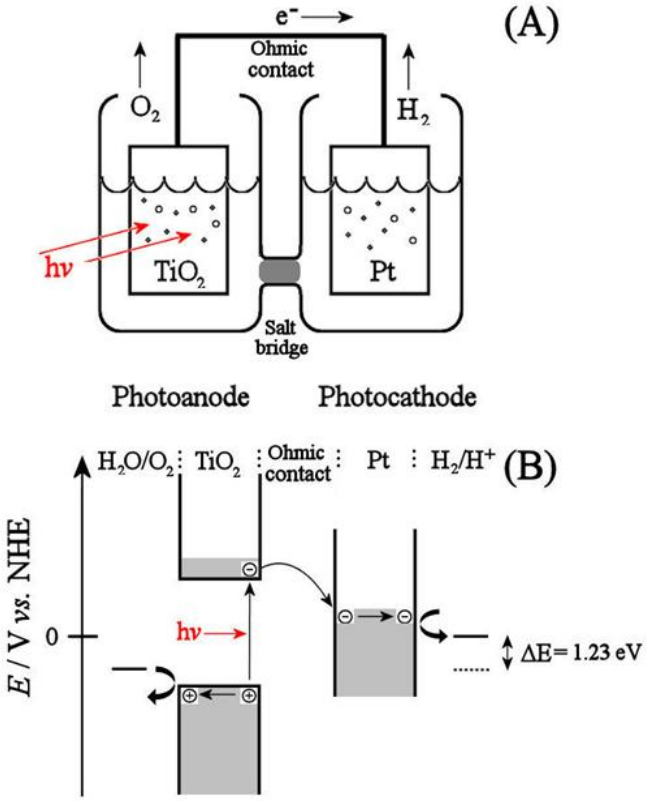

Figure 5.1: (A) Schematic of the photo-electrochemical cell produced by Fujishima and Honda [1,2]. (B) Band structure of the device with the photolysis.

Figure 5.1B is a description of the relative bands of the two electrodes and that of the HOMO and LUMO of water. Illumination of the n-TiO_2 electrode causes an increase in populations of the minority and majority charge carriers in accordance to equation 5.1. This changes the chemical potential of the electrons in the conduction band and the holes in the valance band. The photo-induced holes diffuse/migrate to the n-TiO_2

surface and oxidise water equation 5.2. Photo-promoted electrons in the conduction band of the n-TiO_2 causes an increase in the Fermi level of the cathode. The electrode is coated in a low over potential catalyst, platinum black, which reduces protons equation 5.3. The overall reaction scheme can be expressed as equation 5.4 where the only energy input is the adsorbing radiation. Conservation of charge is maintained throughout the splitting of water and hence both the reduction and oxidation of water must occur simultaneously. The rate of reaction is determined by the slowest process which is typically the evolution of oxygen.

$$TiO_2 + 4h\nu \rightarrow 4e^- + 4h^+ \quad (5.1)$$

$$4h^+(TiO_2) + 2H_2O \rightarrow O_2 + 4H^+ \quad (5.2)$$

$$4e^-(Pt) + 4H^+ \rightarrow 2H_2 \quad (5.3)$$

$$2H_2O + 4h\nu \rightarrow O_2 + 2H_2 \quad (5.4)$$

TiO_2 has a large band gap (>1.23 eV) and the correct band alignment allowing both oxidation/reduction of water to occur without applied external bias [3]. There are numerous materials that split water without applied bias such as $SrTiO_3$, ZrO_2 and $KTaO_3$ [4]. However these tend to have large band gaps (ca. >3 eV) and are unsuitable for terrestrial solar radiation. Metal sulphides and other chalcogenides (e.g. metal selenides/tellurides) have smaller band gaps due to the smaller overlap of the orbital's of the anions and can absorb a larger portion of terrestrial solar radiation. Two of the most studied materials include CdS [5] and MoS_2 [6]. Both of these materials have the correct band alignment however there are two challenges that need to be addressed before commercialisation. The degradation is very severe as by-products (such as photoreduced metallic species ca. Cd^0 and S^0) can be formed at the electrode | electrolyte interface [7]. Another consideration is that the overpotential photovoltage generated upon illumination is relativity low and kinetic barriers hinder the oxidation or reduction of water limiting the efficiency.

Novel strategies have been reported in recent years to tackle the challenge of water splitting. In 1998 Khaselev *et al.* documented the use of a Turner cell [8] as shown in figure 5.2A. Here the photoanode was composed of three different absorbing materials. p-$GaInP_2$ coated with a Pt catalyst was used as a photocathode. Under illumination and steady state conditions the position of the conduction band allows

for the reduction of the protons. However due to the small band gap (ca. 1.8 eV) and incorrect band alignment (i.e. the valence band is higher than the occupied energy level for the oxidation of water) p-$GaInP_2$ cannot oxidise water under illuminated bias. This problem is over come when introducing a second absorbing device composed of p-GaAs/n-GaAs situated behind the p-$GaInP_2$ film and connected via a tunnelling junction. The band gap of the GaAs device is about 1.42 eV and absorbs the transmitted light that penetrated through the p-GaInP (mainly near infrared light) causing the creation of charge carriers. The photogenerated holes from the p-$GaInP_2$ annihilate with the photogenerated electrons in the n-GaAs. The remaining holes will decrease the Fermi level of the secondary electrode (the platinum electrode) causing an oxidation of the water to occur. Based on the short circuit current the efficiency of the device was an impressive 12.4 %.

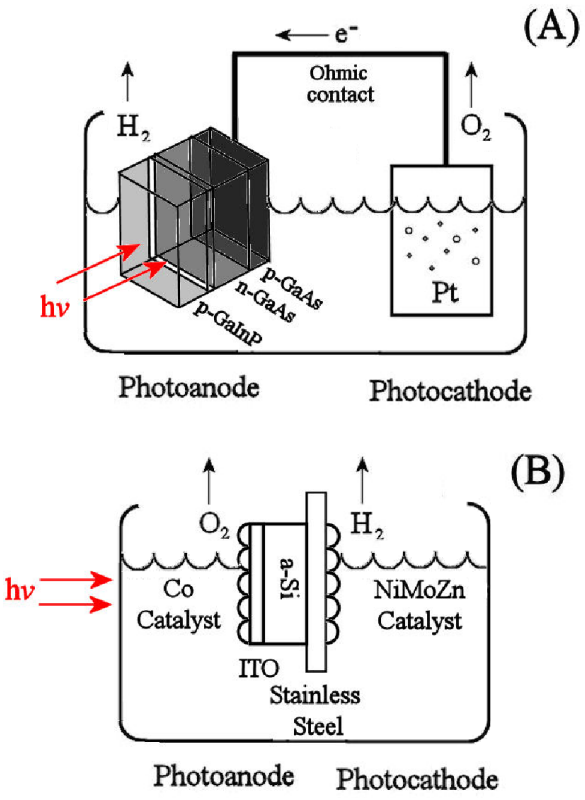

Figure 5.2: (A) Schematic of a Turner cell. Adapted from reference [8]. (B) Schematic of a 'wireless cell', adapted from reference [9]

Figure 5.2B shows a novel design of a photoelectrochemical device which minimises the use of an ohmic contact between the photoanode and the photocathode [9]. Here the device is composed of a 3-junction amorphous silicon absorber layer with one

side in contact with an indium doped tin oxide (ITO) layer and the other a stainless steel film. The ITO layer is decorticated with a cobalt catalyst and acts as the photoanode and the stainless steel has a nickel molybdenum zinc material which is a catalyst for the reduction of water. This configuration is particularly important when scaling up devices as the accumulated resistance caused by the underlying substrate contributes to the series resistance. This can be significant for many conducting oxides (such as ITO or FTO) the resistivity will limit the photoefficiency. Here the authors report a device of 2 % efficiency.

Many semiconductors have smaller band gaps than that of TiO_2 and are more appropriate to absorb light from the solar spectrum however there is a miss-alignment of one of the bands with respect to the energy levels of water. For example, either the conduction band is below the LUMO of the H_2/H^+ or the valance band is above the HOMO of H_2O/O_2. This means that the material acts as either a photoanode or a photocathode but not both. Examples of photocathodes include p-GaInP [8] and p-CISe [10] and examples of photoanodes include n-Fe_2O_3 and n-WO_3 [11].

5.2.2. The study of iron oxide photoanodes

Iron oxide is an abundant, mundane material. It has many crystal forms which include haematite α-Fe_2O_3, magnetite Fe_3O_4 and a gamma phase γ-Fe_2O_3 [12]. Hematite in its intrinsic form is an n-type semiconductor that can be prepared as single crystals or thin films [13]. The photo-electrochemical properties of α-Fe_2O_3 films were first investigated by Hardee and Bard [14]. Here α-Fe_2O_3 films were prepared using chemical vapour deposition on two different substrates (Ti and Pt) both of which behaved in a similar fashion. Thin films of TiO_2 are documented in the same report and were used as a comparison for the photo-electrochemical splitting of water. Here they reported onset of the photo-electrolysis is at about 530 nm for the α-Fe_2O_3 electrodes which is practically more useful than TiO_2 which has an onset of about 400 nm due to its larger band gap ca. $\approx$3.0 eV. It was noted that the α-Fe_2O_3 electrodes are stable in neutral and alkaline conditions however the photoresponse of the films was low. To improve this Kennedy *et al.* investigated the effects of Si^{4+} and

Ti^{4+} dopants on chemical vapour deposition prepared α-Fe_2O_3 films [15]. This decreases the crystal size and causes a different expression of the crystal orientation as the dopants disrupt and segregate crystal lattice growth. Higher photocurrents were observed as a result and this strategy has been repeated to prepare more photoactive and sophisticated devices [16,17].

There are various challenges associated with α-Fe_2O_3 electrodes for use in water splitting. Dare-Edwards *et al.* [18] produced an article in the 1980s giving strong evidence for the slow electron transfer for the oxidation of water at the interface of the α-Fe_2O_3 | electrolyte systems. α-Fe_2O_3 films have a low hole mobility (and hence a small hole diffusion length) [19] which can be addressed somewhat by nanostructuring which decreases the distance for the photogenerated holes to travel [15]. However the miss alignment of the conduction band with the LUMO of water infers that α-Fe_2O_3 electrodes are ineffective at the complete splitting of water. An external bias can be provided from a tandem solar cell (similar to that of a tuner cell) to raise the free energy of the electrodes in the conduction band to drive the hydrogen evolution at the counter-electrode [20]. Surface and bulk recombination are key processes strongly influencing the performance of α-Fe_2O_3 electrodes. A thorough understanding of these detrimental mechanisms as well as charge transfer is needed to manipulate film properties to improve photo-efficiency of devices.

A recent article by Wijayantha *et al.* [21] tried to explain the complex reactions that occur at the surface of the α-Fe_2O_3 electrodes. By simplifying the processes into two pathways (ca. recombination and charge transfer) it is possible to asses the relative magnitude of each rate constant as a function of light intensity and applied bias using photocurrent modulated impedance spectroscopy. Slow charge transfer and surface recombination of electrons and holes shifts the onset of the photocurrent away from the flat band potential. These processes can be minimised by depositing cobalt catalyst which can improve the charge transfer [22] and/or reduce surface recombination [21]. Despite the introduction of a catalyst it has been proposed due to the complex mechanistic pathway and the slow charge transfer, a build up of intermediates at the α-Fe_2O_3 | interface during illumination occurs. These intermediates could be either surface trapped holes or as higher-valent iron species formed at the surface by hole capture. A recent report using pulsed-laser excitation

on α-Fe_2O_3 electrodes has discovered a long-lived transient absorption attributed to surface trapped holes species [23]. The lifetime of which (ca. seconds) is similar to that of the decay of the photocurrents observed. This chapter uses *in situ* absorbance spectroscopy techniques to detect and compare surface intermediate species formed during the oxygen evolution reaction in the dark and under illumination. Normalised fine spectra of the surface trapped holes are obtained by either modulating the potential of the electrode or the intensity of illumination. The absorption spectra obtained is similar to that reported by Pendlebury *et al.* [23]. Impedance of the α-Fe_2O_3 was also conducted to relate the frequency response of the potential modulated spectra to the impedance of the film. Diffusion and lifetime parameters are also estimated by using a transmission line element to fit the impedance data. The hole transport through the film is found to be slow and may occur via a hole hopping mechanism between adjacent Fe surface sites.

5.2.3. Theoretical basis for potential modulated transmission spectroscopy

Spectro-electrochemistry is the combination of both electrochemistry and spectrochemistry. It is typically used to investigate electrochemically-generated coloured intermediates at the electrode | electrolyte interface. The properties of these intermediates such as rate constants or decay lifetimes can be studied. To relate electrochemical signal to the spectrochemical response it is first needed to understand laws that govern optical phenomena. This is taken from Kalaji *et al.* [24] who established the theory.

From the Beer-Lambert law it is known that the optical absorbance, *A*, of a species, whether it is dispersed in a film, liquid or gas, equates to the ratio of intensity of light before, A_0, and after, A_{trans}, sample propagation (equation 5.5). The transmittance, *T*, is the reciprocal of the absorbance.

$$A = \frac{A_0}{A_{trans}} = \frac{1}{T} \tag{5.5}$$

In solid phases the transmittance T of a film is given by the physical parameters, equation 5.6 where α, is the absorption coefficient (m^{-1}), d (m) is the thickness of the film.

$$T = \frac{A_{trans}}{A_0} = \exp(-\alpha d) \tag{5.6}$$

For the spectro-electrochemistry of porous thin films, the thickness parameter and absorption coefficient can be replaced with a surface concentration Γ_n ($molm^{-2}$) and molar absorption cross-sections σ_n (m^2mol^{-1}) which represent the species at the electrode | electrolyte interface absorbing radiation.

$$\frac{I_{trans}}{I_0} = \exp(-\sum \Gamma_n \sigma_n) \tag{5.7}$$

Consider the surface species D(surface) and F^-(surface) that have different absorption spectra and that can be reversibility interchanged by electrochemical means, equation 5.8.

$$D(surface) + e^- \rightleftarrows F^-(surface) \tag{5.8}$$

By applying a modulating potential close to the formal potential of the redox couple the change in relative surface concentrations of the species D(surface) and F^-(surface) (ca. $\Delta\Gamma_D$ and $\Delta\Gamma_{F^-}$) will cause a fluctuation in the Faradaic charge ($Q_{Faradaic}$). This is related to the integral of the Faradaic component of the AC current ($\int I_{Faradaic}(\omega t)dt$).

$$Q_{Faradaic} = \int I_{Faradaic}(\omega t)dt = nF\Delta\Gamma_{F^-} = -nF\Delta\Gamma_D \tag{5.9}$$

Here, n is the number of electrons transferred in the reaction (in this case one) and F is the faraday constant. It is possible to monitor this change in surface concentration by recording the optical response. By modulating the potential between two values (eg V'' and V') it is possible to represent the intensity of

transmitted light (measured at the different potentials) as the change in transmittance over the transmittance $\frac{\Delta T}{T}$ given as:

$$\frac{\Delta T}{T} = \frac{T(V'') - T(V')}{T(V')} = \frac{A_{trans}(V'')A_0^{-1} - A_{trans}(V')A_0^{-1}}{A_{trans}(V')A_0^{-1}} \tag{5.10}$$

$$\text{Giving: } \frac{\Delta T}{T} = \frac{A_{trans}(V'') - A_{trans}(V')}{A_{trans}(V')} \tag{5.11}$$

This change in transmittance is related to the change of concentration of the surface species at the electrode | electrolyte interface $\Delta\Gamma_n$ given by equation 5.12.

$$\frac{\Delta T}{T} = [\exp(-\sum \Delta\Gamma_n \sigma_n)] - 1 \tag{5.12}$$

By applying this to the example and by setting boundary conditions of small voltage perturbation boundary conditions equation 5.12 can be linearised to form:

$$\frac{\Delta T}{T} = \Delta\Gamma\left(\sigma_{F^-} - \sigma_D\right) \tag{5.13}$$

Ignoring capacitive currents and side reactions, the change in surface concentration ($\Delta\Gamma$) can be replaced by the Faradaic charge given in equation 5.9 to give equation 5.14. This relates the normalised change in absorbance to the electrochemical recorded charge.

$$\frac{\Delta T}{T} = \frac{Q_{Faradaic}}{nF}\left(\sigma_{F^-} - \sigma_D\right) \tag{5.14}$$

5.2.4. Total impedance of mesoporous and spectroscopic active systems

To investigate the impedance of the α-Fe_2O_3 electrodes it is necessary to explain some advanced techniques that are used as characterisation tools for mesoporous thin films. The theory of impedance of mesoporous thin films can be explained by Bisquert [25]. The electron transport and electron transfer is described by a transmission model shown in figure 5.3A. The movement of electron and hole transport in mesoporous films is dominated by diffusion. Here the charge carriers are

effectively shielded from an applied macroscopic electric field due to the non-uniform, interpenetrated nature of the film. The series resistance due to the substrate has been omitted. The transmission model describes charge transport throughout the mesoporous film (R_{Trans}) as well as the charge transfer (R_{CT}) and storage of charge (C) at the film | electrolyte. For intrinsic mesoporous insulating films it can be assumed that the measured capacitance is dominated by the pseudocapitance associated with propagation of the extrinsic surface species. Typically for high frequencies the charge transport through the film is a predominate factor however at low frequencies, the transmission line reduces to the parallel RC circuit shown in figure 5.3B, which again is in series resistance with the substrate.

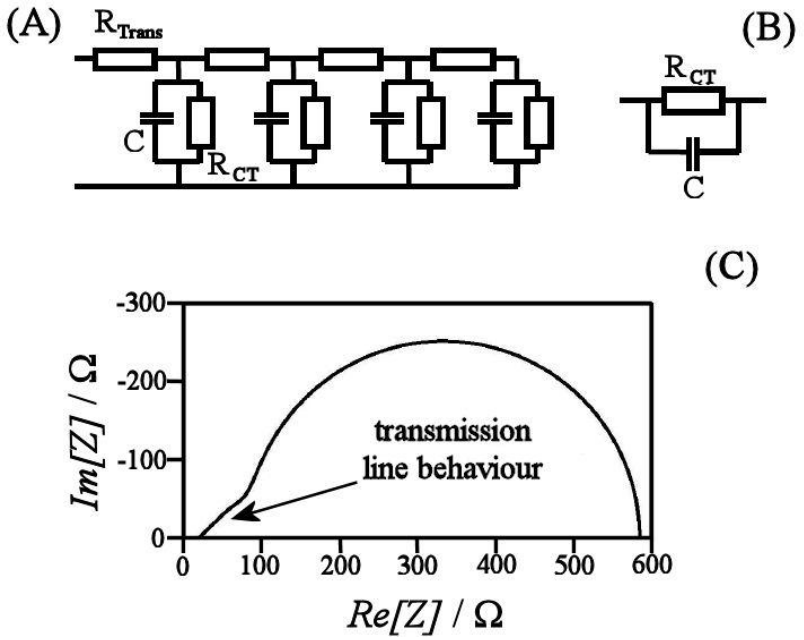

Figure 5.3: (A) Transmission line impedance for high frequencies (B) a parallel RC circuit for low frequencies (C) Nyquist plot for representing the transmission line behaviour at high frequencies and a R(RC) circuit at low frequencies. Calculated from Zplot.

The product of a resistance and capacitance gives a time constant. In complex systems where there can be multiple resistances the magnitude of each has to be considered. For $R_{CT} > R_{series}$ the product of the capacitance and series resistance reflects the resistances originating from the substrate as more charge flows through the smaller resistance. For $R_{series} > R_{CT}$ the product of the charge transfer resistance and pesudocapciatance corresponds to the discharge of the pseudocapacitance

through the Faradaic resistance. This effectively represents the lifetime of the surface-bound redox species.

The AC current observed is comprised of two components: Faradaic and non-Faradaic currents. The Faradaic current is related to the electron transfer between the substrate and the surface species of interest (as well as diffusion of the surface species) to produce a change in absorbance. The non-Faradaic current results from the charging of the electrochemical double layer that exists at the electrode | electrolyte interface.

$$I_{Total} = I_{Faradaic} + I_{non-Faradaic} \tag{5.15}$$

It is possible to relate the optical and electronic responses by recording the total AC current density, I_{Total} which is related to the perturbing voltage ($\tilde{V}$) by ohms law. Here, Z is the film impedance and alternatively this can be expressed in terms of the admittance, Y

$$I_{Total} = \frac{\tilde{V}}{Z} = \tilde{V}Y \tag{5.16}$$

$$\text{Where } \tilde{V} = |V' - V''| \tag{5.17}$$

By integrating equation 5.16 it is possible to attain the periodic component of the charge stored by the pseudocapacitance. A full derivation is found in the reference [26].

$$\tilde{Q}_{Total} = \int I_{Total} dt = \tilde{V} C_{Complex} \tag{5.18}$$

Since the modulation of the absorbance is linearly dependent on the modulation of stored charge (as shown by equation 5.18) both the optical and the electrochemical responses should show a similar frequency dependence. Below is an example of a calculated frequency dependence of the modulated charge stored in the pseudocapacitance.

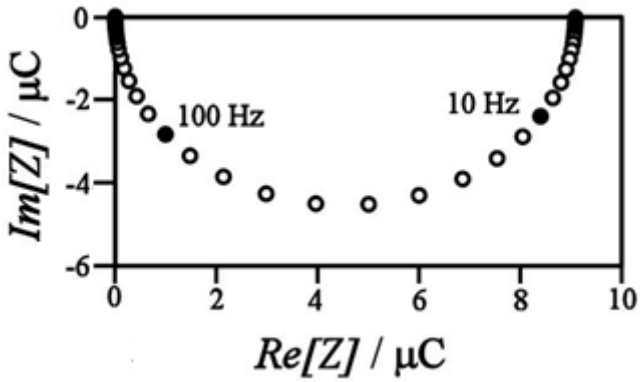

Figure 5.4: Frequency dependence of the modulated charge *Q*F on the pseudocapacitance in Figure 2b calculated for a series resistance of 50 Ω, *R*ct = 500 Ω, $C = 10^{-4}$ F and a modulation amplitude of 100 mV. The potential-modulated absorbance response should exhibit an identical frequency response. Calculated from Zplot.

5.3. Experimental Details

5.3.1. Reagents

NaOH, $FeCl_3$, $HClO_4$, carboxymethylcellulose sodium salt were obtained in analytical reagent grade from Sigma-Aldrich and were used without further purification. Solutions were prepared in deionised and filtered water taken from a Thermo Scientific water purification system (Barnstead Nanopure) with 18.2 MΩcm resistivity.

5.3.2. Instrumentation

A microAutolab III potentiostat system (EcoChemie, NL) was used in standard electrochemical measurements. A platinum counter electrode and a KCl-saturated calomel (SCE, Radiometer) reference electrode were employed for all experiments. The substrate of the working electrode was TEC-8 fluorine doped tin oxide coated glass (FTO) attained from Pilkington, UK. FTO coated glass slides were cleaned in distilled water and ethanol before calcining in air at 500 ^{o}C for 30 minutes to remove organic impurities. For the light induced absorbance measurements the electrodes were housed in a see-through quartz glass cell of dimensions 2 x 3 x 3 cm^3. A soda-lime glass electrochemical cell of the dimensions 1 x 3 x 3 cm^3 was used for all other experiments. All electrochemical experiments were performed in 0.1 M NaOH and without degassing.

5.3.3. Potential modulated transmission measurements

Potentiostat modulated transmittance measurements were performed by using a battery powdered potentiostat to apply a DC bias potential to the working electrode (see figure 5.5A). A superimposed sine wave (frequency 2.7 Hz) generated by a lock-in amplifier (Stanford Research, SR830) was fed into the potentiostat to modulate the working electrode potential. Illumination of the working electrode (in the substrate position) was achieved with a monochromator (M300 Monochromator, Benthan) selecting a specific wavelength from a tungsten lamp light source (Bentham, IL6S). The collection of the transmitted light was achieved with a suitable

silicon photo-detector in a darkened Faraday box, taking care to eliminate stray light. The output of the photo-detector was connected to the lock-in amplifier and the intensity of the transmitted (T) and change in transmitted light with respect to the modulation (dT) were resolved. A phase shift of 90^{o} with respect to the input sine wave was used.

Frequency-resolved optical measurements were performed at fixed DC potential and wavelength using a Solartron 1250 frequency-response analyser. Further information can be found in the literature [24]. Impedance measurements were recorded using the Solartron 1250 in conjugation with the Solartron 1286 electrochemical interface. The peak-to-peak potential modulation was 100 mV for all experiments.

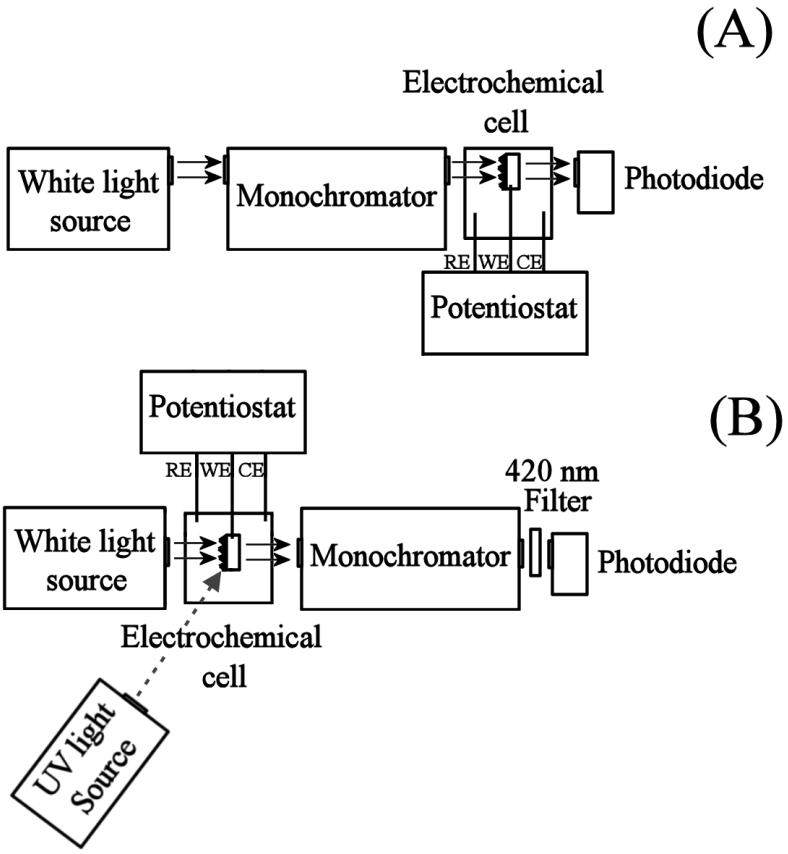

Figure 5.5: Schematics of the two spectroscopic setups, (A) configuration for the potential modulated spectro-electrochemistry and frequency-resolved optical measurements and (B) arrangement for the light induced absorbance spectroscopy.

5.3.4. Light induced absorption spectroscopy

Light induced absorbance spectroscopy of the Fe_2O_3 films was performed using a modulated UV light source to generate the higher oxidation state iron oxide species (see figure 6.5B). The Fe_2O_3 film (immersed in a 0.1 M NaOH electrolyte) and was suspended in a beam of constant white light. The light emitting from an optical fibre from a white light source (Bentham WLS100) is shone through the Fe_2O_3 into the monochromator which selects a chosen wavelength. UV light (375 nm or 405 nm, Thorlabs) is pulsed on to the sample from 45^o angle (Thorlabs LED) which is TTL modulated from a lock-in (Standford Research, SR830). The light emitted from the monochromator passes through a 420 nm filter (GG420 filter) to eliminate any stray UV light before hitting the photodiode. The output of the photo-diode is fed into the lock-in which resolved both the transmitted light (T) and the change in transmitted light (dT) with respect to the modulation with a 90^o phase shift. A potentiostat is used to apply the known potential to the surface of the Fe_2O_3 film.

5.3.5. Formation of Fe_2O_3 films of FTO coated glass substrates

Thin films of mesoporous iron oxide were prepared following a literature method [27]. Sorum's method was used to prepare a colloidal solution containing 4-6 nm hydrous iron oxide nanoparticles. This was done by the forced hydrolysis of a ferric chloride salt in an aqueous environment at elevated temperatures [28]. The hydrous Fe_2O_3 particles were immobilised using the layer-by-layer technique. An FTO coated glass slide was immersed into the 2 mM colloidal solution for one minute to bind a monolayer. After rinsing and drying the film was immersed for one minute into a 1.5 %w/w carboxymethylcellulose sodium salt solution. Rinsing and drying completed one deposition cycle. This process was repeated until the desired number of layers of iron oxide was attained. Films were finally placed in a tube furnace at 500 ^oC in air for 30 minutes to remove the organic components and to give an orange-brown mesoporous iron oxide (hematite) film. Figure 6.6A shows the effect of thickness of the Fe_2O_3 films on the coloration.

5.4. Results and Discussion

5.4.1. Mesoporous Fe_2O_3 films in 0.1 M NaOH: Dark Cyclic Voltammetry

Dark voltammetry of the α-Fe_2O_3 electrodes is important as this can reveal species (or surface states) that can be formed under varying electrochemical conditions opposed to imposing photochemical conditions. Typical cyclic voltammograms for a 10-layer α-Fe_2O_3 film (immersed in 0.1 M NaOH) are shown in figure 5.6B where different anodic limits are imposed on the polarisation curves.

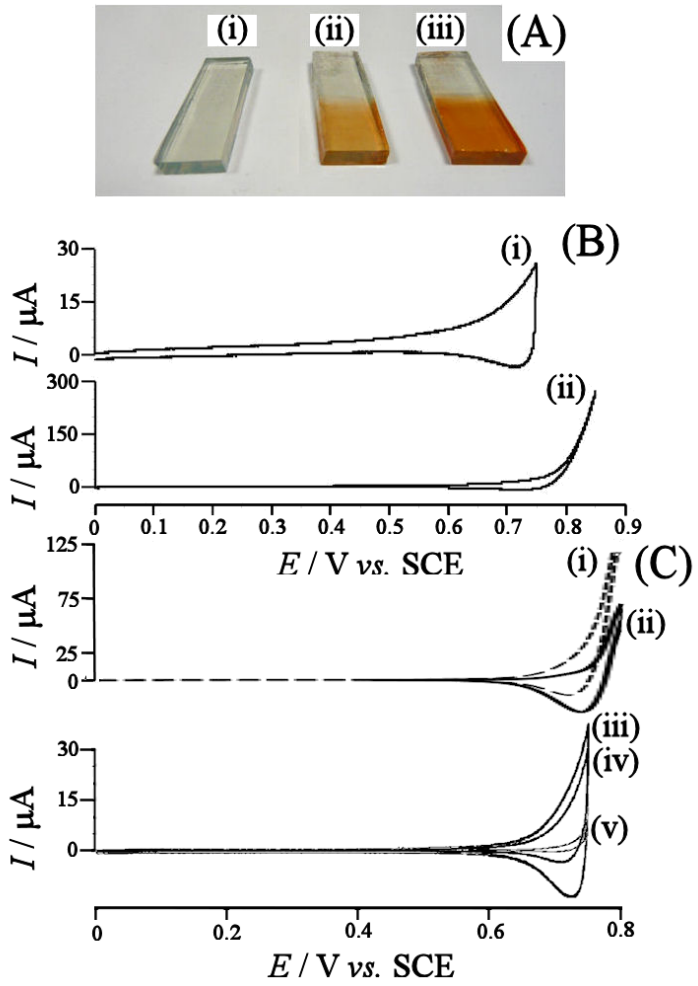

Figure 5.6: (A) Photograph of Fe_2O_3 films on FTO coated glass with (i) 0-layer, (ii) 20-layer, and (iii) 40-layer Fe_2O_3 film thickness. (B) Cyclic voltammograms (area 1 cm^2, scan rate 50 mVs^{-1}) for a 20-layer Fe_2O_3 electrode immersed in 0.1 M NaOH with anodic limits (i) 0.75 V vs. SCE and (ii) 0.85 V vs. SCE. (C) Cyclic voltammograms (area 1 cm^2, scan rate 50 mVs^{-1}) for a 20-layer Fe_2O_3 electrode immersed in 0.1 M NaOH. (i) is the as recorded voltammograms and (ii) is fitted with a tafel slope of 93 mV/decade. Cyclic voltammograms (area 1 cm^2, scan rate (iii) 20, (iv) 50, (v) 100 mVs^{-1}) for a 20-layer Fe_2O_3 electrode immersed in 0.1 M NaOH with anodic limits 0.75 V vs. SCE.

An oxidation signal is present at potentials more positive than +0.65 V vs. SCE (figure 5.6B). From the quasi-reversible behaviour seen at fast scan rate and low anodic limit (figure 5.6Bi) it can be imposed that a long lived intermediate is present. A previous report investigated the catalytic properties of this species and found that it oxidised glucose [27] and was tentatively assigned to an Fe(IV) species (equation 5.19).

$$Fe(III)O(OH)_{interface} \rightleftharpoons Fe(IV)O_{2(interface)} + e^- + H^+ \quad (5.19)$$

$$4\ Fe(IV)O_{2(interface)} + 2\ H_2O \rightleftharpoons O_2 + 4\ Fe(III)O(OH)_{interface} \quad (5.20)$$

Cyclic voltammograms recorded at a maximum potential of +0.85 V vs. SCE (figure 5.6Bii) have a high magnitude of current and are highly irreversible. The formation of the highervalent species is decomposing to oxidise water equation 5.20. This is a typical EC' mechanism as the Fe(III) and Fe(IV) species are in a catalytic cycle, equations 5.19 and 5.20 [29]

In figure 5.6Cii it is possible to simulate the current which is attributed to the splitting of water by assuming of Tafel's law [29] and a 93 mV/decade condition. This can be then subtracted from the cyclic voltammogram (as well as the charging due to the substrate) to investigate the amount of charging due to the production of the higher valence Fe species (equation 5.20). A pseudo capacitance of 25 μCcm^{-2} is attained which can be used to estimate the proportion of the Fe(IV) coverage.

The charge can be converted into the number of species present ca. 10^{14} by multiplying it by the elementary charge. Assuming 2 nm (radius) sized particles fitting into an area of 1 cm^2 with a packing fraction of 0.5 (for a 20 layer film) the total number of particles is $1.19 \times 10^{14}\ cm^{-2}$. This corresponds to an approximate area of 60 cm^2. Assuming the atomic radius of the Fe is 126 pm [30] gives an area exposed of $4.9 \times 10^{-20}\ m^2$ which can be used to estimate the total number of Fe species at the surface (ca. 1.22×10^{17}) which can finally be compared with the number of molecules associated with the charge. Here the ratio of Fe(IV) molecules at the surface of the film being charged is 0.1 % of a monolayer coverage.

The chemical reversibility of the oxidation and re-reduction of the surface bound Fe(IV) species decreases as the applied anodic limit. This is because more species are produced and are reacting with water through the proposed EC' mechanism. For

the potential limit of +0.75 V vs. SCE the scan rate dependence is demonstrated in figure 5.6Ciii, 5.6Civ and 5.6Cv. The chemical reversibility changes from a reversible to and irreversible signal at a transition scan rate of ca. v_{trans} = 0.02 V s^{-1}. By using dimensional analysis [31] this allows the apparent first order rate constant for oxygen evolution to be estimated as

$$k = \frac{v_{trans} \times F}{RT} = 0.8 \text{ s}^{-1}. \quad (5.21)$$

This apparent rate constant for the oxidation of water at the α-Fe_2O_3 | electrolyte interface is very low. In the literature there are examples of using various catalysts which increase the rate by lowering the overpotential for water oxidation at the α-Fe_2O_3 | electrolyte interface. These include a Co catalyst [22], $Co(PO_4)$ [32] and a IrO_2 [33].

5.4.2. Mesoporous Fe_2O_3 films in 0.1 M NaOH: potential modulated transmittance spectrometry

Potential modulated transmittance spectroscopy is a sensitive technique for studying intermediates at the surface of the electrode. By modulating the potential it is possible induce the formation of spectroscopic active intermediates. They can be observed via the change in transmittance of the sample in accordance with equation 5.14. Potential modulated transmittance spectroscopy was recorded for α-Fe_2O_3 films with different thicknesses at different DC potentials (figure 5.7).

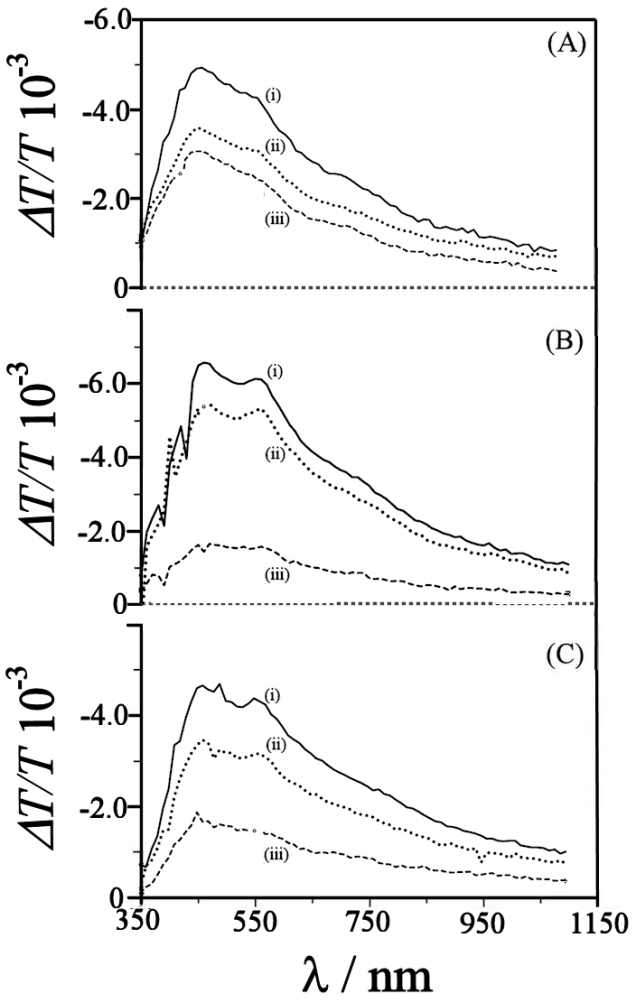

Figure 5.7: Un-smoothed data for potential modulated electrochemical spectroscopy of various Fe_2O_3 films in 0.1 M NaOH (1 cm^2) (A) 10 layer Fe_2O_3 film with a DC applied bias of (i) 0.75 V vs. SCE (ii) 0.85 V vs. SCE and (iii) 0.65 V vs. SCE. (B) 20 layer Fe_2O_3 film with a DC applied bias of (i) 0.75 V vs. SCE (ii) 0.7 V vs. SCE and (iii) 0.65 V vs. SCE. (C) 40 layer Fe_2O_3 film with a DC applied bias of (i) 0.8 V vs. SCE (ii) 0.7 V vs. SCE and (iii) 0.65 V vs. SCE. (unfilled circles are points that have been removed due to system noise).

Potential modulated spectroscopy measures the difference in transmittance between the surface bound Fe(III) and the Fe(IV) species. Figure 5.7A shows the spectra of a 10 layer α-Fe_2O_3 electrode at different DC biases. Here the spectra exhibits a board adsorption which is comprised of two well defined peaks at 460 nm and 560 nm with a slightly shoulder absorption at 770 nm. When viewing thicker films (ca. 20 and 40 layer, 5.7B and 5.7C) it is apparent that the spectral features are similar. For the 10 layer thick film the magnitude of the normalised change in transmittance peaks at a DC voltage of 0.725 V vs. SCE and then decays. In contrast the 40 layer film peaks

at +0.8 V vs. SCE suggesting that film thickness has a small affect on the lifetime of the Fe(IV) species. The position of the adsorption bands are independent of applied DC potential suggesting that only a single intermediate is being observed. From the value recorded from the $\Delta T/T$ it is possible to relate this to the difference in the molar cross sections. Using equation 5.14 it is possible to calculate the difference in absorption cross sections for at 10 layer α-Fe_2O_3 electrode is 0.7 V, 460 nm is 6×10^{-17} cm^2. This corresponds to a difference in molar absorption coefficient of $\varepsilon = 3.6 \times 10^4$ dm^3 mol^{-1} cm^{-1}.

At this wavelength (ca. 460 nm) it is possible to compare and contrast the absorption coefficients of this surface species to absorption spectra reported in the literature. Sharm *et al.* recently reviewed the absorption spectra of aqueous high-valent species iron species (ie Fe(IV), Fe(V) and Fe(VI)) species in solution in the region 400-700 nm [34]. None of these species directly correspond to that seen in the spectra above as Fe(IV) shows a broad peak at 420 nm (ε = 1200 dm^3 mol^{-1} cm^{-1}). Fe(VI) has a broad peak at 510 nm (ε = 1100 dm^3 mol^{-1} cm^{-1}). Fe(V) has a main peak at 400 nm (ε = 900 dm^3 mol^{-1} cm^{-1}) and a second peak at 500 nm (ε = 650 dm^3 mol^{-1} cm^{-1}). Comparing these spectra to that of the surface species recorded here the absorption coefficients appear to be more than an order of magnitude lower, indicating that these do not correlate to the surface state. Other possibilities that can be considered are low spin and high spin iron peroxo species which show charge transfer bands in the visible at around 550 nm [35,36], but these complexes (with organic ligands) also have absorption coefficients in the region of 10^3 dm^3 mol^{-1} cm^{-1}, which is lower than the 10^4 dm^3 mol^{-1} cm^{-1} recorded in the spectra above.

5.4.3. Mesoporous Fe_2O_3 films in 0.1 M NaOH: impedance spectroscopy

The potential modulated absorption spectroscopy response of the α-Fe_2O_3 film operated at a frequency of 2.7 Hz for all experiments. This was because the signal response attenuated at high frequencies. To investigate the origin of this attenuation and the frequency dependence of the α-Fe_2O_3 films impedance measurements were undertaken (in the dark) in the potential range where the higher oxidation state was observed. Figure 5.8 illustrates a typical impedance response of a 40 layer α-Fe_2O_3

film which exhibits two distinct features. At high frequencies transmission line behaviour is observed in the complex plane plot. At low frequencies a typically R(RC) circuit is seen (figure 5.8A). A good fit to the data is attained, as can be seen more easily in the phase angle part of the Bode plot (figure 5.8B).

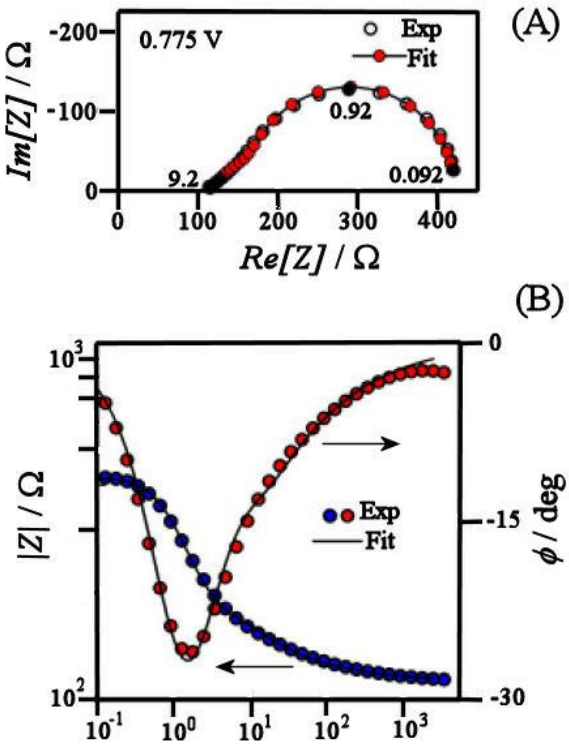

Figure 5.8: (A) Nyquist and (B) Bode plot representing the impedance measured for a 40 layer Fe_2O_3 electrode immersed in a solution of 0.1 M NaOH. A DC potential of 0.775 V vs. SCE was applied to the electrode. Some frequencies are labelled on the plots. R_{CT} = 275 Ω, R_{Trans} = 161 Ω and C = 0.68 mF.

By combining the capacitance measurement for the 20 layer attained by the impedance work ca. ≈0.5 mF with the voltage oscillated ca. 100 mV peak to peak or 0.036 V RMS then its possible (using equation 5.22) to estimate the pseudo capacitance of the film ca. 20 μCcm^{-2} which is similar to that observed from the cyclic voltammetry measurements on a 10 layer film. Due to the small proportion of the film being charged the thickness does not have a big implication on the pseudo capacitance.

$$Q = CV \tag{5.22}$$

The impedance was recorded for a number of DC values for a 40 layer thick film with the variation in R_{CT}, R_{Trans}, Cap resolved from the impedance data. Below in figure 5.9 summarises the trends.

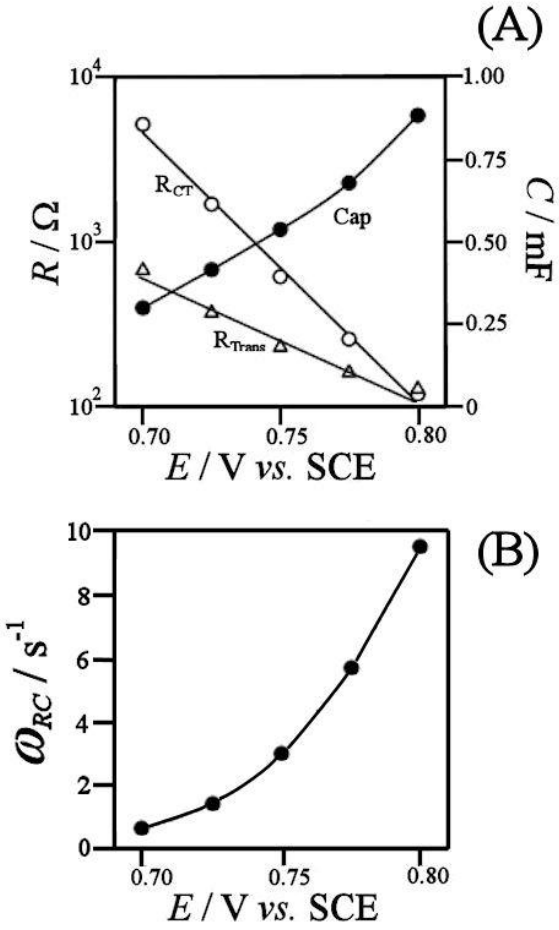

Figure 5.9: (A) Plot representing the transport resistance (R_{Trans}) charge transfer resistance (R_{CT}) and capacitance (Cap) for a 40 layer α-Fe_2O_3 film in 0.1 M NaOH. (B) The time constant of the Fe(IV) state calculated by the multiple of R_{CT} and the Cap.

From figure 5.9A it is seen that the resistances of the film (R_{CT} and R_{Trans}) logarithmically decrease as a function of the applied DC bias with the capacitance increasing. This is consistent with the production of the Fe(IV) state which is diffusing through the material and acting as a charged carrier increasing the conductivity (and capacitance) of the film. As the DC bias is increased from 0.7 V vs. SCE to 0.8 V vs. SCE the time constant (product of the R_{CT} and Cap) which corresponds to the lifetime of the Fe(IV) states decreases from 0.1 s to 10 ms (figure 5.9B). Transmission line behaviour is seen in impedance data which correspond to

applied DC biases of above 0.7 V vs. SCE. The presence of a transmission line suggests slow transport of charge in the mesoporous α-Fe_2O_3 film. Hole transport in α-Fe_2O_3 materials is strongly dependant on direction in the crystal lattice and is known to be slow. A recent theoretical study by Iordanova *et al.* [37] have modelled electron and hole transport in α-Fe_2O_3 using Marcus theory and obtained hole mobilities for transport in the (001) plane and along the [001] axis which correspond to 3.6 x 10^{-7} cm^2 V^{-1} s^{-1} and 1.7 x 10^{-4} cm^2 V^{-1} s^{-1} respectively. By taking the lower value of the mobility and considering an 80 nm film (40 layer a Fe_2O_3) with a R_{Trans} = 100 Ω (measured by impedance spectroscopy) at 0.8 V vs. SCE, the free hole concentration, n_p, can be estimated using equation 5.23:

$$R_{Trans} = \frac{d_{film}}{\sigma} = \frac{d_{film}}{q n_p \mu_p} \tag{6.23}$$

Here d_{film} film is the thickness of the film q the charge and μ_p is the mobility. The free hole concentration, *p*, can be estimated as 1.4 x 10^{18} cm^{-3} which corresponds to a charge of 0.22 Ccm^{-3}. This number of free holes can be converted to a geometric area dividing it by the dimensions of the electrode giving 1.8 μCcm^{-2}. This number of free holes is an order of magnitude smaller compared to the surface states measured from the pseudocapacitance (ca. ≈20 μCcm^{-2}). If the mean mobility is higher then the free hole concentration will be even lower. This suggests that the formation of the Fe(IV) in the bulk is lower than expected and the predominate transport of holes in these mesoporous films is the propagation of holes at the α-Fe_2O_3 | electrolyte interface.

5.4.4. Mesoporous Fe_2O_3 films in 0.1 M NaOH: frequency response

To analyse the films further it is needed to establish a connection between the electrical and optical properties of the film. It is needed to relate the impedance to the frequency dependence of the potential modulated spectroscopy response. By shining light of 460 nm onto a 20 layer α-Fe_2O_3 film, different frequencies of perturbation were studied whilst the $\Delta T / T$ was monitored figure 5.10.

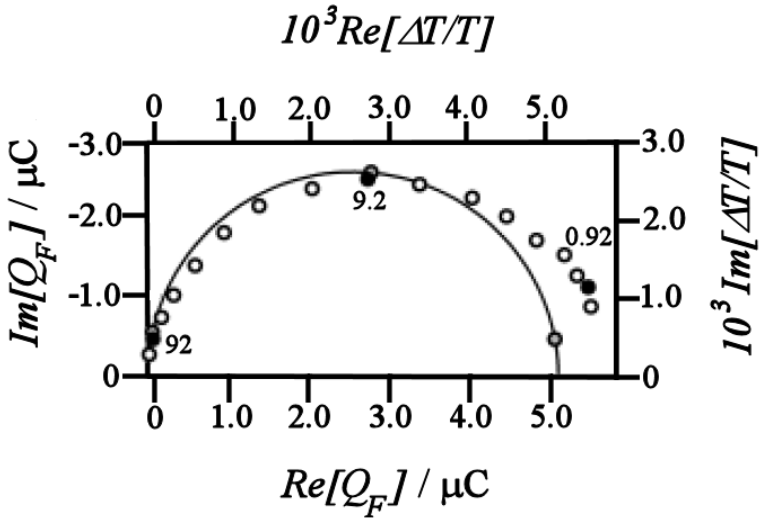

Figure 5.10: Optical response of a 20 layer α-Fe_2O_3 film (immersed in 0.1 M NaOH) held at DC potential of +0.775 V vs. SCE with an AC modulation component of 100 mV peak to peak. Here the (dots) ΔT/T is recorded at different frequencies of perturbation. The line fit of the complex capacitance $C_{Complex}$ (of the charge) is calculated using Zplot and the complex capacitance obtained using values of R_{CT}, Cap and R_{series} derived from the impedance analysis.

Figure 5.10 shows that there is a one to one relationship between the frequency dependence of the measured ΔT/T and the modulated charge of the pseudocapacitance. This validates the model given in theoretical section (equation 5.18) and for this case the frequency attenuation arises predominantly from the combination of series resistance and pseudocapacitance.

5.4.5 Mesoporous Fe_2O_3 films in 0.1 M NaOH: light induced spectroscopy

Studying films under illumination relates the dark electrochemistry to the photo-electrochemistry. The photo-electrochemical oxidation of water occurs at a less of a positive potential compared to the dark. Below in figure 5.11 is a linear sweep voltammogram of an α-Fe_2O_3 electrode with 10 $mWcm^{-2}$ UV irradiation (ca. 375 nm).

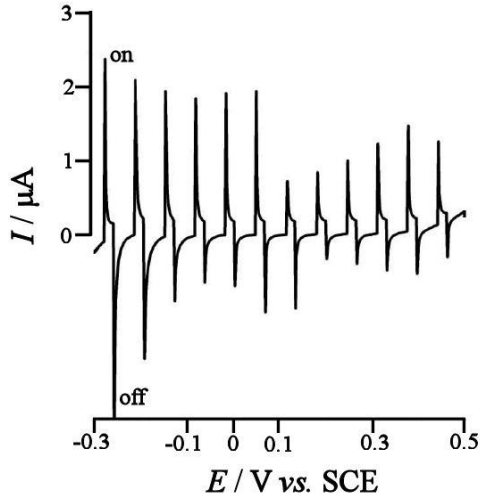

Figure 5.11: Voltammogram of a 40 layer thick α-Fe_2O_3 (substrate illumination) electrode immersed in a solution of 0.1 M NaOH with a sweep rate of 10 mVs^{-1}. The film was exposed to 10 $mWcm^{-2}$ 375 nm radiation

Upon illumination a current spike is observed which decays exponentially until a steady sate value is reached. The observed variation in the magnitude of the spikes of the photocurrent is due to the digitalisation of the autolab sampling hardware. The photocurrents measured from the mesoporous electrodes are considerably smaller than those measured by other authors [22,32] but similar to that recorded by Björkstén et al [38]. Possible explanations for the low photocurrent include the low thickness and therefore high transparency of the electrode as well as the high surface area increasing the effect of surface recombination. Spiked responses are typical for systems with high surface recombination. The onset of the photocurrent could not be determined as applying reductive potentials more negative than -0.3 V vs. SCE causes the reduction of the Fe(III) to the Fe(II) which masks any photocurrent equation 5.24.

$$Fe(III)O(OH)_{interface} + e^- + H^+ \rightleftharpoons Fe(II)(OH)_{2(interface)} \qquad (5.24)$$

The photocurrent of the α-Fe_2O_3 is due to the absorbing of light creating minority and majority carriers which the holes are then travelling to the surface to react with the water. This mechanism is different from the creation of charged carriers from the dark electrochemistry. In contrast the holes (i.e. Fe(IV) species) must be created via a different mechanism. For bulk thin films of Fe_2O_3 the creation of holes (in the absence of light) occurs under inversion conditions at the electrode | electrolyte interface by the tunnelling of the electrons from the valence band to the conduction

within the space charge region. As the electric field and hence the band bending applied to the film is shielded by the interpenetration of the electrolyte due to the mesoporous nature the band bending is minimal. An alternative mechanism is creation of charged species (ca. Fe(IV)) at the triple phase boundary of the electrode | electrolyte | α-Fe_2O_3 sites. The diffusion of these species can occur through the hole hopping (or electron hopping) from one surface site to another. This process is similar for oxidation of absorbed dyes on mesoporous films. The higher valence species generated by the potential modulated experiments is likely to be part of the oxidation of water.

Recent work by Wijayantha *et al.* [21] has documented that a substantial concentration of trapped holes accumulate at the surface of the α-Fe_2O_3 upon illumination. The build up of holes is due to the very slow electron transfer between the α-Fe_2O_3 and the OH^-. Pendlebury *et al.* [23] agreed with this suggestion as a long lived species at the surface of the α-Fe_2O_3 is observed following pulsed laser excitation. A similar photo-electrochemical method is to use light induced spectro-electrochemistry. By modulating the illumination intensity of a UV source whilst measuring the transmittance of a α-Fe_2O_3 sample immersed in an electrochemical cell, a spectra can be attained figure 5.12

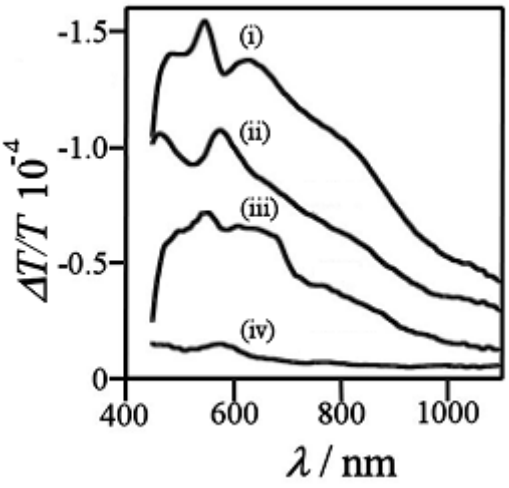

Figure 5.12: Smoothed light induce spectro-electrochemistry of a 40 layer film immersed in a solution of 0.1 M NaOH. Different DC biases were chosen lower than the onset of Fe(IV) signal; (i) +0.4 V vs. SCE, (ii) +0.2 V vs. SCE, (iii) 0 V vs. SCE and (iv) -0.2 V vs. SCE.

Figure 5.12 displays four spectra recorded or a 40 layer electrode at different values of DC bias. The spectra are both similar to that recorded in the potential modulated experiments but also has a board similarity to that recorded by Pendlebury *et al.* [23]. The spectra is approximately 1 order of magnitude smaller than that recorded for the potential modulated spectra indicating a low quantum efficiency. This is most likely due to the high levels of surface recombination and the small thickness (ca. 80 nm). The magnitude of the spectra increases when DC bias's applied are more positive indicating that the potential of the electrode has an effect on the lifetime of Fe(IV) present.

5.5. Conclusions

Documented in this chapter is the study of mesoporous α-Fe_2O_3 electrodes for the oxygen evolution reaction. Despite the high surface area being detrimental to the quantum efficiency this property allowed a unique insight into processes at the α-Fe_2O_3 | electrolyte interface. The combination of both spectroscopic and impedance methodologies has given a deeper insight into the mechanism of water oxidation. Spectroscopic species are detected in potential-modulated and light-modulated transmittance measurements, suggesting that the mechanisms of oxygen evolution involve the similar intermediates whether in the dark and under illumination. The spectra attained did not match those recorded in the literature for hypervalent dissolved iron species however they are similar to that recorded using pulsed laser methodologies on iron oxide films. The idea of surface trapped holes has been adopted. The hole concentrations differ when considering the free holes measured from the transport resistance or surface states measured from the pseudo capacitance. The relatively long lifetimes of these surface trapped holes attained from the impedance data suggest that a kinetic barrier exists for the oxidation of water. The oxidation of water corresponds to the annihilation of 4 holes in the α-Fe_2O_3 which implies a complex mechanism. It is likely that the formation of hyper-valent states (whether they are Fe(IV), (V) or (VI)) must be in close proximity to each other to allow for the oxidation of water to proceed. As a consequence of this the surface mobility of the holes is an important factor and low values can contribute to the slow charge transfer when oxidising water.

5.6 References

[1] A. Fujishima and K. Honda, Nature, 37 (1972) 238

[2] A. Fujishima, K. Kchayakawa, K. Honda, Bull. of the Chem. Soc. of Japan., 48 (1975) 1041

[3] M. Grätzel, Nature, 414 (2001) 338

[4] A. Kudo, Y. Miseki, Chem. Soc. Rev., 38 (2009) 253

[5] H. Gerischer, J. Electro. Chem. Soc., 113 (1966) 1175

[6] L. Schneerneyer, M. Wrighton, J. Am. Chem. Soc., 101 (1979) 6496

[7] D. Fermin, E. Ponomarev, L. Peter, J. Electroanal. Chem., 473 (1999) 192

[8] O. Khaselev, J. Turner, Science, 280 (1998) 425

[9] S. Reece, J. Hamel, K. Sung, T. Jarvi, A. Esswein, J. Pijpers, D. Nocera, Science, 334 (2011) 645

[10] D. Yokoyama, T. Minegishi, K. Maeda, M. Katayama, J. Kubota, A. Yamada, M. Konagai, K. Domen, Electro. Chem. Comm., 12 (2010) 851

[11] M. Butler, R. Nasby,R. Quinn, Sol. Stat. Comm., 19 (1976) 1011

[12] U. Schwertmann, R. Cornell, *Iron Oxides in the Laboratory: Preparaion and characterisation* Wiley-VCH 2nd ed. (2000)

[13] R. Fredlein, A. Bard, Electrochem. Soc., 126 (1979) 1892

[14] K. Hardee, A. Bard, Electrochem. Soc., 123 (1976) 1024

[15] J. Kennedy, R. Shinar, J. Ziegler, J. Electrochem. Soc., 127 (1980) 2307

[16] N. Hahn, C. Mullins, Chem. Mater., 22 (2010) 6474

[17] M. Zhang, W Luo, Z. Li, T. Yu, Z. Zou Appl. Phys. Lett., 97 (2010) 042105

[18] M. Dare-Edwards, J. Goodenough, A. Hamnett P. Trevellick, J. Chem. Soc.., Faraday Trans. I, 79 (1983) 2027

[19] F. Morin, Phys. rev., 93 (1954) 1195

[20] J. Brillet, M. Cornuz, F. Le Formal, J. Yum, M. Grätzel, K. Sivula, K , J. Mat. Res., 25 (2010) 17

[21] K. Upul Wijayantha, S. Saremi-Yarahmadia, L. Peter, Phys. Chem. Chem. Phys., 13 (2011) 5264

[22] A. Kay, I. Cesar, M. Grätzel, J. Am. Chem. Soc., 128 (2006) 15714

[23] S. Pendlebury, M. Barroso, A. Cowan, K. Sivula, J. Tang, M. Grätzel, D. Kluga, P. Durrant, Chem. Commun., 47 (2011) 716

[24] M. Kalaji, L. Peter, J. Chem. Soc., Faraday Trans., 87 (1991) 853

[25] J. Bisquert, J. Electroanal. Chem., 646 (2010) 43

[26] Supporting Information web: C. Cummings, F. Marken, L. Peter, A. Tahir, K. Wijayantha, J. Am. Chem. Soc., 134, (2012) 1228

[27] C. Cummings, M. Bonné, K. Edler, M. Helton, A. McKee, F. Marken, Electro. Chem. Comm., 10 (2008) 1773.

[28] C. Sorum, J. Am. Chem. Soc., 50 (1928) 1263

[29] R. Compton, C. Banks, Understanding Voltammetry, World Scientific Publishing (2007)

[30] P Atkins, J. Paula, *Physical chemistry* OUP Oxford, 7th ed. (2002)

[31] R. French, S. Gordeev, P. Raithby, F. Marken, J. Electroanal. Chem., 632 (2009) 206

[32] M. Barroso, A. Cowan, S. Pendlebury, M. Grätzel, D. Klug, J. Durrant, J. Am. Chem. Soc., 133 (2011) 14868

[33] S. Tilley, M. Cornuz, K. Sivula, M. Grätzel, Angew. Chem. Int. Ed., 49 (2010) 6405

[34] V. K. Sharma, J. Environ. Manage., 92 (2011) 1051

[35] G. Roelfes, V. Vrajmasu, K. Chen, R. Ho, J. Rohde, C. Zondervan, R. la Crois, E. Schudde, M. Lutz, A. Spek, R. Hage, B. Feringa, E. Munck, L. Que, Inorg. Chem., 42 (2003) 2639

[36] N. Eugster, H. Jensen, D. Fermin, H Girault, J. Electroanal. Chem., 560 (2003) 143

[37] N. Iordanova, M Dupuis, K. Rosso, J. Chem. Phys., 122 (2005) 144305

[38] U Björkstén, J. Moser, M. Grätzel J. Chem. Mater., 6 (1994) 858

Chapter 6

Electron Hopping Rate Measurements in ITO Junctions: Charge Diffusion in a Ruthenium-Bipyridyl-Phosphonate – TiO_2 Film

Contents

This work is published as:

C. Cummings, J. Wadhawan, T. Nakabayashi, M. Haga, L. Rassaei, S. Dale, S. Bending, M. Pumera, S. Parker, F. Marken, Journal of Electroanalytical Chemistry 657 (2011) 196–201.

6.1. Abstract

Focused ion beam (FIB) micromachining allowed a sub-micron trench to be cut through tin-doped indium oxide (ITO) film on glass to give a generator – collector junction electrode with narrow gap (ca. 600 nm). A layer-by-layer deposited film composed of a dinuclear bipyridyl-ruthenium(II)-phosphonate (as the negative component) and nanoparticulate TiO_2 (ca. 6 nm diameter, as the positive component) was formed and investigated first on simple ITO electrodes and then on ITO junction electrodes. The electrochemistry on the simple ITO electrodes revealed an immobilised oxidation/reduction signal at +0.92 V vs. SCE which corresponded to the $Ru^{II/III}$ redox couple. The charge transport within this film due to $Ru^{II/III}$ redox switching (electron hopping) was investigated using two different techniques. From the transition from a diffusion controlled signal to an immobilised controlled signal an apparent diffusion coefficient of D_{app} = 1.8 (+/- 1.0) × 10^{-15} m^2s^{-1} was obtained. By the immobilisation of the films into the ITO junction, bi-potentiostatic experiments obtained an apparent diffusion coefficient of D_{app} = 2.5 (+/- 1.0) × 10^{-15} m^2s^{-1}. It is assumed that the apparent diffusion coefficients are obtained with minimal contributions from intramolecular Ru-Ru interactions. The benefits of FIB-cut ITO junctions as a tool in determining charge hopping rates are highlighted.

6.2. Introduction

6.2.1. Nanotechnology and dye sensitised solar cells

Nanoparticulate films are now widely employed in sensors [1], solar cells [2], in electrocatalysis [3], and in other electrochemical devices [4]. The materials that are prepared on the nano-domain exhibit different properties to that of the bulk materials. In the case of sensors, nano-based devices have high surface area which allows for a high sensitivity. Dye-sensitised solar cells have features on the nano-domain as a nanoscale TiO_2 film is coated onto one of the electrodes. This mesoporous, interconnected and high surface area film has dye molecules absorbed into its surface allowing for the conversion of solar energy into electrical energy. Essentially, the dye molecule absorbs light becoming excited and undergoes a charge transfer reaction donating an electron to the mesoporous TiO_2. The electron travels through the TiO_2 network until it is injected into the electrode. As a consequence of this the Fermi energy of the electrode is raised. If the electrode is connected to a secondary (or counter) electrode then a redox mediator, in this case iodine, will be reduced (to tri-iodide) which in turn reduces the dye (figure 6.1).

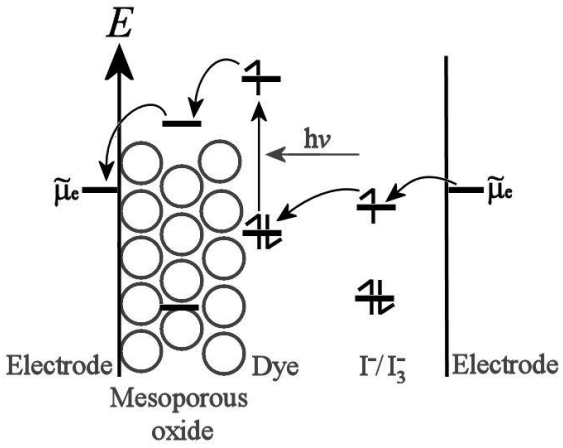

Figure 6.1: A schematic of a dye sensitised solar cell with the corresponding energy levels for the different materials present [5].

Interesting quantum confinement effects can be observed when preparing semiconducting particles or quantum dots. Here the absorption and emission spectrum of a quantum dot particle is altered allowing for the tuning of band gaps of devices [6,7].

Nano-composite films based on nanoparticles and appropriate binder molecules can be readily formed by the layer-by-layer deposition process [8]. From this reproducible deposition method the properties of the resulting films can be studied as a function of thickness (or the number of deposited layers [9]). One particularly interesting aspect of nanocomposite films for use in electrochemistry is the large surface area to volume ratio. Here the film's electrochemical reactivity is dominated by the surface signal and the ability of charges to propagate (or "hop") laterally across the nanoparticle surface. This is of high interest as the rate of propagation of charges across the surface of the material can be a rate determining step and hence controlling reactions [10,11]. In addition, interesting new effects are observed with redox active molecules between substrate electrode and nanoparticle acting as "gate" [12] and high speed conduction in surface redox systems with strong π-π interaction [13].

The measurement of the rate of charge propagation is commonly based on voltammetric or impedance methods as described in the previous chapter. In cyclic voltammetry diffusion-like transport of charges in nanoparticle networks is possible and for planar electrode geometries assuming semi-infinite diffusion the appropriate Randles-Sevcik equation can be employed [14].

$$i_{peak} = 0.446nFA[]_{Bulk}\sqrt{\frac{nFvD}{RT}} \qquad (6.1)$$

Above is the Randles-Sevcik equation, the i_{peak} is the peak current, n is the number of electrons in the A is the effective area of the electrode, D is the diffusion coefficient $[]_{Bulk}$ is the concentration of the bulk material and v is the scan rate. Assumptions such as the effective concentration of redox centres in the film limit the accuracy of this approach.

Impedance techniques can be employed [15] but these also encounter problems for example when the redox system concentration is required or when more complex diffusion conditions apply (e.g. anomalous diffusion in membranes [16]). Methods have been suggested where the transition from semi-infinite diffusion to finite diffusion is employed to further eliminate unknown experimental parameters [17]. Both chronoamperometry over a sufficiently long time [18] or cyclic voltammetry

over a wide range of scan rates [19] can be employed. A further experimentally convenient approach can be based on generator-collector electrode systems such as simple junctions [20,21] or interdigitaed arrays of band electrodes [22]. This latter method is particularly powerful since many unknown experimental parameters can be eliminated from the data analysis by choice of an appropriate inter-electrode gap size. In the study reported here a sub-micron generator-collector junction machined by focused ion beam (FIB) into an ITO electrode is employed.

6.2.2. Introduction to focused ion beam technologies

To understand the principles behind focused ion beam it is first needed to understand SEM, scanning electron microscopy. SEM is an instrument that focuses beam of high energy electrons onto a sample through a vacuum. The beam is scanned (rastered) across the surface and the collection and amplification of backscattered or emitted electrons from the surface allow for an image to be attained. The interaction of the electrons with the sample can give information about the microstructure features such as electric or magnetic fields, composition variations, crystal orientation and electron-fluorescent phases [23].

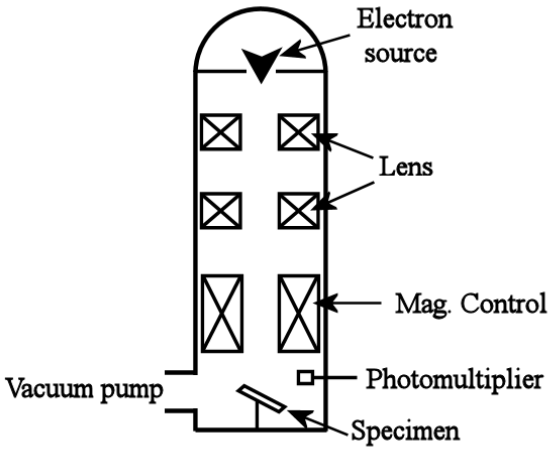

Figure 6.2: A schematic of a scanning electron microscope.

Focus ion beam apparatus operates under similar principles as a scanning electron microscope however instead of a focused beam of electrons it uses a beam of

focused ions. In addition the ions have such a high energy that from collision with the surface that they can locally remove/deposit material. This gives rise to the applications in micro-machining which include: micro-milling and micro-construction. The emission of secondary ions and electrons allows for surface imaging. The different modes of focused ion beam use is shown in figure 6.3

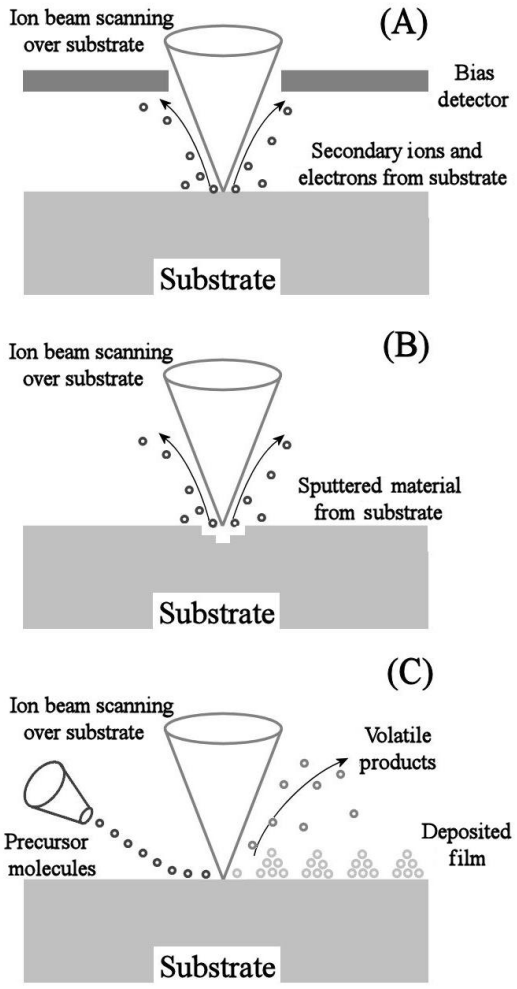

Figure 6.3: Modes of focused ion beam, (A) imaging morphology, (B) micro etch a substrate and (C) construct micro architectures by decomposition an absorbed precursor molecule.

There are some drawbacks when using focused ion beam based techniques as the most significant problem is the structural damaged incurred from the high energy ions impacting the surface (even in imaging mode). Examples of the potential detrimental effect include the conversion of crystalline silicon into amorphous silicon and the creation of dislocation loops on the surface of steels [23]. There are

different sources of the ions used in focused ion beams each with there own advantage and disadvantage.

6.2.3. Introduction to the ruthenium based electrochemistry

Ruthenium-based compounds have reversible electrochemistry as well as exhibiting interesting photochemistry. These readily manipulated properties have lead to ruthenium-based organic systems being proposed as key components in molecular electronics. A number of ruthenium-based compounds have been synthesized and studied from monomers to dimers [24,25,26] to higher oligomers [27].

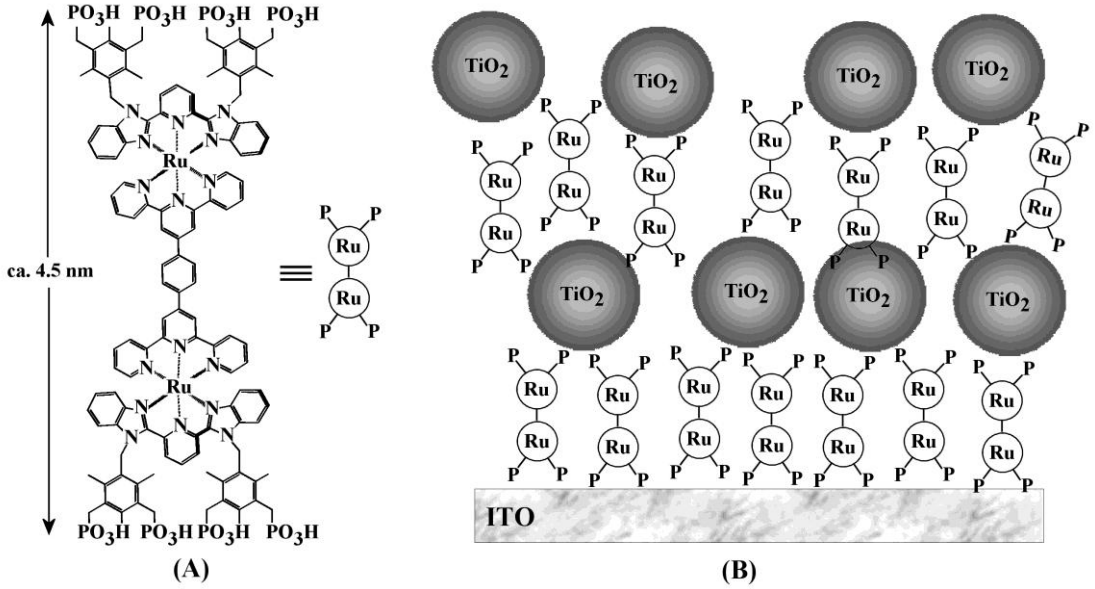

Figure 6.4: (A) Molecular structure of the dinuclear ruthenium(II)-bis(benzimidazolyl)pyridine phosphonate. (B) Schematic drawing of a 2-layer Ru_2 – TiO_2 film deposit on ITO.

The electrochemical system studied here is based on a dinuclear ruthenium(II)-bis(benzimidazolyl)pyridine phosphonate complex, Ru_2, [28] (see figure 6.4A). This type of metal complex very readily binds to metal oxides (such as ITO or TiO_2) due to the phosphate groups located on each ends of the molecule. The electrostatic layer-by-layer deposition method [8] is employed to produce well-defined films of the nano-composite structure (see figure 6.4B).

Charge propagation in films of bipyridyl-ruthenium(II)-phosphonate – TiO_2 films follows a reactivity pattern known for similar structures [12]. With TiO_2 acting as insulating backbone, the $Ru^{II/III}$ redox centers act as paths for electron hopping conduction. For the nanocomposite films shown in figure 6.4, the presence of two distinct $Ru^{II/III}$ redox systems in each molecule (figure 6.5A and 6.5B) should lead to two distinct diffusion coefficients for the charge hopping processes.

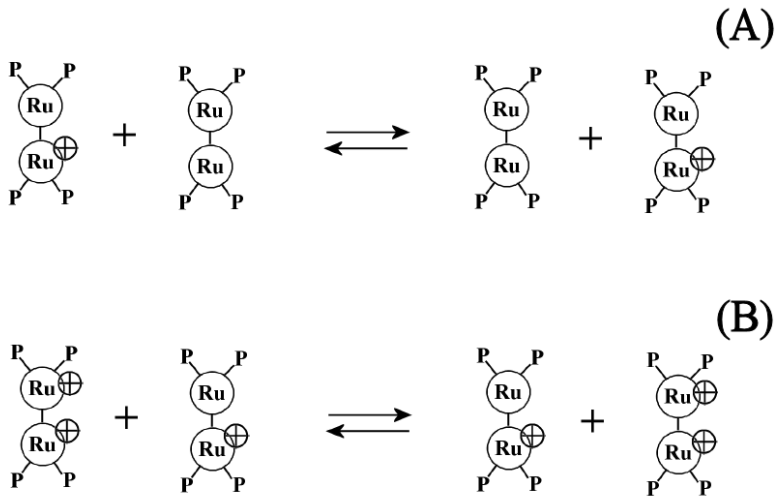

Figure 6.5: Simplified diagrams of two ruthenium dimers in close proximity to each other. (A) and (B) show different conductivity mechanisms proposed for the charge propagation of electrons from one ruthenium dimer to another.

If there is only a weak intramolecular reaction between the ruthenium centres then the processes 6.5A and 6.5B cannot be distinguished (as this would appear as a single signal). A single apparent diffusion coefficient would describe the charge transport process.

In this chapter the preparation of films similar to that of dye sensitised solar cells are prepared. The charge hopping processes between Ru centres is investigated and characterised. Although this mechanism different from the charge propagation in illuminated dye-sensitise solar cells it is nonetheless interesting to investigate for applications in molecular electronics. The charge transport can be described in good approximation by a single apparent diffusion coefficient using FIB prepared junction electrodes. This preliminary work using junction electrodes opens opportunities for experiments to measure the charge transport of more complex systems such as illuminated dye-sensitised solar cells.

6.3. Experimental Details

6.3.1. Reagents

The solutions ammonia (LRG) and HCl (32% LRG) were brought from Fischer Scientific and $HClO_4$ (ACS grade), L-(+)-tartaric acid (ACS grade), oxalic acid dehydrate (ACS grade) were purchased from Sigma Aldrich and used without further purification. 35 %w/w Titania sol (TKS-202) was purchased from Tayca Corporation. Di-nuclear bipyridyl-ruthenium(II)-phosphonate metal complexes or Ru_2 were provided by Haga *et al.* [29]. Demineralised and filtered water was taken from an Elgastat water purification system (Elga, High Wycombe, Bucks) with a resistivity of not less than 18.2 M Ohm cm.

6.3.2. Instrumentation

For voltammetric studies a microAutolab II potentiostat system (EcoChemie, Netherlands) was employed with a Pt gauze counter electrode and a KCl-saturated Calomel (SCE) reference electrode (Radiometer, Copenhagen). Junction measurements were performed with an Autolab PGSTAT12 bipotentiostat system. An Elite tube furnace was used for cleaning ITO electrodes at 500 ^{o}C in air followed by re-equilibration of the ITO electrodes to ambient conditions for at least 12h. Experiments were performed at T = 20 +/- 2 ^{o}C within a Faraday cage and in the dark. Atomic force microscopy (AFM) images were obtained with an Asylum Research MFP-3D stand alone microscope (tips were AC240TS from Olympus, images were obtained in tapping mode). To determine the thickness of the films AFM profiles of contrasting locally removed deposits (attained by scratching) and deposited material were obtained.

6.3.3. Layer-by-layer assembly of Ru_2-TiO_2 films

A solution containing 100 μM of the dinuclear ruthenium(II)-bis(benzimidazolyl)pyridine phosphonate complex, Ru_2, was prepared by dissolving solid crystals in aqueous 0.05 M ammonium hydroxide solution. HCl was used to

adjust the proton activity to pH ≈ 6. This solution was kept in the dark and at 5 ^{o}C. First Ru_2 was adsorbed directly onto an ITO slide to form a redox active film. The film thickness was increased using a layer-by-layer method with Ru_2 (negative binder) and 3 wt% TiO_2 nanoparticles of ca. 6 nm diameter (positive backbone). Electrodes were immersed in a TiO_2 solution for 1 minute rinsed and dried and then immersed into the Ru_2 solution for 4 minutes followed by rinsing and drying.

6.3.4. Preparation for junction electrode experiments

Generator – collector experiments were performed at ITO electrodes. Initially, electrodes were patterned by masking off a "U" pattern (Kel-F tape). ITO etching was then carried out in 1 wt.% tartaric acid and 3 wt.% oxalic acid solution at 35˚C for approximately 20 minutes [30]. The resulting ca. 1 mm wide ITO line (vide infra) was then carefully cut with a focused ion beam (FIB: Ga liquid metal ion source (LMIS), 30 kV, 50 pA ion beam for making a 1 micron deep trench; SEM: Carl Zeiss XB1540) resulting in a ca. 600 nm wide gap or junction. Prior to electrochemical experiments these junction electrodes were cleaned by rinsing with water and ethanol, drying, 30 minutes 500 ^{o}C in air, and re-equilibration to ambient conditions. A typical image of the junction is shown in figure 6.6. The gap size is approximately 600 nm wide and the trench is approximately 1 μm deep with an ITO film of ca. 400 nm thickness. For electrochemical experiments insulating paste was applied to the ITO junction exposing only 4 x 1 mm^2 rectangle of the ITO with the junction approximately in the middle.

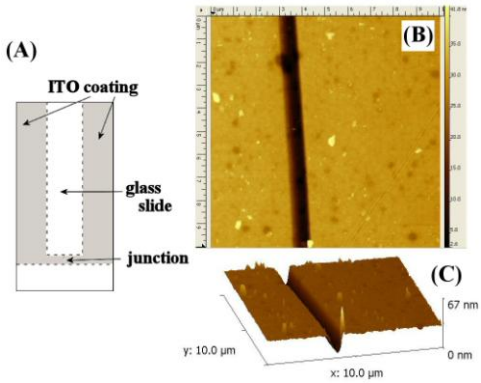

Figure 6.6: (A) Sketch depicting the etched ITO electrode. (B) Topography images and (C) side view of the FIB junction at high resolution taken with an AFM.

6.4. Results and Discussion

6.4.1. Voltammeric characterisation of layer-by-layer films of Ru_2 - TiO_2: formation and characterisation

Initially, a monolayer of Ru_2 was adsorbed onto ITO and investigated by AFM. The surface (see figure 6.7A) shows a smooth, highly dense film with some smaller features approaching the size of individual molecules. The topology of the ITO is superimposed onto the film (e.g. appearance of the grain boundaries). When combined with layers of TiO_2 nanoparticles (figure 6.7B) individual TiO_2 particles can be distinguished. For thicker multi-layer films a clear growth of a composite film occurs with ca. 12 nm per Ru_2 – TiO_2 layer (see figure 6.7E). UV-visible spectra for the absorption band at 520 nm wavelength (in figure 6.7F) are consistent with layer-by-layer film growth.

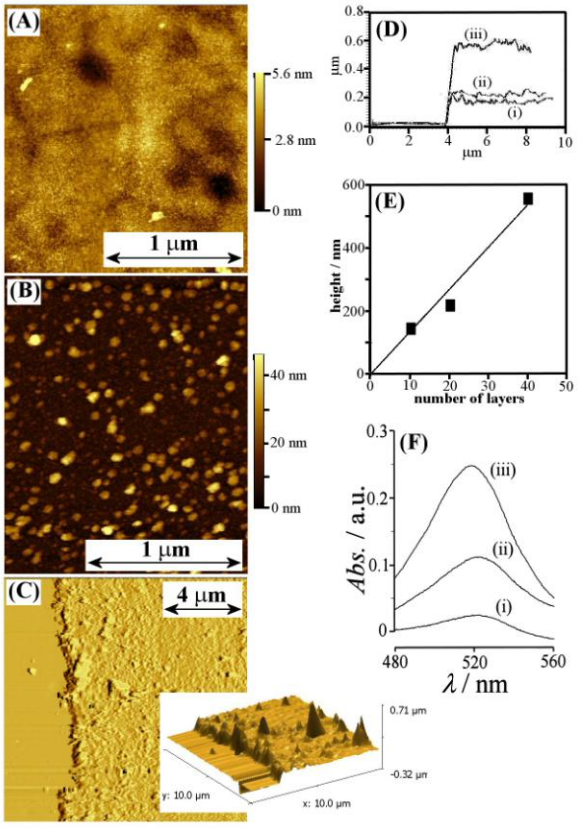

Figure 6.7: (A) AFM topography image of an ITO substrate surface with a monolayer of Ru_2. (B) AFM topography image of a Ru_2 and a TiO_2 layer adsorbed onto ITO. (C) AFM topography image of a scratched 10-layer Ru_2 - TiO_2 film. (D) Cross-section data for (i) 10-layer, (ii) 20-layer, and (iii) 40-layer Ru_2 - TiO_2 composite films. (E) Plot of thickness data versus number of layers. (F) UV-visible spectra for Ru_2 - TiO_2 composite films: (i) 10-layer, (ii) 20-layer, and (iii) 40-layer.

6.4.2. Voltammeric characterisation of layer-by-layer films of Ru_2 - TiO_2: ITO film electrodes

Electrochemical experiments were performed on the various Ru_2–TiO_2 films in a 0.1 M $HClO_4$ electrolyte. The acidic nature of the electrolyte (ca. pH 1) allows for the electrochemical evaluation of redox processes occurring at positive potentials. This is because of the positive nernstian shift in the onset of water oxidation at the electrode surface. Below in figure 6.8A are cyclic voltammograms of different thickness of nanocomposite Ru_2-TiO_2 films in 0.1 M $HClO_4$ electrolyte.

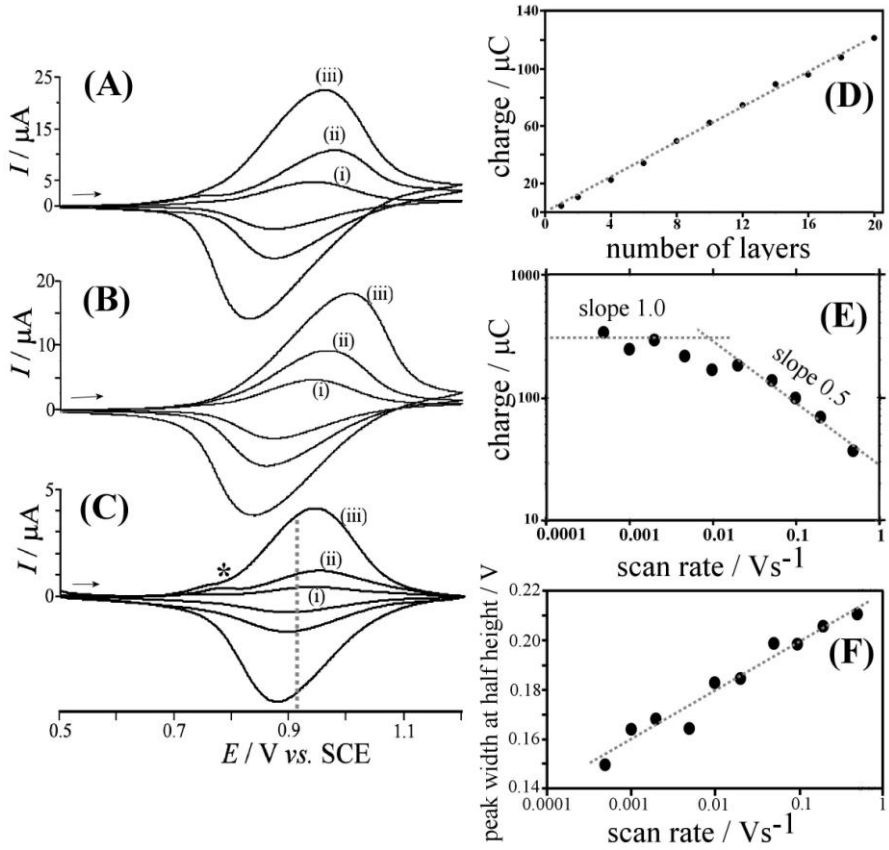

Figure 6.8: (A) Cyclic voltammograms (scan rate 5 mVs^{-1}, area 1 cm^2) for the oxidation of immobilised Ru_2 – TiO_2 films immersed in aqueous 0.1 M $HClO_4$ for (i) a 10-layer, (ii) a 20-layer, and (iii) a 40-layer deposit. (B) Cyclic voltammograms (scan rate (i) 5 mVs^{-1}, (ii) 10 mVs^{-1}, and (iii) 20 mVs^{-1}) for a 10-layer Ru_2 – TiO_2 film. (C) Cyclic voltammograms (scan rate (i) 1 mVs^{-1}, (ii) 2 mVs^{-1}, and (iii) 5 mVs^{-1}) for a 10-layer Ru_2 – TiO_2 film. (D) Plot of charge under the oxidation peak versus the number of layers deposited. (E) Plot of peak charge versus scan rate for a 10-layer Ru_2 - TiO_2 film. (F) Plot of peak width at half height versus scan rate.

Figure 6.8Ai displays the cyclic voltammogram recorded for a 10 layer of the Ru_2 - TiO_2 film in 0.1 M $HClO_4$. A reversible oxidation and re-reduction signal is observed at a potential of E_{mid} = +0.92 V vs. SCE. Despite the reversible nature of the immobilised film a slight shift in the $E_{peak\ ox}$ and $E_{peak\ red}$ away from the E_{mid} indicates that the electron transfer process is slow. A minor, pre-peak present at E_{mid} = +0.75 V vs. SCE is due to the presence of a monomer and is present in all cyclic voltammograms. The charge for the $Ru^{II/III}$ increases when thicker films are investigated (ca. figure 6.8Aii and 6.8Aiii) and a plot of thickness versus charge shows a linear dependence (figure 6.8D). From the plot in figure 6.8D a monolayer charge of 6 μC cm^{-2} consistent with a molecular "footprint" of ca. 10 Å × 10 Å is obtained. This suggests a dense film of Ru_2 on the electrode surface possibly stacked or interacting which is consistent with the AFM image (figure 6.7A). The peak-to-peak separation for oxidation and reduction of the $Ru^{II/III}$ also increases as the thickness of the Ru_2-TiO_2 film increases.

Voltammetric responses obtained over a range of scan rates suggest a transition between semi-infinite and finite charge hopping diffusion (see figure 6.8E). A rough estimate for the apparent charge diffusion coefficient in Ru_2 – TiO_2 can be obtained from the transition point, when considering the transition from linear to square root dependence of peak current on scan rate. This can be done by relating this transition from diffusion controlled kinetics (equation 6.1) to equation 6.2 which describes the peak current for immobilised species [17].

$$I_{peak} = \frac{n^2 F^2}{4RT} v A \delta_{film} [\,]_{film} \qquad (6.2)$$

Here, δ_{film} is the film thickness and $[\,]_{film}$ is the concentration of the electrolyte in the film. At the transition of peak current immobilised to diffusion controlled it is possible to equate equations 6.1 and 6.2 giving equation 6.3 which is true for the scan rate that causes the transition.

$$D_{app} = \frac{v_{trans} F}{RT} \left(\frac{\delta_{film}}{1.784} \right)^2 \qquad (6.3)$$

The apparent charge diffusion coefficient is estimated as D_{app} = 1.8 (+/- 1.0) × 10^{-15} $m^2 s^{-1}$ using equation 6.3 (with the film thickness δ_{film} = 120 nm for a 10-layer film, *F*

the Faraday constant, R the gas constant, T = 293 K, and the transition scan rate approximately 0.01 Vs^{-1}). The apparent diffusion coefficient is low compared to some organic redox systems with extended π-electron systems where the apparent diffusion coefficient can reach $D_{app} = 10^{-9}$ m^2s^{-1} and higher [13]. A complicating factor in this analysis is the presence of some uncompensated iR potential drop in the ITO film electrode.

Based on this estimate, it is possible to evaluate the Dahms-Ruff diffusion parameters [31,32,33] assuming that no physical movement of the ruthenium diffusion occurs) using equation 6.4.

$$k_{SE} = \frac{6D_{app}}{\delta_{Ru-Ru}{}^{2}[]_{film}} \qquad (6.4)$$

Where $\delta_{Ru\text{-}Ru}$ is the average distance between Ru – Ru redox sites (here ca. 8Å), D_{app} is the apparent rate constant and k_{SE} the self-exchange rate constant (here unknown). A self-exchange constant of $k_{SE} = 0.7$ $mol^{-1}dm^3s^{-1}$ is attained which is low and probably due to the rigid nature of the immobilised ruthenium redox centres.

A plot of the peak width at half height versus scan rate is shown in figure 7.9F. At a slow scan rate finite diffusion is observed, this parameter is expected to converge to equation 6.5 [34] which is 89 mV or 45 mV for a one-electron or two-electron process, respectively

$$\Delta E_{PWHH} = 3.53\frac{RT}{nF}. \qquad (6.5)$$

The experimental value of ca. 150 mV attained at the lowest scan rate employed is likely to be caused by two closely separated one-electron redox systems as well as some additional broadening from uncompensated iR potential drop and possibly weak inter-molecular interactions.

6.4.3. Voltammeric characterisation of layer-by-layer films of Ru_2 - TiO_2: ITO junction electrodes

In order to obtain further experimental evidence for the apparent diffusion rate for electrons in the Ru_2 – TiO_2 film, an ITO junction [20,21] was employed. In this experiment on one side of the junction (generator) the potential is scanned whereas on the opposite side (collector) a constant potential is applied. Mobile intermediate species that can diffuse from one side of the gap to another can be sensed using this technique.

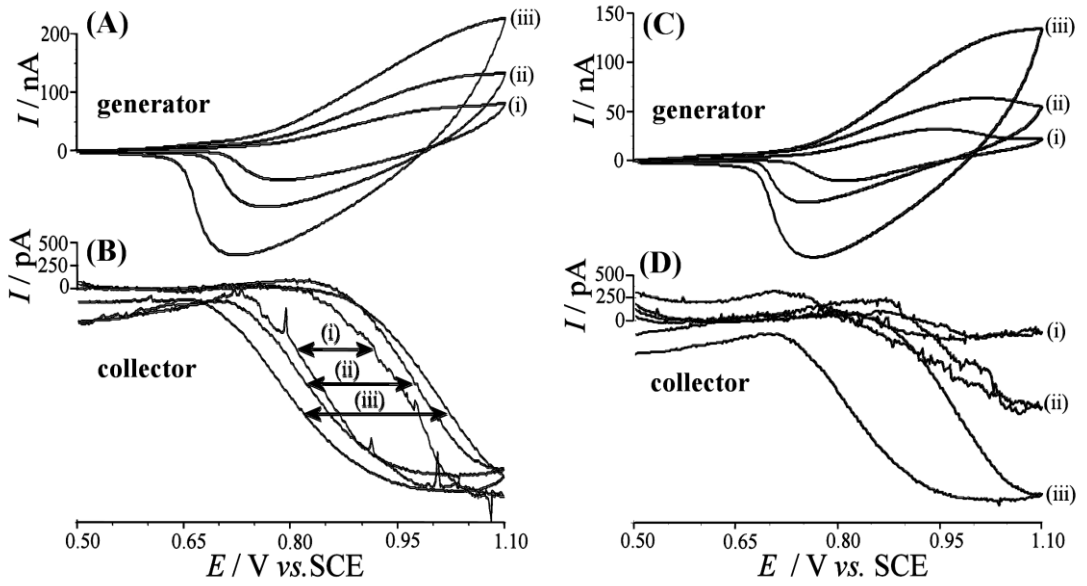

Figure 6.9. (A) Generator and (B) collector voltammograms (scan rate (i) 0.5 mVs^{-1}, (ii) 1 mVs^{-1}, and (iii) 5 mVs^{-1}) for a 40-layer Ru_2 - TiO_2 film immobilised in the ITO junction and immersed in aqueous 0.1 M $HClO_4$. The generator potential scanned from +0.5 to +1.1 V vs. SCE and the collector potential was held at +0.5 V vs. SCE. (C) Generator and (D) collector voltammograms (scan rate 1 mVs^{-1}) for (i) a 10-layer, (ii) a 20-layer, and (iii) a 40-layer Ru_2 - TiO_2 film.

In figure 6.9 the generator current response can be seen to increase with scan rate and with film thickness. The corresponding collector current signal is opposite in sign (reduction during generator oxidation) and much smaller in magnitude. In fact, the generator signal is essentially independent of whether the collector is active or not due to the small magnitude of the feedback current across the ITO junction. The most interesting parameter in the collector current response is the hysteresis parameter (see figure 6.9B). For an ideal junction with fast transport (steady state

conditions) this parameter should approach zero. For the case that diffusional transport (approximately one dimensional) occurs, a simplified expression equation based on the hysteresis parameter was developed by Vuorema *et al* [35]. Equation 6.6 is taken from the report and can be used to obtain an estimate for the apparent diffusion coefficient D_{app}.

$$\Delta E_H = 0.0071 \times \frac{v\delta^2 F}{D_{app} RT} \tag{6.6}$$

In figure 6.9A it can be seen that the hysteresis parameter ΔE_H indeed decreases with lower scan rate, however, the value is strongly affected by the uncompensated iR potential drop. Data in figure 6.9B demonstrate the effect of the film thickness with thinner films (lower generator currents) being less strongly affected. ΔE_H for the 10-layer film is approximately 40 +/- 10 mV, which allows the apparent diffusion coefficient to be estimated as:

$$D_{app} = 0.0071 \times \frac{v\delta_{junction}^{\ 2} F}{\Delta E_H RT} = 2.5\ (+/-\ 1.0) \times 10^{-15}\ \mathrm{m^2 s^{-1}} \tag{6.7}$$

This value is in good agreement with the estimate obtained from the transition from semi-infinite to finite diffusion (shown above). This estimate is likely to be on the slow side and the true apparent diffusion coefficient is probably slightly higher (due to effects of some uncompensated iR potential drop). However, the ITO junction methodology appears to be powerful and useful for the investigation of similar thin film nano-composite deposits. In future, the junction mechanism may also be employed in sensors based on charge hopping rates.

6.5. Conclusions

It has been shown that FIB machined ITO junction electrodes are suitable for layer-by-layer deposition of redox active nano-composite films. The apparent diffusion coefficient for charge hopping processes can be measured with good accuracy and without the need for information about the concentration of the redox species or the film thickness. A Ru_2 - TiO_2 nanocomposite film was investigated where the movement of charge was govern by the hopping (or diffusion) of $Ru^{II/III}$ species through the film. For this Ru_2 – TiO_2 system the apparent diffusion co-efficient was calculated to be D_{app} = 1.8 (+/- 1.0) × 10^{-15} m^2s^{-1} and D_{app} = 2.5 (+/- 1.0) × 10^{-15} m^2s^{-1} using two different techniques. The first apparent diffusion coefficient was attained using dimensional analysis where the transition from diffusion controlled to immobilised controlled cyclic voltammograms allowed to attain an estimate for the diffusion coefficient. The second value was the immobilising the material in the ITO junction and studying its electrochemistry using the hysteresis present in the generator and collector currents. The hysteresis parameter is linked mainly to scan rate, diffusion coefficient, and gap width. Uncompensated iR potential drop causes a considerable distortion of data in this experiment and improvements in the junction design and the experiment will be required in future to improve data quality.

6.6. References

[1] C. Welch, R. Compton, Anal. Bioanal. Chem., 384 (2006) 601

[2] L. Peter, Phys. Chem. Chem. Phys., 9 (2007) 2630

[3] Y. Park, T. Kim, S. Park, J. Mater. Chem., 20 (2010) 3637.

[4] N. Sanvicens, C. Pastells, N. Pascual, M.P. Marco, TRAC-Trends Anal. Chem. 28 (2009) 1243.

[5] B. O'Regan, M. Grätzel, Nature, 335 (1991) 737

[6] I. Kramer, E. Sargent, ACS Nano., 5(2011) 8506

[7] J. Smyder T. Krauss, Mat. Today, 14 (2011) 382

[8] G. Decher, J. Schlenoff, *Multilayer Thin Films*, Wiley-VCH (2003)

[9] E. Milsom, H. Perrott, L. Peter, F. Marken, Langmuir, 21 (2005) 9482

[10] C. Cummings, F. Marken , L. Peter , K. Wijayantha , A. Tahir, J. Am. Chem. Soc., 134 *(*2012) 1228

[11] P. Bonhote, E. Gogniat, S. Tingry, C. Barbe, N. Vlachopoulos, F. Lenzmann, P. Comte, M. Grätzel, J. Phys. Chem. B, 102 (1998) 1498

[12] A. Fattori, L. Peter, S. Belding, R. Compton, F. Marken, J. Electroanal. Chem., 640 (2010) 61

[13] A. Fattori, L. Peter, H. Wang, H. Miura, F. Marken, J. Phys. Chem. C, 114 (2010) 11822

[14] Q. Wang, S. Zakeeruddin, M. Nazeeruddin, R. Humphry-Baker, M. Grätzel, J. Am. Chem. Soc., 128 (2006) 4446

[15] J. Bisquert, J. Electroanal. Chem., 646 (2010) 43

[16] G. Kumara, K. Murakami, M. Shimomura, K. Velauthamurty, E. Premalal, R. Rajapakse, H. Bandara, J. Photochem. Photobiol. A- Chem., 215 (2010) 1

[17] E. Milsom, J. Novak, S. Green, X. Zhang, S. Stott, R. Mortimer, K. Edler, F. Marken, J. Solid State Electrochem., 11 (2007) 1109

[18] R. Forster, L. Keane, J. Electroanal. Chem., 554 (2003) 345

[19] R. French, S. Gordeev, P. Raithby, F. Marken, J. Electroanal. Chem., 632 (2009) 206

[20] S. Shariki, S. Liew, W. Thielemans, D. Walsh, C. Cummings, L. Rassaei, M. Wasbrough, K. Edler, M. Bonné, F. Marken, J. Solid State Electrochem., 15 (2011) 2675

[21] C. Cummings, G. Attard, J. Mitchels, F. Marken, Aust. J. Chem., 65 (2012) 65

[22] M. Leopold, R. Donkers, D. Georganopoulou, M. Fisher, F. Zamborini, R. Murray, Farad. Disc., 125 (2004) 63

[23] D. Brown, *Microscopy of Materials*, Hall, C. R., Ltd (1975)

[24] C. Arana, H. Abruña, Inorg. Chem., 32 (1993) 194

[25] Y. Zhong, S. Wu, S. Burkhardt, C. Yao, H. Abruña, Inorg. Chem., 50 (2011) 517

[26] K. Kobayashi, M. Ishikubo, K. Kanaizuka, K. Kosuge, S Masaoka, K. Sakai, K Nozaki, M Haga, J. Eur. Chem., 17 (2011) 6954

[27] S. Flores-Torres, G. R. Hutchison, L. Soltzberg, H. Abruña, J. Am. Chem. Soc., 128 (2006) 1513

[28] M. Haga, T. Takasugi, A. Tomie, M. Ishizuya, T. Yamada, M. Hossain, M. Inoue, Dalton Trans., 10 (2003) 2069

[29] T. Ishida, K. Terada, K. Hasegawa, H. Kuwahata, K. Kusama, R. Sato, M. Nakano, Y. Naitoh, M. Haga, Appl. Surf. Sci., 255 (2009) 8824

[30] T. Tsai, Y. Wu, J. Electrochem. Soc., 153 (2006) C86

[31] H. Dahms, J. Phys. Chem., 72 (1968) 362

[32] I. Ruff, V. Friedrich, K. Demeter, K. Csillag, J. Phys. Chem., 75 (1971) 3303

[33] L. Keane, C. Hogan, R. Forster, Langmuir, 18 (2002) 4826

[34] A. Bard, L. Faulkner, *Electrochemical Methods*, 2nd ed., Wiley (2001)

[35] A. Vuorema, H. Meadows, N. Bin Ibrahim, J. Del Campo, M. Cortina-Puig, M. Vagin, A. Karyakin, M. Sillanpää, F. Marken, Electroanalysis, 22 (2010) 2889

Chapter 7

Conclusions and Outlook

Contents

7.1. Conclusions

This thesis has documented a variety of topics associated with the harvesting of solar energy for photovoltaic devices. The first experimental chapter documented the preparation and use of a chemically inert material, Mo/$MoSe_2$ for use as a substrate in solar cells. Here, molybdenum films were selenised before the deposition of the CISe absorber material. The Mo/$MoSe_2$ electrodes are shown to be chemically stable and electronically degenerate in nature. The formation of photoactive CISe films on the Mo/$MoSe_2$ electrodes suggests that this substrate could be used in the manufacturing of CISe devices. This is particularly attractive for deposition methods that degrade the quality of the molybdenum back contact.

Chapter 3 documented the use of the rocking disc electrode for the electroformation of large area (ca. 12.1cm^2) films. The rocking disc electrode, rocks or vibrates the cell to induce convection to the electrode surface. Experiments using $Ru(NH_3)_6^{3+}$ allowed the magnitude of convection as a function of position to be investigated. The magnitude was similar regardless of position and the direction of flow was found to occur from the centre of the cell, outwards. The electrodeposition of copper onto Mo/$MoSe_2$ substrates was undertaken under rocking disc conditions and XRD and SEM analysis revealed a very regular deposit free from pits and pores.

Chapter 4 expanded on chapter 3 as uniform CuIn films were electrodeposited within the rocking disc electrode as precursors for CISe films. CuIn films were formed from a tartrate based plating bath onto Mo substrates. The electrochemistry of the bath exhibited distinct reductions for Cu and In and a 1:1 ratio film was easily attained under rocking disc electrodeposition conditions. The selenisation of the CuIn films produced CISe films which had a non-uniform photoactivity which is due to the presence of either Cu_xSe or pin holes within the CISe film. CISe films were exposed to various chemical treatments increase the photoactivity and the uniformity. Diluting the KCN etchant concentration from 5 %w/w to 0.5 %w/w decreased the rate of removal of Cu_xSe from the surface, allowing for a higher process control. By re-annealing the same over-etched film and etching it once again, the photoactivity and uniformity improved. The use of an oxidising etchant in conjugation with the KCN etchant (5 %w/w) was also performed. HClO 5 %w/w was used to form oxides on an over-etched CISe film. The subsequent use of the KCN etch removed the

oxides giving a pristine CISe surface which also gave a high photoactivity and uniformity.

Chapter 5 investigated mesoporous iron oxide electrodes for use in water splitting. The films were prepared from a colloid solution containing 2 nm (radius) hydrous iron oxide particles. The nanoparticles were immobilised using the layer-by-layer technique in conjugation with a polyanion. Films were calcined to give a purely mesoporous iron oxide thin film. The high surface area of the film meant that surface processes could be monitored using electrochemistry and in particular spectro-electrochemistry. The films were investigated using potential modulated spectroscopy and a highly defined spectra of a long lived intermediate the α-Fe_2O_3 | electrolyte was attained. This potential induced intermediate is related to the photo-electrochemical process as light induced absorbed spectroscopy produced similar spectra.

Documented in chapter 6 is the investigation of films composed of a dinuclear bipyridyl-ruthenium(II)-phosphonate (Ru_2) species and TiO_2 nanoparticles. The electrochemistry is dominated by an immobilised $Ru^{II/III}$ signal. A new methodology of measuring charge transfer properties is reported as a focused ion beam was used to prepare trenches in ITO electrodes. Immobilisation of the nanocomposite film within the trench allowed the study of diffusion processes by bi-potentiostatic, generator-collector methods. A diffusion coefficient of D_{app} = 2.5 (+/- 1.0) × 10^{-15} m^2s^{-1} was attained for this system using this method.

7.2. Further Work

There are a number of different areas that can be explored. The versatile and inert nature of $MoSe_2$ electrodes is attractive. Materials such as nanoparticles can be immobilised onto Mo films and undergo selenisation to create new composites. The electrochemistry can be investigated with the knowledge that interference effects from $MoSe_2$ will be minimal. The intercalation of elements into the $MoSe_2$ structure would have to be taken into consideration. Large area rocking disc electrodeposition of other relevant photovoltaic materials can be investigated such as Cu-Sn-Zn films which are precursors to the sustainable, indium-free $Cu_2ZnSnS(e)_4$ absorber layer.

An in depth examination and characterisation of the re-anneal and oxidising etch treatments on CISe films would be interesting and may give insights into the chemical action. Techniques such as x-ray photoelectron spectroscopy (XPS) or scanning microwave microscopy-atomic force microscopy (SMM-AFM) would elude the surface compositions.

Spectro-electrochemical studies on mesoporous iron oxide electrodes with various catalysts immobilised onto the surface may give interesting and unexpected insights into the oxidation of water. The catalyst should decrease the lifetime of the observed surface state as it promotes its decomposition to react with water. Relative rates maybe attained via the spectro-electrochemical methods presented.

ITO junction electrodes are potentially a useful tool in the analysis of nanocomposite thin films. The immobilisation of other nanocomposite thin films into the junction will give insights into the conduction processes that can occur. This is particularly important for nanoparticles were there is often a competition between bulk and surface transport which can be hard to measure. Depending on the relative rates it maybe be possible to distinguish between the two processes.

Appendix

A. Theoretical Electrochemical Basis

A.1. Introduction to Electrochemistry

Electrochemistry is the study of chemical reactions under the influence of electricity. This board description has lead to electrochemistry having a diverse range of applications ranging from chemical sensors to film formation to chemical synthesis. The topic of electrochemical sensors is highly researched as this varies from the detection of low levels analyte to highly obscure analytes and unusual media [1]. Key examples of commercialised electrochemistry include: the production of inorganic chemicals (sodium chlorate, potassium permanganate, manganese dioxide, potassium dichromate and chromic oxide), [2] as well as sensing applications such as heavy metal detection in aqueous environments [3] to glucose sensors for diabetics [4]. In the material science industry it is possible to use electrochemistry to coat substrates in both metals and semiconductors using electrodeposition.

The history of electrochemistry begins from the 1800s whereby Alexander Volta is credited with creating the first battery, the volta pile. Since then various pioneering scientists in the field such as: Humphry Davy, Michael Faraday, Walter Nernst, Julius Tafel and Jaroslav Heyrovky have contributed greatly to the field of electrochemistry.

In electrochemistry the most typical reaction is the one between an electrode and a dissolved species in solution. The site where the electrochemical reaction takes place is the electrode surface and there are five key parameters that any one of which can be the rate determining step. These are shown below in figure A.1.

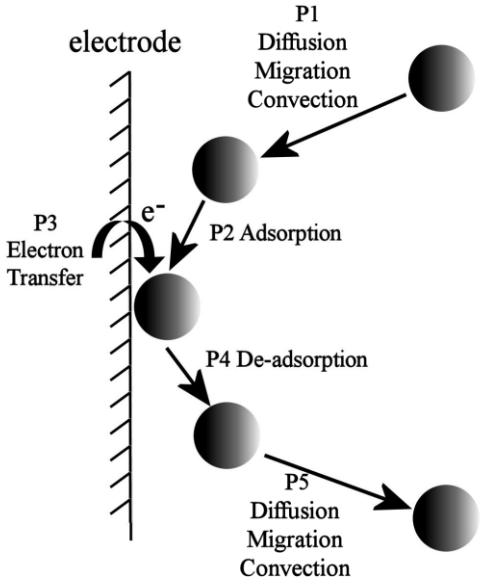

Figure A.1: The five processes that can determine the rate determining step for electrochemical reactions at the electrode | electrolyte interface. The redox active couple analyte is represented by the dark spheres.

Process 1 is the diffusion, migration or convection of an electrochemically active species to the surface of the electrode. Process 2 is the adsorption of a analyte onto the surface of the electrode. Process 3 is a chemical reaction where an electron can transfer to or from the electrode surface which is dependant on both the electrochemical potential of the electrode surface and the analyte. The de-adsorption of the product is process four and the movement of the product away from the electrode is described by process five. In theory any of these processes can be the rate determining step.

These processes are not trivial to explain and credit should be cited to the pioneering chemists/physicists namely W. Nernst, A. Fick, G. Levich, M. Volmer and D. Marcus who investigated these phenomenon. To begin with an explanation of the chemical thermodynamics of electrochemical systems will be elucidated.

A.2. Chemical equilibria and chemical potential

At the heart of electrochemistry is thermodynamics and kinetics which explain the extent (at equilibrium) and rate of reaction (how quickly equilibrium is attained) respectively. In electrochemistry thermodynamics is usually expressed in the form of

the famous Nernst equation. Before discussing electrochemical thermodynamics it is necessary to examine the origin of chemical equilibria and electric potential. The concept of chemical equilibrium for a reaction was first introduced by Le Chatelier and can be applied to any chemical or electrochemical equilibrium [5], equation A.1 demonstrates a theoretical chemical reaction.

$$A(aq) + B(aq) \rightleftharpoons 2C(aq) \tag{A.1}$$

In this hypothetical reaction, reactants $A(aq)$ and $B(aq)$ are converted to product $C(aq)$ by a forward bi-molecular reaction. This process can be reversed as species $C(aq)$ can decompose into $A(aq)$ and $B(aq)$ via a back reaction. At constant temperature and pressure thermodynamics explains the extent of reaction (the position of equilibrium) which is dependant upon the chemical potential of each species present. Below in equation A.2 is the mathematical expression of chemical potential for species j where μ_j is chemical potential (kJmol^{-1}), G is Gibbs free energy (kJmol^{-1}), n_j is the number of moles of species j (mol^{-1}), T is the absolute temperature (K) and n_{Total} is the total number of moles of the species concerned with the reaction.

$$\mu_j = \left(\frac{\partial G}{\partial n_j} \right)_{T, n_j \neq n_{Total}} \tag{A.2}$$

The change in Gibbs free energy for the reaction in question, $\Delta G_{Reaction}$, is given as the sum of the chemical potentials of the products minus the sum of the chemical potential of the reactants, as demonstrated by equation A.3.

$$\Delta G_{Reaction} = \sum_{Products} \nu_i \mu_i - \sum_{Reactants} \nu_i \mu_i \tag{A.3}$$

At equilibrium the change in Gibbs free energy is zero inferring that the system has reached an energy minimum. As a consequence the chemical potential of the reactants should equal that of the products as described by equation A.5

$$0 = \Delta G_{Reaction} = 2\mu_C - (\mu_A + \mu_B) \tag{A.4}$$

$$\mu_A + \mu_B = 2\mu_C \tag{A.5}$$

Using species j as an example, chemical potential can elaborated into the standard chemical potential of species j, μ_j^o, and a concentration dependence term as shown in equation A.6. Where R is the gas constant (8.314 $Jmol^{-1}K^{-1}$), [j] is the concentration of species j (mol^{-1}), $[\ ]^o$ is a standard concentration (mol^{-1}) and γ_j is a parameter that represents the work of interaction of the solute molecules with molecule *j* and is known as the activity coefficient.

$$\mu_j = \mu_j^o + RTIn\left(\gamma_j \frac{[j]}{[\ ]^o}\right) \tag{A.6}$$

Equation A.6 can be expanded further as the product of the activity of the coefficient and concentration are represented as the activity of species j, a_j, which gives;

$$\mu_j = \mu_j^o + RTIn(a_j) \tag{A.7}$$

$$\text{Where, } a_j = \gamma_j \frac{[j]}{[\ ]^o} \tag{A.8}$$

This form of the chemical potential can be substituted into equation A.5 for the model electrochemical reaction giving equation A.9.

$$\mu_A^o + RTIn(a_A) + \mu_B^o + RTIn(a_B) = 2\mu_C^o + 2RTIn(a_C) \tag{A.9}$$

Equation 1.7 can be arranged to have the standard chemical potentials to be replaced by the standard changed in Gibbs free energy, $\Delta G^o_{\text{Reaction}}$, which gives equation A.10.

$$\Delta G^o_{\text{Reaction}} = RTIn(a_A) + RTIn(a_B) - 2RTIn(a_C) \tag{A.10}$$

$$\text{Where, } \Delta G^o_{\text{Reaction}} = 2\mu_C^o - (\mu_A^o + \mu_B^o) \tag{A.11}$$

The equilibrium constant is shown below:

$$\Delta G^o_{\text{Reaction}} = -RTInK \tag{A.12}$$

$$\text{with} \quad K = \frac{a_C{}^2}{a_A a_B} \tag{A.13}$$

This is a general description of a reversible bimolecular reaction for an uncharged system. Within electrochemistry the columbic interaction of charged species has to be taken into account, which is the basis of which is explained the following section [6].

A.3. Electrostatic potential of particles

Electrostatics has a major role in electrochemistry and to link chemical potential to electrochemical potential it is first needed to see the origin of the electrical potential for discrete molecules/particles. The fundamental law of electrostatics of two charged particles in a vacuum can be described by coulombs law, equation A.14, where *f* is the force (Newton, N), Q_x is the valence of the charge (Coulomb, C), ε_0 is the permittivity of the vacuum (a.u.), r is the distance between the two charges (m) and $\hat{r}$ represents the unit vector.

$$f = \frac{Q_1 Q_2}{4\pi\varepsilon_0 r^2}\hat{r} \tag{A.14}$$

Emitting from a single charged particle is phenomenon of an electric field, E_{ele}, which by definition is expressed as the gradient of the electric potential, V_{ele}.

$$E_{ele} = -gradV_{ele} \tag{A.15}$$

Furthermore for a spherical object equation (A.15) can be integrated to give the electric potential, V_{ele}, as a function of position, *r*.

$$V_{ele}(r) = \frac{Q}{4\pi\varepsilon_0 r} \tag{A.16}$$

Equation (A.16) relates the electrical potential to the charge and distance away from the charged particle and as a consequence as the electric potential decreases as the reciprocal of the distance (r).

A.4. Electric potential at interfaces

Free electrons in bulk materials are subject to an isotropic force field due to the symmetrical nature of the electrostatic forces exerted. At a metal surface, such as a metal | vacuum interface as shown in figure A.2, the symmetry is broken and an anisotropic force is projected onto the electrons. Electrons at the surface of the interface are attracted to the vacuum as this extends the electron cloud which reduces their kinetic energy. This is counterbalanced by the columbic charge which attaches them back to the metal bulk. A metal surface containing fixed positive point charges and freely mobile negative charges can be modelled using a Jellium model. This gives an electron density overspill into the vacuum resulting in a di-polar system containing a positive surface charge and an excess of electrons in the vacuum.

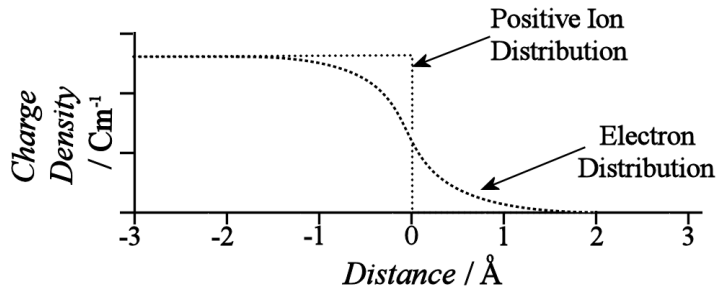

Figure A.2: A plot of charge density against distance at the metal | vacuum interface using a Jellium model. Adapted from reference [6].

Consider the scenario whereby a metal is immersed into an aqueous solution containing a metal salt (such as 0.1 M NaCl). It can be envisaged that the surface of the metal will exhibit an excess of charge (in this case positive charge) and the electric potential will extend into the solution. As a consequence of the presence of an electric potential at the interface, species close to the surface of the metal will be under the influenced of the electric potential. In this case the water molecules will orientate themselves in accordance with the electric potentials and anions present in the solution will be attracted to the surface of the electrode increasing the concentration. This effect can be seen more clearly in figure A.3A and A.3B.

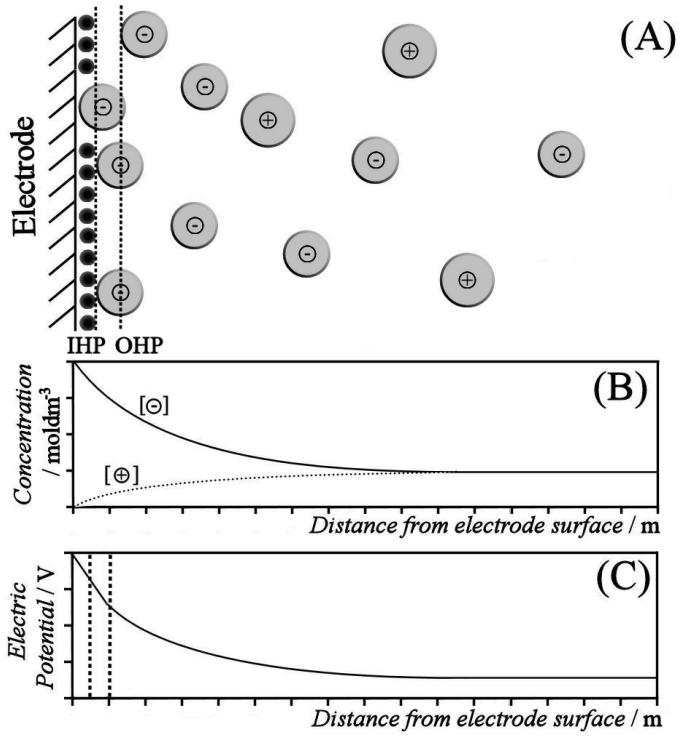

Figure A.3: The metal | aqueous interface with a solute of 0.1 M sodium chloride. (A) Schematic of the metal | solution interface with the metal having an excess of positive charge attaching anions in solution and the orientation of water molecules. (B) Concentration profile of the cations and anions as a function of distance from the metal surface. (C) Plot of electric field as a function of distance from the metal surface [5].

Figure A.3C shows the electric field as a function of distance from the electrode surface. When the electric potential of the metal does not match that of the solution phase the difference is known as the potential difference. Over a small distance (Å) the electric potential decays to that of the solution potential. Initially the decay is liner due to the coverage of anions and orientated dipolar molecules at the metal | solution interface. This layer of anions is known as the outer Helmholtz plane (OHP). Outside of the OHP is the outer diffuse layer the decay is reciprocal in accordance with equation A.16 until the electric potential is the same as the electric potential of the bulk solution.

This description of the metal | aqueous interface is known as the stern model. It is the combination of both the Helmholtz and Gouy-Chapman models which essentially takes into account the attraction of the anions and orientation of polar solvents with thermal motion. If the metal is exposed to a phase where there are very few charge carriers such an organic electrolyte, the potential drop, ca. the distance extended into

the solution for the electric potential to equal that of the solution will be large. In electrochemistry the kinetics of electron transfer depend on having a highly defined and reproducible potential distribution of the electrode surface and hence an excess of a charged salt (known as a background electrolyte) is dissolved in the electrolyte. This depresses the electric potential drop so it extends only a distance of 10-20 Å into the solution.

A.5. Electrochemical potential

The theory that dictates chemical equilibrium can also be applied to electrochemistry. The main difference is that an electrode (a source or sink of electrons) is placed into contact with the reacting species. Consider the electrochemical reaction of two aqueous species $D(aq)$ and $F^-(aq)$ which can be converted into each other via fast electron transfer kinetics.

$$D(aq) + e^- \rightleftharpoons F^-(aq) \qquad \text{(A.17)}$$

Some real examples include the redox chemistry of ferri/ferrocyanide and ferri/ferrocenium ions, equations A.18 and A.19.

$$Fe(CN)_6^{3-}(aq) + e^- \rightleftharpoons Fe(CN)_6^{4-}(aq) \qquad \text{(A.18)}$$

$$Fe(Cp)_2^{+}(aq) + e^- \rightleftharpoons Fe(Cp)_2(aq) \qquad \text{(A.19)}$$

For this reaction to occur a source or sink of electrons must be provided to either donate or remove electrons. A chemically inert conductive material (such as platinum) can be introduced into the solution to become an electrode. Initially before any electron transfer, the potential difference and the change in Gibbs free energy for this reaction will not be zero figure A.4A. This will drive the reaction until equilibrium has been attained for nernstian processes (figure A.4B).

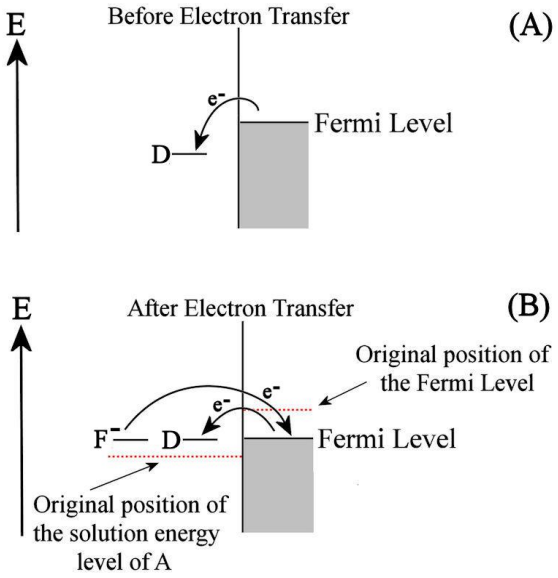

Figure A.4: Plots of the electrode | electrolyte interface including the relative energies of the molecular orbitals of the aqueous species and the bands of the metallic electrode. (A) Before electron transfer and (B) after electron transfer between the flaccid reaction equation 1.17. Picture is adapted from [7]

For the forward reaction to occur electrons from the metal are being transferred to $D(aq)$ to form $F^{-}(aq)$. For the backward reaction to occur, $F^{-}(aq)$ donates an electron to the electrode forming $D(aq)$. Aqueous redox species have molecular energy levels dictated by molecular orbital theory which in contrast to a metallic electrode which posses a continuum of energy levels where the bands have overlapped or are only half filled. The Fermi level of the electrode describes the position of the highest filled band for a metal and is equal to the chemical potential of an electron in a metal. The energy miss alignment of the Fermi level of the metal and the chemical potential of the reactants and product is minimised to zero. This is facilitated by the transfer of electrons from the electrode to the solution lowering the Fermi energy of the electrode. Hence raising the electrochemical potential of product of $D(aq)$ and $F^{-}(aq)$. This electron transfer results in a deficiency in electrons on the surface of the metal electrode. An ion association between the deficiency of electrons on the surface of the electrode and the anions of the solution (in this case $F^{-}(aq)$) can occur [7].

The net result of both the forward and backward reactions, i.e. the position of equilibrium, is either a depletion or an excess of electrons on the surface of the

electrode as is dependant on the electrochemical potentials of the species $D_{(aq)}$, $F^-_{(aq)}$ and $e^-_{(eletrode)}$. To quantity this we need to examine the electrochemical potential for a species j, as shown in equation A.20. The electrochemical potential (of species j), $\overline{\mu_i}$, is defined as the sum of the chemical potential of species j , μ_i, and an electrostatic term which include the products of valence of species j , Z_i , the Faraday constant (96485 Cmol^{-1}) F, and an electrical potential term ϕ (Volt, JC^{-1}).

$$\overline{\mu_j} = \mu_j + Z_j F\varphi^{phase} \tag{A.20}$$

Equation A.7 can be substituted into the above equation to replace the chemical potential with the standard chemical potential and equilibrium factor.

$$\overline{\mu_j} = \mu_j^o + RT\ln a_j + Z_j F\phi^{phase} \tag{A.21}$$

Given this equation and can be applied to the above electrochemical reaction to give the electrochemical Gibbs free energy, $\Delta\overline{G}$, as the electrochemical potentials of the products minus the reactants.

$$\Delta\overline{G} = \overline{\mu}_{F^-} - (\overline{\mu}_D + \overline{\mu}_{e^-}) \tag{A.22}$$

Using equation A.20 this can be expanded further to give:

$$\Delta\overline{G} = [\mu^o_{F^-} + RT\ln a_{F^-} + F\varphi^{solution}] - [\mu^o_D + RT\ln a_D] - [\mu^o_{e^-} + F\varphi^{metal}] \tag{A.23}$$

Rearranging equation A.24 gives:

$$F\left(\varphi^{metal} - \varphi^{solution}\right) = [\mu^o_{F^-} - \mu^o_D - \mu^o_{e^-}] - RTIn\left(\frac{a_{F-}}{a_D}\right) \tag{A.24}$$

The sum standard electrochemical potentials equals the standard Gibbs free energy ΔG^o which can be inserted to give

$$F\left(\varphi^{metal} - \varphi^{solution}\right) = \Delta G^o - RTIn\left(\frac{a_{F-}}{a_D}\right) = -\Delta G \tag{A.25}$$

Where $-\Delta G$ is the Gibbs free energy for the chemical contribution from the reduction of species D(aq) to species F^-(aq) and ΔG^o is the standard Gibbs free

energy. Coincidently the difference in electrical potentials between the metal and solution, $\left(\phi^{metal} - \phi^{solution}\right)$, is the potential difference.

A.6. The Nernst equation

The potential difference is not a measurable quantity as it is impossible to measure the chemical potential difference across a single interface without introducing another interface. This issue is overcome by the introduction of another interface which creates its own steady state (time independent) potential difference between the solution and itself $\left(\phi^{reference} - \phi^{solution}\right)$. By setting this second interface as a reference the electrochemical potential of the initial, working electrode (where the reaction of interest is occurring) can be measured. This gives rise to the Nernst equation, equation A.26:

$$E(V) = V_{working} - V_{\mathrm{Re}\,ference} = E^{o} - \frac{RT}{F} In\left(\frac{a_{F-}}{a_{D}}\right) \quad vs.\ reference \qquad \text{(A.26)}$$

Where $E(V)$ is the measured electrochemical potential measured in volts, $V_{working}$ and $V_{\mathrm{Re}\,ference}$ are the Galvani potential differences between the solution and working references respectively and $E^{o}_{\mathrm{Re}\,f}$ is the electrochemical potential measured for the reaction (equation A.17) under standard conditions against the reference. Assuming that concentrations of ions associated with the reference reaction remain constant this electrochemical potential difference will remain constant. Typical reactions used as references are the silver | silver chloride and the calomel saturated potassium chloride. These can be related to the reduction/oxidation of hydrogen at platinum electrodes under standard conditions which by definition occurs at zero volts. All these references can be interconverted into one another which is useful as the standard hydrogen electrode is not practical in the working environment. The Ag | AgCl | KCl and Hg | Hg_2Cl_2 | KCl reactions are generally placed within their own vessel but are in contact with the bulk solution. From equation A.27 and A.28 the only variable affecting the potential at the interfaces is the concentration of chloride ions surrounding the electrode. The chloride concentration is typically saturated to keep it constant. The contact between the vessel and the solution is generally a glass

frit which minimises the leaching of chloride from the solution. Figure 1.5 is a pictorial image of an SCE electrode

$$AgCl(s) + e^- \rightarrow Ag(s) + Cl^-(aq) \quad \text{(A.27)}$$

$$1/2Hg_2Cl_2(s) + e^- \rightarrow Hg(l) + Cl^-(aq) \quad \text{(A.28)}$$

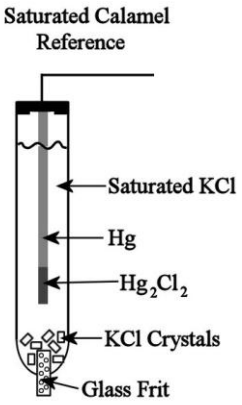

Figure A.5: Schematic of a saturated calomel electrode and its different compartments. Adapted from reference [7] The cell notation is $Cl^-(aq)|Hg_2Cl_2(s)|Hg(l)|Pt(s)$.

In conclusion, a link has been shown between thermodynamics and the measured electrochemical potential of the chemical system in question. The use of stable chemical equilibria to act as a reference for the measured electrochemical at the working electrode is performed.

A.7. Diffusion

The previous section displayed the importance the role of the thermodynamics and its relation to electrochemical potential at equilibrium. But to allow electron transfer to and from the electrode and a dissolved analyte, the molecule must be present at the surface of the electrode as depicted in figure A.6A This is because the method of electron transfer occurs via quantum mechanical tunnelling between the two phases. There are three regions depicted in figure A.6B the first of which is the wavefunction of an electron found in the metal electrode. The second (figure A.6Bii) is the wavefunction of the electron at a function of distance away from the electrode surface and finally (figure A.6Biii) is the wavefunction of an electron bound to a

species. The probability of tunnelling exponentially decreases as a function of distance away from the surface of the electrode. This is because it requires overlap of the quantum mechanical wavefunctions of the donor and acceptor, the electrode and analyte or vice versa. For this process to occur the analyte must be either adsorbed on to or in a close proximately to the electrode surface.

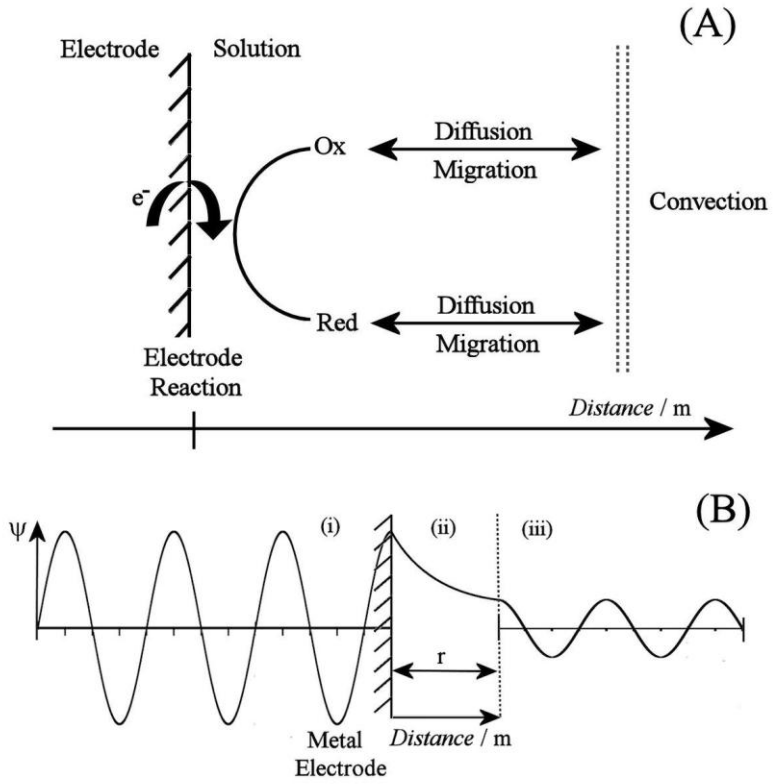

Figure A.6: (A) The movement of analytes to and from the electrode surface. (B) Electron tunnelling occurring from a metal electrode surface (r = 0) to distance r. It is seen that the probability (wavefunction squared) of the electron tunnelling decreases exponentially as a function of distance.

In a liquid there are three modes of transport to induce the movement of aqueous species to the electrode surface: these include migration, convection and diffusion (figure A.6A). Of these migration and diffusion are important for the movement of species on the molecular scale, as these processes bring analytes into close contact (ca. 10-20 Å) to the electrode surface. Migration is the movement of charged ions under the influence of an electric field. Typically transport due to migration is ignored in electrochemistry due to the presence of a background electrolyte.

Convection is the bulk movement electrolyte under the influence of an external force whether it is thermal or physical agitation. Finally, diffusion is the random movement of a chemical species that when an ensemble is considered it is the movement of species from an area of high concentration to an area of low. Diffusion is a consequence of entropy, in particular the second law of thermodynamics as a system is going from an ordered system to a more disordered system. At room temperature (298 K) the kinetic energy of a species is dictated by the Maxwell-Boltzmann distribution [5]. When considering the low mass of a gaseous molecule or atom and the amount of kinetic energy each individual molecule has at room temperature, gases are very dynamic. In the case of liquids, despite the fast mean speeds the retarding interaction with other molecules limits the movement, however most cases are considered to be dynamic.

The random movement of an ensemble of molecules is defined as diffusion and was investigated empirically by Adolf Fick during the 1850s [8] and theoretically Albert Eistein in the early 1900s [9]. Adolf Fick was the first to observe that molecules diffuse down the concentration gradient as shown in figure A.7 as the ensemble of molecules will want to diffuse from an area of high concentration to an area of low concentration.

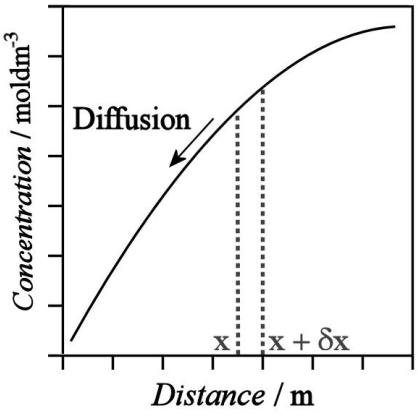

Figure A.7: Plot of concentration against distance. Diffusion occurs from areas of high concentration to areas of low concentration. Adapted from reference [7].

This movement can be quantified by setting boundary conditions (dimensions) of a volume of space where species can diffuse in and out. The term flux is defined as the net result of diffusion into the defined area minus the diffusion out. From figure A.7

it is possible to calculate the diffusive flux of a species by using Fick's first law (equation A.29).

$$Flux(\mathrm{j}) = -D_j \frac{\partial[\mathrm{j}]}{\partial x} \tag{A.29}$$

The terms are defined the $flux(\mathrm{j})$, the amount of species j moving through a unit area in unit time, $\frac{\partial[\mathrm{j}]}{\partial x}$ is the concentration gradient of species j at distance x and D_j is the diffusion coefficient of species j. The diffusion coefficient is specific to each individual molecule and the medium it is surrounded in. The Einstein-Stokes equation relates the diffusion coefficient of a solute molecule subjected to a frictional force to physical parameters (equation 1.30).

$$D_j = \frac{k_B T}{6\pi\eta r_j} \tag{A.30}$$

Here, η is the kinematic viscosity of the medium (measured in cP) k_B is the Boltzmann constant and r_j is the cross sectional area of the molecule in question. Fick's second law concerns the change in concentration (at a known position) with time, $\frac{\partial[\mathrm{j}]}{\partial t}$, which is related to the product of the diffusion coefficient, D, with the double differentiation of the concentration gradient , $\frac{\partial^2[\mathrm{j}]}{\partial x^2}$.

$$\frac{\partial[\mathrm{j}]}{\partial t} = D_j \frac{\partial^2[\mathrm{j}]}{\partial x^2} \tag{A.31}$$

The laws of diffusion not only applied to an electrochemical context as they have applications in both physical sciences and engineering. Diffusion in gases is very fast and dynamic whereas dissolved analytes are slower and typical values are ≈1 x 10^{-10} m^2s^{-1}. From equation A.30 the diffusion coefficient in liquids can be altered by changing the medium, analyte or temperature. Mobile charges in solid state semiconductors also have a diffusion coefficient associated with them. Here it is derived by the measurement of the drift current and can vary considerably [10].

A.8. Adsorption processes

The third key process concerning the probability of an electrochemical reaction occurring is adsorption or de-adsorption of the analyte. During the exchange of an electron between a molecule in solution and the electrode, the molecule must discard any solvating molecules, migrate to the electrode | electrolyte interface and adjust its hydration sphere to receive/donate electrons. This is usually a beneficial process as electrode surfaces can act as heterogeneous catalysts. There is an Arrhenius like dependence for the rate constant for the adsorption of species onto an electrode surface. This gives an activation energy Ea (joule/molecule) for the adsorption of species onto an electrode surface.

$$k_{Adsorption} = A_{Adsorption} \exp\left(\frac{-Ea}{k_B T}\right) \tag{A.32}$$

For most cases the adsorption/de-adsorption of an analyte is a labile process is not a rate determining step. However, an example where the adsorption of species is important is the study of hydrogen evolution. The sorption (adsorption or absorption) of proton, intermediates and hydrogen onto different metals can vary. This variation gives rise to different current densities observed when polarising the electrodes [7].

A.9. Electrode dynamics

To study electrochemical reactions a standard electrochemical cell must be constructed. The electrochemical cell is comprised of a working electrode, a counter electrode, a reference electrode and an electrolyte. Below is a figure of a typical solution electrochemical cell.

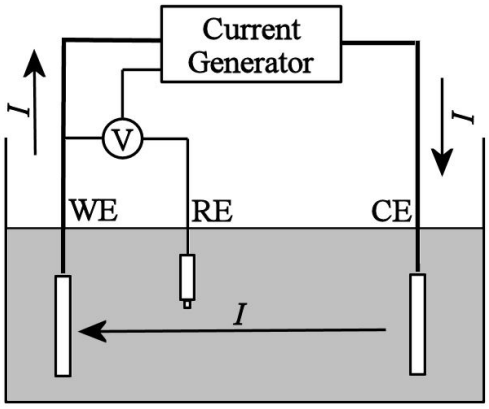

Figure A.8: A standard electrochemical cell where WE is the working electrode, RE is the reference electrode and CE is the counter electrode are immersed in an electrolyte.

The working electrode is composed of typically a highly conducting material (for example, boron-doped diamond, tin-doped indium oxide, glassy carbon). The reference is a high impedance voltmeter. As stated earlier the voltage applied across the interface between the working electrode and solution cannot be measurement directly however, the potential difference between the working and a reference electrode is measured. A feedback loop of the measured potential (a voltage follower) between the working and the reference is fed back into the current generator (power source) so that it does not deviate from the applied potential. The counter electrode is present to complete the circuit as the charge removed/donated from the electrolyte is counterbalanced by counter electrode donating/removing charge to keep the electrolyte electrically neutral. In this case a current follower is used. Counter electrodes are usually made of an inert material such as platinum so that they don't contaminate the solution. The electrolyte is the solution that immerses all three electrodes. The electrolyte has to be electrically conductive, but it can be aqueous, non-aqueous or molten. A background electrolyte is added to ensure the electrolyte has a reasonable conductivity and depresses the potential drop at the surface of the electrode. The power supply is the source of either electrochemical potential or current to the electrochemical cell.

Electrochemistry can be divided into two main experimental techniques which include galvanostatic and potentiostatic. Poteniostatic is the direct measurement of current at a value(s) of voltage. Potentiostatic techniques include: potential step, the

measurement of current when a sudden change in voltage of an electrode occurs and cyclic voltammetry which is the measure of current at a variable voltage. In cyclic voltammetry various waveforms can be superimposed onto a voltage-time waveform to increase sensitivity of the instrument which gives rise to square wave and pulse voltammetry. Current (*I*) refers to the number of electrons flowing through the cell at any one time and is related to the charge by:

$$Q = \int_0^t I dt \qquad \text{(A.33)}$$

Where *I* is current expressed in amps, t is time and Q is the charge. Galvanostatic is the direct measurement of voltage at a value(s) current. Galvanostatic methods are an older technique, however less information can be attained and hence electrochemists prefer potentiostatic measurements. However, it is typically used in electrodeposition with a 2 electrode. Potentiostatic measurements are preferred and more widely used experimental technique in electrochemistry as it is extremely useful for evaluation of redox systems present [11]. Before elaborating potentiostatic techniques in electrochemistry it is necessary to understand the presence of non-faradic and faradic processes on electrode surfaces that govern electrode dynamics.

A.10. Non-faradic or capacitive currents

Capacitive currents originate in the non-homogeneity of a system in question. At any interface there will be some current attributed to capacitive charging. The simplest case of any capacitor is to envisage two conducting metal plates separated by a vacuum figure A.13A

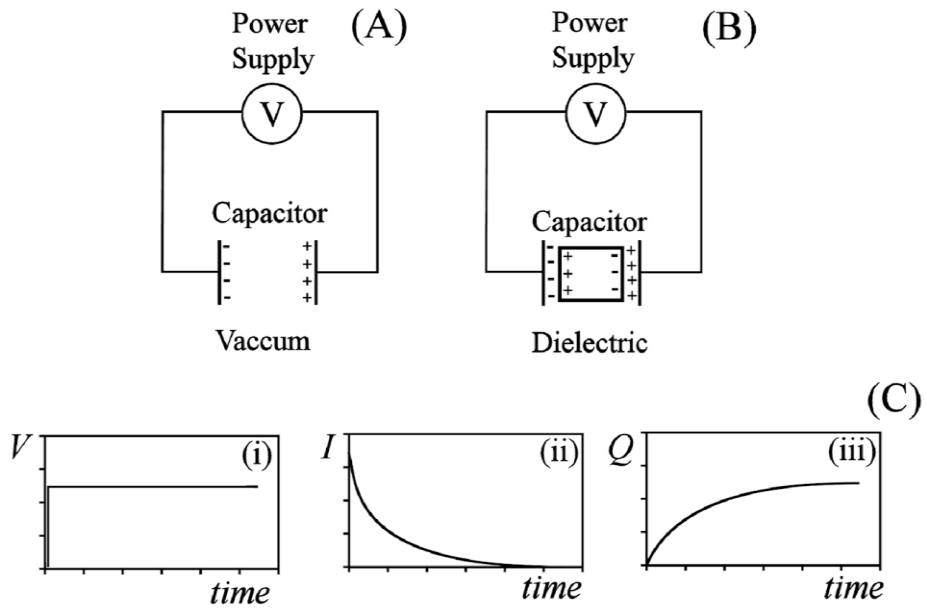

Figure A.9: A schematic of a capacitor connected in an electronic circuit where the space in between is occupied by (A) a vacuum or (B) a dielectric. (C) Represents the time dependence when charging a capacitor for the (i) voltage measured between the plates, (ii) current flow to the plates and (iii) the charge collecting on the plates.

If a fixed electrochemical potential gradient is applied between the two plates an electric field is generated. It is this electric field that drives initially a small amount of current around the circuit charging of the plates. On a very quick time scale certain amount of current will flow from the power source to the plates to charge the surface of the plates (figure A.9) giving rise to a constant capacitance. The charge (Q) stored is proportional to the voltage (V) by relating it to the capacitance (Farad, CV^{-1}) C, equation A.34 :

$$Q = CV \tag{A.34}$$

For this capacitor, the capacitance is dependant upon to the ε_0 dielectric constant of the vacuum ($CV^{-1}m^{-1}$), S the area of the plates (m^2) and d the distance between the plates (m).

$$C = \frac{\varepsilon_0 S}{d} \tag{A.35}$$

If the space between the two plates is filled with an insulating material, a material which has a vastly different dielectric constant, the capacitance measured increases greatly. Essentially, for the same capacitive charge recorded, a smaller electric potential is required due to the dielectric atoms contributing to the total polarisation

charge. A general expression can be deduced for this configuration given by equation A.36:

$$C = \frac{\varepsilon_0 \varepsilon_R S}{d} \qquad \text{(A.36)}$$

Here, an additional dimensionless term is included ε_R which is known as the relative permittivity. This is a proportionality constant that links the capacity of the configuration to the capacitor including the medium to the vacuum scenario.

This explanation can be applied to the double layer that exists at the interface of a metal | electrolyte (figure A.3). As explained in a previous section, for a metal immersed in an electrolyte solution there is an inherent Galvani potential difference between the metal and the bulk solution. If the metal is connected to a potentiostat like that shown in figure A.8 it is possible to probe the capacitance of the interface by cycling the voltage. The current that originates from the cycling can be integrated to attain the charge of the double layer. The capacitance of a system is not constant as different perturbation frequencies cause the capacitance to change but on most electrochemical timescales it can be assumed to be constant. By applying a triangular waveform between two voltage values and recording the current it is possible to attain the capacitance of the interface. A typical response is shown below:

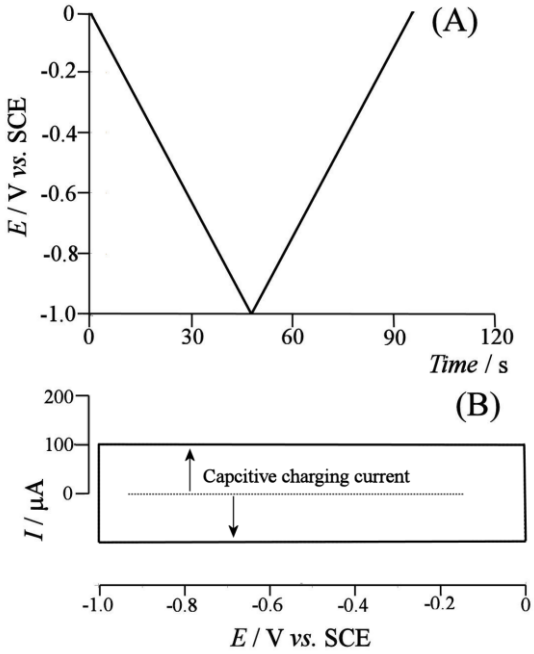

Figure A.10: (A) The voltage waveform applied across an electrode | electrolyte double layer (B) resultant current response for an electrode | electrolyte interface.

The capacitance (on this time scale) originates from the orientation of polar molecules at the electrode | electrolyte interface. This analogous to the charging of the capacitance plates but originates from charging of the double layer. Each region described in figure A.3 the inner Helmholtz plane and the outer Helmholtz plane has its own capacitance associated with it and can be regarded as capacitors in series and this follows the law:

$$\frac{1}{\mathrm{C_{Total}}} = \sum_{j=1}^{n} \frac{1}{C} \tag{A.37}$$

Which is the sum of the inverse of all capacitances and for the electrochemistry of a metallic electrode

$$\frac{1}{\mathrm{C_{Total}}} = \frac{1}{C_{IHP}} + \frac{1}{C_{OHP}} \tag{A.38}$$

The capacitance measured changes as a function of frequency of perturbation. This is due to the relative permittivity of the electrolyte which is not constant. Returning to the experimental set up in figure A.9B, at very high frequency the relative permittivity (and hence the capacitance measured) is dependant on the polarisation of the medium molecules as all other process are slow on the time scale of the modulated voltage. Decreasing the frequency causes contribution to the capacitance from first vibration, then liberation and finally rotation and reorientation of dipoles.

A.11. Faradic currents and cyclic voltammetry

Section A.5 described the effect of electrochemical potential upon the ratio of products to reactants or vice versa. This section concerns the description behind the kinetics (ca. rate) of electron transfer for faradic currents. Faradic currents refer to electron transfer reactions whereby a species present at the electrode surface (either immobilised or adsorbed from the solution) undergoing an electron transfer. Consider an electrochemical set up as shown in figure A.12, used in a potentiostatically controlled manner with presence of dissolved species $\mathrm{D(aq)}$ and an excess of background electrolyte. Species $\mathrm{D(aq)}$ can undergo a reduction to form $\mathrm{F^{-}(aq)}$ as shown in equation A.17. Below is the applied waveform of the voltage

and the resulting cyclic voltammograms which is a plot of applied voltage versus measured current.

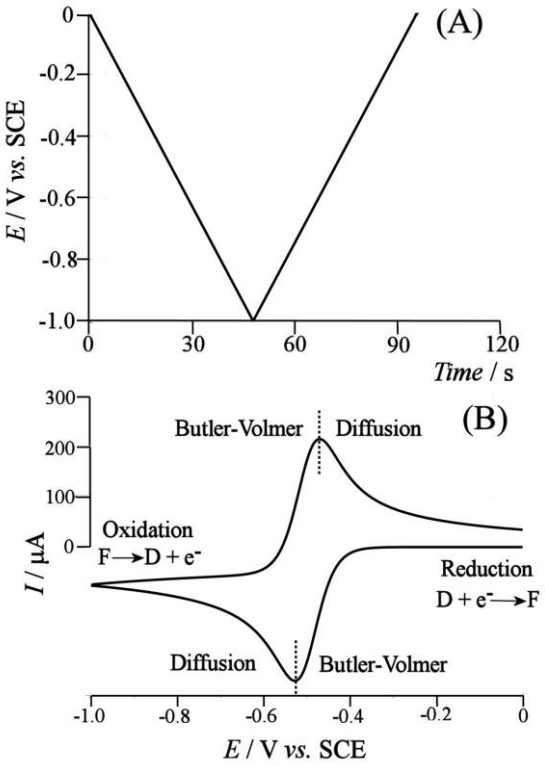

Figure A.11: Linear sweep voltammograms for $D(aq)$ being reduced to $F^{-}(aq)$. (A) Applied waveform of voltage with time and (B) the resultant voltammogram of a diffusion controlled species D, simulated using digisim [12].

The application of the waveform in this manner is known as cyclic voltammetry. Initially at the start of the voltammograms (ca. 0 V vs. SCE) there is a small amount of current flowing, this originates from the capacitance of the double layer. At approximately -0.4 V vs. SCE there is an exponential increase in the current which reaches a maximum before exponentially decreasing. This peak can be split up into two distinct regions where the kinetics of reduction are controlled by two different process. At the onset of cathodic current the kinetics are dictated largely due to Butler-Volmer kinetics. To explain Butler-Volmer kinetics it is necessary to consider the electron transfer between the aqueous species $D(aq)$ to $F^{-}(aq)$. As this reaction is reversible it can be regarded as two separate reactions equations A.39 and A.40.

$$D(aq) + e^{-} \xrightarrow{k_{Red}} F^{-}(aq) \qquad (A.39)$$

$$F^{-}(aq) \xrightarrow{k_{Ox}} D(aq) + e^{-} \quad \text{(A.40)}$$

Where k_{Red} and k_{Ox} are rate constants for the reduction of $D(aq)$ and the oxidation of $F^{-}(aq)$. By measuring the current it is possible to infer the net process of which reaction is occurring.

$$i_{measured} = nFA[k_{Red}[D]_{electrode} - k_{Ox}[F^{-}]_{electrode}] \quad \text{(A.41)}$$

At equilibrium the product of the rate constant and the concentration for both the forward and backward reaction should be equal, meaning that zero current should be observed, however the surface concentration of species $D(aq)$ and $F^{-}(aq)$ are not the same. This gives rise to an inequality in the rate constants of k_{Red} and k_{Ox}. The rate constants of k_{Red} and k_{Ox} are potential dependant and the Galvani potential i.e. the difference in the potential of the electrode and the bulk solution will govern which reaction will predominate for the non equilibrium case. Both the rate constants k_{Red} and k_{Ox} can be given an Arrhenius like dependence which relates the activation energy of the transition state.

$$k_{Red} = A'_{Red} \exp\left(\frac{-\Delta G^{+}_{Red}}{RT}\right) \quad \text{(A.42)}$$

$$k_{Ox} = A'_{Ox} \exp\left(\frac{-\Delta G^{+}_{Ox}}{RT}\right) \quad \text{(A.43)}$$

Where ΔG^{+}_{Red} and ΔG^{+}_{Ox} are the activation energies for the transition states ($kJmol^{-1}$) for the forward and backward reaction and the pre-exponential factors A'_{Red} and A'_{Ox} have a frequency term associated with them. By imposing an electrode potential $E_{applied}(V)$ at the working electrode different from the equilibrium potential E_{eq} the terms ΔG^{+}_{Red} and ΔG^{+}_{Ox} can be expanded to give:

$$\Delta G^{+}_{Red} = \Delta G^{0}_{Red} - \alpha nF\eta \quad \text{(A.44)}$$

$$\Delta G^{+}_{Ox} = \Delta G^{0}_{Ox} + (1-\alpha)nF\eta \quad \text{(A.45)}$$

$$\text{Where } \eta = (E_{applied} - E_{eq}) \quad \text{(A.46)}$$

Where $\Delta G^0_{\mathrm{Red}}$ and ΔG^0_{Ox} are the standard Gibbs energy of formation of the transition state, α is known as the charge transfer coefficient and represents the fraction of Gibbs free energy operating on the transition state and η is known as the overpotential. This can be represented graphically where a transition state plot below.

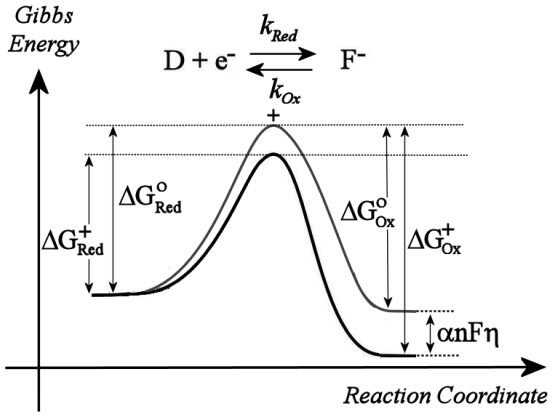

Figure A.12: A plot of the Gibbs free energy versus the reaction coordinate for reduction of $\mathrm{D(aq)}$ to $\mathrm{F^-(aq)}$. Here there are two situations considered the grey line constituents to the formation of the transition state under standard conditions with no applied potential, giving rise to $\Delta G^0_{\mathrm{Red}}$ and ΔG^0_{Ox}. Whereas the black is the plot of the formation of the transition state when a reducing potential is applied to the surface of the electrode, the extra $\alpha nF\eta$ constitute to the energy input from the electrode surface.

Equations for the reduction and oxidation (equations A.44 and A.45) can be substituted into equations (A.42 and A.43) to give:

$$k_1 = A'_{\mathrm{Red}} \exp\left(\frac{-\Delta G^0_{\mathrm{Red}}}{RT}\right)\exp\left(\frac{-\alpha nF\eta}{RT}\right) \qquad \text{(A.47)}$$

$$k_2 = A'_{Ox} \exp\left(\frac{-\Delta G^0_{Ox}}{RT}\right)\exp\left(\frac{-(1-\alpha)nF\eta}{RT}\right) \qquad \text{(A.48)}$$

Assuming the formal redox potential barrier is symmetrical and that the pre-exponential factors and the standard Gibbs free energy for the transition state are equal, equations A.47 and A.48 can be simplified to:

$$k_1 = k^0 \exp\left(\frac{-\alpha nF\eta}{RT}\right) \tag{A.49}$$

$$k_2 = k^0 \exp\left(\frac{-(1-\alpha)nF\eta}{RT}\right) \tag{A.50}$$

$$\text{Where } k^0 = A_{\mathrm{Red}} \exp\left(\frac{-\Delta G^0_{\mathrm{Red}}}{RT}\right) = A_{Ox} \exp\left(\frac{-\Delta G^0_{Ox}}{RT}\right) \tag{A.51}$$

Substituting these two equations into equation A.41 gives a basic form of the Butler-Volmer equation. Here it is seen that the overpotential has a huge effect of the rate constant of reaction and explains the exponential growth in current at the onset of the reaction. This dependence of the electrochemical rate constant on the electrode potential usually dominates the behaviour of the electrode processes.

$$i_{measured} = nFAk^0\left[\exp\left(\frac{-\alpha nF\eta}{RT}\right)[\mathrm{D}]_{electrode} - \exp\left(\frac{-(1-\alpha)nF\eta}{RT}\right)[\mathrm{F}^-]_{electrode}\right] \tag{A.52}$$

It follows that the electrochemical potential has an exponential effect on the rate constants of reaction. This is in agreement with the simulated voltammograms showed in figure A.11B at the onset of the reduction. A peak is observed as after a certain point there is a deficiency in the amount of available analyte at the electrode surface and as a consequence diffusion from the bulk has to occur to replenish the analyte $\mathrm{D(aq)}$. The kinetics of electrochemical reduction or oxidation are given by the Fick's laws of diffusion as discussed in section A.7. As the overpotential is large, the rate constant for the reduction is large and hence any analyte arriving at the electrode will be reduced very quickly. This diffusion controlled rate of reaction for the reduction of D(aq) past the peak can be explained by the following expression:

$$\frac{I_{red}}{nF} = -D_{\mathrm{D}}\left(\frac{\partial[\mathrm{D}]}{\partial x}\right)_{x=0} \tag{A.53}$$

A useful quantity to define in electrochemical terms is the diffusion length profile $\delta_{diffusion}$. This is defined as length/area/volume where the concentration gradient of any species does not equal zero and hence diffusion occurs. In electrochemical terms this is the distance between the electrode surface and the bulk of the electrolyte and is due to the depletion/accumulation of species during cycling.

Below in figure A.13 a plot of the diffusion length profile during different points of the cyclic voltammograms recorded in figure 1.11B. Here at the start of the cycle (t_1) only a small amount of electrolyte is converted at the surface of the electrode. As the reaction proceeds the diffusion length profile becomes bigger (t_2) before reaching t_3 which has the highest gradient and therefore the highest diffusion (equation A.29). Past t_3 the electrode is depleted of analyte and diffusion is now the limiting step to replenish the electrolyte at the surface of the electrode.

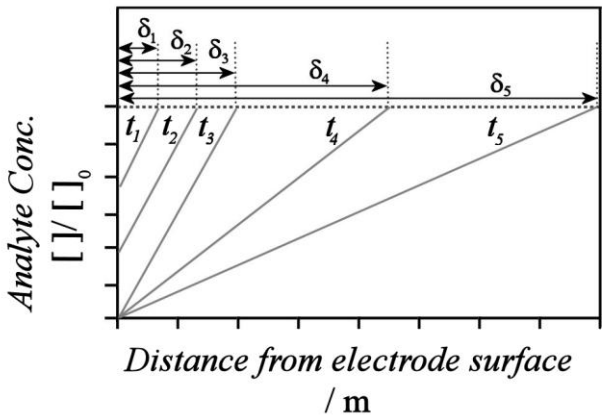

Figure A.13: A plot representing of the diffusion length profiles measured at different times (t_1, t_2, t_3, t_4 and t_5) during a cyclic voltammogram. Each diffusion time has a diffusion length associated with it ca. δ_1, δ_2, δ_3, δ_4 and δ_5.

The system described above is reversible and for such as system the peak current observed (ca. the maximum current for oxidation or reduction) is given by the following equation:

$$I_{peak} = 0.469\alpha^{1/2} n^{3/2} FA[\ ]_{Bulk}\sqrt{\frac{FDv}{RT}} \qquad \text{(A.54)}$$

A.12. Immobilised systems

Immobilised systems include those whereby a surface bound analyte is probed using electrochemistry. The main difference from that of a diffusion controlled electrochemical reaction is that the analyte is not replenished from the bulk. The surface bound analyte can be considered to form a film which can vary in morphology from a dense mono layer to a porous network as shown below:

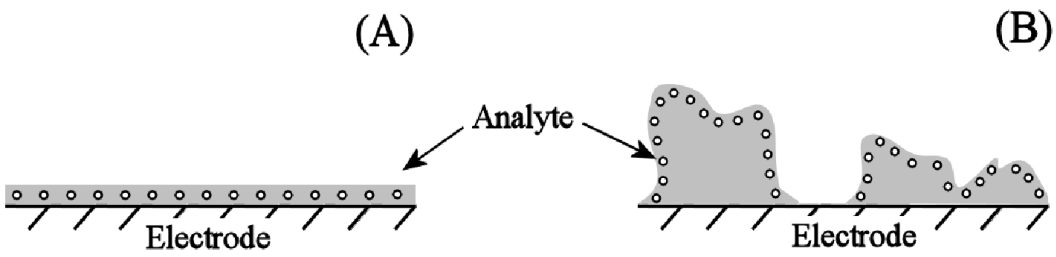

Figure A.14: Different scenarios of an immobilised system (A) dense monolayer and (B) porous covered electrode.

A porous electrode has complications arising from a discontinuous film formation, substrate contribution and electron transfer propagating through the film kinetics and hence the dense monolayer (figure A.14A) will be taken as an example. It is possible to imagine that analyte $D(s)$ can be immobilised onto an electrode surface to give a complete homogeneous monolayer (of 100 % coverage). This electrode can be assembled in a standard 3 electrode cell, immersed in a background electrolyte (figure A.8) and as before species $D(s)$ can be reversibly electrochemically reduced to $F^{-}(s)$ by the following equation.

$$D(s) + e^{-} \rightleftharpoons F^{-}(s) \tag{A.55}$$

The amount of $D(s)$ and $F^{-}(s)$ at the electrode surface can be quantified by introducing the surface coverage which for species j is, Γ_j (molcm^{-2}). This represents the amount of analyte at the electrode surface in contact with the electrolyte and electrode.

$$\Gamma_D + \Gamma_{F^-} = \Gamma_{(Total)} \tag{A.56}$$

From the Nernst equation A.26 it is possible rearrange the formulas to form.

$$E = E^o - \frac{RT}{nF}\log\left(\frac{\Gamma_D}{\Gamma_{F^-}}\right) \tag{A.57}$$

$$\frac{\Gamma_D}{\Gamma_{F^-}} = \exp\left(\frac{nF\left(E - E^o\right)}{RT}\right) \tag{A.58}$$

It is then possible to rearrange equation A.58 by substitution into equation A.56 to give the surface coverage as a function of species

$$\Gamma_D = \frac{\exp\left(\frac{nF\left(E-E^o\right)}{RT}\right)\Gamma_{Total}}{1+\exp\left(\frac{nF\left(E-E^o\right)}{RT}\right)} \tag{A.59}$$

$$\Gamma_{F^-} = \frac{\Gamma_{Total}}{1+\exp\left(\frac{nF\left(E-E^o\right)}{RT}\right)} \tag{A.60}$$

As can bee seen from the above equations when changing the voltage away from the equilibrium case to an over potential exponentially affects the ratio of different species at the electrode surface (much the same way as shown for Faradaic currents diffusion controlled).

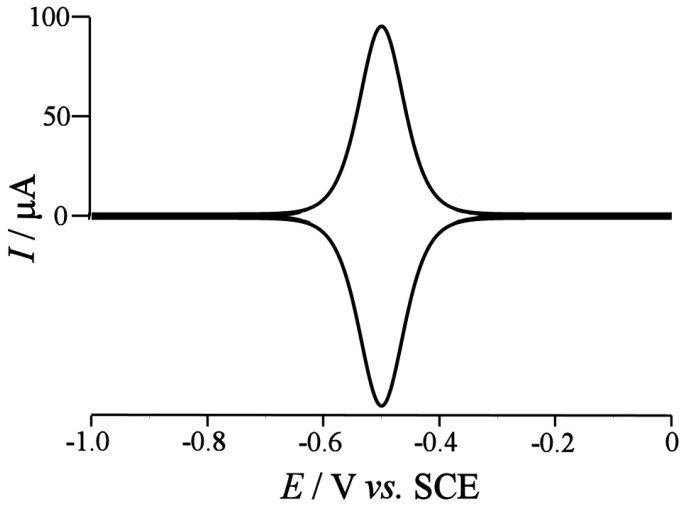

Figure A.15: A simulated cyclic voltammogram for an immobilised species on the surface of an electrode. The waveform of the applied voltage is shown in figure A.11. Simulated using digisim [12]

Above is a simulated cyclic voltammograms of an immobilised monolayer. At potentials more positive than the reversible potential for the reduction reaction the current observed is small and due to capacitive charging. The current exponentially increases upon the onset of the reduction for the same reason as the diffusion controlled case. The peak signifies depletion in the concentration of the D(s) at the

electrode surface leading to a reduction in magnitude of current measured. The current measured is related to the amount of species at the surface of the electrode by the following expression.

$$\frac{I}{FA} = \frac{\partial \Gamma_{F^-}}{\partial t} = -\frac{\partial \Gamma_D}{\partial t} \tag{A.61}$$

The charge can be calculated by integrating the charge from 0 V to -1 V for the reduction for this reaction and is directly related to the amount of material present at the electrode surface.

$$Q = \int_0^{Total} I dt = AF\Gamma_D \tag{A.62}$$

Depending on the nature of the analyte | electrolyte and the analyte | electrode interfaces the possibility of different capacitive charging must be taken into consideration. For the case of the immobilised species the peak current can be estimated as

$$I_{peak} = \frac{F^2 \nu A \Gamma_{Total}}{4RT} \tag{A.63}$$

Considering the scenario where the electrode is covered by a porous electrode the situation is very different. Due to the porous nature of the film current contributions from the electrode | electrolyte interface as well as diffusion throughout the film must be taken into consideration. The mechanism of charging the film is usually by injecting electrons (via the triple phase boundary of electron | film | electrolyte) into the films which can diffuse throughout the material.

A.13. Sweep rate for diffusion and immobilised systems

A unique parameter of the cyclic voltammetry is that the speed at which the applied potential can be varied between the chosen limits (ca. the scan rate). This typically dictates the magnitude of the current flowing to or from the electrode at any given time. Figure A.15 displays simulated examples of the effect of scan rate for diffusion and immobilised controlled species.

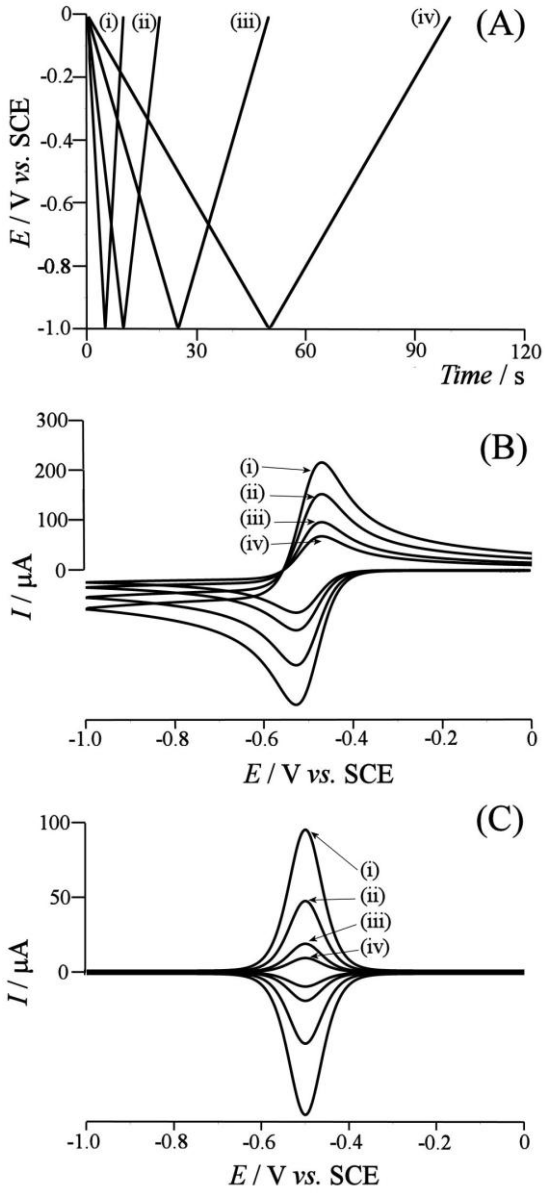

Figure A.15: Theoretical plots from Digisim [12] of cyclic voltammograms of a diffusional and immobilised controlled species (A) Time-voltage waveform at different scan rates (i) 100 mVs^{-1} (ii) 50 mVs^{-1} (iii) 20 mVs^{-1} and (iv) 10 mVs^{-1}. Typical faradaic response for both (B) a diffusion controlled species and (C) an immobilised species.

As can be seen in figure A.15A increasing the scan rate decreases the time it takes for the voltage to be scanned between the voltage limits. The corresponding cyclic voltammograms measured for the diffusion controlled and immobilised systems are shown in figures A.15B and A.15C. By increasing the scan rate the magnitude of the peak current increases in accordance with the two equations A.54 and A.63 which describe the peak current for a diffusion and immobilised controlled species. For the

immobilise case the peak current is dependent linearly on the scan rate whereas for the diffusion controlled case the current is dependent on the square root of scan rate. Plots of scan rate versus peak currents are useful as they can distinguish between diffusion controlled and immobilised systems.

A.14. Electrodeposition

Electrodeposition is a form of electrochemistry whereby either metal or metalloid ions in solution are typically reduced to neutral species. This neutral species precipitates out of solution onto an electrode surface (equation A.64). This can be achieved by either potentiostatic (applied potential, recorded current) or galvanostatic (applied current, recorded potential) techniques.

$$M^{n+}_{(aq)} + ne^- \rightarrow M_{(s)} \tag{1.64}$$

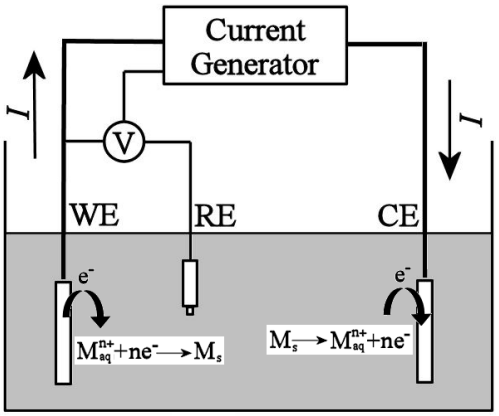

Figure A.16: An electrochemical cell used to electrodeposit an analyte onto the working electrode whilst simultaneously dissolving the counter electrode to keep the conservation of charge. What can be done is to anodically dissolve the counter electrode to keep a constant concentration of analyte in solution.

The electrodeposition or electroplating of metallic films has been known for a long time, with applications in manufacture of metallic mirrors, corrosion resistant surfaces and more recently semiconductors [13]. There are several key advantages when using electro-deposition.

- The technique has been known and developed for many years.
- It is possible to attain very uniform films on large substrates that may not be planar.
- The composition of the electrodeposit can be extensively controlled; this includes modulated structures and compositions that are non-equilibrium.
- Can be low cost, high throughput and easily scalable.

Despite these advantages there are a variety of challenges associated with electrodeposition of thin films. A number of methods; electrochemical, physical, mechanical and spectroscopic are used to evaluate the films formed allowing for optimisation [14].

Michael Faraday is acknowledged for discovering and characterising electroplating. Two key laws of electrolysis are:

1. Faraday's First law: "The total amount of chemical change produced by an electric current is proportional to the total charge passing through the electrolyte".
2. Faraday's Second law: "The masses of the different substance liberated in the electrolysis are proportional to their chemical equivalent weights" [13].

The statements can be expressed together mathematically. Below is an equation that relates mass change to the amount of current passed during the experiment (charge).

$$\Delta m = \frac{QM_w}{nF} \tag{A.65}$$

Δm is the change in mass, Q is the charge, (integrated current over time), M_w is the molar mass of the substance, n is the number or electrons transferred and F is the faraday constant. By knowing the charge, area of electrode and density of the material it is possible to designate a cut off value for the amount (and thickness) of material to be electroplated.

A.15. Electrochemical impedance spectroscopy

Impedance spectroscopy is a technique that obtains physical parameters of a system using circuit analysis (figure A.17A). In electrochemical impedance spectroscopy this is typically done by modulating the voltage of an electrode and measuring the current response. It is possible to fit the impedance data using circuit elements which follow known electrical laws. For this we have to examine the four possible electrical components figure A.17B.

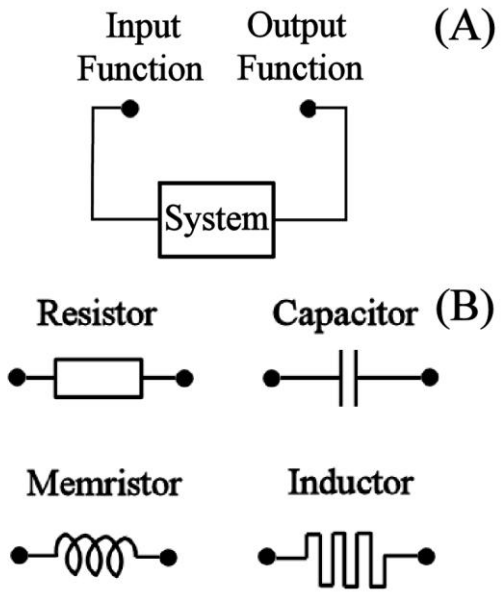

Figure A.17: (A) Representation of an impedance experiment here the system changes an input function which can be model using circuit analysis. (B) The four circuit elements; the resistor, capacitor, memristor and inductor and their symbols.

In electrochemistry, the two most common observed circuit elements are the resistor and the capacitor. A resistor links voltage and current (equation A.66) and it can be inferred that a resistor loses energy as heat to the surrounds. A capacitor relates the charge (which is the integration of the current with time) to the applied voltage (equation A.67). Essentially a capacitor stores charge as an electric field and relates the charge to the voltage.

$$dV = RdI \tag{A.66}$$

$$dq = CdV \tag{A.67}$$

An inductor links a magnetic field (φ) to current and a memristor which links magnetic field to charge. In electrochemical terms the only circuits that are used are typically either resistors or capacitors. However, an inductor effects have to be taken into consideration at very high frequencies ca. >1 MHz.

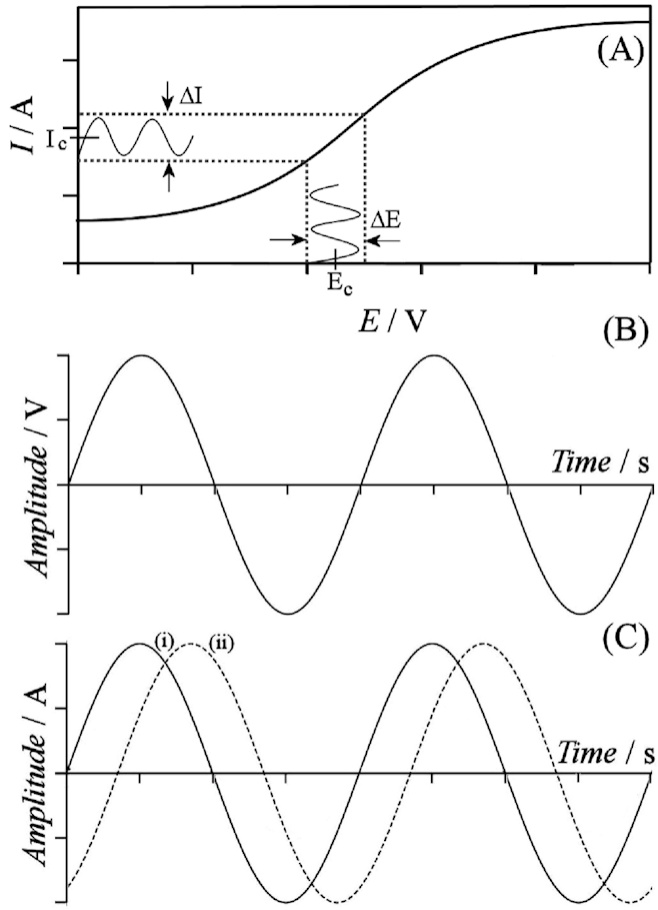

Figure A.18: (A) A linear sweep voltammograms for a redox system at the electrode surface. A DC voltage can be chosen and a small modulated voltage can be superimposed with measurement of the modulation in current. Sinoudioal plots of the applied voltage (B) and measured current (C) for two different cases: (i) a resistor and (ii) a resistor and capacitor.

Impedance (Z) is a transfer function to equate the change in voltage and current. Electrochemical impedance is performed in a standard three electrode cell. Typically small perturbations (5 to 10 mV_{RMS}) in voltage are superimposed onto a fixed DC voltage (versus a reference) as seen in figure A.18A. The small perturbations ensure a linear current response. Figure A.18B is applied voltage waveform to the electrode surface and figure A.18C is the measured current response. Here the frequency, phase and amplitude are set and the system can respond to the imposed voltage sine

wave giving two possible outcomes. It is possible that the current measured is in phase (e.g. no time lag) suggesting that the impedance is equivalent to the resistance A.18Ci. The resistance can be described by Ohm's law equation A.68.

$$R = \frac{V}{I} \tag{A.68}$$

An ideal resistor is frequency independent and as a result the proportion of the decrease in amplitude will be constant for any frequency. This means that the electrical resistance is the measured impedance.

$$Z_{(resistor)} = \frac{\Delta V}{\Delta I} \tag{A.69}$$

A second scenario can be thought of as a phase shift superimposed onto the resistance waveform (figure A.18Ci). This originates from the cell acting as a capacitor as the energy is stored and released at a later time figure A.18Cii. Impedance measured from capacitors is frequency dependant however the capacitance itself is frequency independent. Assessing the time dependant capacitance is not trivial. A mathematical expression of the sine wave superimposed onto a DC voltage is given by;

$$E_t = E_0 \sin(\omega t) \tag{A.70}$$

Here E_t is the voltage applied (V), E_0 is the DC voltage applied (V), ω is the angular frequency and t is the time. From equation A.67 it is known that a capacitance relates the charge to the applied voltage. The charge can be converted to current (by differentiation) to give for the applied voltage;

$$I_t = C\frac{\partial E_0 \sin(\omega t)}{\partial t} \tag{A.71}$$

$$I_t = \omega C E_0 (\cos \omega t) \tag{A.72}$$

This equation can be converted back into a Sin wave by including a phase shift

$$I_t = \omega C E_0 \left(\sin \omega t + \frac{\pi}{2} \right) \tag{A.73}$$

A general consideration is that at high frequency a capacitor will not store charge as the perturbations are too quick to allow charging of the surface whereas at a lower frequency the capacitor will store charge and inhibit the flow of current. It is useful to define a term the capacitive reactance χ_C which is equal to the inverse of the frequency multiplied by the capacitance (ca. $\chi_C = 1/\omega C$).

$$I_t = \frac{E_0}{\chi_C}\left(\sin \omega t + \frac{\pi}{2}\right) \tag{A.74}$$

Equation A.75 represents the impedance due to the resistance and capacitance. The time dependence of the impedance due to capacitance can be distinguished from resistance by times it by a complex number (j).

$$Z = \left(R - j\chi_C\right) = \frac{\Delta V}{\Delta I} \tag{A.75}$$

The impedance can be separated further into the real $(Z_{\mathrm{Re}al})$ and imaginary parts (jZ_{imag}).

$$Z = Z_{\mathrm{Re}al} - jZ_{imag} \tag{A.76}$$

The magnitude and phase of the impedance can be obtained by the following equations (equations A.77 and A.78):

$$Z^2 = {Z_{\mathrm{Re}al}}^2 - j{Z_{imag}}^2 = R^2 - \chi_C^2 \tag{A.77}$$

$$\tan\phi = \frac{Z_{imag}}{Z_{\mathrm{Re}al}} = \frac{\chi_C}{R} = \frac{1}{\omega RC} \tag{A.78}$$

The impedance can be graphically represented in two ways. Either log |Z| and ϕ can be plotted versus ω, this is known as a Bode plot. Alternatively, it is possible represent the impedance in a Nyquist plot which is where $Z_{\mathrm{Re}al}$ is plotted versus Z_{imag}.

References

[1] S. Dale, C. Cummings, F. Marken, Electro. Chem. Comm. 13 (2011) 154

[2] D. Pletcher, F. Walsh, *Industrial electrochemistry*, 2nd ed., Blackie Academic & Professional (1993)

[3] Metrohm 797 VA Computrace for trace analysis and metal speciation, web: http://info.metrohmusa.com/products/electrochem_797VA_ov.asp

[4] A. Cass, G. Davis, G. Francis, H. Hill, W. Aston, I. Higgins, E. Plotkin, L. Scott, A. Turner, Anal. Chem., 56 (1984) 667

[5] P. Atkins, J. Paula, *Physical Chemistry*, Oxford University Press (2002)

[6] H. Girault, *Analytical and physical electrochemistry*, EPFL Press (2004)

[7] R. Compton, C. Banks *Understanding Voltammetry*, World Scientific Publishing Co. Pte. Ltd. (2007)

[8] A. Fick, J. of Science, 16 (1855) 30

[9] A. Einstein Annalen de Physik, 17 (1905) 549

[10] H. Rosenberg, *The Solid State* 3rd ed., Oxford science Publications (1988)

[11] C. Hamann, A. Hamnett, W. Vielstich, *Electrochemistry*, 2nd ed., Wiley-VCH (1998)

[12] Digisim, BASi. Web: http://www.basinc.com/products/ec/digisim/

[13] R. Pandey, S. Sahu, S. Chandra, *Handbook of Semiconductor Electrodeposition*, Marcel Dekker, Inc. (1996)

[14] A. Vagramyan, Z. Soloveva, *Technology of Electrodeposition*, Robert Draper Ltd., (1959)